Self-consistent methods for interacting lattice bosons with U(1)-symmetry-breaking

Dissertation
der Fakultät für Physik
der Ludwig-Maximilians-Universität München

vorgelegt von

Dario Frank Hügel
aus München

2018

Erstgutachter: Prof. Dr. Lode Pollet
Zweitgutachter: Prof. Dr. Frank Pollmann
Datum der Abgabe: 10. Januar 2018
Datum der mündlichen Prüfung: 26. Februar 2018

Kurzfassung

Diese Arbeit befasst sich mit der Entwicklung selbstkonsistenter Methoden für die numerische Simulation von wechselwirkenden bosonischen Gittersystemen. Das Ziel ist die Herleitung von Methoden mit niedriger numerischer Komplexität und hoher Zuverlässigkeit, die auf komplexe Gitterprobleme angewandt werden können, welche für gängige Methoden wie Pfadintegral Quanten Monte Carlo (QMC) oder die density matrix renormalization group außer Reichweite sind.

Im ersten Teil entwickeln wir die Selbst-Energie Funktional Theorie (SFT) für bosonische Systeme. Der Formalismus erweitert frühere Arbeiten zum Fall spontaner $U(1)$-Symmetriebrechung, und kann sowohl auf translationsinvariante Systeme als auch auf Systeme mit endlicher Unordnung durch Störstellen angewandt werden. SFT beinhaltet die bosonische Version von dynamical mean-field theory, kann aber auch als genereller nicht-perturbativer Formalismus zur Entwicklung anderer diagrammatisch korrekter Näherungen im thermodynamischen Limes verwendet werden. Indem wir nur drei variationale Parameter verwenden, sind wir in der Lage sowohl im translationsinvarianten Bose-Hubbard Modell (BHM) als auch im BHM mit endlicher Unordnung numerisch exakte QMC Ergebnisse mit hoher Genauigkeit durch SFT zu reproduzieren. Des weiteren, analysieren wir systematisch lokale Spektralfunktionen, welche durch QMC nicht vollständig aufgelöst werden können. Wir beobachten, dass der Phasenübergang für endliche Unordnung von der suprafluiden zur Bose-Glas Phase bei starker Wechselwirkung durch die Perkolation suprafluider Regionen getrieben wird, welche in der Nähe doppelt besetzter Gitterplätze entstehen und zu einem kleinen endlichen Kondensatanteil über einem stark lokalisierten Hintergrund führen.

Im zweiten Teil entwickeln wir den reciprocal cluster mean-field (RCMF) Formalismus und wenden diesen auf das stark wechselwirkende Harper-Hofstadter-Mott Modell (HHMM) an. In RCMF wird das volle Gitter im thermodynamischen Limes auf Cluster mit einer endlichen Anzahl von Gitterplätzen projeziert. Durch eine mean-field Näherung werden in einem nächsten Schritt diese Cluster voneinander auf eine Art entkoppelt, die die Translationsinvarianz des Systems, und dadurch die Symmetrien der Dispersionsrelation erhält. Das mit RCMF berechnete Grundzustands-Phasendiagram des HHMM beinhaltet band-isolierende, suprafluide, und suprasolide Phasen. Außerdem beobachten wir unkondensierte flüssige Phasen ohne Energielücke bei ganzzahliger Füllung, sowie metastabile fraktionale Quanten-Hall (fQH) Phasen. Die fQH Phasen, die von anderen Methoden als Grundzustand gefunden werden, werden vermutlich durch den RCMF Ansatz unterschätzt. Wir zeigen auch, dass eine quasi-eindimensionale Zylindergeometrie topologisch nicht-triviale Phasen mit endlicher Energielücke im HHMM stabilisiert. Wir beobachten quasi-eindimensionale Analoge von fQH Grundzuständen bei halbzahliger Füllung, sowie unkonventionelle nicht-entartete Grundzustände mit quantisierter Leitfähigkeit bei ganzzahliger Füllung. Durch den systematischen Vergleich von Ergebnissen aus RCMF und exakter Diagonalisierung (ED), sind wir in der Lage endgültige Vorraussagen zu den Phasengrenzen des HHMM auf dem Zylinder zu treffen. Dies ist möglich, da die zwei Methoden sich dem thermodynamischen Limes von verschiedenen Seiten aus nähern (RCMF bevorzugt Phasen ohne Energielücke, ED welche mit endlicher Energielücke).

Abstract

This thesis is dedicated to the derivation and benchmarking of self-consistent numerical methods that can be applied to interacting bosonic lattice models. The central goal is to derive methods with low numerical complexity but high accuracy, to be applied to complex systems which are out-of reach for established methods such as path integral quantum Monte Carlo (QMC) or the density matrix renormalization group.

In the first part we derive the self-energy functional theory (SFT) for bosons. Building upon previous works on lattice systems without $U(1)$-symmetry-breaking, we systematically extend SFT to the possibility of a broken $U(1)$-symmetry and the presence of disorder. SFT incorporates bosonic dynamical mean-field theory as a certain limit, and represents a general non-perturbative framework, enabling the construction of diagrammatically sound approximations in the thermodynamical limit that are controlled in the number of optimization parameters. Using just three variational parameters, we are able to study the Bose-Hubbard model both in its clean version and in the presence of local disorder, showing excellent agreement with numerically exact QMC results. We systematically analyze the corresponding spectral functions, which cannot be fully captured by QMC. In particular, we find that in the presence of disorder the phase transition from the Bose glass to the superfluid phase at strong interactions is driven by the percolation of superfluid lakes which form around doubly occupied sites, leading to a small condensate fraction over a strongly-localized background.

The second part is dedicated to the derivation of reciprocal cluster mean-field theory (RCMF) and its application to the strongly-interacting Harper-Hofstadter-Mott model (HHMm). In RCMF the full lattice in the thermodynamical limit is projected onto finite-size clusters, which are decoupled in reciprocal space through a mean-field decoupling approximation, crucially preserving the symmetries of the non-interacting dispersion. The resulting groundstate phase diagram of the HHMm exhibits band insulating, striped superfluid, and supersolid phases. Furthermore, we observe gapless uncondensed liquid phases at integer fillings, and a metastable competing fractional quantum Hall (fQH) phase. The fQH phase, predicted as the groundstate by other methods, is most likely underestimated by RCMF. We then show how a quasi-one-dimensional geometry stabilizes gapped topologically non-trivial groundstates in the HHMm. We observe quasi-one-dimensional analogues of fQH phases at fillings $\nu = 1/2$ and $3/2$, and unconventional gapped non-degenerate groundstates at integer filling with quantized Hall responses. By systematically comparing results computed with RCMF and exact diagonalization (ED), we are able to give conclusive quantitative answers on the phase boundaries of the system, as the two methods approach the thermodynamical limit from opposite sides, since RCMF favours gapless and ED gapped phases.

Publications

This work is based on the following publications and preprints which are partially reprinted.

Dario Hügel and Lode Pollet
Thermodynamics of the Bose-Hubbard model in a Bogoliubov+U theory
Physical Review B 91, 224510 (2015) [1]

In this work we derived the Bogoliubov+U formalism to study the thermodynamical properties of the Bose-Hubbard model. The theory containing just three parameters that are determined self-consistently reproduces the groundstate phase diagrams of the three-dimensional and two-dimensional Bose-Hubbard model with an accuracy of 1% or better, while it looses accuracy at finite temperature. Chapter 5 closely follows this publication.

Dario Hügel, Philipp Werner, Lode Pollet, and Hugo U. R. Strand
Bosonic self-energy functional theory
Physical Review B 94, 195119 (2016) [2]

In this work we derived the self-energy functional theory for bosonic lattice systems with broken $U(1)$ symmetry. The formalism simplifies to bosonic dynamical-mean field theory when constraining to local fields, whereas when neglecting kinetic contributions of non-condensed bosons it reduces to the static mean-field approximation. To benchmark the theory we studied the Bose-Hubbard model on the two- and three-dimensional cubic lattice, showing excellent agreement with numerically exact results from path integral quantum Monte Carlo using just three variational parameters. We also studied the frustrated square lattice with next-nearest neighbor hopping, and computed spectral functions without having to resort to analytic continuation. This is both beyond the reach of Monte Carlo simulations. Secs. 4.1, 4.4, 4.5.1, and Chapter 6 closely follow this publication.

Dario Hügel, Hugo U. R. Strand, Philipp Werner, and Lode Pollet
The anisotropic Harper-Hofstadter-Mott model: competition between condensation and magnetic fields
Physical Review B 96, 054431 (2017) [3]

In this work we derived the reciprocal cluster mean-field (RCMF) method to study the strongly-interacting bosonic Harper-Hofstadter-Mott model with hopping anisotropy. The system exhibits a rich phase diagram featuring band insulating, striped superfluid, and supersolid phases. Furthermore, we observed gapless uncondensed liquid phases at integer fillings, which are analyzed by exact diagonalization. Incompressible metastable states at fractional filling are also observed, indicating competing fractional quantum Hall phases. We further introduced a suitable measure for non-trivial many-body topological properties. Chapters 8 and 9 closely follow this publication.

Filip Kozarski, Dario Hügel, and Lode Pollet
Quasi-one-dimensional Hall physics in the Harper-Hofstadter-Mott model
New J. Phys. https://doi.org/10.1088/1367-2630/aab081 (2018) [4]

In this work we studied the groundstate phase diagram of the strongly-interacting Harper-Hofstadter-Mott model on a quasi-one-dimensional lattice consisting of a single magnetic flux quantum in y-direction. In addition to superfluid phases with various density patterns, we observed quasi-one-dimensional analogues of fractional quantum Hall phases at fillings $\nu = 1/2$ and $3/2$, and gapped non-degenerate ground-states, which at $\nu = 1$ show an odd "fermionic" Hall conductance, while the Hall response at $\nu = 2$ consists of the transverse transport of a single particle-hole pair. The results are obtained by exact diagonalization and RCMF. Chapter 10 closely follows this preprint.

Dario Hügel, Hugo U. R. Strand, Philipp Werner, and Lode Pollet
Self-energy functional theory with symmetry breaking for disordered lattice bosons
arXiv:1801.07274 (preprint 2018) [5]

In this work we extended self-energy functional theory for bosons to the case of disorder. Using only three variational parameters, we were able to reproduce numerically exact quantum Monte Carlo results in the Bose-Hubbard model with box disorder with high accuracy. By systematically analyzing thermodynamical observables and the spectral function, we found that in the strongly-interacting Bose glass particles delocalize into isolated superfluid lakes over a strongly localized background around maximally-occupied sites whenever these sites are particularly rare. Our results indicate that the transition from the Bose glass to the superfluid phase around unit filling at strong interactions is driven by the percolation of superfluid lakes which form around doubly occupied sites. Chapter 7 closely follows this preprint.

Contents

1

Introduction

Ever since the first experimental works on superfluid Helium [7], the field of interacting bosonic systems allowing for spontaneous $U(1)$-symmetry-breaking [8, 9] has been a very active field of research. However, the study of the microscopic properties of interacting particles in the periodic potentials of realistic materials can be extremely challenging both experimentally and theoretically, due to the interplay of multi-orbital single-particle bands, potential defects and non-local interactions. In theoretical condensed matter physics, this has been the initial driving force behind the development of effective lattice models through the tight-binding approximation [10]. In this framework, assuming that the particles (in our case bosons) are localized in the minima of the potential, the complex continuous problems are mapped onto effective discrete Hamiltonians, while restricting the motion of the bosons to just the lowest single-particle band(s). The resulting effective models therefore possess far fewer degrees of freedom than the original continuous problem, facilitating the theoretical treatment in the hope that the fundamental many-body effects are still captured by this simpler approach.

The prototypical bosonic lattice model derived in this way is the Bose-Hubbard model [9, 11] (BHm). In this model the basic assumption is that the bosons can only hop onto neighboring sites with a translationally-invariant hopping amplitude J and interact only locally through the two-particle interaction strength U. As a function of the effective parameters of the system, the resulting groundstate phases of this model are the Mott insulator – characterized by a finite many-body gap, zero compressibility, and integer density – and the gapless compressible superfluid phase – which in three dimensions is characterized by the bosons (partially) condensing into the minimum of the non-interacting dispersion, spontaneously breaking the $U(1)$-symmetry of the system through a finite condensate order parameter ϕ [12, 13].

In the following we will discuss two generalizations of the BHm. The first one is the disordered BHm [9, 14, 15, 16]. Here, the assumption of translational invariance is abandoned through the introduction of an additional random local potential. The finite disorder introduces an additional groundstate phase intervening between the superfluid and the Mott insulator: the Bose glass. The physics of this phase are dominated by disorder-induced fluctuations which lead to an insulating yet gapless and compressible behavior [15, 16] through the interplay between isolated localized and delocalized bosonic modes.

The second generalization of the BHm studied in this work is the inclusion of magnetic fields. The effect of magnetic fields on charged particles can be simulated in the tight-binding limit through the Perierls substitution [17], i.e. the introduction of complex phases in the effective hopping amplitudes. The simplest interacting bosonic model derived in such a way is the Harper-Hofstadter-Mott model [18, 19, 20, 21] (HHMm) in two dimensions, where the particles experience an effective homogeneous magnetic flux piercing the system through each placquette. The resulting single-particle bands are topologically non-trivial, which, if the on-site interaction suppresses condensation, can lead to gapped topologically non-trivial many-body phases [22, 23, 24]. Unlike the phases mentioned above, these phases are not characterized by a local order parameter, but by a non-zero topological invariant [22, 25, 26], which describes a non-

trivial global many-body behavior of the system. Prime examples of this are the integer quantum Hall effect [27, 28, 29], characterized by a quantized integer conductance, and the fractional quantum Hall (fQH) effect [30, 31, 32, 33], where the interaction induces long-range-entangled degenerate groundstates leading to quasiparticle excitations transporting fractional charges (and therefore to a quantized fractional conductance).

The advent of cold atom experiments [12, 34] has further invigorated the research into the effective lattice models mentioned above. The properties of cold atomic gases trapped in an optical lattice can be tuned and controlled very precisely, providing a powerful tool for the simulation of these low-energy effective Hamiltonians [12]. Dramatic experimental progress in this field, such as the observation of the Mott insulator to superfluid phase transition in the BHm [12] or the realization of the Harper-Hofstadter model [35], have galvanized the condensed matter community. In such setups, interactions can be controlled by exploiting Feshbach resonances [12, 36], while magnetic fields can be simulated through the introduction of artificial gauge fields [37, 38, 39, 40, 41, 42, 43]. To this date, heating processes in the regime of strong interactions still represent a problem for cold atom experiments with artificial gauge fields [44]. However, recent experimental progress gives hope that this can be controlled in the near future [45, 46].

Very successful for the numerical treatment of interacting bosonic lattice models have been path integral quantum Monte Carlo (QMC) simulations with worm-type updates [47] establishing an unprecedented quantitative agreement between numerical data and experiments [48, 49]. Despite all its impressive successes, however, QMC suffers from a prohibitive sign-problem in the presence of e.g. gauge fields [37, 38, 39] or other complex terms such as spin-orbit coupling [50, 51, 52]. Furthermore, in order to compute dynamical quantities such as spectral functions, it has to resort to analytic continuation [53, 54], which cannot resolve sharp features, such as e.g. high-energy resonances. Another powerful numerical method is the density matrix renormalization group (DMRG) [55, 56, 57, 58, 59] which provides a similar accuracy in low-dimensional systems. However, in the case of higher dimensions the numerical complexity represents a problem and the algorithm can no-longer be applied, as the entanglement within the system is too large to be captured by the matrix product state ansatz of DMRG.

Motivated by the evident need for other numerical methods, in this work we turn to what we here call self-consistent methods. Unlike QMC and DMRG, these approximate methods are directly defined in the thermodynamical limit, as the full lattice is solved by means of a numerically less complex auxiliary system sharing the same interaction (and disorder distribution), which – depending on the method – is referred to as solver, impurity, or reference system.

A well known example of such a method is the mean-field decoupling approximation [9, 60, 61]. Here, the creation and annihilation operators of the bosons are expanded around their mean value, i.e. the condensate order parameter ϕ, neglecting non-local quadratic fluctuations of uncondensed particles. As such, mean-field is a perturbative approach, in the sense that it is only self-consistent on the level of ϕ, while the connected Green's function – i.e. the two-point propagator of the uncondensed bosons – is treated only perturbatively. As a consequence, mean-field methods systematically overestimate condensed phases.

A non-perturbative approach which is also self-consistent on the level of quadratic fluctuations is the bosonic dynamical mean-field theory (BDMFT) [62, 63, 64, 65, 66, 67]. In addition to the self-consistent calculation of ϕ, here, the self-energy of the lattice is approximated by its counterpart on the reference system, consisting of a single-site impurity with variational non-interacting propagators that are computed through an iterative scheme. It is known that BDMFT provides excellent agreement (of the order of 1% in three dimensions) with experimental and QMC data [65] for the standard BHm and improves remarkably on static mean-field theory. BDMFT is hence a promising candidate to deal with more complicated systems by including more sites in the reference system in order to capture the important correlations of systems with larger unit cells. However, the solution of the single-site impurity consists of a continuous-time

Monte Carlo simulation [68, 69, 65, 67], which in the case of symmetry-broken phases or complex hoppings is subject to a sign-problem.

The purpose of this thesis is therefore the derivation and benchmarking of alternative self-consistent methods which do not run into this problem, while showing a comparable accuracy. As a first step, in order to filter out the indispensable ingredients needed for such precise results, we develop the Bogoliubov+U theory (B+U). This *ad hoc* framework can be viewed as the zero-frequency limit of BDMFT, but equally well as an extension of the mean-field decoupling approximation in which pair creation and annihilation of uncondensed particles is taken into account. The theory contains just three variational parameters, such that the reference system can be solved by diagonalizing a simple single-site Hamiltonian avoiding any potential sign-problem. Remarkably, despite the reduced number of degrees of freedom of the reference system, it reproduces the groundstate phase diagrams of the three-dimensional and two-dimensional BHm with an accuracy of 1% or better, while it looses accuracy as the temperature is increased.

In order to derive a more general framework, we consider the self-energy functional theory (SFT), originally derived for fermions [70, 71, 72, 73]. Building upon previous works [6, 74, 75], we systematically extend SFT to lattice bosons including the possibility of a broken $U(1)$-symmetry. SFT incorporates BDMFT as a certain limit, but can be viewed as a more general variational principle, where the specific form of the reference system's free propagators can be chosen freely. As it is a non-perturbative approach, it becomes exact if the reference system is identical to the lattice system. To benchmark the theory, we study the BHm in two and three dimensions, using the same reference system as in B+U and comparing with exact QMC results. We also study the frustrated square lattice with next-nearest neighbor hopping, which is beyond the reach of QMC simulations. We find that the three variational parameters are sufficient to quantitatively describe phase-boundaries and thermodynamical observables, as well as the enhancement of kinetic fluctuations in the frustrated case. A further advantage of the low numerical complexity of the reference system is that we are able to compute spectral functions without having to resort to analytic continuation. On the basis of these findings we propose SFT as the omnibus framework for treating bosonic lattice models, in particular in cases where QMC suffers from severe sign-problems and DMRG cannot be applied.

In a next step, we expand SFT to be able to treat disordered bosonic lattice systems. We derive an arithmetically-averaged formalism, which depends only on the self-energies of the disorder-averaged propagators where the translational invariance has been restored. Just as the version for clean systems, we find that SFT incorporates a disorder-averaged version of BDMFT in a certain limit, but can also be generalized to other reference systems. Using the same reference system with just three variational parameters, we apply SFT to the BHm with local box disorder on a cubic lattice. We mainly investigate the disordered BHm in the vicinity of the so-called superfluid finger, i.e. the region of the superfluid phase extending to much larger interactions as in the clean system. We observe excellent agreement between the thermodynamic quantities computed with SFT and QMC, as long as the disorder does not dominate over both the interaction and the non-interacting bandwidth. In this case, the restricted reference system containing just three variational parameters is no-longer sufficient to stabilize a stationary solution. By systematically analyzing the local excitations of the SFT spectral functions and comparing to analytic results in the atomic limit, we find that the strongly-interacting Bose glass is characterized by different regimes, depending on which local occupations n are activated as a function of the disorder strength Δ. While local observables are described well by the atomic limit, we find that the particles delocalize into isolated superfluid lakes over the atomic-limit background around highly-occupied sites whenever these sites are particularly rare. Our results indicate that the transition from the strongly interacting Bose glass to the superfluid is driven by the percolation of superfluid lakes which form around doubly occupied sites. As Δ is further increased and the density of doublons increases accordingly, the particles are localized by the

increasing particle-number fluctuations and interaction energy, explaining the reentrant behavior of the superfluid finger at larger Δ.

In summary, SFT represents a very general framework which can incorporate $U(1)$-symmetry-breaking and disorder both at zero and finite temperature. In order to treat systems with more complex unit-cells, in the future it can be used in combination with larger cluster reference systems (i.e. with effective Hamiltonians containing more than a single site), as was done already for fermions [76] and $U(1)$-symmetry-preserving bosons [75].

As a first step in this direction, we next extend the mean-field decoupling approximation to cluster reference systems. Unlike previous cluster mean-field methods [77, 78], we aim to do this in a way that preserves the translational invariance, and thereby the symmetries and topological properties of the non-interacting dispersion. This is done by decoupling the system in reciprocal space in combination with momentum coarse-graining, introduced in the context of the dynamical cluster approximation [79]. We term this new method reciprocal cluster mean-field theory (RCMF). It is defined in the thermodynamic limit, becomes exact for infinite cluster reference systems, and variationally approaches both condensed and uncondensed phases in models with non-trivial unit-cells and dispersions, yielding more accurate results than previous mean-field methods.

We apply RCMF to the strongly-interacting HHMm with hopping anisotropy. While exact diagonalization (ED) [33, 80, 81] and DMRG [82, 83, 84] are very useful in this context – providing strong evidence of bosonic fractional quantum Hall [33, 80, 81, 82, 83, 84] and integer quantum Hall [82, 85] phases – they cannot fully capture critical or condensed phases. They therefore tend to overestimate gapped phases. RCMF, on the other hand, tends to the opposite, as it systematically overestimates the condensate. The groundstate phase diagram computed with RCMF features band insulating, striped superfluid, and supersolid phases. Furthermore, for finite hopping anisotropy we observe gapless uncondensed liquid phases at integer fillings. The liquid phases at fillings (per unit cell) 1 and 3 exhibit the same band fillings as the fermionic integer quantum Hall effect, while the phase at filling 2 is $\mathcal{CT}$-symmetric with zero charge response. Incompressible metastable states at fractional filling are also observed, indicating competing fQH states which are most likely underestimated by RCMF.

We then turn to investigating the HHMm on a quasi-one-dimensional lattice consisting of a single magnetic flux quantum and periodic boundaries in y-direction. Such a quasi-one-dimensional setup can be expected to increase the many-body gap and thereby lead to new gapped phases. Indeed, in addition to superfluid phases with various density patterns, the groundstate phase diagram now features also gapped phases at integer and fractional fillings, whose topological properties are analyzed by means of a newly introduced winding measure. We observe quasi-one-dimensional analogues of fQH phases at fillings $\nu = 1/2$ and $3/2$, where the latter is only found due to the hopping anisotropy and the quasi-one-dimensional geometry. At integer fillings - where in the full two-dimensional system the groundstate is expected to be gapless - we observe unconventional gapped non-degenerate groundstates: At $\nu = 1$ it shows an odd "fermionic" Hall conductance, while the Hall response at $\nu = 2$ consists of the transverse transport of a single particle-hole pair, resulting in a net zero Hall conductance. For the gapped phases we systematically compare to ED calculations, showing excellent agreement.

This thesis is organized as follows. Part I is dedicated to "preliminaries", i.e. the theoretical background that is needed in order to understand the work presented in this thesis. We discuss the tight-binding limit and lattice models derived from it in Chapter 2. A short overview over the realization of these models in cold atom experiments is given in Chapter 3, while established self-consistent methods for the numerical treatment of interacting lattice bosons are reviewed in Chapter 4. In Part II we discuss SFT. B+U is introduced in Chapter 5, while the general framework of SFT for clean systems is derived and benchmarked in Chapter 6. In Chapter 7 we extend SFT to the case of disordered systems and apply it to the disordered BHm. Part III is

dedicated to RCMF and the HHMm. We derive and benchmark RCMF in Chapter 8 and study the HHMm in two dimensions (Chapter 9) and in the quasi-one-dimensional setup (Chapter 10). Finally, in Chapter 11 we present the conclusion and an outlook on future work.

Part I.

Preliminaries

2

Bosonic lattice models

The microscopic properties of realistic materials can be extremely challenging to resolve both experimentally and numerically due to the intricate interplay between multi-orbital single-particle bands, interactions and lattice defects. This has been the initial driving force behind the development of so-called "toy-models". These models rely on the discretization of the original continuous many-body problem based on the tight-binding limit, while restricting the particles to just the lowest single-particle band(s). The resulting effective models are much simpler to handle theoretically due to the reduced number of degrees of freedom, in the hope that the resulting physics contain insight into the properties of the more complicated continuous problem. The development of cold atom experiments in optical lattices (see Chapter 3) has further invigorated this field of research, as these toy models are now experimentally realizable in a clean and controllable way using both fermionic and bosonic atoms.

In this section we introduce and discuss examples of such bosonic lattice models, concentrating on the Hamiltonians treated in this work. In Sec. 2.1 we show how general lattice models can be derived from the tight-binding approximation, while in Sec. 2.2 we discuss the most prominent bosonic system derived in such a way: the Bose-Hubbard model (BHm). In Sec. 2.3 we discuss how the BHm changes if local disorder is introduced, while in Sec. 2.4 we discuss the effect of magnetic fields concentrating on the Harper-Hofstadter model (HHm) and Harper-Hofstadter-Mott model (HHMm).

2.1. From tight binding to second quantized lattice models

2.1.1. Bloch and Wannier functions

In order to derive the lattice models discussed in this thesis, we start from a free particle in a periodic potential V with lattice constant $\mathbf{R}$, i.e. $V(\mathbf{r}+\mathbf{R}) = V(\mathbf{r})$, with a Hamiltonian given by [10]

$$H_0(\mathbf{r}) = -\frac{\hbar^2}{2m}\nabla_{\mathbf{r}}^2 + V(\mathbf{r}). \tag{2.1}$$

For low magnitudes of the potential $\Delta V = V_{\max} - V_{\min}$, where the kinetic term dominates and particles tend to delocalize over the shallow wells of the potential, the typical first ansatz for the eigenstates of such a system consist of Bloch-states [10], i.e. plain waves with wavevector $\mathbf{k}$ with $e^{i\mathbf{k}(\mathbf{r}+\mathbf{R})} = e^{i\mathbf{kr}}$, where the amplitude is modulated by a periodic function $u_{n,\mathbf{k}}(\mathbf{r}+\mathbf{R}) = u_{n,\mathbf{k}}(\mathbf{r})$, i.e.

$$\Psi_{n,\mathbf{k}}(\mathbf{r}) = u_{n,\mathbf{k}}(\mathbf{r})e^{i\mathbf{kr}}, \tag{2.2}$$

where the index n accounts for possible multiple states (i.e. bands) in $\mathbf{k}$-space.

On the other hand, if ΔV is large, the particles are strongly confined by the deep wells of the potential. This limit is commonly referred to as tight-bindig limit [10]. The particles are now localized around the minima of the potential at position $\mathbf{R}$, and a more local basis than the Bloch states of Eq. (2.2) is introduced. These basis states are known as the Wannier functions [10]

$$\omega_{n,\mathbf{R}}(\mathbf{r}) = \mathcal{N} \sum_{\mathbf{k}} e^{-i\mathbf{k}\mathbf{R}} \Psi_{n,\mathbf{k}}(\mathbf{r}) = \mathcal{N} \sum_{\mathbf{k}} e^{i\mathbf{k}(\mathbf{r}-\mathbf{R})} u_{n,\mathbf{k}}(\mathbf{r}) \tag{2.3}$$

with a scalar normalization factor $\mathcal{N}$. These functions are localized around the potential minima as $\lim_{|\mathbf{r}-\mathbf{R}|\to\infty} (\omega_{n,\mathbf{R}}(\mathbf{r})) = 0$, and form a complete basis set of orthonormal states with

$$\int d\mathbf{r} \left(\omega_{n,\mathbf{R}}(\mathbf{r})\right)^* \omega_{n',\mathbf{R}'}(\mathbf{r}) = \delta_{n,n'} \delta_{\mathbf{R},\mathbf{R}'}. \tag{2.4}$$

2.1.2. Second quantization

In order to study the many-body properties of bosons in such a system, we introduce the second-quantized creation and annihilation operators, $b^\dagger_{\mathbf{R}}$ and $b_{\mathbf{R}}$, which create/destroy a boson which is strongly localized at $\mathbf{R}$ and obey the commutation relations [86]

$$\left[b_{\mathbf{R}}, b^\dagger_{\mathbf{R}'}\right] = \delta_{\mathbf{R},\mathbf{R}'}, \;\; [b_{\mathbf{R}}, b_{\mathbf{R}'}] = \left[b^\dagger_{\mathbf{R}}, b^\dagger_{\mathbf{R}'}\right] = 0 \tag{2.5}$$

When using the Fock basis on a system with L different potential minima $\mathbf{R}_n$ and basis states $|n_{\mathbf{R}_1}, n_{\mathbf{R}_2}, \ldots, n_{\mathbf{R}_L}\rangle$, where $n_{\mathbf{R}_i}$ is the number of bosons at the minimum $\mathbf{R}_i$, the creation/annihilation operators act as [86]

$$\begin{aligned}
b^\dagger_{\mathbf{R}} \left|n_{\mathbf{R}_1}, n_{\mathbf{R}_2}, \ldots, n_{\mathbf{R}}, \ldots, n_{\mathbf{R}_L}\right\rangle &= \sqrt{n_{\mathbf{R}}+1} \left|n_{\mathbf{R}_1}, n_{\mathbf{R}_2}, \ldots, n_{\mathbf{R}}+1, \ldots, n_{\mathbf{R}_L}\right\rangle, \\
b_{\mathbf{R}} \left|n_{\mathbf{R}_1}, n_{\mathbf{R}_2}, \ldots, n_{\mathbf{R}}, \ldots, n_{\mathbf{R}_L}\right\rangle &= \sqrt{n_{\mathbf{R}}} \left|n_{\mathbf{R}_1}, n_{\mathbf{R}_2}, \ldots, n_{\mathbf{R}}-1, \ldots, n_{\mathbf{R}_L}\right\rangle, \\
\hat{n}_{\mathbf{R}} \left|n_{\mathbf{R}_1}, n_{\mathbf{R}_2}, \ldots, n_{\mathbf{R}}, \ldots, n_{\mathbf{R}_L}\right\rangle &= n_{\mathbf{R}} \left|n_{\mathbf{R}_1}, n_{\mathbf{R}_2}, \ldots, n_{\mathbf{R}}, \ldots, n_{\mathbf{R}_L}\right\rangle,
\end{aligned}$$

where the particle number operator is given by $\hat{n}_{\mathbf{R}} = b^\dagger_{\mathbf{R}} b_{\mathbf{R}}$.

As the Wannier functions introduced in Sec. 2.1.1 form a complete basis, a general field operator $\Psi^\dagger(\mathbf{r})$ in continuous space creating a boson at position $\mathbf{r}$, can be expanded as [86]

$$\Psi^\dagger(\mathbf{r}) = \sum_{n,\mathbf{R}} \left(\omega_{n,\mathbf{R}}(\mathbf{r})\right)^* b^\dagger_{\mathbf{R}}. \tag{2.6}$$

2.1.3. Effective lattice model

Assuming a two-body interaction between the bosons, the full many-body Hamiltonian can now be written as,

$$H = H_{\mathrm{mb},0} + H_{\mathrm{mb},1}, \tag{2.7}$$

$$H_{\mathrm{mb},0} = \int d\mathbf{r} \Psi^\dagger(\mathbf{r}) H_0(\mathbf{r}) \Psi(\mathbf{r}), \tag{2.8}$$

$$H_{\mathrm{mb},1} = \frac{1}{2} \int d\mathbf{r} \int d\mathbf{r}' \Psi^\dagger(\mathbf{r}) \Psi^\dagger(\mathbf{r}') u\left(\mathbf{r}, \mathbf{r}'\right) \Psi(\mathbf{r}) \Psi(\mathbf{r}'), \tag{2.9}$$

with some interaction amplitude u which typically depends on the relative distance between the two interacting particles, i.e. $u\left(\mathbf{r}, \mathbf{r}'\right) = u\left(|\mathbf{r} - \mathbf{r}'|\right)$.

In order to derive the models in the next sections, from here on we will drop the band-index n, as we assume that the wells (and the temperature) are deep enough such that higher bands are not occupied and the particles are confined to the lowest band $n = 0$.

Using Eqs. (2.6-2.9) and relabeling the minima of the potential $\mathbf{R}_j$ as discrete lattice sites $\mathbf{R}_j \equiv j$, we can now simplify the Hamiltonian (2.7) as an effective discrete lattice model, yielding

$$H = \sum_{i,j} t_{i,j} b_i^\dagger b_j + \frac{1}{2} \sum_{i,j,k,l} U_{i,j,k,l} b_i^\dagger b_j^\dagger b_k b_l, \tag{2.10}$$

where the kinetic term (2.8) has been rewritten using

$$t_{i,j} = \int d\mathbf{r} \left(\omega_{\mathbf{R}_i}(\mathbf{r})\right)^* H_0(\mathbf{r}) \omega_{\mathbf{R}_j}(\mathbf{r}), \tag{2.11}$$

while the interaction term (2.9) has been rewritten using

$$U_{i,j,k,l} = \int d\mathbf{r} d\mathbf{r}' \left(\omega_{\mathbf{R}_i}(\mathbf{r}) \omega_{\mathbf{R}_j}(\mathbf{r}')\right)^* u\left(\mathbf{r}, \mathbf{r}'\right) \omega_{\mathbf{R}_k}(\mathbf{r}) \omega_{\mathbf{R}_l}(\mathbf{r}'). \tag{2.12}$$

2.2. Bose-Hubbard model

2.2.1. Model

The Bose-Hubbard model (BHm) is the simplest non-trivial model that can be derived from the effective lattice model (2.10). The basic assumption is that the Wannier functions of Sec. 2.1 are so strongly localized, that in the kinetic term (2.11) reduces to

$$t_{i,j} = \begin{cases} -\mu & \text{if } |\mathbf{R}_i - \mathbf{R}_j| = 0, \\ -J & \text{if } |\mathbf{R}_i - \mathbf{R}_j| = \mathbf{R}, \\ 0 & \text{else.} \end{cases} \tag{2.13}$$

The integral in (2.11) is therefore assumed to be zero if the two particles at $\mathbf{R}_i$ and $\mathbf{R}_j$ are not on the same site (where it yields the chemical potential μ) or nearest-neighbors (where it yields the nearest-neighbor hopping amplitude J).

Equivalently, for the interacting term of (2.10) the assumption is that the integral (2.12) is non-zero only if it involves local terms, giving the contact interaction U as

$$U_{i,j,k,l} = \begin{cases} U & \text{if } \mathbf{R}_i = \mathbf{R}_j = \mathbf{R}_k = \mathbf{R}_l, \\ 0 & \text{else.} \end{cases} \tag{2.14}$$

The resulting Hamiltonian is therefore

$$H = -J \sum_{\langle i,j \rangle} b_i^\dagger b_j + \frac{U}{2} \sum_i b_i^\dagger b_i^\dagger b_i b_i - \mu \sum_i b_i^\dagger b_i \,,$$

which using the commutations relations of Sec. 2.1.2 can be rewritten into the more common form

$$H = -J \sum_{\langle i,j \rangle} b_i^\dagger b_j + \frac{U}{2} \sum_i \hat{n}_i \left(\hat{n}_i - 1\right) - \mu \sum_i \hat{n}_i \,, \tag{2.15}$$

where $b_i^\dagger$ is a bosonic single-particle creation operator on lattice-site i, $\hat{n}_i$ is the particle-number operator, J denotes the tunneling amplitude, U the on-site interaction, μ the chemical potential, and $\langle i, j \rangle$ means that we sum over nearest neighbors.

While the chemical potential μ fixes the density in the grandcanonical ensemble, the rest of the Hamiltonian describes the competition of the kinetic hopping term with amplitude J and a local interaction U.

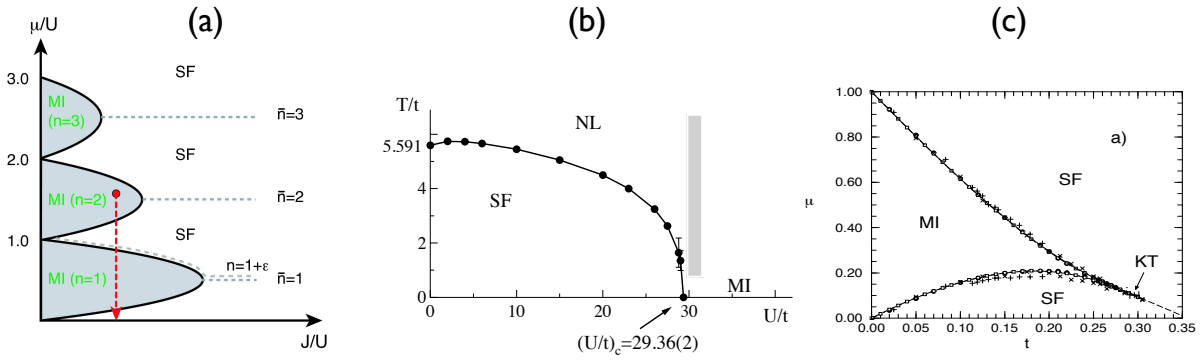

Figure 2.1.: (a) Schematic groundstate phase diagram of the BHm in high dimensions, where the Mott-insulating phase is denoted as MI and the superfluid phase as SF. The dashed blue lines show the discussed sweeps with fixed density, while the red dashed line shows a sweep in chemical potential. (b) Finite temperature phase diagram of the BHm on a cubic lattice. At low enough temperature, the MI domain is loosely defined as the part of the phase diagram to the right of the gray line, while at higher temperature the system is in a normal liquid (NL) phase. (c) Groundstate phase diagram of the one-dimensional BHm. The dashed line represents the line at fixed density $n = 1$, while the arrow 'KT' shows the location of the BKT transition. (a) is reprinted from Ref. [12], (b) from Ref. [87] and (c) from Ref. [88]. In the notation of (b) and (c) the hopping amplitude J is replaced by the letter t.

2.2.2. Properties in high dimensions

We start discussing the properties of the BHm by analyzing the groundstate properties on a three-dimensional cubic lattice in the thermodynamic limit, however at zero temperature the same considerations can also be made for the two-dimensional system.

In the case of $U = 0$, the system is non-interacting and diagonal in momentum space with dispersion $\epsilon_{\mathbf{k}} = -2J\left(\cos(k_x) + \cos(k_y) + \cos(k_z)\right)$, where k_x, k_y, and k_z are the components of the three-dimensional quasi-momentum $\mathbf{k}$. As free bosons at zero temperature condense in the minima of the dispersion, here at $\mathbf{k} = 0$, in the absence of interactions the groundstate of the system forms a perfect Bose-Einstein condensate [12, 13]

$$\Psi_{\mathrm{GS}} \propto e^{\sqrt{N} b^\dagger_{\mathbf{k}=0}} |0\rangle = \prod_{\mathbf{R}} \left(e^{\sqrt{N/N_{\mathrm{L}}} b^\dagger_{\mathbf{R}}} |0\rangle_{\mathbf{R}} \right), \tag{2.16}$$

where $b^\dagger_{\mathbf{k}} = \frac{1}{\sqrt{N_{\mathrm{L}}}} \sum_{\mathbf{R}} e^{i\mathbf{k}\mathbf{R}} b^\dagger_{\mathbf{R}}$ creates a delocalized boson with momentum $\mathbf{k}$, N_{L} is the number of lattice sites, N the number of particles, $|0\rangle$ is the vacuum state of having no particles in the entire lattice, and $|0\rangle_{\mathbf{R}}$ is the vacuum state of a single site $\mathbf{R}$, with $|0\rangle = \prod_{\mathbf{R}} |0\rangle_{\mathbf{R}}$.

As the entire system forms a macroscopic condensate, the particle density is given by $n = N/N_{\mathrm{L}} = n_0$, where

$$n_0 = |\phi|^2 = |\langle b_{\mathbf{R}} \rangle|^2 \tag{2.17}$$

is the condensate density. The finite translationally-invariant condensate order parameter ϕ breaks particle number conservation, yielding a finite superfluid response [61, 13], and is a signature of a spontaneous $U(1)$ symmetry-breaking, since – as opposed to the Hamiltonian in Eq. (2.15) – $\phi = \langle b \rangle$ is not invariant with respect to the transform

$$b \to e^{-i\theta} b, \tag{2.18}$$

$$b^\dagger \to e^{i\theta} b^\dagger. \tag{2.19}$$

As U is increased to a finite value, the system becomes no-longer analytically solvable as the repulsive interaction when multiple bosons occupy the same site depletes the condensate, such that $n = n_0 + \delta n$, where δn is the density of uncondensed particles which no longer occupy the macroscopic state (2.16). Nonetheless, as long as ϕ is finite, the system is in a gapless compressible superfluid phase, and spatial correlations tend towards a non-zero constant value [9, 61, 13], i.e.

$$\lim_{|\mathbf{r}|\to\infty} \langle b^\dagger_{\mathbf{R}+\mathbf{r}} b_{\mathbf{R}} \rangle = n_0. \tag{2.20}$$

In the opposite case at $J = 0$, the system is again analytically solvable. The single sites of the system are completely decoupled and each occupied by an integer number of particles determined by the ratio μ/U. The single-site energy as a function of the density is given by $E(n) = Un\left((n-1)/2 - \mu/U\right)$, such that the integer density of the groundstate at $J = 0$ is given by

$$n = \left\lfloor 1 + \frac{\mu}{U} \right\rfloor. \tag{2.21}$$

The many-body groundstate is gapped with respect to the addition/removal of particles by the repulsive interaction U and therefore in an incompressible Mott insulating phase, with groundstate [12]

$$\Psi_{\mathrm{GS}} \propto \prod_{\mathbf{R}} \left(b^\dagger_{\mathbf{R}} \right)^n |0\rangle. \tag{2.22}$$

As J is increased to a finite value, kinetic hopping processes lead to fluctuations in the occupations of the different lattice sites, which are no longer decoupled. The simple product state of (2.22) is no longer valid and due to kinetic fluctuations with more/less than $n = \lfloor 1 + \frac{\mu}{U} \rfloor$ particles on a single site, the relative gap of adding/removing a quasiparticle to a single site decreases. As long as this gap is finite however, even though the particles delocalize more and more with increasing J, the system remains in the Mott phase, which on average still has an integer homogeneous density $n = \langle \hat{n} \rangle$ and exponentially decaying spatial correlations

$$\lim_{|\mathbf{r}|\to\infty} \langle b^\dagger_{\mathbf{R}+\mathbf{r}} b_{\mathbf{R}} \rangle = 0. \tag{2.23}$$

The critical value $(J/U)_{\mathrm{c}}$, at which the gap of the Mott insulator goes to zero, coincides to the one where the condensate of the superfluid phase is fully depleted, with the system showing a sharp quantum phase transition from a gapped incompressible phase (Mott insulator) to a gapless compressible phase with long-range order (superfluid). The order parameter of this phase transition is therefore the condensate ϕ which is non-zero in the superfluid phase and zero in the Mott insulator.

The schematic phase diagram is shown in Fig. 2.1a. As the Mott insulator can only have integer densities, the phase is characterized by different so-called Mott lobes, i.e. regions with constant density as a function of μ/U and J/U. As the critical value of the phase transition is determined by the ratio between the kinetic energy gained by delocalizing over the entire lattice and the interaction energy suppressing large local occupations, with increasing density (and therefore increasing average interaction energy) the size of the Mott lobes decreases.

If the phase diagram is swept in J/U at constant densities (see dashed lines in Fig. 2.1a), a phase transition can only happen at integer densities, as the Mott insulator only exists at those values. These critical values correspond to the tips of the Mott lobes, where the system is particle-hole symmetric and the phase transition is described by the effective field theory of a

$d+1$-dimensional XY-model [9, 61]. If instead the density is e.g. $n = 1+\epsilon$, the system remains in a superfluid phase as long as J is finite (see Fig. 2.1a), as a small fraction ϵ of particles delocalizes on top of a frozen homogeneous Mott background with density $n = 1$ [12]. The situation changes when the density is no longer kept constant, such as is the case e.g. when changing the chemical potential μ/U. In this more generic case the critical behavior changes: when starting in the Mott insulating phase either the gap of adding or of removing a single particle to the system decreases linearly with the distance from the boundary of the Mott lobe [9, 61], eventually going to zero with the system entering the superfluid phase at $n = 1 \pm \epsilon$.

If the temperature T is increased from zero, the quantum order of the superfluid phase is eventually destroyed by thermal fluctuations and the order parameter ϕ goes to zero. Also the Mott phase is affected by T, as thermal fluctuations can close the many-body gap without the bosons condensing, leading to a gapless compressible phase named normal liquid, which can also take non-integer values of the density. The resulting phase diagram is shown in Fig. 2.1b. At $U/J < (U/J)_c$, where $(U/J)_c$ is the critical value of the transition between the superfluid and Mott phase at zero temperature, the system is either in the superfluid ($\phi \neq 0$) or in the normal liquid phase ($\phi = 0$) as there is no many-body gap at zero temperature. At $U/J > (U/J)_c$ on the other hand the transition from the Mott to the normal liquid phase is driven by the ratio between the energy of thermal fluctuations and the many-body gap of the groundstate.

2.2.3. Properties in low dimensions

As in the following we will study problems in either three dimensions or in two dimensions at zero temperature, the discussion in this section will be less detailed than for the high-dimensional case of Sec. 2.2.2.

While the Mott insulator persists up to low dimensions, the nature of the superfluid phase changes drastically. In fact, the Mermin-Wagner theorem [89] states that in the groundstate of one-dimensional short-range Hamiltonians, no true long-range order can arise due to the spontaneous breaking of a continuous symmetry. It follows, that in the one-dimensional BHm a superfluid phase cannot display a finite condensate order parameter ϕ.

However, at low enough temperatures and interactions, it is indeed possible to find a gapless phase with a finite superfluid density [90]

$$\rho_s \propto \left(\frac{\partial^2 \Omega(\theta)}{\partial \theta^2} \right) \Bigg|_{\theta=0} , \tag{2.24}$$

where $\Omega(\theta)$ is the free energy of the system with size L and twisted boundary conditions $|\Psi(x+L)\rangle = e^{i\theta} |\Psi(x)\rangle$.

While not showing true long-range order in the sense of Eq. (2.20), the low-dimensional superfluid also does not show an exponential decay as is the case for the Mott insulator of Eq. (2.23). Instead, the low-dimensional superfluid phase is characterized by a quasi-long-range order, showing an algebraic decay in the correlation function as [91, 92]

$$\langle b^\dagger_{x+r} b_x \rangle \propto |r|^{-\nu} . \tag{2.25}$$

In fact, by mapping the quantum phase transition of the one-dimensional system at fixed integer density onto the two-dimensional XY-model of the same universality class, it can be shown that this phase transition is driven by the unbinding of vortices and anti-vortices in (x, τ)-space, where τ is the imaginary time. The transition is therefore of Berezinsky-Kosterlitz-Thouless (BKT) kind [91], such that the shape of the tip of the Mott phase at integer density changes drastically, as shown in Fig. 2.1c.

2.3. Disordered Bose-Hubbard model

Suppose we now introduce a random additional potential $V_{\text{dis}}(\mathbf{r})$ to the systems discussed in Sec. 2.1, such that the total potential is given by $V(\mathbf{r}) + V_{\text{dis}}(\mathbf{r})$. In this case all terms computed in Sec. 2.1.3 will loose their translational invariance. However, here for simplicity we will assume that V_{dis} is low enough for the assumptions of the BHm of Sec. 2.2.1 to hold and that its effect on the hopping amplitude J and the interaction U are negligible. We therefore arrive at the disordered BHm, with Hamiltonian

$$H_{\boldsymbol{\eta}} = -J \sum_{\langle i,j \rangle} b_i^\dagger b_j + \frac{U}{2} \sum_i \hat{n}_i \left(\hat{n}_i - 1\right) - \sum_i \left(\mu - \eta_i\right) \hat{n}_i \,, \tag{2.26}$$

where the local potentials $\boldsymbol{\eta} = (\eta_1, \eta_2, \ldots, \eta_L)$ are random and distributed according to a given uncorrelated probability distribution

$$P(\boldsymbol{\eta}) = \prod_i p(\eta_i), \tag{2.27}$$

with disorder strength Δ. Here, for simplicity we will assume a boxed disorder distribution, i.e. $p\left(|\eta| < \Delta\right) = 1/(2\Delta)$ and $p\left(|\eta| > \Delta\right) = 0$.

In addition to the Mott insulating and superfluid phases of the clean system, the groundstate phase diagram shown in Fig. 2.2, displays a new phase at finite disorder strength Δ: the Bose glass [9, 14, 15, 16]. The Bose glass is an insulating phase comprised of finite regions which are best described either as localized atomic levels or as isolated superfluid lakes [15]. While certain single-particle states can show a high (but not macroscopic) occupation, the disorder does not allow for long-range-order as observed in the superfluid. The statistical fluctuations of η_i, on the other hand, mimic local shifts in chemical potential which locally exceed the gaps of adding/removing a particle [15], creating gapless regions which induce a non-vanishing density of states at zero energy [16]. Unlike the Mott insulator, the Bose glass is therefore gapless and characterized by a finite compressibility.

The transition from the Mott insulator to the Bose glass is therefore driven by rare lattice sites, where the local potential η_i exceeds the particle- or hole-gaps of the clean system, leading to an inhomogeneous density distribution. As at the transition these sites are extremely rare, the finite compressibility of the Bose glass close to the Mott insulating phase is extremely low and the transition is of Griffiths type [15]. Through the theorem of inclusions it can be shown that for generic transitions in a disordered system one can always find rare regions of the competing phase on either side of the transition line [93, 15]. It follows that the Griffiths region of the Bose glass will always intervene between the Mott insulating and the superfluid phase at finite disorder strength Δ (see Fig. 2.2). However, the exponentially small compressibility and the rareness of the gapless but uncondensed regions makes it extremely hard both numerically and experimentally to resolve it, as exponentially large system-sizes are needed to capture it.

In the groundstate phase diagram of the disordered BHm on a cubic lattice (see Fig. 2.2) the superfluid phase extends to surprisingly large values of the interaction U and the disorder strength Δ. For low/intermediate interactions and high disorder it can be argued that this is related to the percolation between localized states, as moving a boson from one occupied site to another costs an energy on the order of U, while moving it to an empty site requires a much larger energy on the order of Δ [15]. At stronger interaction and lower disorder the phase diagram is characterized by the so-called "superfluid finger" which extends to much larger interactions than the critical value of the clean system [i.e. $(U/J)_{\text{c}}$ at $\Delta = 0$]. This region is characterized by an extremely low condensate fraction n_0/n. The critical temperature on which the condensate ϕ vanishes is thus extremely low, making it very hard to access this regime in experiments.

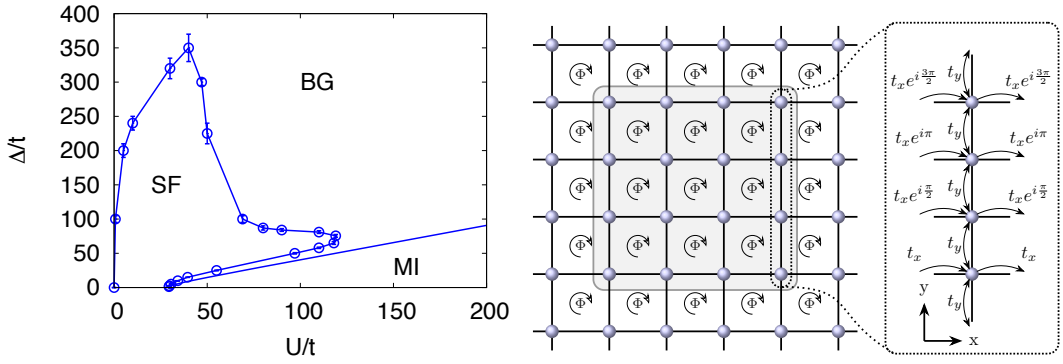

Figure 2.2.: Left panel: groundstate phase diagram of the disordered BHm on a cubic lattice at unity filling computed with path integral quantum Monte Carlo. Here, the tunneling amplitude J is denoted as t, and the groundstate phases are the Mott insulator (MI), the superfluid (SF), and the Bose glass (BG). Right panel: setup of the single-particle hopping in the HHm where each plaquette is pierced by a flux of Φ. The 4×1 unit cell for $\Phi = \pi/2$ is shown (dotted lines), where the arrows indicate the direction of the corresponding hopping processes. The left panel is reprinted from Ref. [15].

2.4. Magnetic fields in the tight binding approximation

2.4.1. Peierls substitution

The general effect of a non-zero magnetic field $\mathbf{B} = \nabla \times \mathbf{A}$ with vector potential $\mathbf{A}$ on a single-particle Hamiltonian such as (2.1), consists in shifting the momentum operator $\hat{p} = -i\hbar\nabla$ as $\hat{p} \to \hat{p} - q\mathbf{A}$, where q is the charge of the particle [10]. In the following for simplicity we will absorb the constants q and $\hbar$ into the operators ∇ and $\mathbf{A}$, yielding

$$H_{\mathbf{A}}(\mathbf{r}) = \frac{1}{2m}\left(\hat{p} - \mathbf{A}(\mathbf{r})\right)^2 + V(\mathbf{r}). \tag{2.28}$$

The effect of the vector potential on the Bloch states of Eq. (2.2) therefore consists of shifting the quasi-momentum $\mathbf{k}$ by the vector potential $\mathbf{A}(\mathbf{r})$, which for the Wannier functions of Eq. (2.3) implies

$$\omega^{\mathbf{A}}_{n,\mathbf{R}}(\mathbf{r}) = e^{i\int_{\mathbf{R}}^{\mathbf{r}} \mathbf{A}(\mathbf{r}')d\mathbf{r}'}\omega_{n,\mathbf{R}}(\mathbf{r}) \tag{2.29}$$

The only effect of the vector potential on the Wannier functions lies therefore in the Aharonov-Bohm phase [10] $\int_{\mathbf{R}}^{\mathbf{r}} \mathbf{A}(\mathbf{r}')d\mathbf{r}'$ picked up by the particles when moving through the magnetic field, with

$$H_{\mathbf{A}}(\mathbf{r})\omega^{\mathbf{A}}_{n,\mathbf{R}}(\mathbf{r}) = e^{i\int_{\mathbf{R}}^{\mathbf{r}} \mathbf{A}(\mathbf{r}')d\mathbf{r}'}H_0(\mathbf{r})\omega_{n,\mathbf{R}}(\mathbf{r}), \tag{2.30}$$

where H_0 and $\omega_{n,\mathbf{R}}(\mathbf{r})$ are the Hamiltonian and Wannier function in the absence of magnetic fields of Sec. 2.1.1.

The effective hopping amplitudes computed in Sec. 2.1.3 change accordingly through the so-called Peierls substitution [17] as

$$\begin{aligned} t_{l,j}^{\mathbf{A}} &= \int d\mathbf{r} \left(\omega_{\mathbf{R}_l}^{\mathbf{A}}(\mathbf{r})\right)^* H_{\mathbf{A}}(\mathbf{r}) \omega_{\mathbf{R}_j}^{\mathbf{A}}(\mathbf{r}) \\ &= \int d\mathbf{r} e^{i\left(\int_{\mathbf{R}_j}^{\mathbf{r}} \mathbf{A}(\mathbf{r}')d\mathbf{r}' - \int_{\mathbf{R}_l}^{\mathbf{r}} \mathbf{A}(\mathbf{r}')d\mathbf{r}'\right)} \left(\omega_{\mathbf{R}_l}(\mathbf{r})\right)^* H_0(\mathbf{r}) \omega_{\mathbf{R}_j}(\mathbf{r}) \\ &\approx e^{i\int_{\mathbf{R}_j}^{\mathbf{R}_l} \mathbf{A}(\mathbf{r}')d\mathbf{r}'} t_{l,j} = e^{i\Phi_{l,j}} t_{l,j}, \end{aligned} \tag{2.31}$$

where in the last line we have assumed, that the vector potential $\mathbf{A}(\mathbf{r})$ varies only slowly over the spacing $\mathbf{R}_l - \mathbf{R}_j$, such that the integral in the exponent is essentially independent of the path, i.e.

$$\int_{\mathbf{r}}^{\mathbf{R}_l} \mathbf{A}(\mathbf{r}')d\mathbf{r}' + \int_{\mathbf{R}_j}^{\mathbf{r}} \mathbf{A}(\mathbf{r}')d\mathbf{r}' \approx \int_{\mathbf{R}_j}^{\mathbf{R}_l} \mathbf{A}(\mathbf{r}')d\mathbf{r}'. \tag{2.32}$$

The effect of the magnetic field in the tight-binding approach therefore is reduced to a phase factor $\Phi_{l,j}$ picked up by the particles when hopping from site j to site l.

2.4.2. Harper-Hofstadter model

Assuming that the potential $V(\mathbf{r})$ is such that the particles are effectively confined to the (x, y)-plane (i.e. are moving in a two-dimensional system), that there is no interaction between the particles $[u(\mathbf{r}, \mathbf{r}') = 0]$, that $t_{i,j}$ is non-zero only for nearest-neighbors [as we also did for the BHm in Eq. (2.13)], and that we have a homogeneous magnetic field

$$\mathbf{B} = -\Phi \mathbf{e}_z, \tag{2.33}$$

where $\mathbf{e}_z$ is the unit vector in z-direction, we arrive at the so-called Harper-Hofstadter model [20, 21] (HHm). Due to the gauge freedom of the vector potential $\mathbf{A}$, there are different ways to implement this model. Here, we will use the Landau gauge $\mathbf{A}(\mathbf{r}) = y\phi\mathbf{e}_x$, where $\mathbf{r} = (x, y)$ and for the sake of simplicity $\mathbf{R}_i = \mathbf{R}_{X,Y} = (X, Y)$ with integer X and Y (i.e. the lattice spacing is set to one). This yields the simple phase factors

$$\Phi_x(Y) = \int_{\mathbf{R}_{X,Y}}^{\mathbf{R}_{X+1,Y}} \mathbf{A}(\mathbf{r})d\mathbf{r} = \int_X^{X+1} Y\Phi dX = Y\Phi \tag{2.34}$$

for hopping processes in the x-direction, and

$$\Phi_y = \int_{\mathbf{R}_{X,Y}}^{\mathbf{R}_{X,Y+1}} \mathbf{A}(\mathbf{r})d\mathbf{r} = 0 \tag{2.35}$$

for hopping processes in the y-direction.

The resulting single-particle Hamiltonian is

$$H_\Phi = -\sum_{X,Y} \left(t_x e^{iY\Phi} a_{X+1,Y}^\dagger a_{X,Y} + t_y a_{X,Y+1}^\dagger a_{X,Y}\right) + h.c., \tag{2.36}$$

where *h.c.* means taking the hermitian conjugate of the part preceding it, and we have assumed that the hopping amplitude $t_{i,j}$ can take different values for hopping processes in x- $(t_{i,j} = t_x)$ and y-direction $(t_{i,j} = t_y)$, respectively. Here, we have deliberately chosen the notation $a^\dagger$ and a for the creation and annihilation operator, as we want to discuss both bosons and fermions in this section.

As shown in Fig. 2.2, the system now consists of a square lattice, where each placquette

is pierced by a magnetic flux Φ, as for a closed path in clockwise direction around a single placquette, a particle picks up a phase Φ_m

$$\begin{aligned}\Phi_\mathrm{m} &= \left(\int_{\mathbf{R}_{X+1,Y}}^{\mathbf{R}_{X,Y}} + \int_{\mathbf{R}_{X,Y}}^{\mathbf{R}_{X,Y+1}} + \int_{\mathbf{R}_{X,Y+1}}^{\mathbf{R}_{X+1,Y+1}} + \int_{\mathbf{R}_{X+1,Y+1}}^{\mathbf{R}_{X+1,Y}}\right)\mathbf{A}(y)d\mathbf{r} \\ &= -\Phi_x(Y) + 0 + \Phi_x(Y+1) + 0 = \Phi. \end{aligned} \tag{2.37}$$

As also shown in Fig. 2.2 for the case of $\Phi = \pi/2$, the unit-cell of the system for a flux of $\Phi = 2\pi/N_\Phi$, with integer N_Φ, consists of N_Φ sites in Y-direction, resulting in N_Φ different single-particle bands. In fact, more generally, it was shown that the band structure of the HHm shows a fractal structure named Hofstadter butterfly, where the number of bands and bandgaps in the system depends on the value of $\Phi/2\pi$ [20, 21].

As discussed in Sec. 2.4.1, the basic assumption of the Peierls substitution consists of having a slowly varying vector potential over the distance $\mathbf{R}_{X,Y} - \mathbf{R}_{X\pm1,Y\pm1}$ (i.e. in our case over a single placquette). For $\Phi \ll 1$, this is indeed the case, and Eq. (2.32) is a good approximation. This limit of the HHm is referred to as continuum limit, as it directly connects to the continuous problem. For stronger magnetic fluxes Φ however the continuum limit is abandoned, as the assumption (2.32) no longer connects the discrete lattice to the original problem. In this case new properties can arise due to the strongly discretized nature of the problem.

One direct connection to the continuous problem known from solid-state physics that survives up to strong fluxes is the integer quantum Hall effect [27]. In this case we consider having a band gap between two bands of the HHm, where the lower one is completely filled by fermions at zero temperature. In this case one would typically expect the fermions to be in a trivial band-insulating state with zero conductance. The bands of the HHm however are topologically non-trivial, which on a finite system leads to the appearance of edge modes on the boundaries of the system, which lie within the band gap and connect the two bands leading to a finite conductance. As each of the edge modes can only transport a single particle, the Hall conductance σ_{xy} (normalized to the number of transported particles) is quantized to an integer number. For an introduction into the topic of topological insulators see Ref. [94].

A direct connection between the Hall conductance and band-topology can be shown through Kubos formula [95], which relates the Hall conductance to the topological invariant of the many-body state, i.e. the Chern number C [25, 26], as

$$\sigma_{xy} = C = \frac{1}{2\pi}\int_0^{2\pi} d\theta_x \int_0^{2\pi} d\theta_y \left(\partial_{\theta_x}\mathcal{A}_y(\theta_x,\theta_y) - \partial_{\theta_y}\mathcal{A}_x(\theta_x,\theta_y)\right), \tag{2.38}$$

where $\mathcal{A}_j(\theta_x,\theta_y) = i\langle\Psi(\theta_x,\theta_y)|\partial_{\theta_j}|\Psi(\theta_x,\theta_y)\rangle$ is the Berry connection [25, 26], and $\Psi(\theta_x,\theta_y)$ is the many-body groundstate under the twisted boundary conditions $\Psi(x+L_x,y) = e^{i\theta_x}\Psi(x,y)$, $\Psi(x,y+L_y) = e^{i\theta_y}\Psi(x,y)$, with L_x and L_y the system sizes in x and y direction, respectively.

As the many-body state of a gapped band completely filled with fermions at zero temperature is a simple product state, the integral of Eq. (2.38) can be reduced to

$$C = \sum_{n\in\mathrm{occ}} c_n, \tag{2.39}$$

where the sum runs over all occupied bands and c_n is the Chern number of the nth band defined as [25, 26]

$$c_n = \frac{i}{2\pi}\int_0^{2\pi} dk_x \int_0^{2\pi} dk_y \left(\partial_{k_x}\langle u_n(\mathbf{k})|\partial_{k_y}|u_n(\mathbf{k})\rangle - \partial_{k_y}\langle u_n(\mathbf{k})|\partial_{k_x}|u_n(\mathbf{k})\rangle\right), \tag{2.40}$$

where $\mathbf{k} = (k_x, k_y)$ is the two-dimensional quasi-momentum and $|u_n(\mathbf{k})\rangle$ are the single-particle

eigenstates of the nth band.

Non-interacting fermions therefore can display non-trivial topological properties in the HHm by being in a so-called symmetry protected topological (SPT) phase [22, 23, 24] (in this case the integer quantum Hall phase), which is characterized as a gapped non-degenerate groundstate with short-range entanglement and a non-zero topological invariant [23, 24] (in this case the Chern number). It is this topological invariant – a global property of the many-body state – and not a local order parameter, that marks the difference between the SPT and a trivial band-insulator. This invariant – and therefore also the presence of conducting edge modes in the band gap – is robust against local perturbations, as long as the underlying symmetry protecting the order (in this case the $U(1)$-symmetry) is not spontaneously broken [23, 24].

Bosons on the other hand will condense in the absence of interactions, leading to a topologically trivial gapless phase. This is why for bosons the focus lies on interacting systems when studying topological properties, as a finite interaction can deplete the condensate and lead to non-trivial gapped many-body states.

2.4.3. Harper-Hofstadter-Mott model

The Harper-Hofstadter-Mott model (HHMm) is the extension of the HHm to locally interacting bosons. Just as for the BHm (see Sec. 2.2.1) we assume that the interaction term (2.12) is only non-zero if the involved particles are on the same lattice site. As in this case the phase factors of Eq. (2.29) cancel in Eq. (2.12) (as they also do in the chemical potential $\mu = -t_{i,i}$), the local terms are identical to the ones of the BHm, yielding the Hamiltonian

$$\begin{aligned} H_\Phi = &- \sum_{X,Y} \left(t_x e^{iY\Phi} b^\dagger_{X+1,Y} b_{X,Y} + t_y b^\dagger_{X,Y+1} b_{X,Y} + h.c. \right) \\ &+ \frac{U}{2} \sum_{X,Y} \hat{n}_{X,Y} \left(\hat{n}_{X,Y} - 1 \right) - \mu \sum_{X,Y} \hat{n}_{X,Y}. \end{aligned} \tag{2.41}$$

As discussed in detail in Refs. [23] and [24], in the presence of (strong) interactions bosons can exhibit symmetry protected topological order at integer fillings ν (i.e. particles per unit cell). Such is the case for the bosonic equivalent of the integer quantum Hall phase [28], which was observed on the honeycomb lattice with correlated hopping [29], in the HHMm with additional diagonal hopping [85], and more recently in the standard HHMm discussed here at filling $\nu = 2$ [82]. As its fermionic counterpart, this phase is protected by the $U(1)$-symmetry and characterized by a quantized integer Hall conductance of (neutral) bosons [i.e. an integer many-body Chern number, which has to be computed directly from (2.38) as it can no longer be mapped onto the non-interacting bands due to the interaction]. In contrast to the fermionic case, however, it can be shown that this phase can only arise for even integer conductances, while for an odd-integer Chern number the involved particles must be either fermionic or in a degenerate groundstate [28].

The finite interaction can also give rise to a new kind of phase at fractional fillings: as for interacting electrons in a strong magnetic field [30, 31], bosons can form fractional quantum Hall states, which are characterized by a fractional conductance/Chern number. These groundstates are gapped, degenerate, and show intrinsic topological order. In contrast to symmetry protected topological phases, groundstates with intrinsic topological order show long-range entanglement and its topological invariant is protected against any kind of local perturbation. The degeneracy of the groundstates leads to the system displaying fractional quasi-particle excitations with anyonic statistics (i.e. behaving neither like bosons nor like fermions) [96]. These quasiparticles carry only a fractional charge through the edge modes, leading to the fractional conductance. Such phases have been predicted for the HHMm and were observed numerically for the case of filling

$\nu = 1/2$ using exact diagonalization (ED) [33, 80, 81], and the density matrix renormalization group (DMRG) on cylinder [82, 83], and (for lower fields) square geometries [84].

A simple picture from the continuous problem that gives an intuitive approach to the fractional quantum Hall states is the composite fermion picture [32, 97, 81]. Composite fermions are weakly interacting quasiparticles composed of a boson with an attached vortex (canceling an effective flux of $\Phi_{\text{vort}} = 2\pi$). At fractional filling ν, i.e. density $n = \nu/N_\Phi$ (where the flux per placquette is $\Phi = 2\pi/N_\Phi$), they essentially behave as free fermions in an effective magnetic field arising from the new effective flux per placquette $\Phi' = 2\pi\left(1 \pm \nu\right)/N_\Phi$ (where the two signs correspond to attaching vortices of opposite sign) [81]. This leads to a Fermi-sea behavior in new effective bands corresponding to the HHm at flux Φ'. If these bands are completely filled, the system is in an effective integer quantum Hall phase of composite fermions and gapped. As was shown in Ref. [81], while showing good agreement in the continuum limit of low Φ, at strong fluxes the overlap between composite fermion trial wavefunctions and numerical results decreases, implying that for strong fluxes the fractional quantum Hall states of the HHMm have no counterpart in the continuum.

3

Cold atoms in optical lattices

While the effective lattice models introduced in Chapter 2 have long been used as theoretical approximations to more complex continuous problems in realistic materials, the advent of cold atom experiments in optical lattices has revolutionised the field enabling the experimental realization of such simple and clean systems.

In these experiments, (bosonic or fermionic) atoms are trapped in an optical potential at extremely low temperatures (in the sub-mK regime). As the potentials can be tuned to have lattice spacings which are orders of magnitude larger than the ones in real materials, and their properties can be tuned in a controlled and accurate way, the realization of perfectly homogeneous and translationally invariant lattices is within experimental reach.

The effective parameters of the resulting tight-binding Hamiltonians, such as the hopping amplitude or two-particle interactions, can be tuned in a controlled way by making use of the internal degrees of freedom of the atoms, and even artificial magnetic fields – mimicking the effect of magnetic fields on charged particles for the neutral atoms – can be induced through additional light fields or periodic modulations. This enables the study of many-body physics on a microscopic level in clean systems and in parameter regimes and temperatures which are inaccessible in real materials.

While dramatic experimental progress in this field – such as the observation of the Mott insulator to superfluid phase transition in the Bose-Hubbard model [12] or the realization of the Harper-Hofstadter model [35] – have galvanized the condensed matter community, heating processes arising from scattering processes and the laser fields employed in the experiments can destroy the quantum nature of the many-body state through thermal fluctuations, making the experimental realization of more complex systems such as e.g. the strongly-interacting Harper-Hofstadter-Mott model currently out of reach.

3.1. Optical lattices

The central concept behind the confinement of ultracold atoms in optical lattices is the dipole force experienced by the atoms when interacting with an off-resonant laser field with detuning $\Delta = \omega_{\mathrm{L}} - \omega_0$ [98]. Here, ω_{L} is the frequency of the laser and ω_0 corresponds to a transition frequency to an excited state of the atom. Assuming that the time scale of the center-of-mass motion of the atoms is much slower than ω_{L}, the potential experienced by the atoms due to the dipole force is given by

$$V_{\mathrm{dip}}(\mathbf{r}) = \frac{3\pi c^2}{2\omega_0^3}\frac{\Gamma}{\Delta} I(\mathbf{r}), \tag{3.1}$$

where $\Gamma \ll |\Delta|$ is the decay rate of the excited state and $I(\mathbf{r})$ is the spatial intensity profile of the laser field [12].

Depending on the sign of the detuning Δ, atoms can therefore be trapped in the minima/maxima

of the laser field. In a standing wave of two counter-propagating laser fields, the atoms will therefore experience a periodic potential such as the one introduced in Sec. 2.1. While a three-dimensional lattice can be constructed by using orthogonal standing waves of the laser field in all three spatial directions, effective two- or one-dimensional systems can also be achieved, by confining the atoms with a trapping potential with one single minimum in one or two dimensions, respectively.

The momentum distribution of a many-body state in an optical lattice can be measured through so-called time-of-flight measurements [12]. In these measurements the laser fields (and any non-negligible interactions) are turned off either suddenly or adiabatically and the atoms will expand freely according to the momentum distribution as a superposition of plain waves. The momentum distribution of the many-body state can therefore be extracted from the resulting interference pattern, which can be measured through standard absorption techniques, and the time-of-flight, i.e. the time in which the atomic cloud expanded. Such a technique has been used e.g. to observe the superfluid to Mott transition, as the superfluid is strongly peaked at quasi-momentum 0, while the Mott insulator shows a broad momentum distribution [48].

While periodic potentials can be created through standing waves, non-translational-invariant random density profiles $I(\mathbf{r})$ can induce disorder such as discussed in Sec. 2.3. One prominent way to achieve this, is to use laser speckles [99, 100, 101, 102]. In this technique an additional beam from the same laser as used for the optical trap is passed through a diffusive plate, creating a (quasi-)random interference pattern. The resulting intensity profile therefore breaks translational invariance, inducing randomness in the optical dipole force and therefore in the potential experienced by the atoms.

3.2. Two-body interactions

For atomic gases in the sub-mK regime the lowest-angular-momentum two-particle collisions dominate the scattering processes, corresponding to s-wave scattering for bosons [12]. Suppose now that the collision between two particles has two reaction channels: an open channel corresponding to the scattering in the continuum, and a closed channel corresponding to energetically forbidden processes. A Feshbach resonance arises whenever a bound state induced by the inter-atomic potential in the closed channel couples resonantly with the kinetic energy of the scattering continuum in the open channel. The two channels can correspond for instance to different configurations of the internal states of the atoms, such as e.g. spins [12].

The Feshbach resonance will capture the particles temporarily in a quasi-bound state, heavily affecting the scattering length. This effect can be used in cold-atom experiments in order to tune the interaction (i.e. the scattering) between particles. One approach that is typically used for this is to introduce an external uniform magnetic field [36]. As the open and closed channel possess different magnetic moments, the relative energy difference – i.e. the energetical distance to a Feshbach resonance – can be tuned through the magnetic field strength.

3.3. Artificial magnetic fields

In order to illustrate the fundamental principles of artificial gauge fields, let us consider an atom with a two-level internal structure consisting of an internal ground- ($|\mathrm{g}\rangle$) and excited ($|\mathrm{e}\rangle$) state. We assume that in addition to the optical potential $V(\mathbf{r})$, which does not couple to the internal states, there is an external spatially dependent field U that couples the internal states $|\mathrm{g}\rangle$ and

$|e\rangle$. The resulting single-particle Hamiltonian is

$$H = \left(\frac{\mathbf{p}^2}{2m} + V\right)\mathbf{1} + \mathbf{U}. \tag{3.2}$$

Here, the 2×2 identity $\mathbf{1}$ and the matrix

$$\mathbf{U}(\mathbf{r}) = \frac{\hbar\Omega(\mathbf{r})}{2}\begin{pmatrix} \cos(\theta(\mathbf{r})) & e^{-i\phi(\mathbf{r})}\sin(\theta(\mathbf{r})) \\ e^{i\phi(\mathbf{r})}\sin(\theta(\mathbf{r})) & -\cos(\theta(\mathbf{r})) \end{pmatrix}, \tag{3.3}$$

act on the two internal states of the atom, where Ω, θ, and ϕ are the generalized Rabi frequency, the mixing-, and the phase-angle, respectively, which can be tuned e.g. by modifying the intensity, phase and frequency of an external laser field [43].

At a point $\mathbf{r}$ the eigenstates of $\mathbf{U}$ are given by

$$|\chi_1(\mathbf{r})\rangle = \begin{pmatrix} \cos(\theta(\mathbf{r})/2) \\ e^{i\phi(\mathbf{r})}\sin(\theta(\mathbf{r})/2) \end{pmatrix}, \; |\chi_2(\mathbf{r})\rangle = \begin{pmatrix} -e^{-i\phi(\mathbf{r})}\sin(\theta(\mathbf{r})/2), \\ \cos(\theta(\mathbf{r})/2) \end{pmatrix} \tag{3.4}$$

with eigenvalues $\pm\hbar\Omega(\mathbf{r})/2$.

Let us now assume that the initial internal state of the atom is given by $|\chi_1\rangle$ and that the time evolution of the internal state is adiabatic, such that it never couples to $|\chi_2\rangle$. The resulting eigenstate of the particle will be given by

$$|\Psi(\mathbf{r},t)\rangle = \psi(\mathbf{r},t)\,|\chi_1(\mathbf{r})\rangle\,, \tag{3.5}$$

and the projection of the time-dependent Schrödinger equation onto the internal state $|\chi_1\rangle$ yields

$$i\hbar\partial_t\psi(\mathbf{r},t) = \langle\chi_1(\mathbf{r})|\,H\,|\Psi(\mathbf{r},t)\rangle = H_{\text{eff}}\psi(\mathbf{r},t). \tag{3.6}$$

By

$$\begin{aligned}\langle\chi_1(\mathbf{r})|\,\mathbf{p}^2\,|\Psi(\mathbf{r},t)\rangle = -\Big(&\nabla^2\psi(\mathbf{r},t) + 2\nabla\psi(\mathbf{r},t)\,\langle\chi_1(\mathbf{r})|\,\nabla\,|\chi_1(\mathbf{r})\rangle \\ &+ \psi(\mathbf{r},t)\,\langle\chi_1(\mathbf{r})|\,\nabla\,|\chi_1(\mathbf{r})\rangle^2 - \psi(\mathbf{r},t)\,|\langle\chi_1(\mathbf{r})|\,\nabla\,|\chi_2(\mathbf{r})\rangle|^2\Big)\,,\end{aligned} \tag{3.7}$$

where we have used the completeness relation $\mathbf{1} = |\chi_1(\mathbf{r})\rangle\,\langle\chi_1(\mathbf{r})| + |\chi_2(\mathbf{r})\rangle\,\langle\chi_2(\mathbf{r})|$, the resulting effective Hamiltonian experienced by the wavefunction $\psi(\mathbf{r},t)$ is given by

$$H_{\text{eff}} = \frac{(\mathbf{p}-\mathbf{A})^2}{2m} + V + \frac{\hbar\Omega}{2} + W, \tag{3.8}$$

with a scalar field

$$W(\mathbf{r}) = \frac{\hbar^2}{2m}\,|\langle\chi_1(\mathbf{r})|\,\nabla\,|\chi_2(\mathbf{r})\rangle|^2\,, \tag{3.9}$$

and a vector potential

$$\mathbf{A}(\mathbf{r}) = i\hbar\,\langle\chi_1(\mathbf{r})|\,\nabla\,|\chi_1(\mathbf{r})\rangle = -\sin^2(\theta/2)\,\nabla\phi, \tag{3.10}$$

which – if it can no-longer be eliminated from (3.8) through a gauge transform – leads to an effective magnetic field experienced by the atoms as [43]

$$\mathbf{B}(\mathbf{r}) = \nabla\times\mathbf{A} = \frac{\hbar}{2}\,(\nabla\cos(\theta))\times\nabla\phi. \tag{3.11}$$

4

Self-consistent methods

Path integral quantum Monte Carlo simulations represent a very successful numerical tool for the simulation of a large class of bosonic lattice systems. Unlike fermions, bosons do not possess an intrinsic sign-problem, leading to numerically exact results in systems such as e.g. the Bose-Hubbard model [47, 49, 48, 87]. In the presence of more complex Hamiltonians however, such as lattices with artificial gauge fields [37, 38, 39], or other complex terms such as spin-orbit coupling [50, 51, 52], the lattice itself can introduce a sign-problem in the Monte Carlo simulations. The density-matrix-renormalization group (DMRG)) [55, 56, 57, 59] and exact diagonalization (ED), on the other hand, work very well in low dimensions, but in higher dimensions and in the presence of critical phases the numerical complexity and the required system sizes represent a problem.

While the methods mentioned above treat the full lattice on finite system sizes with high accuracy, in this work we turn to a different class of numerical methods which we dub "self-consistent methods". In these algorithms, by using perturbative (see e.g Sec. 4.2) or non-perturbative (Sec. 4.5) approximations, the full lattice in the thermodynamic limit is solved in a self-consistent way with the help of a simpler exactly solvable auxiliary system, which – depending on the method – is referred to as solver, impurity, or reference system. In the following we discuss examples of established self-consistent methods for bosonic lattice problems, using these terms interchangeably, depending on the context. Secs. 4.1, 4.4 and 4.5.1 closely follow Ref. [2].

4.1. Propagators and free energy

In order to derive approximations for the numerical treatment of translationally invariant bosonic lattice systems we start by considering a general system of lattice bosons with local interactions and Hamiltonian

$$H = \sum_i (b_i^\dagger F_i + F_i^\dagger b_i) + \sum_{ij} t_{ij} b_i^\dagger b_j + \hat{V}_3 + \hat{V}_4 \,, \tag{4.1}$$

where $b_i^\dagger$ (b_i) creates (annihilates) a boson at site i, t_{ij} is the single-particle hopping, F is an external field, which couples linearly to the bosonic operators, and $\hat{V}_3$ and $\hat{V}_4$ are general interactions with three and four legs, respectively. Using Einstein summation and the Nambu operators $\mathbf{b}_\alpha^\dagger = \mathbf{b}_{i\nu}^\dagger = (b_i^\dagger, b_i)_\nu$ with commutator $[\mathbf{b}^\alpha, \mathbf{b}_\beta^\dagger] = (\mathbf{1} \otimes \sigma_z)_\beta^\alpha$, where α is a composite index comprising the site and Nambu indices i and ν, the Hamiltonian can be written compactly as

$$H = \mathbf{F}_\alpha^\dagger \mathbf{b}^\alpha + \frac{1}{2} \mathbf{b}_\alpha^\dagger \mathbf{t}_\beta^\alpha \mathbf{b}^\beta + \hat{V}_3 + \hat{V}_4 \,, \tag{4.2}$$

$$\hat{V}_3 = V^{(3)}_{\alpha\beta\gamma}\, \mathbf{b}^\alpha \mathbf{b}^\beta \mathbf{b}^\gamma \,, \quad \hat{V}_4 = V^{(4)}_{\alpha\beta\gamma\delta}\, \mathbf{b}^\alpha \mathbf{b}^\beta \mathbf{b}^\gamma \mathbf{b}^\delta \,. \tag{4.3}$$

where $\mathbf{t}^{\alpha}_{\beta} = \mathbf{t}^{i\eta}_{j\nu} = t_{ij} \otimes \mathbf{1}_{\eta\nu}$, up to an irrelevant constant. For brevity in the following we will drop all tensor indices whenever contractions are well defined.

The partition function $\mathcal{Z}$ is given by the trace of the imaginary-time-ordered exponential $\mathcal{Z} = \mathrm{Tr}[\mathcal{T} e^{-S}]$, where S is the action

$$\begin{aligned} S[\mathbf{b}] &= -\int_0^\beta d\tau \left(\frac{1}{2} \mathbf{b}^\dagger(\tau) \partial_\tau \sigma_z \mathbf{b}(\tau) - H\left[\mathbf{b}^\dagger(\tau), \mathbf{b}\ (\tau)\right] \right) \\ &= \int_0^\beta d\tau (\hat{V}_3[\mathbf{b}(\tau)] + \hat{V}_4[\mathbf{b}(\tau)]) + \int_0^\beta d\tau \mathbf{F}^\dagger \mathbf{b}(\tau) \\ &\quad - \frac{1}{2} \iint_0^\beta d\tau d\tau' \mathbf{b}^\dagger(\tau) \mathbf{G}_0^{-1}(\tau, \tau') \mathbf{b}(\tau') \,, \end{aligned} \tag{4.4}$$

β is the inverse temperature, $\mathcal{T}$ the imaginary-time-ordering operator, and the hopping t_{ij} is absorbed in the non-interacting propagator

$$\mathbf{G}_0^{-1}(\tau, \tau') = \delta(\tau - \tau')(-[\mathbf{1} \otimes \sigma_z]\partial_{\tau'} - \mathbf{t}) \,. \tag{4.5}$$

The partition function's functional dependence on $\mathbf{F}$ and $\mathbf{G}_0^{-1}$, $\mathcal{Z} = \mathcal{Z}[\mathbf{F}, \mathbf{G}_0^{-1}]$, make the free energy $\Omega[\mathbf{F}, \mathbf{G}_0^{-1}] \equiv -\ln[\mathcal{Z}]/\beta$ a generating functional for the propagators

$$\beta \frac{\delta \Omega}{\delta \mathbf{F}^\dagger} = \langle \mathbf{b} \rangle \equiv \mathbf{\Phi} \,, \tag{4.6}$$

$$2\beta \frac{\delta \Omega}{\delta \mathbf{G}_0^{-1}(\tau', \tau)} = -\langle \mathbf{b}(\tau) \mathbf{b}^\dagger(\tau') \rangle = \mathbf{G}(\tau, \tau') - \mathbf{\Phi}\mathbf{\Phi}^\dagger \,, \tag{4.7}$$

where $\mathbf{\Phi}$ is the expectation value of the bosonic Nambu annihilation operator $\mathbf{b}$, $\mathbf{G}$ is the connected single-particle Green's function, and the expectation value of an operator $\hat{O}(\tau)$ is defined as the time-ordered trace $\langle \hat{O}(\tau) \rangle = \mathrm{Tr}[\mathcal{T} e^{-S} \hat{O}(\tau)]/\mathcal{Z}$.

4.2. Mean-field decoupling approximation

Bosons on a lattice with general Hamiltonian

$$H = \sum_{ij} t_{ij} b_i^\dagger b_j + \sum_i \left(\hat{V}_i - \mu n_i \right) \,, \tag{4.8}$$

with some local interaction $\hat{V}_i$ (e.g. a density-density interacion $U\hat{n}_i^2$) and chemical potential μ can condense into a macroscopic state characterized by a non-zero condensate order parameter $\phi_i = \langle b_i \rangle$ [61, 13].

This possibility of a broken $U(1)$-symmetry makes it possible to expand the creation/annihilation operators around their expectation value, i.e.

$$b_i = \phi_i + \delta b_i, \tag{4.9}$$

$$b_i^\dagger = \phi_i^* + \delta b_i^\dagger, \tag{4.10}$$

where the fluctuations $\delta b_i^{(\dagger)}$ represent uncondensed bosons.

Using Eqs. (4.9) and (4.10), we can rewrite the Hamiltonian (4.8) as

$$H[\{\phi_i\},\{\phi_i^*\}] = H_{\text{loc}} + \Delta H[\{\phi_i\},\{\phi_i^*\}], \tag{4.11}$$

$$H_{\text{loc}} = \sum_i \left(\hat{V}_i - \mu n_i\right), \tag{4.12}$$

$$\Delta H[\{\phi_i\},\{\phi_i^*\}] = \sum_{ij} t_{ij}\left(\phi_i^*\delta b_j + \delta b_i^\dagger \phi_j + \delta b_i^\dagger \delta b_j + \phi_i^*\phi_j\right). \tag{4.13}$$

The crucial part of the mean-field decoupling approximation [9, 60, 61] lies in neglecting non-local quadratic fluctuations of uncondensed bosons, i.e.

$$\delta b_i^\dagger \delta b_j \approx 0 \tag{4.14}$$

which by $\delta b^{(\dagger)} = b^{(\dagger)} - \phi^{(*)}$ reduces $\Delta H[\{\phi_i\},\{\phi_i^*\}]$ to

$$\Delta H[\{\phi_i\},\{\phi_i^*\}] \approx \sum_{ij} t_{ij}\left(\phi_i^* b_j + b_i^\dagger \phi_j - \phi_i^*\phi_j\right). \tag{4.15}$$

This decouples the full Hamiltonian into a set of local Hamiltonians H_i^{eff}, where the non-local parts are approximated by scalar mean-fields as

$$H_{\text{eff}}[\{\phi_i\},\{\phi_i^*\}] = \sum_i H_i^{\text{eff}}[\{\phi_i\},\{\phi_i^*\}] - \sum_{ij} t_{ij}\phi_j^*\phi_i, \tag{4.16}$$

$$H_i^{\text{eff}}[\{\phi_i\},\{\phi_i^*\}] = \left(\sum_j t_{ij}\phi_j\right) b_i^\dagger + \left(\sum_j t_{ji}\phi_j^*\right) b_i + \hat{V}_i - \mu n_i. \tag{4.17}$$

For the sake of simplicity in the following we will assume that the Hamiltonian is completely translationally invariant and has only nearest-neighbor hopping processes, i.e.

$$\sum_{ij} t_{ij} b_i^\dagger b_j \to -J \sum_{\langle ij\rangle} b_i^\dagger b_j\,, \tag{4.18}$$

as is the case in the Bose-Hubbard model (see Sec. 2.2). Note however that a similar procedure can also be done for more complicated locally interacting Hamiltonians. This enables us to assume that the condensate is homogeneous, i.e.

$$\phi_i = \langle b_i\rangle = \phi. \tag{4.19}$$

The system is therefore decoupled into a set of identical local impurities with Hamiltonian [9]

$$H_{\text{MF}}\left[\phi,\phi^*\right] = \hat{V} - \mu n - zJ\left(\phi^* b + b^\dagger \phi - |\phi|^2\right), \tag{4.20}$$

where z is the coordination number, i.e. the number of nearest-neighbors.

Through the mean-field decoupling approximation the solution of the full lattice system therefore reduces to finding the value of the condensate order parameter ϕ and solving the simple impurity Hamiltonian (4.20). The value of ϕ can be found by requiring that the free-energy of the effective mean-field Hamiltonian (4.20)

$$\beta\Omega_{\text{MF}}\left[\phi,\phi^*\right] = -\ln\left[\text{Tr}\left[e^{-\beta H_{\text{MF}}[\phi,\phi^*]}\right]\right], \tag{4.21}$$

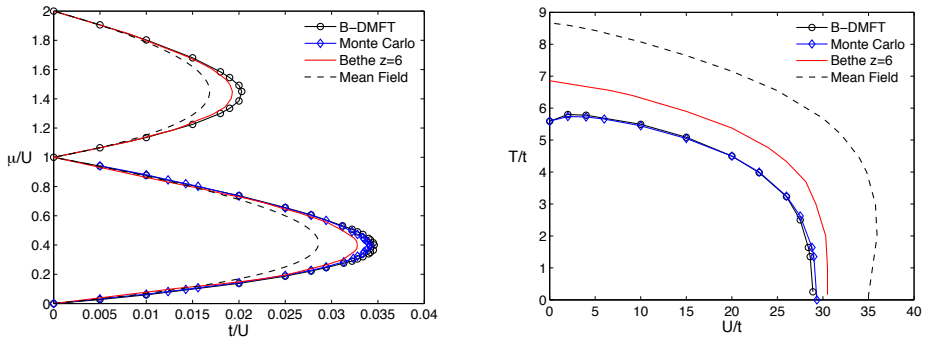

Figure 4.1.: Left panel: groundstate phase diagram of the Bose-Hubbard model on a cubic lattice as a function of hopping amplitude t (used in these figures instead of J), chemical potential μ and interaction strength U. Right panel: phase diagram of the Bose-Hubbard model at density $n = 1$ on a cubic lattice as a function of hopping amplitude t, temperature T and interaction strength U. The results are computed with quantum Monte Carlo (blue diamonds), BDMFT (black circles), mean-field (dashed black line) and BDMFT on a Bethe lattice (red line, not discussed here). The figures are reprinted from Ref. [65]

is stationary in ϕ, i.e.

$$\beta \frac{\delta \Omega_{\mathrm{MF}}\left[\phi, \phi^*\right]}{\delta \phi} = \beta \frac{\delta \Omega_{\mathrm{MF}}\left[\phi, \phi^*\right]}{\delta \phi^*} = 0, \tag{4.22}$$

which yields the self-consistency condition [9]

$$\phi = \langle b \rangle_{H_{\mathrm{MF}}}, \tag{4.23}$$

where the notation $\langle \dots \rangle_{H_{\mathrm{MF}}}$ means taking the expectation value with respect to the eigenstates of the Hamiltonian (4.20).

There are multiple procedures in order to find the solution of the lattice system within the mean-field decoupling approximation. One consists in doing the variation of the free-energy in ϕ directly, searching for a stationary solution with (4.22). Another one, most commonly used, consists in an iterative scheme where one starts with some initial guess for ϕ, plugs it into the Hamiltonian (4.20) (step 1), computes a new guess for ϕ through the expectation value (4.23) (step 2), and repeats step 1 and 2 until the value of ϕ is converged and (4.23) is fulfilled.

By the approximation (4.14) mean-field can be expected to work well when non-local quadratic fluctuations become negligible, i.e. $\langle \delta b_i^\dagger \delta b_j \rangle \ll 1$, for $i \neq j$. If this is not the case, the fraction of uncondensed bosons in the system is systematically underestimated (and the condensate order parameter ϕ therefore systematically overestimated). In the three-dimensional Bose-Hubbard model at zero temperature neglecting quadratic fluctuations works very well deep in the superfluid phase, where the particle density is given by $n \approx |\phi|^2$ and the fraction of uncondensed particles is very low, as well as deep in the Mott phase, where $\phi = 0$, but the particles are strongly localized by the interaction and non-local correlations are negligible. At intermediate couplings mean-field interpolates between these two extreme cases and deviates from the numerically exact quantum Monte Carlo results [49, 47, 48, 87, 103]. This can be seen in the groundstate phase diagram (left panel) of Fig. 4.1, where mean-field overestimates the superfluid phase. At finite temperature mean-field further looses accuracy, as it does not include any thermal fluctuations in the formalism, as can be seen in the finite-temperature phase diagram of Fig. 4.1 (right panel). In the left panel of Fig. 4.2 we see how the condensate is systematically overestimated by mean-field, especially close to the phase transition, while the kinetic energy (right panel) goes to zero as soon

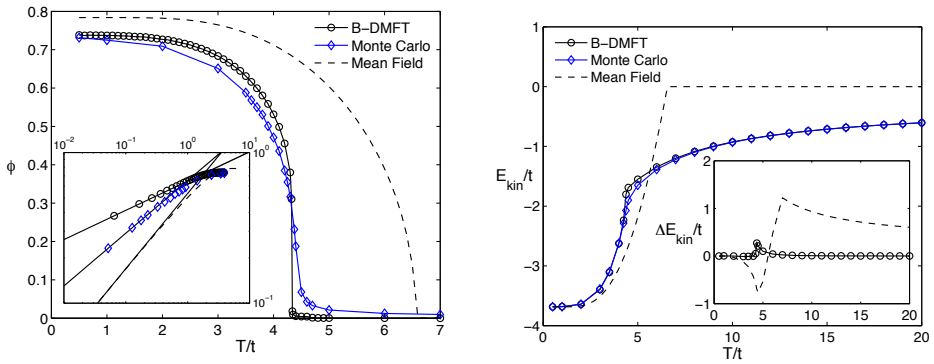

Figure 4.2.: Left panel: condensate order parameter ϕ of the Bose-Hubbard model on a cubic lattice as a function of the temperature T and hopping amplitude t (used in these figures instead of J). Right panel: kinetic energy E_{kin} of the Bose-Hubbard model on a cubic lattice as a function of the temperature T and hopping amplitude t. The results are computed with quantum Monte Carlo (blue diamonds), BDMFT (black circles), and mean-field (dashed black line), at fixed chemical potential $\mu/U = 0.4$ and interaction strength $U/t = 20$. The figures are reprinted from Ref. [65]

as the superfluid phase is abandoned, as the uncondensed contributions to the kinetic energy are neglected by the decoupling approximation (4.14).

For systems where a phase transition is not driven by condensation of bosons, mean-field will characterize the gapless phase by an artificial finite condensate ϕ. This is the case in low-dimensional systems such as e.g. in the Bose-Hubbard model in one dimension where the superfluid phase is uncondensed [13], leading to mean-field behaving much worse as in Figs. 4.1 and 4.2. Finally, it should be noted that, unlike the methods discussed after Sec. 4.4, mean-field is a perturbative approach, as the full Hamiltonian of the lattice system is approximated by neglecting quadratic fluctuations. Due to this approach mean-field is only self-consistent on the level of the condensate through Eq. (4.23) but looses any self-consistency on the level of two-point functions such as the Green's function [Eq. (4.7)].

4.3. Cluster Gutzwiller mean-field theory

In the case of more complicated Hamiltonians or when studying phases in which non-local correlations are essential, one would like to use methods which instead of solving single-site impurities and neglecting all non-local correlations as in Sec. 4.2, uses an impurity consisting of a cluster of sites, containing all crucial short-range correlations. One such method is a straight-forward extension of the mean-field decoupling approximation to clusters named cluster Gutzwiller mean-field (CGMF) [77, 104].

In this approach the full lattice system is partitioned into N_c/N_L smaller clusters of N_c sites dubbed "$\mathcal{C}$", where N_L is the total number of lattice sites. The crucial point of CGMF is that the Hamiltonian within the clusters $\mathcal{C}$ is left unchanged, while only terms which couple the cluster $\mathcal{C}$ with other clusters are treated through the mean-field decoupling approximation. In short, building upon Sec. 4.2, this means that $\delta b_i^\dagger \delta b_j \approx 0$ is used in Eq. (4.13) only if the sites i and j belong to different clusters, yielding the effective CGMF Hamiltonian [77, 104],

$$H_{\mathcal{C}}\left[\{\phi_j\},\{\phi_j^*\}\right] = \sum_{i\in\mathcal{C},j\in\mathcal{C}} t_{ij} b_i^\dagger b_j + \sum_{i\in\mathcal{C}} \left(\hat{V}_i - \mu n_i\right) + \sum_{i\in\mathcal{C},j\notin\mathcal{C}} \left(t_{ij} b_i^\dagger \phi_j + t_{ji}\phi_j^* b_i\right), \tag{4.24}$$

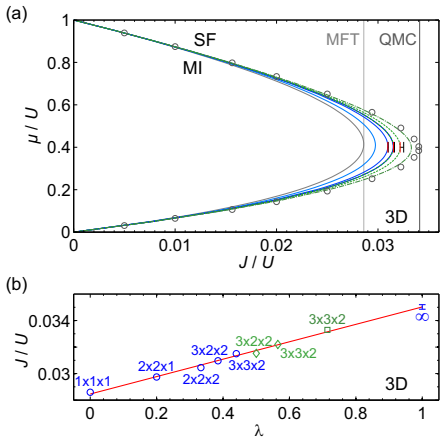

Figure 4.3.: (a) Groundstate phase diagram of the Bose-Hubbard model on a cubic lattice as a function of hopping amplitude J, chemical potential μ and interaction strength U computed with CGMF for different clusters $\mathcal{C}$, compared to QMC data from Ref. [87] (black circles). (b) Critical coupling J/U at the tip of the Mott lobe as a function of the dimensionless parameter λ, where the value of $\lambda = 1$ ("∞") represents the QMC result. Clusters with open boundaries are shown as blue circles/lines, clusters with periodic boundaries in one direction as green diamonds/lines, while periodic boundaries in two directions are shown as green squares/dashed lines. The figures are reprinted from Ref. [77]

which again can be solved through the generalization of the self-consistency condition (4.23), i.e.

$$\phi_i = \langle b_i \rangle_{H_\mathcal{C}}. \tag{4.25}$$

By applying the mean-field decoupling approximation only to terms on the boundary of the cluster $\mathcal{C}$ while treating the other terms exactly, CGMF however breaks the translational invariance of the cluster. In fact, in the absence of condensation, i.e. $\phi = 0$, the lattice system is reduced to a set of decoupled clusters with open boundaries. Further, the eigenstates of (4.24) will feel a strong influence of the boundaries if the cluster is not large enough, introducing artificial density and condensate modulations. These effects can be mitigated if one artificially introduces periodic boundaries on the cluster [77], partially restoring the translational invariance.

When the cluster size N_c increases and the boundary effects become less important, the accuracy of the method increases accordingly, until at $N_c = N_L$ (i.e. if the cluster is as large as the full lattice), the approximation becomes exact. This is shown in Fig. 4.3, where the groundstate phase diagram of the Bose-Hubbard model on a cubic lattice computed with CGMF converges towards the QMC results with increasing cluster size. As can be seen, the simulations where periodic boundaries were used are more accurate, while the critical coupling at the tip of the Mott lobe converges towards the numerically exact QMC value with increasing dimensionless parameter $\lambda = B_\mathcal{C} / (B_\mathcal{C} + B_{\delta\mathcal{C}})$. Here, $B_\mathcal{C}$ is the number of bonds within the cluster that are treated exactly, while $B_{\delta\mathcal{C}}$ is the number of bonds on the boundary which are treated by the mean-field decoupling approximation, such that $\lambda = 1$ when $N_c = N_L$ (and therefore $B_{\delta\mathcal{C}} = 0$). A similar mean-field approach to CGMF with the same properties discussed here has also been derived under the name cluster composite boson mapping method in Ref. [78].

4.4. Baym-Kadanoff effective action

The effective action formulation is a useful starting point for approximations to the many-body system beyond mean-field (i.e. including quadratic terms). It is based on a Legendre transform of the free energy functional Ω in both $\mathbf{F}$ and $\mathbf{G}_0^{-1}$ [see Eqs. (4.6) and (4.7)] to the interacting system propagators $\mathbf{\Phi}$ and $\mathbf{G}$, see Refs. [105, 106] for an overview.

The resulting functional $\Gamma_{\mathrm{BK}} = \Gamma_{\mathrm{BK}}[\mathbf{\Phi}, \mathbf{G}]$ was derived by Baym and Kadanoff [107, 108] for fermions and generalized to bosons by De Dominicis and Martin [109, 110] and later to relativistic systems [111]. The functional has the form

$$\Gamma_{\mathrm{BK}}[\mathbf{\Phi}, \mathbf{G}] = S_0[\mathbf{\Phi}] + \frac{1}{2}\mathrm{Tr}[\mathbf{G}_0^{-1}\mathbf{G}] + \frac{1}{2}\mathrm{Tr}\ln[-\mathbf{G}^{-1}] + \Phi_{\mathrm{LW}}[\mathbf{\Phi}, \mathbf{G}], \tag{4.26}$$

where S_0 is the non-interacting part of the system action, $S_0[\mathbf{\Phi}] = \mathbf{F}^\dagger\mathbf{\Phi} - \frac{1}{2}\mathbf{\Phi}^\dagger\mathbf{G}_0^{-1}\mathbf{\Phi}$. For explicit definitions of the products and traces, see Appendix A.1. The Baym-Kadanoff functional Γ_{BK} is stationary in $\mathbf{\Phi}$ and $\mathbf{G}$ at the physical solution

$$\frac{\delta\Gamma_{\mathrm{BK}}}{\delta\mathbf{\Phi}^\dagger} = 0\,, \quad \frac{\delta\Gamma_{\mathrm{BK}}}{\delta\mathbf{G}} = 0\,. \tag{4.27}$$

In Eq. 4.26, the whole complexity of the many-body system is contained in the Luttinger-Ward functional $\Phi_{\mathrm{LW}}[\mathbf{\Phi}, \mathbf{G}] \equiv \Phi_{\mathrm{LW}}[\mathbf{\Phi}, \mathbf{G}, \hat{\nu}_3, \hat{V}_4]$ [112] which contains all two-particle irreducible diagrams (2PI) in $\mathbf{G}$ with the three- and four-point vertices $\hat{\nu}_3 = \hat{V}_3 + \hat{V}_4\mathbf{\Phi}$ and $\hat{V}_4$, respectively [1]. Note that the Luttinger-Ward functional Φ_{LW} is a universal functional, in that it depends only on the interacting one- and two-point propagators ($\mathbf{\Phi}$ and $\mathbf{G}$ respectively) and the three- and four-point interaction vertices ($\hat{V}_3$ and $\hat{V}_4$). In particular, Φ_{LW} does not depend on the free propagator $\mathbf{G}_0$ of the system. Using the diagrammatic notation

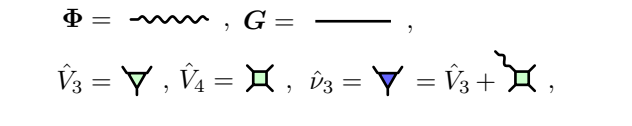

(4.28)

the lowest order diagrams in Φ_{LW} can be written as

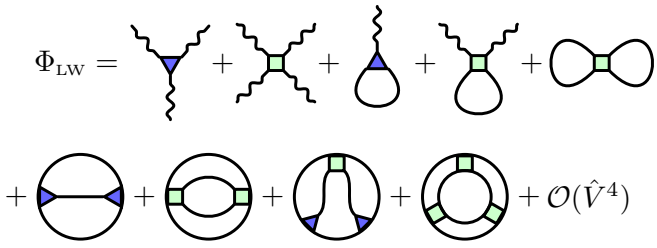

when omitting constant prefactors [105]. The functional derivative $\delta_{\mathbf{\Phi}^\dagger}\Phi_{\mathrm{LW}}$ amounts to removing one $\mathbf{\Phi}^\dagger$ term in the first order terms and in the effective three point vertex $\hat{\nu}_3 = \hat{V}_3 + \hat{V}_4\mathbf{\Phi}$, which yields a one-point 2PI vertex

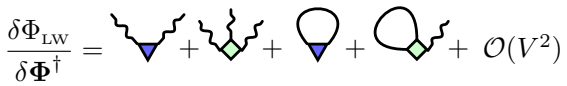

[1] Note that the Luttinger-Ward functional Φ_{LW} for symmetry broken bosons with only a four-particle interaction vertex ($\hat{V}_3 = 0$, $\hat{V}_4 \neq 0$) still acquires an effective three-particle vertex [105] ($\hat{\nu}_3 = \hat{V}_4\mathbf{\Phi}$).

while $\delta_{\mathbf{G}}\Phi_{\text{LW}}$ corresponds to cutting one propagator line $\mathbf{G}$, which yields a two-point 2PI vertex

$$\frac{\delta\Phi_{\text{LW}}}{\delta\mathbf{G}} =$$ 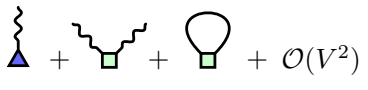 $$+ \mathcal{O}(V^2)$$

The explicit form of the stationary condition [Eq. (4.27)] gives the equations of motion for the propagators

$$\frac{\delta\Gamma_{\text{BK}}}{\delta\mathbf{\Phi}^\dagger} = \mathbf{F} - \mathbf{G}_0^{-1}\mathbf{\Phi} + \frac{\delta\Phi_{\text{LW}}}{\delta\mathbf{\Phi}^\dagger} = 0\,, \tag{4.29}$$

$$\frac{\delta\Gamma_{\text{BK}}}{\delta\mathbf{G}} = \frac{1}{2}\mathbf{G}_0^{-1} - \frac{1}{2}\mathbf{G}^{-1} + \frac{\delta\Phi_{\text{LW}}}{\delta\mathbf{G}} = 0\,. \tag{4.30}$$

In the last equation we directly identify the two-point 2PI vertex as the self-energy $\delta_{\mathbf{G}}\Phi_{\text{LW}} = -\mathbf{\Sigma}/2$. The one-point vertex is less renowned, and will be denoted here as $\delta_{\mathbf{\Phi}^\dagger}\Phi_{\text{LW}} = -\mathbf{\Sigma}_{1/2}$. Hence, the stationary condition yields the Dyson equations

$$\mathbf{G}_0^{-1}\mathbf{\Phi} = \mathbf{F} - \mathbf{\Sigma}_{1/2}\,, \tag{4.31}$$

$$\mathbf{G}^{-1} = \mathbf{G}_0^{-1} - \mathbf{\Sigma}\,. \tag{4.32}$$

The power of the effective action formalism is that approximations of the Luttinger-Ward functional Φ_{LW} produce non-perturbative approximations, i.e., sums to all orders in the interactions $\hat{V}_3$ and $\hat{V}_4$ and the non-interacting propagator $\mathbf{G}_0$, that still obey the symmetries of the original system. In particular the approximations conserve total energy, density, and momentum [107, 108]. In (relativistic) quantum field theory it is common to make consistent approximations in Φ_{LW} to a given "loop-order" in the 2PI diagrams [113].

Recently, interesting issues regarding the single-valuedness of the Luttinger-Ward functional Φ_{LW} have been raised within the framework of truncated (but high-order) expansions using diagrammatic Monte Carlo, dynamical mean-field theory, and the GW-approximation [114, 115]. The findings show that particular self-consistent schemes to sum the boldified diagrams to infinite order can produce non-physical solutions, where a solution is given by the resulting propagator(s) $\mathbf{G}$ (and $\mathbf{\Phi}$) and self-energy(s) $\mathbf{\Sigma}$ (and $\mathbf{\Sigma}_{1/2}$). This should come as no surprise as the construction of the Baym-Kadanoff functional Γ_{BK} is a Legendre-transform of the free energy Ω. Thus, while Γ_{BK} and Ω have the same stationary points, there is no guarantee that maximas and inflection points of Ω do not become minimas of Γ_{BK}. In such a case a stationary point of Ω, which is not a local minimum, can very well become a local minimum of Γ_{BK} and hence an attractive fix-point for self-consistent calculations of Γ_{BK} through the evaluation of Φ_{LW}.

4.5. Bosonic dynamical mean-field theory

4.5.1. Dynamical mean-field approximation

An interesting class of approximations to the effective action amounts to evaluate the exact Luttinger-Ward functional, but only for a selected subset of propagators. One example is the local real-space approximation

$$\Phi_{\mathrm{LW}}[\mathbf{\Phi}, \mathbf{G}] \approx \Phi_{\mathrm{LW}}[\mathbf{\Phi}, \mathbf{G}_{ii}]\,, \tag{4.33}$$

which accounts for all diagrams with site-local propagators $\mathbf{G}_{ii}$ of the lattice. For number conserving systems ($\mathbf{\Phi} = \mathbf{F} = 0$), Eq. (4.33) becomes an equality in the limit of infinite dimensions [116, 117] yielding the exact solution. Only accounting for local diagrams in Φ_{LW} trivially generates a site-local self-energy

$$-2\delta_{\mathbf{G}_{ij}}\Phi_{\mathrm{LW}}[\mathbf{\Phi}, \mathbf{G}_{ll}] = \delta_{ij}\mathbf{\Sigma}_{ii}\,. \tag{4.34}$$

This approximation is not interesting *per se* as the calculation of $\Phi_{\mathrm{LW}}[\mathbf{\Phi}, \mathbf{G}_{ii}]$ remains a formidable problem. The ingenuity of dynamical mean-field theory (DMFT), however, is the observation that there exists a simpler and exactly solvable many-body system with the same local Luttinger-Ward functional. In fact, there is a reference system (here denoted with primed quantities) with the same propagators $\mathbf{\Phi}$ and $\mathbf{G}_{ii}$, and thus the same Luttinger-Ward functional $\Phi_{\mathrm{LW}}[\mathbf{\Phi}, \mathbf{G}_{ii}]$, but with *a priori* unknown local sources $\mathbf{F}'_i$ and $\mathbf{G}'_{0,ij} = \delta_{ij}\mathbf{G}'_0$. By the approximation (4.33) and Eq. (4.34) the full lattice and the reference system have the same self-energies. This is commonly known as the DMFT approximation [116, 117]

$$\mathbf{\Sigma}_{ij} = \delta_{ij}\mathbf{\Sigma}'_{ii}, \tag{4.35}$$

$$\mathbf{\Sigma}_{1/2} = \mathbf{\Sigma}'_{1/2}. \tag{4.36}$$

The corresponding reference-system effective action,

$$\Gamma'_{\mathrm{BK}} = S'_0[\mathbf{\Phi}] + \frac{1}{2}\mathrm{Tr}[\mathbf{G}'^{-1}_0\mathbf{G}_{ii}] + \frac{1}{2}\mathrm{Tr}\ln[-\mathbf{G}^{-1}_{ii}] + \Phi_{\mathrm{LW}}[\mathbf{\Phi}, \mathbf{G}_{ii}]\,, \tag{4.37}$$

is also stationary at $\mathbf{\Phi}$ and $\mathbf{G}_{ii}$, $\delta_{\mathbf{\Phi}^\dagger}\Gamma'_{\mathrm{BK}} = \delta_{\mathbf{G}_{ii}}\Gamma'_{\mathrm{BK}} = 0$.

The DMFT effective action can be constructed as the difference, $\Gamma_{\mathrm{DMFT}} = \Gamma_{\mathrm{BK}} - \Gamma'_{\mathrm{BK}}$, which remains stationary, $\delta_{\mathbf{\Phi}}\Gamma_{\mathrm{DMFT}} = \delta_{\mathbf{G}_{ii}}\Gamma_{\mathrm{DMFT}} = 0$, and whose variations give

$$\frac{\delta\Gamma_{\mathrm{DMFT}}}{\delta\mathbf{\Phi}^\dagger_i} = \sum_j \mathbf{G}^{-1}_{0,ij}\mathbf{\Phi}_j - \mathbf{G}'^{-1}_0\mathbf{\Phi}_i - \mathbf{F}_i + \mathbf{F}'_i = 0\,, \tag{4.38}$$

$$\frac{\delta\Gamma_{\mathrm{DMFT}}}{\delta\mathbf{G}_{ii}} = [\mathbf{G}^{-1}_0]_{ii} + [-\mathbf{G}^{-1}]_{ii} - \mathbf{G}'^{-1}_0 - [-\mathbf{G}_{ii}]^{-1} = [\mathbf{G}_{ii}]^{-1} + \mathbf{\Sigma}_{ii} - \mathbf{G}'^{-1}_0 = 0\,. \tag{4.39}$$

These stationarity conditions are equivalent to the DMFT self-consistency equations [117] which are used to determine the reference system's source fields $\mathbf{F}'$ and $\mathbf{G}'^{-1}_0$; Eq. (4.39) fixes the reference system's Weiss field $\mathbf{G}'_0$ [117] and Eq. (4.38) determines the effective symmetry breaking field $\mathbf{F}'$ of the reference system in the bosonic generalization of DMFT [62, 63, 64, 65, 66, 67].

Solving the reference system while imposing these relations yields a non-trivial and non-perturbative solution of the original lattice system, including all local diagrams in Φ_{LW}. Note that the reference system, commonly called "the impurity problem" in DMFT, has a general (retarded) non-interacting propagator $\mathbf{G}'^{-1}_0$, and exact solutions can only be obtained by infinite summations of diagrams using, e.g., continuous-time quantum Monte Carlo solvers [68, 69].

4.5.2. Reference system

In order to derive the bosonic DMFT (BDMFT) reference system, we start from the Hamiltonian (2.15) (we specifically discuss the Bose-Hubbard model here, however the procedure can also be trivially extended to more general dispersions), and treat the partition function of the full system in the presence of retardation as $\mathcal{Z} = \mathrm{Tr}[\mathcal{T}e^{-S}]$ with the action S given by

$$\begin{aligned} S = &\frac{1}{2}\int_0^\beta d\tau \left(\sum_i \mathbf{b}_i^\dagger(\tau)\partial_\tau \sigma_z \mathbf{b}_i(\tau) - J\sum_{\langle i,j\rangle} \mathbf{b}_i^\dagger(\tau)\mathbf{b}_j(\tau) \right) \\ &+ \int_0^\beta d\tau \sum_i \left(\frac{U}{2} b_i^\dagger(\tau) b_i^\dagger(\tau) b_i(\tau) b_i(\tau) - \mu n_i(\tau) \right), \end{aligned} \tag{4.40}$$

where we use the Nambu notation introduced in the beginning of this chapter.

As in Sec. 4.2, we expand the Nambu operator $\mathbf{b}_j(\tau) = \mathbf{\Phi} + \delta\mathbf{b}_j(\tau)$ around its site- and imaginary-time-independent mean-field value $\mathbf{\Phi} = \langle \mathbf{b} \rangle$, giving us

$$\begin{aligned} S &= S_o + S_{\mathrm{ext}} + \Delta S, \\ S_o &= \int_0^\beta d\tau \left(\frac{1}{2}\mathbf{b}_o^\dagger(\tau)\partial_\tau\sigma_z\mathbf{b}_o(\tau) + \frac{U}{2} n_o(\tau)(n_o(\tau)-1) - \mu n_o(\tau) - zJ\mathbf{\Phi}^\dagger \mathbf{b}_o(\tau) \right), \\ \Delta S &= -J\int_0^\beta d\tau \sum_{\langle i,o\rangle} \delta\mathbf{b}_i^\dagger(\tau)\delta\mathbf{b}_o(\tau), \end{aligned} \tag{4.41}$$

where S_o is local at the impurity-site 'o', ΔS couples 'o' with neighboring sites, while S_{ext} does not include any terms at site 'o'. We wish to separate the full partition function as $Z = Z_{\mathrm{ext}} Z_o$. Here, Z_{ext} is the full (and unknown) partition of the system determined by the terms in the action not involving the site o, i.e. S_{ext}. It is treated as an irrelevant number in the following. The partition function Z_o contains the full local action S_o as well as the correlations introduced by "ext" on the origin as follows,

$$Z_o = \mathrm{tr}\left[e^{-S_o - \langle \Delta S \rangle_{S_{\mathrm{ext}}}} \right] \tag{4.42}$$

where the expectation value $\langle \Delta S \rangle_{S_{\mathrm{ext}}}$ is approximated by the cumulant expansion to second order,

$$\begin{aligned} \langle \Delta S \rangle_{S_{\mathrm{ext}}} \approx &- \int_0^\beta d\tau J \left\langle \sum_{\langle i,o\rangle} \delta\mathbf{b}_i^\dagger(\tau)\delta\mathbf{b}_o(\tau) \right\rangle_{S_{\mathrm{ext}}} \\ &- \frac{1}{2}\int_0^\beta d\tau d\tau' J^2 \left\langle \sum_{\langle i,o\rangle} \delta\mathbf{b}_i^\dagger(\tau)\delta\mathbf{b}_o(\tau) \sum_{\langle j,o\rangle} \delta\mathbf{b}_j^\dagger(\tau')\delta\mathbf{b}_o(\tau') \right\rangle_{S_{\mathrm{ext}}} \\ = 0 &- \int_0^\beta d\tau d\tau' \frac{1}{2}\delta\mathbf{b}_o^\dagger(\tau)\mathbf{\Delta}(\tau-\tau')\delta\mathbf{b}_o(\tau'), \end{aligned} \tag{4.43}$$

as $\langle \delta\mathbf{b}_i^\dagger(\tau) \rangle = 0$ by definition. $\mathbf{\Delta}(\tau - \tau')$ here is an unknown 2×2 Nambu matrix commonly referred to as hybridization function [62, 63, 64, 65, 66, 67] with entries $\Delta_{00}(\tau) = \Delta_{11}(-\tau)$ and $\Delta_{01}(\tau) = \Delta_{10}^*(\tau)$, which have to be determined self-consistently.

Plugging Eq. (4.43) into Eq. (4.41) leads to the effective BDMFT impurity action [65, 67]

$$S_{\mathrm{BDMFT}} = \int_0^\beta d\tau \left(\frac{1}{2}\mathbf{b}_o^\dagger(\tau)\partial_\tau\sigma_z\mathbf{b}_o(\tau) - zJ\mathbf{\Phi}^\dagger\mathbf{b}_o(\tau) \right) \tag{4.44}$$

$$- \int_0^\beta d\tau d\tau' \frac{1}{2} \delta \mathbf{b}_o^\dagger(\tau) \mathbf{\Delta}(\tau - \tau') \delta \mathbf{b}_o(\tau') + \int_0^\beta d\tau \left(\frac{U}{2} n_o(\tau)(n_o(\tau) - 1) - \mu n_o(\tau) \right),$$

which is completely local at site 'o' and has a free propagator,

$$\mathbf{G}_0'^{-1}(i\omega_n) = i\omega_n \sigma_z + \mu \mathbf{1} + \mathbf{\Delta}(i\omega_n), \tag{4.45}$$

and symmetry-breaking field,

$$\mathbf{F}'^\dagger = (\Delta_{00}(i\omega_0) + \Delta_{01}(i\omega_0) - zJ)\, \mathbf{\Phi}^\dagger. \tag{4.46}$$

Unlike for the impurity Hamiltonians of the mean-field approaches of Secs. 4.2 and 4.3, which can be diagonalized in Fock space, the partition function corresponding to the BDMFT action of Eq. (4.44) is still a non-trivial functional integral which has to be solved by continuous-time quantum Monte Carlo simulations [68, 69, 65, 67]. In the case of a condensed phase with $\phi \neq 0$, the symmetry-breaking terms introduce a sign-problem in the Monte Carlo simulation [65, 67]. This makes it very hard to expand this approach to cluster impurities, as was done for mean-field in Sec. 4.3. Furthermore, in the case of lattices which already introduce a sign-problem in QMC simulations [49, 47, 48, 87, 103] (such as e.g. artificial gauge fields with complex hoppings) the sign-problem can also return in the Monte Carlo solver in the absence of symmetry-breaking.

4.5.3. Implementation and results

For practical purposes the self-consistency relations derived in Sec. 4.5.1 can be further simplified through the Dyson equations (4.31) and (4.32). By (4.31) we have for the reference system,

$$\mathbf{\Sigma}'_{1/2} = \mathbf{F}' - \mathbf{G}_0'^{-1}(i\omega_0) \langle \mathbf{b} \rangle_{S_{\mathrm{BDMFT}}}, \tag{4.47}$$

where $\langle \dots \rangle_{S_{\mathrm{BDMFT}}}$ means taking the expectation value with respect to the action (4.44). For the lattice system on the other hand since $\mathbf{F} = 0$ we have

$$\mathbf{\Phi} = -\mathbf{G}_0(k = 0, i\omega_0) \mathbf{\Sigma}_{1/2}, \tag{4.48}$$

where $\mathbf{G}_0^{-1}(k, i\omega_n) = i\omega_n \sigma_z + (\mu - \epsilon_k)\, \mathbf{1}$. Taking these two expressions with Eq. (4.36), the self-consistency condition (4.38) and the definition of $\mathbf{F}'$ (4.46) gives us the general self-consistency conditions for the condensate,

$$\mathbf{\Phi} = \langle \mathbf{b} \rangle_{S_{\mathrm{BDMFT}}} \tag{4.49}$$

$$\mathbf{F}'^\dagger = (\Delta_{00}(i\omega_0) + \Delta_{01}(i\omega_0) - zJ) \langle \mathbf{b}^\dagger \rangle_{S_{\mathrm{BDMFT}}}. \tag{4.50}$$

By (4.35), the lattice Green's function is given by

$$\mathbf{G}^{-1}(k, i\omega_n) = \mathbf{G}_0^{-1}(k, i\omega_n) - \mathbf{\Sigma}'(i\omega_n). \tag{4.51}$$

which gives us the local Green's function

$$\mathbf{G}_{ii}(i\omega_n) = \int dk \left[\mathbf{G}_0^{-1}(k, i\omega_n) - \mathbf{\Sigma}'(i\omega_n) \right]^{-1}, \tag{4.52}$$

from which by the self-consistency condition (4.39) and Eq. (4.45) we can compute the hybridiza-

tion as,

$$\mathbf{G}_{ii}(i\omega_n) = \mathbf{G}'(i\omega_n) \tag{4.53}$$

$$\boldsymbol{\Delta}(i\omega_n) = \mathbf{G}_{ii}^{-1}(i\omega_n) + \boldsymbol{\Sigma}'(i\omega_n) - i\omega_n\sigma_z - \mu\mathbf{1}, \tag{4.54}$$

Now everything is in place in order to devise an iterative scheme to find the values of the parameters $\mathbf{F}'$ and $\boldsymbol{\Delta}$: starting from initial guesses for $\mathbf{F}'$ and $\boldsymbol{\Delta}$, one computes the reference systems condensate $\boldsymbol{\Phi}'$ and self-energy $\boldsymbol{\Sigma}'$ from the action (4.44) by a continuous-time quantum Monte Carlo simulation [68, 69, 65, 67] (step 1). Using the values of $\boldsymbol{\Phi}'$ and $\boldsymbol{\Sigma}'$ one then computes new values for $\mathbf{F}'$ and $\boldsymbol{\Delta}$ through Eqs. (4.50), (4.52) and (4.54) (step 2). Step 1 and 2 are then repeated untill the self-consistency conditions (4.49) and (4.53) are met and the algorithm is converged.

As the cumulant expansion in the reference system [Eq. (4.43)] was only performed up to second order, the DMFT approach can be expected to work well only if higher-order terms in the non-condensed non-local fluctuations, i.e. non-local terms of order $\mathcal{O}\left[\left(J\delta\mathbf{b}^\dagger\right)^3\right]$, can be neglected. This is especially the case when $\boldsymbol{\Delta} \ll 1$ and BDMFT reduces to mean-field, such as deep in high-dimensional superfluid phases where uncondensed bosons are negligible, or in the strongly interacting regime, where non-local processes are suppressed. Further, by the DMFT approximation (4.35), BDMFT is expected to work well whenever non-local terms in the self-energy can be neglected. In three dimensions or two dimensions and zero temperature this is often the case for bosons, as they tend to condense when they delocalize, such that the non-local part of the problem is taken care of by the condensate $\boldsymbol{\Phi}$. In lower dimensions, where superfluid phases are uncondensed, non-local processes of uncondensed bosons become much more prominent, leading to a worse behavior of BDMFT. It should be noted however that the method is self-consistent only on a local level according to (4.53). Non-local two-point quantities can be evaluated by (4.51), but are not guaranteed to be good approximations due to the local nature of $\boldsymbol{\Sigma}'$.

In higher dimensions in the Bose-Hubbard model, BDMFT shows a remarkable accuracy, reproducing the phase-diagram on the cubic lattice in excellent agreement with QMC both at zero temperature (left panel Fig. 4.1) and finite temperature (right panel Fig. 4.1). The same is true for local observables such as the condensate order parameter (left panel Fig. 4.2) or the kinetic energy (right panel Fig. 4.2), which deviate from the exact results only very close to the phase transition. A similar behavior can be observed in the two-dimensional case at zero temperature [65, 67], while lower-dimensional systems are no-longer captured as well, due to the uncondensed non-local nature of the underlying phases.

Part II.

Self-energy functional theory

5

Bogoliubov+U theory

While excelling with high numerical accuracy, the bosonic dynamical mean-field theory (BDMFT, see Sec. 4.5) is numerically rather complex due to the imaginary-time dependency of the hybridization term. At finite temperature the impurity problem has to be solved by continuous time quantum Monte Carlo methods [65, 67], where, due to the difference in sign between the normal and the anomalous Green's function, a sign problem arises in the symmetry broken phase.

In this chapter, we filter out the ingredients of the BDMFT reference system that are indispensable for its accuracy and arrive at a simpler formalism. This is the Bogoliubov+U theory (B+U), which makes use of a simplified effective impurity Hamiltonian, similar to the action of extended mean field theory, which was developed in the high-energy community [118, 119] but differs conceptually from our formalism. B+U has a negligible computational cost and is not prone to numerical instabilities. The premise of our theory is that the Bose-Hubbard model (see Sec. 2.2) can be fully characterized at zero temperature by the three parameters ϕ, Σ_{00}, and Σ_{01} (the condensate order parameter, and the normal and the anomalous self-energy, respectively) if the self-energy is treated as a variational parameter, providing a far better approximation to finite-temperature properties than simple mean-field theory. B+U can be seen as a simplified BDMFT where only a single Matsubara frequency is kept. It is different from the variational cluster approximation (VCA) by also considering non zero values of pair creation and annihilation of depleted particles [120]. It is also the simplest accurate extension of the weakly interacting Bose gas theory [103] to lattice systems with a superfluid to Mott insulator transition. It further provides a very natural framework compared to the collective quantum field theory developed by Kleinert *et al.* [121] and the two collective fields proposed by Cooper *et al.* [122, 123, 124], and behaves quantitatively much better. It has a similar functional degree of freedom as the projector technique introduced by Trefzger and Sengupta [125] for finite lattices.

Note that this chapter should be considered as a first ad hoc modification of BDMFT to be used in combination with the simple reference system introduced here. We will later systematically derive an entirely non-perturbative framework which can be used with the same reference system, the self-energy functional theory, in Chapters 6 and 7.

This chapter closely follows Ref. [1] and is organized as follows. In Sec. 5.1 the B+U formalism is introduced for the Bose-Hubbard model, while in Sec. 5.2 the details of the variational calculation of the optimal self-energy are shown. We furthermore summarize the full self-consistent scheme of B+U and show how thermodynamic quantities can be calculated from it in Sec. 5.3, while some simple limits of B+U are explained in Sec. 5.4. Finally, in Sec. 5.5 we present results on the Bose-Hubbard model at zero and finite temperature comparing them with QMC and BDMFT.

5.1. Solver and self-consistency condition

In this section we introduce the B+U formalism for the Bose-Hubbard model in equilibrium. In order to derive an effective Hamiltonian, we start from the full Bose-Hubbard Hamiltonian (see Sec. 2.2),

$$H_{\mathrm{BH}} = -J \sum_{\langle i,j \rangle} b_i^\dagger b_j + \frac{U}{2} \sum_i n_i \left(n_i - 1\right) - \mu \sum_i n_i, \tag{5.1}$$

In order to determine the thermodynamic properties of the system, we have to compute the condensate density and the connected Green's function, defined respectively as

$$\mathbf{\Phi} = \langle \mathbf{b} \rangle, \tag{5.2}$$

$$\mathbf{G}_{i,j}(\tau) = -\left\langle \mathbf{b}_i(\tau) \mathbf{b}_j^\dagger(0) \right\rangle + \mathbf{\Phi}\mathbf{\Phi}^\dagger, \tag{5.3}$$

with Nambu notation $\mathbf{b}_i(\tau) = \begin{pmatrix} b_i(\tau) \\ b_i^\dagger(\tau) \end{pmatrix}$, and $\mathbf{\Phi} = \begin{pmatrix} \phi \\ \phi^* \end{pmatrix}$. As in mean-field (see Sec. 4.2) and BDMFT (Sec. 4.5), the possibility of a broken $U(1)$ symmetry forces b_j to be expanded around its mean-field value $\phi = \langle b_j \rangle$ (which we take to be site independent and can always be chosen real) by $b_j = \phi + \delta b_j$. If we concentrate on the site at the origin b_o, the Hamiltonian can be rewritten as

$$\begin{aligned} H &= H_o + H_{\mathrm{ext}} + \Delta H, \\ H_o &= \frac{U}{2} n_o(n_o - 1) - \mu n_o - zJ\phi \left(b_o + b_o^\dagger\right), \\ \Delta H &= -J \sum_{\langle i,o \rangle} \left(\delta b_i^\dagger \delta b_o + \delta b_o^\dagger \delta b_i\right), \end{aligned} \tag{5.4}$$

where H_{ext} contains all terms of the Hamiltonian (5.1) not containing the origin "o". The notation $\langle i, o \rangle$ means that we sum over the nearest neighbors of o, and z is the coordination number. As in standard BDMFT (see Sec. 4.5.2) we now wish to separate the full partition function $Z = \mathrm{tr}\left[e^{-\beta H}\right]$ as $Z = Z_{\mathrm{ext}} Z_o$ (although starting from the static Hamiltonian and not from the action as in BDMFT). Here, Z_{ext} is the full (and unknown) partition of the system determined by the terms in the Hamiltonian not involving the site o. It is treated as an irrelevant number in the rest of the chapter. The partition function Z_o contains the full local Hamiltonian H_o as well as the correlations introduced by "ext" on the origin as,

$$Z_o = \mathrm{tr}\left[e^{-\beta\left(H_o + \langle \Delta H \rangle_{H_{\mathrm{ext}}}\right)}\right]. \tag{5.5}$$

We approximate the expectation value $\langle \Delta H \rangle_{H_{\mathrm{ext}}}$ by the cumulant expansion to second order

$$\begin{aligned} \langle \Delta H \rangle_{H_{\mathrm{ext}}} &\approx -J \left\langle \sum_{\langle i,o \rangle} \delta \mathbf{b}_i^\dagger \delta \mathbf{b}_o \right\rangle_{H_{\mathrm{ext}}} - \frac{1}{2} J^2 \left\langle \sum_{\langle i,o \rangle} \delta \mathbf{b}_i^\dagger \delta \mathbf{b}_o \sum_{\langle j,o \rangle} \delta \mathbf{b}_j^\dagger \delta \mathbf{b}_o \right\rangle_{H_{\mathrm{ext}}} \\ &= 0 - \frac{1}{2} \delta \mathbf{b}_o^\dagger \mathbf{\Delta} \delta \mathbf{b}_o, \end{aligned} \tag{5.6}$$

where $\langle \Delta H \rangle$ and $\langle \Delta H \Delta H \rangle$ are rewritten in terms of Nambu operators and $\mathbf{\Delta}$ is an unknown 2×2 real-valued matrix with two independent components $\Delta_{00} = \Delta_{11}$ and $\Delta_{01} = \Delta_{10}$ which describes a correction to the common mean-field impurity Hamiltonian. The anomalous term Δ_{01}, containing processes of the type δb^2, is explicitly taken to be finite in this notation, since it is known from the Bogoliubov theory that deep in the superfluid phase it becomes equally

important to the normal (diagonal) term Δ_{00}, containing the $\delta b^\dagger \delta b$ terms. By (5.6) we arrive at the effective impurity Hamiltonian

$$H_E = -\frac{1}{2}\delta \mathbf{b}_o^\dagger \mathbf{\Delta} \delta \mathbf{b}_o - zJ\phi \left(b_o + b_o^\dagger\right) + \frac{U}{2} n_o(n_o - 1) - \mu n_o. \tag{5.7}$$

As can be seen by comparing to Sec. 4.5.2, this effective impurity Hamiltonian is equivalent to BDMFT in the limit

$$\mathbf{\Delta}(\tau_1 - \tau_2) \to \mathbf{\Delta}\delta(\tau_1 - \tau_2). \tag{5.8}$$

Since $\mathbf{\Delta}$ is independent on the Matsubara frequency $i\omega_n$, i.e.

$$\begin{aligned} \mathbf{G'}^{-1}(i\omega_n) &= \mathbf{G'}_0{}^{-1}(i\omega_n) - \mathbf{\Sigma'}(i\omega_n) \\ &= i\omega_n \sigma_z + \mu \mathbf{I} + \mathbf{\Delta} - \mathbf{\Sigma'}(i\omega_n). \end{aligned} \tag{5.9}$$

the BDMFT self-consistency condition (4.54) can no-longer be fulfilled exactly for all Matsubara frequencies. Here, $\mathbf{G'}$, $\mathbf{G'_0}$, and $\mathbf{\Sigma'}$ are the connected Green's function, the non-interacting Green's function and the self-energy of the impurity, respectively. Eq. (4.54) from BDMFT therefore has to be evaluated only for a single Matsubara value in order to determine the value of $\mathbf{\Delta}$. The Green's function which mirrors the symmetry relations assumed for $\mathbf{\Delta}$ is the one evaluated at $\omega_n = 0$. The central characteristic of B+U theory is that we demand that the condensate and the Green's function of the Bose-Hubbard model evaluated at o *for zero (Matsubara) frequency* coincide with the one of system (5.7), i.e.,

$$\Phi \equiv \langle b_o \rangle_{H_E}, \tag{5.10}$$

$$\mathbf{G}_{o,o}(\omega_n = 0) \equiv -\left\langle (\mathbf{b}_o \mathbf{b}_o^\dagger)(\omega_n = 0) \right\rangle_{H_E} + \Phi\Phi^\dagger. \tag{5.11}$$

The paradoxical compatibility of Eqs.(5.11) and (5.8) is specific for bosonic systems [see also below Eq. (5.12)]. The equations constitute a self-consistency problem, whose solution also fixes the factors Δ_{00} and Δ_{01}. This can be solved in a unique way if $\mathbf{\Delta}[\mathbf{G}, \phi]$ is invertible, or, technically speaking, if the Luttinger-Ward functional is unique. Since the static mean-field limit (i.e., the decoupling approximation with $\Delta_{00} = \Delta_{01} = 0$) is always a solution, it is easy to convince oneself that multiple (local) minima occur (cf. Ref. [114] for a recent discussion). Nevertheless, we have been able to determine the physically correct solution without problem in all parameter regimes (see below). In practice, one uses an iteration scheme to solve the self-consistency problem. To this end, we approximate the self-energies of both the full lattice and the reference system by an unknown variational self-energy $\mathbf{\Sigma} \approx \mathbf{\Sigma'} \approx \mathbf{\Sigma}_E$. The factors Δ_{00} and Δ_{01} then follow from the Dyson equation on the impurity site at zero Matsubara frequency, which using (5.10) and (5.11) becomes [see also the equivalent equation in BDMFT (4.54)]

$$\mathbf{\Delta} = \mathbf{\Sigma}_E(\omega_n = 0) + \mathbf{G}_{o,o}(\omega_n = 0)^{-1} - \mu \mathbf{I}. \tag{5.12}$$

The local connected Green's function on the impurity site $\mathbf{G}_{o,o}$ is calculated through the Green's function on the lattice by

$$\mathbf{G}_{o,o}(\omega_n = 0) = \frac{1}{(2\pi)^d} \int d^d k \mathbf{G}(\omega_n = 0, k), \tag{5.13}$$

and the Dyson equation of the full lattice

$$\mathbf{G}^{-1}(\omega_n = 0, k) = \mathbf{G}_0{}^{-1}(\omega_n = 0, k) - \mathbf{\Sigma}_E(\omega_n = 0), \tag{5.14}$$

with the bare Green's function given by $\mathbf{G}_0{}^{-1}(\omega_n, k) = [\mu - \epsilon(k)]\,\mathbf{I} + i\omega_n \sigma_z$, where $\epsilon(k)$ is the

dispersion relation of the lattice and $\omega_n = \frac{2\pi}{\beta} n$ are the Matsubara frequencies.

The approximation (5.8) shows that the B+U theory has the same functional form as the decoupling approximation in the non broken phase. In that case only Δ_{00} is present but it acts as a shift in chemical potential. For the broken phase, Δ_{00} and μ are combined with different operators. They control the density of the condensed and depleted atoms, whereas Δ_{01} mainly determines the anomalous density. According to the Bogoliubov theory of the weakly interacting Bose gas, the anomalous propagator is equally important (but opposite in sign) as the normal propagator deep in the superfluid phase. In this way, the deep superfluid regime is taken care of appropriately in our formalism. The Mott localization is enabled by the exact treatment of the density fluctuations on the impurity.

5.2. Variation of the self-energy

If instead of the unknown self-energy $\mathbf{\Sigma}_E$ one uses the exact self-energy of the simplified impurity/reference system $\mathbf{\Sigma}'$ in the self-consistency conditions (5.12) and (5.14) [as would be done in BDMFT, see Eq. (4.36)], one can run into solutions breaking certain physical constraints discussed in this section [Eqs. (5.21-5.23)]. Instead, the self-energy in B+U, $\mathbf{\Sigma}_E$, is left explicitly unknown as a variational parameter. In order to come as close as possible to the exact value of $\mathbf{\Sigma}'$ (where the free energy of the impurity Ω' is stationary, i.e. $\partial_{\mathbf{\Sigma}'}\Omega' = 0$), while complying with the physicality-constraints introduced below, we consider the minimization of its grand potential Ω' with respect to the self-energy $\mathbf{\Sigma}_E$. The minimum with respect to the kinetic condensate term $zJ\phi$, $\frac{\delta\Omega'}{\delta(zJ\phi)} = \frac{\delta\Omega'}{\delta(zJ\phi^*)} = 0$, is already taken care of by the self-consistency condition (5.10) [see also the equivalent derivations of the mean-field (4.23) and BDMFT (4.49) self-consistency relations]. ϕ is thus kept constant during the variational calculation of the self-energy. We therefore have to minimize

$$\frac{\delta\Omega'}{\delta\mathbf{\Sigma}} = \frac{\delta\Omega'}{\delta\Delta_{00}}\frac{\delta\Delta_{00}}{\delta\mathbf{\Sigma}} + \frac{\delta\Omega'}{\delta\Delta_{01}}\frac{\delta\Delta_{01}}{\delta\mathbf{\Sigma}}. \tag{5.15}$$

We are able to find an analytic expression of $\frac{\delta\Omega'}{\delta\Delta_{ij}}$, since the grand potential is defined as $\Omega'(\mathbf{\Delta},\phi) = -\ln Z(\mathbf{\Delta},\phi)$ with $Z(\mathbf{\Delta},\phi) = \mathrm{Tr}[e^{-\beta H_E(\mathbf{\Delta},\phi)}]$, giving us

$$\frac{\delta\Omega'(\mathbf{\Delta},\phi)}{\delta\Delta_{00}} = \langle 2\phi b_o - n_o\rangle_{H_E(\mathbf{\Delta},\phi)} - |\phi|^2, \tag{5.16}$$

$$\frac{\delta\Omega'(\mathbf{\Delta},\phi)}{\delta\Delta_{01}} = \langle 2\phi b_o - b_o^2\rangle_{H_E(\mathbf{\Delta},\phi)} - |\phi|^2. \tag{5.17}$$

After integration, this gives us the relation

$$\Omega'(\mathbf{\Sigma},\phi) = A(\mathbf{\Delta}(\mathbf{\Sigma}),\phi) + B(\mathbf{\Delta}(\mathbf{\Sigma}),\phi) + C. \tag{5.18}$$

with some irrelevant constant C and

$$A(\mathbf{\Delta}(\mathbf{\Sigma}),\phi) = \frac{\delta\Omega'(\mathbf{\Delta}(\mathbf{\Sigma}),\phi)}{\delta\Delta_{00}}\Delta_{00}(\mathbf{\Sigma}), \tag{5.19}$$

$$B(\mathbf{\Delta}(\mathbf{\Sigma}),\phi) = \frac{\delta\Omega'(\mathbf{\Delta}(\mathbf{\Sigma}),\phi)}{\delta\Delta_{01}}\Delta_{01}(\mathbf{\Sigma}). \tag{5.20}$$

In order to avoid unphysical results, we have to introduce upper bounds on $|\Delta_{ij}|$. From (5.6) we see that $\mathbf{\Delta}$ cannot exceed the kinetic energy of a double hopping process of depleted particles,

$$|\Delta_{01}| \leq |\Delta_{00}| \leq (zJ)^2\langle \delta b_o^\dagger \delta b_o\rangle. \tag{5.21}$$

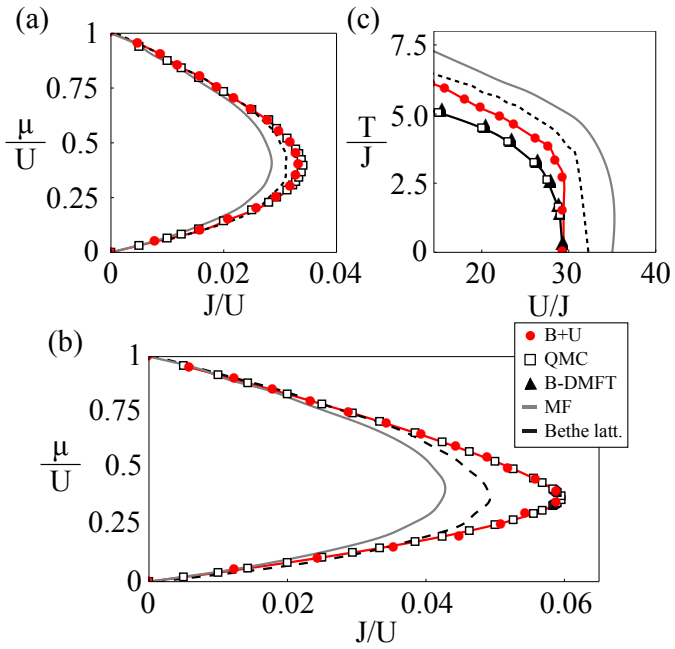

Figure 5.1.: (a),(b) Zero-temperature phase diagram of a (a) 3D cubic and (b) 2D square lattice in the vicinity of the $\langle n \rangle = 1$ Mott lobe calculated with B+U (red dots) compared with mean-field (gray line) and QMC [87] (white boxes) results. For simplicity, the BDMFT results are not shown here, since they overlap with the QMC data within 1% [65] (cf. left panel in Fig. 4.1). (c) Temperature-dependent phase diagram of a 3D cubic lattice with chemical potential $\mu/U = 0.4$ calculated with B+U (red dots), compared with mean-field (gray line), QMC [87] (white boxes, mostly overlapping with BDMFT) and BDMFT [65] (black triangles) results. The B+U results for a semi-circular density of states (Bethe lattice, $z = 6$) are shown as a black dashed line. The systematic error bar is smaller than the size of the dots.

Furthermore, we require that for all momenta k, $G_{00}^{-1}(\omega_n = 0, k) \leq -\epsilon$ and $\det[\mathbf{G}^{-1}(\omega_n = 0, k)] \geq \epsilon$ [where a small ϵ is introduced for stability requirements when inverting the 2x2 matrix $\mathbf{G}^{-1}(\omega_n = 0, k)$ in (5.14)], giving us additional bounds on the self-energy

$$\Sigma_{00} \geq \mu + zJ + \epsilon, \tag{5.22}$$

$$|\Sigma_{01}| \leq \sqrt{(\Sigma_{00} - zJ - \mu)^2 - \epsilon^2}. \tag{5.23}$$

Once the optimal value of $\mathbf{\Sigma}_E$ which minimizes (5.18) while obeying these constraints $\mathbf{\Sigma}_{\text{opt}}$ is found, it is taken as the self-energy in the B+U self-consistency, i.e. $\mathbf{\Sigma}_E = \mathbf{\Sigma}_{\text{opt}}$.

5.3. Full scheme and observables

By combining Secs. 5.1 and 5.2 we can write down the full iterative scheme for the B+U theory. Starting from an initial guess for ϕ and $\mathbf{\Delta}$ (usually the converged mean-field values for $\mathbf{\Delta} = \mathbf{0}$), we calculate a new value for ϕ through Eq. (5.10), by diagonalizing the Hamiltonian (5.7) in Fock space. Then we search for the optimal value of the self-energy by minimizing (5.18) while keeping ϕ constant. This is done by varying $\mathbf{\Sigma}_E$ within the bounds (5.22) and (5.23) and calculating $\mathbf{\Delta}(\mathbf{\Sigma}_E)$ by Eqs. (5.12)-(5.14), keeping in mind the bound on $\mathbf{\Delta}$ (5.21). Once the optimal value $\mathbf{\Sigma}_{\text{opt}}$ is found, the new value for $\mathbf{\Delta}$, $\mathbf{\Delta}(\mathbf{\Sigma}_{\text{opt}})$, is plugged into (5.7), from which a new value for ϕ is

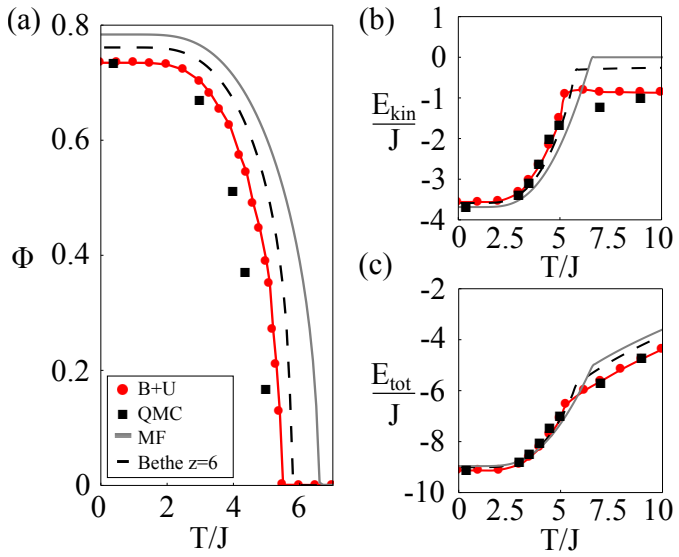

Figure 5.2.: Temperature dependence of (a) the superfluid order parameter ϕ , (b) the kinetic energy E_{kin}, and (c) the total energy E_{tot} for $\mu/U = 0.4$ ($\langle n\rangle \approx 1$) and $U/J = 20$ in a 3D cubic lattice calculated with B+U (red dots) compared with mean-field (gray line) and QMC [87] (black boxes) results. The B+U results for a semicircular density of states (Bethe lattice, $z = 6$) are shown as a black dashed line. The systematic error bar is smaller than the size of the dots.

calculated. This procedure is repeated until convergence is reached. In the B+U self-consistency all bonds adjacent to o are included in H_E, whereas when computing the quantities per site, all bonds have to be counted only once. In order to calculate the correct thermodynamic quantities per site once convergence is reached, one therefore has to divide $\mathbf{\Delta}$ by 2, giving us e.g. for the density per site $\langle n\rangle = N/V$,

$$\langle n\rangle \to \langle n_o\rangle_{H_E(\mathbf{\Delta}/2,\phi)}. \tag{5.24}$$

We can further divide the Hamiltonian into a kinetic [upper line in (5.7)] and a potential term [lower line in (5.7)], giving us expressions for the kinetic and potential energy per site

$$E_{\text{kin}} = -\frac{1}{2}\left(\Delta_{00}\langle \delta b_o^\dagger \delta b_o\rangle + \Delta_{01}\langle \delta b_o^2\rangle\right) - zJ|\phi|^2, \tag{5.25}$$

$$E_{\text{pot}} = \frac{U}{2}\left(\langle n_o^2\rangle - \langle n_o\rangle\right) - \mu\langle n_o\rangle, \tag{5.26}$$

where the total energy per site is given by $E_{\text{tot}} = E_{\text{kin}} + E_{\text{pot}}$. It should further be noted that even though we do not need to calculate $\mathbf{G}'(\tau)$ explicitly in the solver and we do not include any retardation in our formalism, we can still calculate correlation functions of the kind $\langle A(\tau)B(0)\rangle$ by

$$\langle A(\tau)B(0)\rangle_{H_E} = \frac{1}{Z}\text{tr}\left[e^{-(\beta-\tau)H_E}Ae^{-\tau H_E}B\right], \tag{5.27}$$

or directly in energy space through the eigenvalues of H_E. Since the B+U solver consists of a single impurity, in order to compute momentum-dependent quantities, one has to resort to the approximate expression

$$\mathbf{G}^{-1}(i\omega_n, k) = {\mathbf{G}_0}^{-1}(i\omega_n, k) - \mathbf{\Sigma}'(i\omega_n), \tag{5.28}$$

with

$$\mathbf{\Sigma}'(i\omega_n) = i\omega_n\sigma_z + \mu\mathbf{I} + \mathbf{\Delta} - {\mathbf{G}'}^{-1}(i\omega_n). \tag{5.29}$$

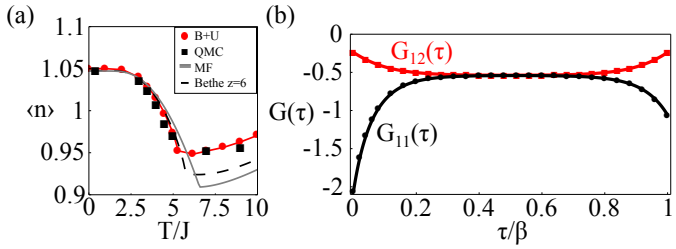

Figure 5.3.: (a) Temperature dependence of the local density per site $\langle n \rangle$ for $\mu/U = 0.4$ and $U/J = 20$ in a 3D cubic lattice calculated with B+U (red dots) compared with mean-field (gray line), Bethe lattice (dashed black line), and QMC [87] (black boxes) results. (b) Imaginary time dependence of the components of the Green's function on the impurity $\mathbf{G}'(\tau)$ in the superfluid phase for the same parameters and $T/J = 1$. The normal component $G'_{11}(\tau) = -\langle b_o(\tau) b_o^\dagger(0) \rangle$ is shown in black dots , while the anomalous component $G'_{12}(\tau) = -\langle b_o(\tau) b_o(0) \rangle$ is shown in red squares.

By a Fourier transformation this enables us to compute such quantities as the momentum-dependent density

$$n(k) = -\mathbf{G}(k, \tau = 0^+) - 1, \tag{5.30}$$

or the critical quasi particle and quasi hole energies at zero momentum $\epsilon_{p/h}$ which can be evaluated from the asymptotic behavior of $\mathbf{G}(k = 0, \tau)$ at zero temperature through [87, 126]

$$\mathbf{G}(k = 0, \tau) \to \begin{cases} Z_p e^{\epsilon_p \tau} & \tau \to +\infty, \\ Z_m e^{-\epsilon_m \tau} & \tau \to -\infty, \end{cases} \tag{5.31}$$

where $Z_p = Z_m - 1$.

5.4. Simple limits

From the relation (5.21) it is clear that $\mathbf{\Delta} \to \mathbf{0}$ as $J \to 0$. Furthermore, also, as U goes to zero, $\mathbf{\Delta}$ vanishes, since $\langle \delta b_o^\dagger \delta b_o \rangle \to 0$. Therefore in both cases the mean-field limit is recovered (see also the equivalent discussion on the BDMFT hybridization in Sec. 4.5.3). In the case of $U \ll J$ the mean-field limit is consistent with the weakly interacting Bose gas theory [103], where the self-energy is frequency independent as is the case for B+U in our approach. Another simple limit of B+U is the Bethe lattice for a semicircular density of states given by

$$D(\epsilon) = \frac{1}{2\pi z J^2} \sqrt{4 z J^2 - \epsilon^2}, \ |\epsilon| \leq 2\sqrt{z} J, \tag{5.32}$$

as was also implemented for BDMFT [65, 67] , which reduces the self-consistency of B+U to one single equation,

$$\mathbf{\Delta} = -z J^2 \mathbf{G}'(\omega = 0). \tag{5.33}$$

As can be seen in Sec. 5.5 for the 3D case this leads to good agreement with the full self-consistency of a cubic lattice with a much lower numerical cost, since the minimization routine described in Sec. 5.2 is no longer necessary.

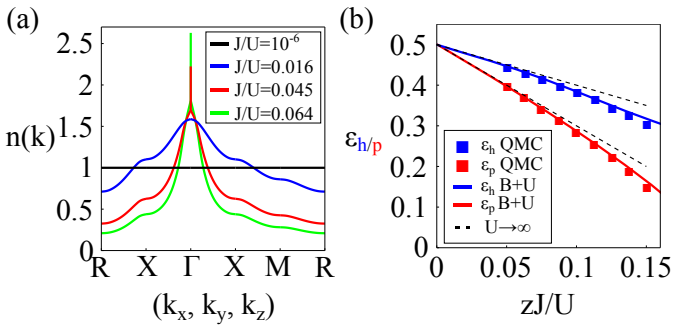

Figure 5.4.: (a) Momentum dependence of the density $n(k)$ at zero temperature for $\mu/U = 0.5$ and different values of J/U in the Mott (black, blue) and superfluid phase (red, green). (b) Quasi particle and quasi hole energies at zero momentum $\epsilon_{p/h}$ in the Mott phase at zero temperature for B+U (solid lines), QMC [126] (squares), and the analytic zeroth-order solution for $U \to \infty$ (dashed) for $\mu/U = 0.5$ and zero temperature.

5.5. Results

In Fig. 5.1 the phase diagram at zero temperature is shown for both a three-dimensional (3D) cubic and a two-dimensional (2D) square lattice. We compare the results with mean-field theory, path integral Monte Carlo simulations with worm-type updates (QMC) from Ref. [87], and BDMFT results from Ref. [65]. The results are identical with the BDMFT results and agree within a percent with the QMC data both for the 3D and the 2D cases. The results for a Bethe lattice with coordination number $z = 6$ are shown as black dashed lines. As can be seen, for the 3D case the simplified self-consistency for the Bethe lattice works very well, showing deviations only near the tip of the Mott lobe. In Fig. 5.1(c) the temperature-dependent phase diagram for $\mu/U = 0.4$ is shown and compared to BDMFT, QMC, and mean-field results for a 3D cubic lattice. In this case the lack of retardation in the B+U formalism leads to a bigger deviation from the BDMFT results. However, the B+U results are still far more precise than the ones obtained in static mean field theory.

In Fig. 5.2 the temperature dependence of the condensate order parameter ϕ, the kinetic energy E_{kin}, and the total energy E_{tot} are shown and compared to mean-field and QMC for $\mu/U = 0.4$ ($\langle n \rangle \approx 1$) and $U/J = 20$. It should be noted that, since the optimization in $\mathbf{\Sigma}_E$ is very sensitive close to the phase transition, we cannot and wish not to make any statements with respect to the order of the phase transition in Fig. 5.2: A local theory such as B+U should be judged for its accuracy on local observables and is by construction unable to capture long wavelength physics. Information on critical phenomena is hence outside its realm of applicability. The kinetic energy is very accurate for low temperatures, but in the normal phase we find a plateau just as in the decoupling approximation. The corresponding local density $\langle n \rangle$ per site is shown in Fig. 5.3 for the same parameters, where also the full local Green's function on the impurity in imaginary time $\mathbf{G}'(\tau) = -\langle \mathbf{b}_o(\tau)\mathbf{b}_o^\dagger(0)\rangle_{H_E}$ calculated by (5.27) is shown for the same parameters and temperature $T/J = 1$.

In Fig. 5.4(a) we plot the density in momentum-space $n(k) = n_{\text{dp}}(k) + n_0\delta_{k,0}$ for $\mu/U = 0.5$ and different values of J/U at zero temperature, where $n_{\text{dp}}(k)$ are the depleted particles calculated from the connected Green's function and $n_0 = |\phi|^2$ is the condensate fraction. In Fig. 5.4(b) the quasi-particle and quasi-hole energies in the Mott phase at zero momentum are extrapolated from the imaginary-time dependence of the zero-momentum Green's function through (5.31) and compared to QMC results from Ref. [126] and the analytic zeroth-order solution for $U \to \infty$.

6

Self-energy functional theory for bosons

In the previous chapter we have derived and benchmarked the Bogoliubov+U theory (B+U), showing how bosonic lattice models such as the Bose-Hubbard model can be solved with high accuracy by using a local impurity Hamiltonian in combination with just three variational parameters. The goal of this chapter is to derive a more general theory which makes use of this simple effective Hamiltonian within a diagrammatically sound framework.

The approach we start from is the self-energy functional theory (SFT) [70, 71, 72, 73], originally developed for fermionic systems. While the formalism contains the dynamical mean-field theory (DMFT, see Refs. [117, 127] for fermions and Sec. 4.5 for bosons) in the limit of local fields (with retardation effects) [70] it has also been extended to non-local correlations [76] and disorder [128]. The bosonic version of SFT, initially formulated without symmetry breaking [74], was recently extended to incorporate superfluidity [6]. However, in Ref. [6] no attempt was made to connect SFT to previous works on diagrammatic theory and the bosonic effective-action formalism [109, 110] discussed in Sec. 4.4. In fact, we show that the ansatz for the one-point propagator's equation of motion used in Ref. [6] is in contradiction with standard literature [109, 110]. To remedy this, we will put bosonic SFT on firm diagrammatic, functional, and variational grounds, paying special attention to the intricacies of bosonic $U(1)$ symmetry breaking. The result will be a functional which differs in a subtle, but significant way from the one proposed in Ref. [6].

We derive a self-energy effective action Γ_{SE} for symmetry-broken interacting lattice bosons starting from De Dominicis and Martin's generalization [109, 110] of the Baym-Kadanoff effective action Γ_{BK} [107, 108] discussed in Sec. 4.4. In analog to the fermionic formulation by Potthoff [70], this involves a Legendre transform of the universal part of Γ_{BK}, the two particle irreducible (2PI) Luttinger-Ward functional Φ_{LW} [112]. The transform changes the functional dependence from the one- and two-point response functions, $\mathbf{\Phi}$ and $\mathbf{G}$, to their respective self-energies $\mathbf{\Sigma}_{1/2}$ and $\mathbf{\Sigma}$, producing a universal self-energy functional $\mathcal{F} \equiv \mathcal{F}[\mathbf{\Sigma}_{1/2}, \mathbf{\Sigma}]$.

Using the self-energy effective action Γ_{SE} we formulate the self-energy functional theory (SFT) approximation by exploiting the universality of $\mathcal{F}$, which enables an exact evaluation of Γ_{SE} in the sub-space of self-energies of any reference system having the same interactions as the original lattice system [70]. By constraining the variational principle of Γ_{SE} to this subspace we arrive at the bosonic generalization of the SFT functional Γ_{SFT}. We show that for a local reference system with a completely general imaginary-time dependent hybridization function $\mathbf{\Delta}(\tau)$ the variations of Γ_{SFT} yield the self-consistency equations of bosonic dynamical mean-field theory (BDMFT) [62, 63, 64, 65, 66, 67] discussed in Sec. 4.5. On the other hand, when omitting the hybridization function completely and neglecting the kinetic energy contributions of non-condensed bosons, static mean-field theory [9, 61] is recovered (see Sec. 4.2).

As a proof of concept, we use SFT to study the Bose-Hubbard model [9] at finite temperature on the two- and three-dimensional cubic lattice with nearest neighbor hopping. For this purpose we make use of the effective Hamiltonian employed in B+U (see Sec. 5.1), i.e. the simplest imaginable Hamiltonian reference system comprising a single bosonic state and three variational parameters: a symmetry-breaking field F' coupling to the particle-creation/annihilation operators

(b and $b^\dagger$) and the two fields Δ_{00} and Δ_{01} that are coupled with the density ($b^\dagger b$) and pair-creation/annihilation operators (bb and $b^\dagger b^\dagger$), respectively. Hence, the fields Δ_{00} and Δ_{01} enter as an instantaneous imaginary-time Nambu hybridization function $\mathbf{\Delta}(\tau) = \delta(\tau)\mathbf{\Delta}$ in the reference system action.

We compare our SFT results, employing the minimal reference system, to exact lattice quantum Monte Carlo (QMC) results [87] and find quantitative agreement on the location of phase-boundaries, energetics, and local observables throughout the normal and superfluid phases. We also compare with BDMFT results [65, 67], corresponding to the local SFT approximation with an infinite number of variational parameters. The deviation of the three parameter SFT from QMC (and BDMFT) is surprisingly small and only noticeable close to the normal to superfluid phase transition, where kinetic quantum fluctuations become prominent.

The B+U calculations in Sec. 5.5 use the same reference system Hamiltonian and show excellent agreement with QMC at zero temperature. The SFT method presented here, however, gives quantitative agreement with QMC also at finite temperature. We also study the spectral function in both the normal and symmetry broken phase and provide a detailed analysis of the high-energy resonances.

While the calculations presented here employ a local self-energy approximation, SFT trivially extends to non-local self-energies and cluster reference systems [76]. The great promise of the SFT formalism lies in its ability to treat systems with gauge fields [37, 38, 39] and other complex terms such as spin-orbit coupling [50, 51, 52], where lattice quantum Monte Carlo approaches suffer from a sign problem. To explicitly show that SFT is sign-problem agnostic we study the frustrated Bose-Hubbard model on the square lattice with next-nearest neighbor hopping, and find a substantial shift of the phase-boundaries with respect to the Bose-Hubbard model without frustration, due to the enhancement of kinetic fluctuations in the frustrated regime.

The fermionic version of SFT has also been extended to systems out of equilibrium [129, 130]. This makes bosonic SFT an interesting alternative to the recently developed real-time dynamical mean-field theory [131] and its bosonic generalization [132], for studies of, e.g., the superfluid to normal phase transition in quenched or driven non-equilibrium systems.

This chapter closely follows Ref. [2] and is organized as follows. In Sec. 6.1 we derive the self-energy effective action Γ_{SE} as a Legendre transform of the Baym-Kadanoff functional Γ_{BK}. The SFT formalism is then developed in Sec. 6.2 for a general bosonic lattice system (Sec. 6.2.1), and a general reference system (Sec. 6.2.2). We further show how BDMFT (Sec. 6.2.3) and the mean-field approximation (Sec. 6.2.4) are obtained as limits of SFT. In Sec. 6.3 we introduce the Bose-Hubbard model, and the minimal reference system (Sec. 6.3.1). We further discuss how to compute observables (Sec. 6.3.2) and the numerical implementation of the algorithm (Sec. 6.3.3). Sec. 6.4 is devoted to numerical results, in particular phase boundaries (Sec. 6.4.1) and thermodynamical observables (Sec. 6.4.2). We also discuss the superfluid phase transition in Sec. 6.4.3 and the Hugenholtz-Pines relation in Sec. 6.4.4, while in Sec. 6.4.5 we compare our approach with the one of Ref. [6]. Finally, we present the lattice spectral function in Sec. 6.4.6 and study the effect of frustration due to next-nearest neigbor hopping in Sec. 6.4.7.

6.1. Self-energy effective action

An interesting reformulation of the Baym-Kadanoff functional Γ_{BK} (see Sec. 4.4) has been devised by Potthoff [70] for fermions. The starting point is a Legendre transform of the Luttinger-Ward functional Φ_{LW}, changing the functional dependence from the dressed propagators $\mathbf{\Phi}$ and $\mathbf{G}$ to the one- and two-point vertices $\mathbf{\Sigma}_{1/2}$ and $\mathbf{\Sigma}$. Here we generalize this procedure for the bosonic action. Using the main results of Sec. 4.4, i.e. the Dyson equations [Eqs. (4.31) and (4.32)] we

can write $\Gamma_{\rm BK}$ [Eq. (4.26)] as

$$\Gamma_{\rm BK}[\mathbf{\Phi},\mathbf{G}] = \frac{1}{2}\mathbf{\Phi}^\dagger\mathbf{G}_0^{-1}\mathbf{\Phi} + \frac{1}{2}\mathrm{Tr}\ln[-\mathbf{G}^{-1}] + \Phi_{\rm LW}[\mathbf{\Phi},\mathbf{G}] + \mathbf{\Sigma}_{1/2}^\dagger\mathbf{\Phi} + \frac{1}{2}\mathrm{Tr}[\mathbf{\Sigma}\mathbf{G}], \tag{6.1}$$

where the last line can be viewed as a Legendre transform of $\Phi_{\rm LW}$ [133]. This is possible because the two last terms are in fact derivatives of $\Phi_{\rm LW}$, *i*.e., the last line can be replaced by the universal functional

$$\begin{aligned}\mathcal{F}[\mathbf{\Sigma}_{1/2},\mathbf{\Sigma}] &= \Phi_{\rm LW}[\mathbf{\Phi},\mathbf{G}] - (\delta_{\mathbf{\Phi}}\Phi_{\rm LW})\mathbf{\Phi} - \mathrm{Tr}[(\delta_{\mathbf{G}}\Phi_{\rm LW})\mathbf{G}] \\ &= \Phi_{\rm LW}[\mathbf{\Phi},\mathbf{G}] + \mathbf{\Sigma}_{1/2}^\dagger\mathbf{\Phi} + \frac{1}{2}\mathrm{Tr}[\mathbf{\Sigma}\mathbf{G}]\,,\end{aligned} \tag{6.2}$$

that depends only on the one- and two-point self-energies $\mathbf{\Sigma}_{1/2}$ and $\mathbf{\Sigma}$, having (by construction) the variations

$$\delta_{\mathbf{\Sigma}_{1/2}^\dagger}\mathcal{F} = \mathbf{\Phi}\,, \quad \delta_{\mathbf{\Sigma}}\mathcal{F} = \mathbf{G}/2\,. \tag{6.3}$$

In terms of $\mathcal{F}$ the Baym-Kadanoff functional $\Gamma_{\rm BK}[\mathbf{\Phi},\mathbf{G}]$ can be rewritten as a self-energy effective action $\Gamma_{\rm SE}$ parametrized by the self-energies of $\mathbf{\Sigma}_{1/2}$ and $\mathbf{\Sigma}$

$$\Gamma_{\rm SE}[\mathbf{\Sigma}_{1/2},\mathbf{\Sigma}] \;=\; \frac{1}{2}(\mathbf{F}-\mathbf{\Sigma}_{1/2})^\dagger\mathbf{G}_0(\mathbf{F}-\mathbf{\Sigma}_{1/2}) + \frac{1}{2}\mathrm{Tr}\ln[-(\mathbf{G}_0^{-1}-\mathbf{\Sigma})] + \mathcal{F}[\mathbf{\Sigma}_{1/2},\mathbf{\Sigma}], \tag{6.4}$$

which remains stationary at the physical solution, as the variations with respect to $\mathbf{\Sigma}_{1/2}$ and $\mathbf{\Sigma}$ still yield the Dyson equations [Eqs. (4.31) and (4.32)]

$$\frac{\delta\Gamma_{\rm SE}}{\delta\mathbf{\Sigma}_{1/2}^\dagger} = -\mathbf{G}_0(\mathbf{F}-\mathbf{\Sigma}_{1/2}) + \mathbf{\Phi} = 0\,, \tag{6.5}$$

$$2\frac{\delta\Gamma_{\rm SE}}{\delta\mathbf{\Sigma}} = -(\mathbf{G}_0^{-1}-\mathbf{\Sigma})^{-1} + \mathbf{G} = 0\,. \tag{6.6}$$

This self-energy effective action $\Gamma_{\rm SE} = \Gamma_{\rm SE}[\mathbf{\Sigma}_{1/2},\mathbf{\Sigma}]$ can be used to construct generalized approximations in the spirit of dynamical mean-field theory. The resulting class of approximations is commonly denoted as *self-energy functional theory* (SFT) approximations [70].

We note that the self-energy effective action $\Gamma_{\rm SE}$ derived here in Eq. (6.4) differs from the one previously derived in Ref. [6]. The difference lies in the one-point Dyson equation [Eq. (6.5)] obtained at stationarity of the self-energy functional $\Gamma_{\rm SE}$. The result we arrive at in Eq. (6.5) is a direct consequence of the bosonic Baym-Kadanoff effective action $\Gamma_{\rm BK}$ [Eq. (4.26)] and its one-point Dyson equation [Eq. (4.31)], while Ref. [6] uses an ansatz for the one-point Dyson equation [Eq. (6.43)] that is inconsistent with $\Gamma_{\rm BK}$ and standard literature [109, 110], see Sec. 6.4.5 for a detailed discussion.

6.2. Self-energy functional

As pointed out in the seminal work of Potthoff [70], the universality of the self-energy functional $\mathcal{F} = \mathcal{F}[\mathbf{\Sigma}_{1/2},\mathbf{\Sigma}]$ can be used to construct a generalized class of approximations to interacting many-body systems. It is instructive to recall the main steps in the construction of the dynamical mean-field theory approximation in Section 4.5.1. It was based on (i) an initial approximation of the universal part of the effective action [Eq. (4.33)] (the Luttinger-Ward functional $\Phi_{\rm LW}$), (ii) the introduction of an exactly solvable reference system with the same universal functional [Eq. (4.37)], and (iii) the use of the variational principle of the effective action to obtain self-consistent equations for the reference system [Eqs. (4.38) and (4.39)]. In the construction of self-energy

functional theory the approximation is moved from the functional to the variational principle.

6.2.1. Functional formulation

Let us now introduce an (analytically or numerically) exactly solvable reference system, with general linear field $\mathbf{F}'$ and free propagator $\mathbf{G}'_0$. The self-energy effective action Γ'_{SE} of the reference system is then given by

$$\Gamma'_{\text{SE}}[\boldsymbol{\Sigma}_{1/2}, \boldsymbol{\Sigma}] = \frac{1}{2}(\mathbf{F}' - \boldsymbol{\Sigma}_{1/2})^\dagger \mathbf{G}'_0 (\mathbf{F}' - \boldsymbol{\Sigma}_{1/2}) + \frac{1}{2}\mathrm{Tr}\ln[-(\mathbf{G}_0'^{-1} - \boldsymbol{\Sigma})] + \mathcal{F}[\boldsymbol{\Sigma}_{1/2}, \boldsymbol{\Sigma}]\,, \tag{6.7}$$

which, at the physical solution $\boldsymbol{\Sigma}_{1/2} = \boldsymbol{\Sigma}'_{1/2}$ and $\boldsymbol{\Sigma} = \boldsymbol{\Sigma}'$, is stationary, $\delta_{\boldsymbol{\Sigma}'_{1/2}} \Gamma'_{\text{SE}}[\boldsymbol{\Sigma}'_{1/2}, \boldsymbol{\Sigma}'] = \delta_{\boldsymbol{\Sigma}'} \Gamma'_{\text{SE}}[\boldsymbol{\Sigma}'_{1/2}, \boldsymbol{\Sigma}'] = 0$, and equal to the reference system's free energy

$$\Gamma'_{\text{SE}}[\boldsymbol{\Sigma}'_{1/2}, \boldsymbol{\Sigma}'] = \beta\Omega'[\mathbf{F}', \mathbf{G}'_0]\,. \tag{6.8}$$

We can now use the universality of $\mathcal{F}$ to evaluate the self-energy effective action Γ_{SE} of the original lattice system at the physical solution ($\boldsymbol{\Sigma}'_{1/2}$ and $\boldsymbol{\Sigma}'$) of the reference system. The Γ_{SE} functional evaluated at $\boldsymbol{\Sigma}_{1/2} = \boldsymbol{\Sigma}'_{1/2}$ and $\boldsymbol{\Sigma} = \boldsymbol{\Sigma}'$ is given by

$$\begin{aligned}\Gamma_{\text{SE}}[\boldsymbol{\Sigma}', \boldsymbol{\Sigma}'_{1/2}] = \beta\Omega' &+ \frac{1}{2}(\mathbf{F} - \boldsymbol{\Sigma}'_{1/2})^\dagger \mathbf{G}_0 (\mathbf{F} - \boldsymbol{\Sigma}'_{1/2}) \\ &- \frac{1}{2}(\mathbf{F}' - \boldsymbol{\Sigma}'_{1/2})^\dagger \mathbf{G}'_0 (\mathbf{F}' - \boldsymbol{\Sigma}'_{1/2}) + \frac{1}{2}\mathrm{Tr}\ln\left[\frac{\mathbf{G}_0^{-1} - \boldsymbol{\Sigma}'}{\mathbf{G}_0'^{-1} - \boldsymbol{\Sigma}'}\right]\,,\end{aligned} \tag{6.9}$$

where we have replaced $\mathcal{F}$ in Eq. (6.4) using the equations of the reference system [Eqs. (6.7) and (6.8)].

In solving the reference system exactly, the self-energies $\boldsymbol{\Sigma}'_{1/2}$ and $\boldsymbol{\Sigma}'$ are parametrized by $\mathbf{F}'$ and $\mathbf{G}'_0$, i.e., $\boldsymbol{\Sigma}'_{1/2} = \boldsymbol{\Sigma}'_{1/2}[\mathbf{F}', \mathbf{G}'_0]$ and $\boldsymbol{\Sigma}' = \boldsymbol{\Sigma}'[\mathbf{F}', \mathbf{G}'_0]$ and we can formally construct the self-energy functional theory approximation Γ_{SFT} to the self-energy effective action Γ_{SE} according to

$$\Gamma_{\text{SFT}}[\mathbf{F}', \mathbf{G}'_0] = \Gamma_{\text{SE}}[\boldsymbol{\Sigma}'_{1/2}[\mathbf{F}', \mathbf{G}'_0], \boldsymbol{\Sigma}[\mathbf{F}', \mathbf{G}'_0]]\,. \tag{6.10}$$

In terms of Γ_{SFT} we can now approximate the self-energy effective action variational principle $\delta_{\boldsymbol{\Sigma}_{1/2}} \Gamma_{\text{SE}} = \delta_{\boldsymbol{\Sigma}} \Gamma_{\text{SE}} = 0$ [Eqs. (6.5) and (6.6)] by constraining the variations to the subspace of self-energies spanned by the reference system, giving the Euler equations

$$\frac{\delta\Gamma_{\text{SFT}}}{\delta\mathbf{F}'^\dagger} = 0\,, \quad \frac{\delta\Gamma_{\text{SFT}}}{\delta\mathbf{G}_0'^{-1}} = 0\,. \tag{6.11}$$

If we explicitly perform the variations, using the variational relations of the free energy [Eq. (4.6) and (4.7)], only the self-energy dependent variations are nonzero, and the Euler equations take the form

$$0 = \frac{\delta\Gamma_{\text{SFT}}}{\delta\mathbf{F}'^\dagger} = \frac{\delta\Gamma_{\text{SE}}}{\delta\boldsymbol{\Sigma}'_{1/2}}\frac{\delta\boldsymbol{\Sigma}'_{1/2}}{\delta\mathbf{F}'^\dagger} + \frac{\delta\Gamma_{\text{SE}}}{\delta\boldsymbol{\Sigma}'}\frac{\delta\boldsymbol{\Sigma}'}{\delta\mathbf{F}'^\dagger} = (\boldsymbol{\Phi}' - \boldsymbol{\Phi})\frac{\delta\boldsymbol{\Sigma}'_{1/2}}{\delta\mathbf{F}'^\dagger} + \frac{1}{2}(\mathbf{G}' - \mathbf{G})\frac{\delta\boldsymbol{\Sigma}'}{\delta\mathbf{F}'^\dagger}\,, \tag{6.12}$$

$$0 = \frac{\delta\Gamma_{\text{SFT}}}{\delta\mathbf{G}_0'^{-1}} = \frac{\delta\Gamma_{\text{SE}}}{\delta\boldsymbol{\Sigma}'_{1/2}}\frac{\delta\boldsymbol{\Sigma}'_{1/2}}{\delta\mathbf{G}_0'^{-1}} + \frac{\delta\Gamma_{\text{SE}}}{\delta\boldsymbol{\Sigma}'}\frac{\delta\boldsymbol{\Sigma}'}{\delta\mathbf{G}_0'^{-1}} = (\boldsymbol{\Phi}' - \boldsymbol{\Phi})\frac{\delta\boldsymbol{\Sigma}'_{1/2}}{\delta\mathbf{G}_0'^{-1}} + \frac{1}{2}(\mathbf{G}' - \mathbf{G})\frac{\delta\boldsymbol{\Sigma}'}{\delta\mathbf{G}_0'^{-1}}\,, \tag{6.13}$$

where the self-energy variations of Γ_{SE} are obtained using Eq. (6.9). From the form of these

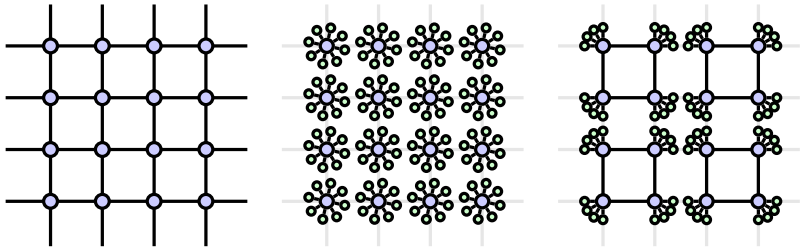

Figure 6.1.: Schematic examples of a physical system and two types of reference-system constructions. Left: A two-dimensional square lattice with correlated sites (big blue circles). Center: Reference systems with local non-interacting Green's functions $\mathbf{G}'_{0,ij} = \delta_{ij}\mathbf{G}'_{0,i}$ and additional non-interacting bath sites (small green circles). Right: Two-by-two plaquette reference system, with a non-local free-propagator $\mathbf{G}'_0$ and non-local self-energy $\mathbf{\Sigma}'$.

equations one can see that the approximate variational principle for Γ_{SFT} [Eq. (6.11)] corresponds to finding the stationary point of Γ_{SE} with respect to $\mathbf{\Sigma}_{1/2}$ and $\mathbf{\Sigma}$ projected onto the plane of reference-system representable self-energies $\mathbf{\Sigma}_{1/2} = \mathbf{\Sigma}'_{1/2}$ and $\mathbf{\Sigma} = \mathbf{\Sigma}'$.

The self-energy functional theory approximation Γ_{SFT} of the self-energy effective action [Eqs. (6.9) and (6.10)] and its corresponding variational principle [Eqs. (6.12) and (6.13)] are the two main results of this chapter.

6.2.2. Reference system

The versatility of the self-energy functional theory approach lies in the freedom of constructing the reference system. While keeping a subset of lattice sites i with the same interaction vertices as the physical system [$\hat{V}_3$ and $\hat{V}_4$ in Eq. (4.3)] the reference system's free propagator $\mathbf{G}'_0$ can be parametrized by hybridizing the interacting lattice sites with non-interacting "bath sites". In the case of a two-dimensional square lattice, two such choices of reference systems are shown schematically in Fig. 6.1. In general $\mathbf{G}'_{0,ij}$ can be written as

$$\mathbf{G}'^{-1}_{0,ij}(i\omega_n) = \sigma_z i\omega_n + \mathbf{1}(\mu - \mathbf{t}'_{ij}) - \mathbf{\Delta}_{ij}(i\omega_n)\,, \tag{6.14}$$

where $\mathbf{\Delta}(i\omega_n) = \mathbf{\Delta}_{ij}(i\omega_n)$ is the reference system hybridization function, parametrized by the non-interacting bath sites. Labeling the bath sites with Greek indices and denoting the reference-system hopping with $\mathbf{t}'$ the hybridization function can be expressed as

$$\mathbf{\Delta}_{ij}(i\omega_n) = \frac{1}{2}\sum_{\alpha\beta} \mathbf{t}'_{i\alpha}\tilde{\mathbf{G}}_{0,\alpha\beta}(i\omega_n)\mathbf{t}'_{\beta j}\,, \tag{6.15}$$

where $\tilde{\mathbf{G}}^{-1}_{0,\alpha\beta}(i\omega_n) = \sigma_z i\omega_n - \mathbf{1}\mathbf{t}'_{\alpha\beta}$ is the free propagator restricted to the bath sites. Under these assumptions the reference system can be written in Hamiltonian form

$$H'[\mathbf{F}', \mathbf{t}'] = \hat{V}_3 + \hat{V}_4 + \sum_i (b_i^\dagger F'_i + F'^*_i b_i) + \mathbf{b}^\dagger \mathbf{t}' \mathbf{b}\,, \tag{6.16}$$

where $\mathbf{b}^\dagger$ is a Nambu vector in both correlated and bath sites. As H' comprises a finite number of bosonic states the reference system free energy Ω' and self-energies $\mathbf{\Sigma}'_{1/2}$ and $\mathbf{\Sigma}'$ can be calculated using exact diagonalization, see Sec. 6.3.1. With these results the SFT functional Γ_{SFT} [Eq. (6.9)]

can be evaluated and its stationary points with respect to variations in $\mathbf{F}'$ and $\mathbf{t}'$,

$$\frac{\delta\Gamma_{\mathrm{SFT}}}{\delta\mathbf{F}'^{\dagger}} = 0\,, \quad \frac{\delta\Gamma_{\mathrm{SFT}}}{\delta\mathbf{t}'} = 0\,, \tag{6.17}$$

can be located using, e.g., a multi-dimensional root solver. This general formalism will be applied to the canonical model for interacting lattice bosons, the Bose-Hubbard model, in Sec. 6.3.

6.2.3. Dynamical mean-field theory limit

The self-energy functional theory approximation contains the bosonic version of dynamical mean-field theory as a special limit (see Sec. 4.5), in direct analogy to the fermionic case [70]. When allowing the reference system to have a completely general (retarded) but local free propagator $\mathbf{G}'_{0,ij} = \delta_{ij}\mathbf{G}'_{0,ii}$, the Euler equations of SFT [Eqs. (6.12) and (6.13)] simplify to the DMFT self-consistency equations [Eqs. (4.38) and (4.39)]. In terms of the reference system parametrization of the previous section, this amounts to taking the limit of an infinite number of bath sites.

With $\mathbf{G}'_0$ being local, also the reference system's self-energy is local, $\mathbf{\Sigma}'_{ij} = \delta_{ij}\mathbf{\Sigma}'_{ii}$, and the $\mathbf{\Sigma}'$-variation in the SFT Euler equation [Eq. (6.13)] reduces to $2\delta_{\mathbf{\Sigma}'_{ii}}\Gamma_{\mathrm{SE}} = \mathbf{G}'_{ii} - \mathbf{G}_{ii}$. Furthermore, the retardedness of $\mathbf{G}'_0$ provides sufficient freedom to fulfill the SFT Euler equations [Eqs. (6.12) and (6.13)] by enforcing that the local Green's functions and the symmetry breaking order parameters of the physical and reference systems are identical

$$\mathbf{\Phi}' - \mathbf{\Phi} = 0\,, \quad \mathbf{G}'_{ii} - \mathbf{G}_{ii} = 0\,. \tag{6.18}$$

Using the Dyson equation [Eq. (4.32)] on the last relation directly gives the DMFT self-consistency equation for the reference system's Weiss field $\mathbf{G}_0'^{-1} = [\mathbf{G}_{ii}]^{-1} + \mathbf{\Sigma}'_{ii}$ [Eq. (4.39)]. The analogous relation for the symmetry breaking order parameters requires the insertion of the Dyson equation for $\mathbf{\Sigma}'_{1/2}$ [Eq. (4.31)] twice. In terms of the imagnary-time products defined in Appendix A.1 this reads

$$0 = \mathbf{\Phi}' - \mathbf{\Phi} = \mathbf{G}_0\left[\mathbf{G}_0^{-1}\mathbf{\Phi}' - \mathbf{G}_0'^{-1}\mathbf{\Phi}' - \mathbf{F} + \mathbf{F}'\right], \tag{6.19}$$

where the relation in brackets is equal to zero, in direct agreement with the DMFT self-consistency relation for the symmetry breaking field $\mathbf{F}'$ [Eq. (4.38)].

6.2.4. Static mean-field theory limit

While dynamical mean-field theory is a specific limit of self-energy functional theory, the static mean-field theory (MFT) approximation (see Sec. 4.2) can only be obtained by making one further approximation. Contrary to SFT, the static mean-field theory is perturbative and only accounts for the kinetic energy of the bosonic condensate, neglecting all kinetic energy contributions from non-condensed bosons. Hence, to arrive at MFT from SFT one has to drop the trace log term in the SFT functional [Eq. (6.9)], which accounts for the kinetic energy contributions from non-condensed bosons. Upon dropping the trace log terms the variations of Γ_{SFT} [Eqs. (6.12) and (6.13)] reduce to

$$(\mathbf{\Phi} - \mathbf{\Phi}')\,\frac{\delta\mathbf{\Sigma}'_{1/2}}{\delta\mathbf{F}'^{\dagger}} = 0\,, \quad (\mathbf{\Phi} - \mathbf{\Phi}')\,\frac{\delta\mathbf{\Sigma}'_{1/2}}{\delta\mathbf{G}_0'^{-1}} = 0\,, \tag{6.20}$$

which are trivially fulfilled if the lattice and reference systems' one-point propagators are equal, $\mathbf{\Phi} = \mathbf{\Phi}'$. As the only variational parameter in mean-field theory is the symmetry breaking field $\mathbf{F}'$ the reference-system free propagator is fixed to $\mathbf{G}_0'^{-1} = \sigma_z i\omega_n + \mu\mathbf{1}$. Thus, stationarity

$\mathbf{\Phi} = \mathbf{\Phi}'$ amounts to inserting $\mathbf{G}_0'$ in Eq. (6.19), which for a homogeneous lattice system with nearest-neighbor hopping J and coordination number z, reduces to

$$\mathbf{F}' = \mathbf{F} - (\mathbf{G}_0^{-1} - \mathbf{G}_0'^{-1})\mathbf{\Phi}' = \mathbf{F} - zJ\mathbf{\Phi}' \,. \tag{6.21}$$

The resulting equation for the reference-system linear symmetry breaking field $\mathbf{F}'$ is identical to the self-consistency relation of the static mean-field approximation (see Sec. 4.2).

6.3. SFA3

To test our generalization of self-energy functional theory to bosons we apply it to the canonical model for interacting lattice bosons, the Bose-Hubbard model (see Sec. 2.2), which is described by the Hamiltonian

$$H = -J \sum_{\langle i,j \rangle} (b_i^\dagger b_j + b_j^\dagger b_i) + \frac{U}{2} \sum_i b_i^\dagger b_i^\dagger b_i b_i - \mu \sum_i \hat{n}_i \,, \tag{6.22}$$

with nearest neighbor hopping J, local pair interaction U, and chemical potential μ, where $b_i^\dagger$ (b_i) creates (annihilates) a boson at site i and $\hat{n}_i = b_i^\dagger b_i$ is the density operator. We will consider the model on the two- and three-dimensional square lattice and study its phase boundaries, observables, and energetics at finite temperature.

6.3.1. SFA3 reference system

For the reference system we focus on the simplest possible construction, and use a single bosonic state with the Hamiltonian

$$H'[\mathbf{F}', \mathbf{\Delta}] = \frac{U}{2} b^\dagger b^\dagger b\, b - \mu \hat{n} + \mathbf{F}'^\dagger \mathbf{b} + \frac{1}{2} \mathbf{b}^\dagger \mathbf{\Delta} \mathbf{b} \quad , \tag{6.23}$$

where $\mathbf{b}^\dagger = (b^\dagger \; b)$ is a Nambu operator, and $\mathbf{F}'$ and $\mathbf{\Delta}$ are defined as

$$\mathbf{F}' = \begin{pmatrix} F' & F'^* \end{pmatrix} \,, \quad \mathbf{\Delta} = \begin{pmatrix} \Delta_{00} & \Delta_{01} \\ \Delta_{01}^* & \Delta_{00} \end{pmatrix} \,. \tag{6.24}$$

Hence, the reference system is parametrized by the three parameters F', Δ_{00}, and Δ_{01}. The linear symmetry breaking field F' is the conjugate variable to the anomalous expectation value $\langle b \rangle$ while Δ_{00} and Δ_{01} are conjugate to the density $\langle b^\dagger b \rangle$ and the anomalous density $\langle bb \rangle$, respectively. In the normal phase the number of variational parameters reduces to only Δ_{00} as the absence of symmetry breaking requires $F' = \Delta_{01} = 0$. Henceforth, we will denote this three parameter self-energy functional theory approximation as SFA3.

Clearly, the restriction of the reference system to a single bosonic state is a drastic approximation. Temporal retardation effects can be treated by adding additional non-interacting bath sites to the reference system, producing additional variational parameters, where in the limit of infinite number of bath-sites the BDMFT solution [65, 67] is obtained. However, as we will show, already SFA3 quantitatively describes the Bose-Hubbard model, both deep in the superfluid and the Mott/normal phase.

Note that the SFA3 minimal reference system Hamiltonian in Eq. (6.23) has the same variational degrees of freedom as the reference system employed in B+U (see Sec. 5.1).

To compute properties of the reference system with the Hamiltonian H' in Eq. (6.23) we use the occupation number states $|\psi_n\rangle$ of the single bosonic state, where $n \geq 0$. Annihilating

and creating a boson yields $b|\psi_n\rangle = \sqrt{n}|\psi_{n-1}\rangle$ and $b^\dagger|\psi_n\rangle = \sqrt{n+1}|\psi_{n+1}\rangle$, respectively (see Sec. 2.1.2). In this basis we generate matrix representations of H' and the bosonic second quantization operators $\mathbf{b}$ and $\mathbf{b}^\dagger$. However, as the occupation number n of a bosonic state is not bound from above we introduce an occupation number cut-off $N_{\max}$, as to obtain a finite matrix representation, and disregard all occupation number states $|\psi_n\rangle$ with $n > N_{\max}$. All reference system calculations thus have to be converged in $N_{\max}$. For the calculations presented here we find that 10 - 20 states suffice.

To calculate static observables and dynamic response functions we first diagonalize H' to determine its eigenvalues E_n and eigenstates $|n\rangle$, where $H'|n\rangle = E_n|n\rangle$. Repeatedly using the closure relation $1 = \sum_n |n\rangle\langle n|$ one can then determine the partition function $\mathcal{Z}$,

$$\mathcal{Z} = \mathrm{Tr}[e^{-\beta H'}] = \sum_n e^{-\beta E_n}\,, \tag{6.25}$$

the reference system free energy $\Omega' = -\ln[\mathcal{Z}]/\beta$, static expectation values such as

$$\mathbf{\Phi}' = \langle \mathbf{b} \rangle = \frac{1}{\mathcal{Z}} \mathrm{Tr}[e^{-\beta H'} \mathbf{b}] = \frac{1}{\mathcal{Z}} \sum_n e^{-\beta E_n} \langle n|\mathbf{b}|n\rangle\,, \tag{6.26}$$

and the full single particle Green's function $\tilde{\mathbf{G}}'$,

$$\begin{aligned} \tilde{\mathbf{G}}'^{\eta}_{\nu}(\tau) &= -\langle \mathbf{b}^\eta(\tau) \mathbf{b}^\dagger_\nu \rangle = -\frac{1}{\mathcal{Z}} \mathrm{Tr}[e^{-\beta H'} e^{\tau H'} \mathbf{b}^\eta e^{-\tau H'} \mathbf{b}^\dagger_\nu] \\ &= -\frac{1}{\mathcal{Z}} \sum_{nm} e^{-\beta E_n + \tau(E_n - E_m)} \langle n|\mathbf{b}^\eta|m\rangle\langle m|\mathbf{b}^\dagger_\nu|n\rangle\,. \end{aligned} \tag{6.27}$$

In the last equation, the time dependent operators are defined in the Heisenberg representation $\mathbf{b}(\tau) = e^{\tau H'} \mathbf{b} e^{-\tau H'}$. Given $\tilde{\mathbf{G}}'$ and $\mathbf{\Phi}'$ the connected Green's function $\mathbf{G}'$, defined in Eq. (4.7), is obtained as

$$\mathbf{G}'(\tau) = \tilde{\mathbf{G}}'(\tau) + \mathbf{\Phi}' \mathbf{\Phi}'^\dagger\,. \tag{6.28}$$

To solve the Dyson equations [Eqs. (4.31) and (4.32)] we use the Matsubara frequency representation of the Green's functions. Transforming the τ dependence in Eq. (6.27) then gives

$$e^{-\beta E_n} \int_0^\beta d\tau\, e^{\tau(i\omega_n + E_n - E_m)} = \begin{cases} -\frac{e^{-\beta E_n} - \xi e^{-\beta E_m}}{i\omega_n + E_n - E_m}\,, & i\omega_n + E_n - E_m \neq 0 \\ \beta e^{-\beta E_n}\,, & i\omega_n + E_n - E_m = 0 \end{cases}\,, \tag{6.29}$$

and the full Matsubara frequency Green's function can be expressed by the generalized Lehmann [134] expression

$$\begin{aligned} \tilde{\mathbf{G}}'^{\eta}_{\nu}(i\omega_n) &= \frac{1}{\mathcal{Z}} \sum_{nm} \frac{\langle n|\mathbf{b}^\eta|m\rangle\langle m|\mathbf{b}^\dagger_\nu|n\rangle}{i\omega_n + E_n - E_m} (e^{-\beta E_n} - \xi e^{-\beta E_m}) \\ &\quad - \beta \delta_{\omega_n,0} \frac{1}{\mathcal{Z}} \sum_n e^{-\beta E_n} \langle n|\mathbf{b}^\eta|n\rangle\langle n|\mathbf{b}^\dagger_\nu|n\rangle\,, \end{aligned} \tag{6.30}$$

where we have assumed no accidental degeneracies $E_n \neq E_m$, $\forall\ m \neq n$, in the last zero-frequency term. Note that the connected Green's function $\mathbf{G}'(i\omega_n)$ has an additional zero-frequency contribution, as seen in Eq. (6.28), which becomes

$$\mathbf{G}'(i\omega_n) = \tilde{\mathbf{G}}'(i\omega_n) + \beta \delta_{\omega_n,0} \mathbf{\Phi}' \mathbf{\Phi}'^\dagger \tag{6.31}$$

in Matsubara frequency space.

Apart from $\mathbf{\Phi}'$ and $\mathbf{G}'$ the evaluation of the SFT functional [Eq. (6.9)] also requires the non-

interacting Green's function $\mathbf{G}'_0$ and self-energies $\mathbf{\Sigma}'_{1/2}$ and $\mathbf{\Sigma}$ of the reference system. Setting the interaction U to zero in the reference system Hamiltonian in Eq. (6.23), $\mathbf{G}'_0$ is obtained as

$$\mathbf{G}_0'^{-1}(i\omega_n) = \sigma_z i\omega_n + \mathbf{1}\mu - \mathbf{\Delta}\,, \tag{6.32}$$

and the self-energies are determined by Dyson's equations [Eq. (4.31) and (4.32)]

$$\mathbf{\Sigma}'_{1/2} = \mathbf{F}' - \mathbf{G}_0'^{-1}(i\omega_0)\mathbf{\Phi}'\,, \tag{6.33}$$

$$\mathbf{\Sigma}'(i\omega_n) = \mathbf{G}_0'^{-1}(i\omega_n) - \mathbf{G}^{-1}(i\omega_n)\,. \tag{6.34}$$

6.3.2. Lattice system

To compute the response functions of the Bose-Hubbard model defined in Eq. (6.22) at the self-energies $\mathbf{\Sigma}'_{1/2}$ and $\mathbf{\Sigma}'$ of the reference system we transform to momentum space. The nearest neighbor single particle hopping in Eq. (6.22) gives the dispersion

$$\epsilon_{\mathbf{k}} = -2J\sum_{i=1}^{d}\cos(k_i)\,, \tag{6.35}$$

where d is the dimension of the hypercubic lattice ($d = 2,\ 3$). Thus the free lattice Green's function can be written in Nambu form as

$$\mathbf{G}_0^{-1}(\mathbf{k}, i\omega_n) = \sigma_z i\omega_n + \mathbf{1}(\mu - \epsilon_{\mathbf{k}})\,, \tag{6.36}$$

and using the Dyson equation [Eq. (4.32)] the interacting lattice Green's function evaluated at the reference system self-energy $\mathbf{\Sigma}'$ is given by

$$\mathbf{G}^{-1}(\mathbf{k}, i\omega_n) = \mathbf{G}_0^{-1}(\mathbf{k}, i\omega_n) - \mathbf{\Sigma}'(i\omega_n)\,. \tag{6.37}$$

Further, by using $\mathbf{\Sigma}'_{1/2}$ we can determine the condensate of the lattice system by

$$\mathbf{\Phi} = -\mathbf{G}_0(\mathbf{k} = \mathbf{0}, i\omega_0)\mathbf{\Sigma}'_{1/2}\,, \tag{6.38}$$

where we have used the fact that there is no symmetry-breaking field on the lattice system, $\mathbf{F} = 0$. From the connected lattice Green's function $\mathbf{G}_{\mathbf{k}}$ and the one-point propagator $\mathbf{\Phi}$ we can compute a number of observables for the lattice system. The momentum space single-particle density matrix $\rho_{\mathbf{k}}$ of non-condensed bosons is given by the trace of $\mathbf{G}$ at fixed momentum $\mathbf{k}$

$$\rho_{\mathbf{k}} = \langle\hat{n}_{\mathbf{k}}\rangle = \frac{1}{2\beta}\mathrm{Tr}[-\mathbf{G}(\mathbf{k})] = -\frac{1}{2\beta}\sum_{\mu n} e^{i\omega_n(-1)^\mu 0^+}\mathbf{G}^\mu_\mu(\mathbf{k}, i\omega_n)\,, \tag{6.39}$$

while the condensate density ρ_c is given by the one-point propagator $\rho_c = \frac{1}{2}\mathbf{\Phi}^\dagger\mathbf{\Phi}$ and the total density n and the kinetic energy E_{kin} are obtained by integrating $\mathbf{k}$ over the Brillouin zone,

$$n = \mathrm{Tr}[\rho_{\mathbf{k}}] + \rho_c\,, \tag{6.40}$$

$$E_{\mathrm{kin}} = \mathrm{Tr}[\epsilon_{\mathbf{k}}\rho_{\mathbf{k}}] + \epsilon_{\mathbf{k}=0}\rho_c\,. \tag{6.41}$$

Finally the interaction energy can be obtained from the trace of the Green's function and self-energy [134]

$$E_{\mathrm{int}} = -\frac{1}{4\beta}\mathrm{Tr}[\mathbf{\Sigma}'\mathbf{G}]\,. \tag{6.42}$$

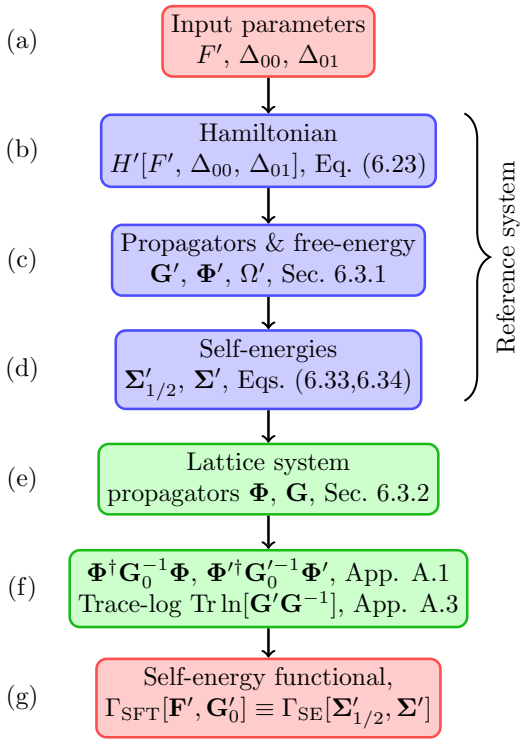

Figure 6.2.: Flow chart for the evaluation of the SFT functional $\Gamma_{\mathrm{SFT}} \equiv \Gamma_{\mathrm{SFT}}[F', \Delta_{00}, \Delta_{01}]$ for given values of F', Δ_{00} and Δ_{01}. The functional Γ_{SFT} is used to numerically locate stationary points $\nabla\Gamma_{\mathrm{SFT}} = \mathbf{0}$.

6.3.3. Numerical implementation

To find stationary solutions of the SFT functional Γ_{SFT} [Eq. (6.9)] for the Bose-Hubbard model [Eq. (6.22)] and the reference system [Eq. (6.23)] we implement a direct evaluation of Γ_{SFT} and use a root finder [1] in combination with numerical evaluation of the gradient $\nabla\Gamma_{\mathrm{SFT}}$ to locate stationary solutions $\nabla\Gamma_{\mathrm{SFT}} = \mathbf{0}$. The procedure for evaluating Γ_{SFT} is shown schematically in Fig. 6.2 and consists of the steps: (a) starting from given values of F', Δ_{00} and Δ_{01}, (b) construct the reference systems Hamiltonian H' using Eq. (6.23), (c) compute the free-energy Ω' and the one- and two-point propagators $\mathbf{\Phi}'$ and $\mathbf{G}'$ of the reference system using Eqs. (6.25) to (6.31), (d) compute the reference system self-energies $\mathbf{\Sigma}'_{1/2}$ and $\mathbf{\Sigma}'$ using the one- and two-point Dyson Equations (6.33) and (6.34), (e) compute the lattice system one- and two-point propagators $\mathbf{\Phi}$ and $\mathbf{G}$ using the relations in Sec. 6.3.2, (f) calculate the products $\mathbf{\Phi}^\dagger \mathbf{G}_0^{-1} \mathbf{\Phi}$ and $\mathbf{\Phi}'^\dagger \mathbf{G}_0'^{-1} \mathbf{\Phi}'$ using the algebraic rules in Appendix A.1 and the trace log $\mathrm{Tr}\ln[\mathbf{G}'\mathbf{G}^{-1}]$ using Eq. (A.42) in Appendix A.3, and finally (g) evaluate the self-energy functional Γ_{SFT} using Eq. (6.9).

In order to achieve high accuracy in the evaluation of Γ_{SFT}, the trace log term in Eq. (6.9) is evaluated using Eq. (A.42) and third-order high-frequency tail coefficients. Calculations at temperatures $T/J \sim 1 - 10$ then require $10^3 - 10^4$ Matsubara frequencies in order to reach a relative accuracy of 10^{-9}, for details see Appendix A.3. Once as stationary point of Γ_{SFT} is located in terms of the reference system parameters F', Δ_{00} and Δ_{01} (i.e. $\nabla\Gamma_{\mathrm{SFT}}[F', \Delta_{00}, \Delta_{01}] = \mathbf{0}$), lattice system observables can be computed as described in Sec. 6.3.2.

[1] The hybrd and hybrj methods of MINPACK as wrapped in SciPy [135].

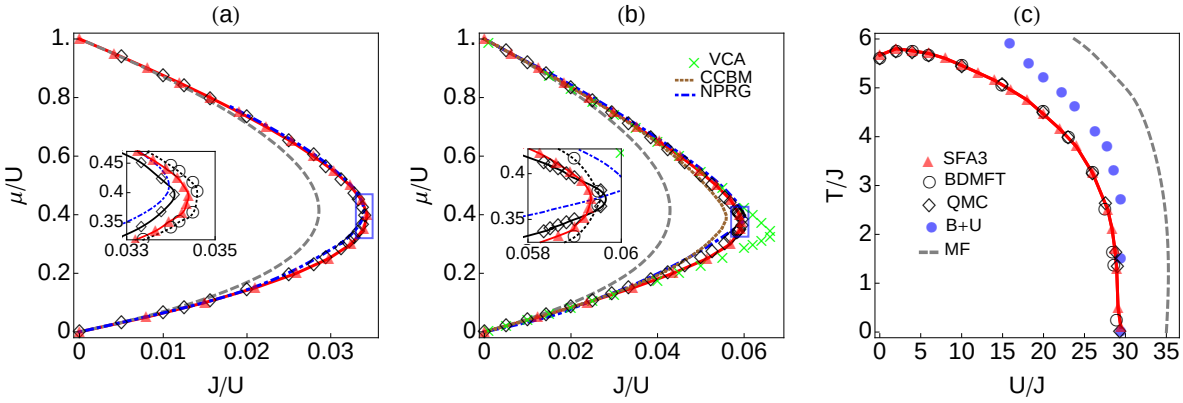

Figure 6.3.: Phase boundaries for the Bose-Hubbard model, at temperature zero on the three-dimensional [panel (a)] and two-dimensional [panel (b)] cubic lattices, and for unit-filling ($n = 1$) in three dimensions at finite temperature [panel (c)]. The SFA3 results (red triangles) are compared with MFT (dashed gray line), B+U (blue dots, see Sec. 5.1), QMC [87] (diamonds), BDMFT [65, 67] (circles), VCA [75, 120] (green crosses), CCBM [78] (dashed brown line) and NPRG [136, 137] (dashed blue line). The B+U results are suppressed in panel (a) and (b), since they overlap with the QMC data within 1%, for the same reason the BDMFT results are only partially shown [insets in panel (a) and (b)].

6.4. Bose-Hubbard model

The Bose-Hubbard model is an ideal model for benchmarking SFA3 as ample numerical results are already available on the two- and three-dimensional cubic lattices. In particular, since the model is free of sign problems, quantum Monte Carlo (QMC) [87] provides numerically exact results (after finite size scaling). However, since SFT is inherently an approximate method we also compare with the other approximate schemes: static mean-field theory (MFT, see Sec. 4.2) [9], Bogoliubov+U theory (B+U, see Sec. 5.1), bosonic dynamical mean-field theory (BDMFT, see Sec. 4.5) [65, 67], the pseudo-particle based variational cluster approximation (VCA) [75, 120], the cluster composite boson mapping method (CCBM) [78], and the nonperturbative renormalization group (NPRG) [136, 137].

6.4.1. Superfluid phase boundaries

The zero-temperature SFA3 results for the phase boundary between the superfluid and the Mott-insulator at unit-filling on the three- and two-dimensional lattice are shown in Figs. 6.3a and 6.3b, respectively.

At zero temperature mean-field is already expected to give qualitatively correct results for the three-dimensional lattice [61]. Quantitatively, however, kinetic fluctuation corrections beyond mean-field stabilize the Mott phase and strongly shift the tip of the unit-filling Mott-lobe to larger J/U, see Fig. 6.3a. However, as shown in previous BDMFT studies [65, 67], local self-energy approximations are sufficient to quantitatively capture these kinetic fluctuations. Surprisingly our SFA3 results, where kinetic effects are tuneable by only two variational parameters (Δ_{00} and Δ_{01}), yield the same level of accuracy as BDMFT. We expect the SFA3 phase-boundary, see inset in Fig. 6.3a, to move towards the BDMFT result when extending the reference system with additional bath sites. While SFA3 and BDMFT slightly but systematically overestimate the critical value of J/U, see inset in Fig. 6.3a, we expect this behavior to diminish when accounting for short-range non-local fluctuations by extending to multi-site (cluster) reference systems. This

is in contrast to methods where both local and non-local fluctuations are treated approximately, such as NPRG, which both over- and under-estimates the cricital J/U depending on μ/U, see inset in Fig. 6.3a.

The Bose-Hubbard model on the two-dimensional lattice is an even greater challenge for local approximations such as SFA3, as non-local correlations grow in importance with reduced dimension. For this model interesting results are available from the two semi-local schemes VCA [75, 120] and CCBM [78]. The VCA results employ an eight-site cluster comprising three edge sharing two-by-two plaquettes and determine the phase-boundary from the closing of the Mott gap [75], while the CCBM calculations are performed using a single two-by-two plaquette cluster. Hence, both methods require the solution of much more complex effective models than the single-site SFA3 reference system. However, while SFA3 yields quantitatively correct results, see Fig. 6.3b, apart from a narrow region at the tip of the Mott-lobe (see inset), VCA and CCBM show large deviations in this region, even though both methods are semi-local and incorporate short-ranged non-local correlations. This behavior indicates that for the phase transition at the tip of the Mott-lobe treating all kinetic fluctuations with an approximate local self-energy (as in SFA3 and BDMFT) is more important than treating short ranged non-local fluctuations exactly (as in VCA and CCBM). We also note that while NPRG [136, 137] excels over both VCA and CCBM in two dimensions it can not compete with SFA3 and BDMFT. Seemingly the upwards shift in μ/U of the NPRG phase boundary in the vicinity of the tip of the Mott-lobe becomes more severe with reduced dimension.

On the three-dimensional lattice we further present results on the temperature driven normal to superfluid phase transition at unit-filling ($\langle\hat{n}\rangle = 1$), see Fig. 6.3c. Also in this case the phase boundary of SFA3 lies on top of both the BDMFT and QMC results, while MFT and B+U deviate substantially. SFA3 also captures the weakly interacting Bose gas (WIBG) limit, indicated by a downturn in the critical temperature at low U/J. For a detailed discussion in the context of BDMFT see Ref. [67].

6.4.2. Energetics and observables

To further characterize SFA3 we study local observables and energy components of the Bose-Hubbard model on the three-dimensional lattice as a function of temperature at fixed interaction $U/J = 20$ and chemical potential $\mu/U = 0.4$, see Fig. 6.4.

The SFA3 superfluid order parameter $\phi = \langle b\rangle$ reproduces the BDMFT results quantitatively, see Fig. 6.4a. The phase transition occurs at the SFA3 critical temperature $T_c/J \approx 4.39778$, to be compared to BDMFT ($T_c/J \approx 4.365(3)$) and QMC ($T_c/J \approx 4.43(3)$) [67]. Note that the QMC results for ϕ in Fig. 6.4 are computed for a finite system with 40^3 sites, yielding a crossover rather than the (thermodynamical limit) phase transition. The QMC critical temperature T_c, however, is extrapolated to the thermodynamical limit using finite size scaling [67]. We further note that MFT and finite-temperature B+U are not precise in locating the phase transition, as they both over-estimate T_c by more than 20%, see Fig. 6.4.

For the average local density $n = \langle\hat{n}\rangle$, shown in Fig. 6.4b, we find that SFA3 agrees quantitatively with QMC in both phases, with slight deviations only in the immediate proximity of the phase transition, improving significantly on the MFT and B+U results.

The kinetic energy E_{kin} and total energy E_{tot} are shown in Fig. 6.4c and 6.4d respectively. The SFA3 result for E_{tot} is again in quantitative agreement with QMC (and BDMFT). For the kinetic energy E_{kin} on the other hand we find a small but discernible deviation of SFA3 from QMC (and BDMFT) close to the phase transition in the normal phase. This deviation directly shows the difference between accounting for kinetic fluctuations in the normal phase (where $\Delta_{01} = F' = 0$) using a completely general imaginary-time dependent hybridization function $\Delta(\tau)$ (as in BDMFT) and using a single variational parameter Δ_{00} (as in SFA3). However, from

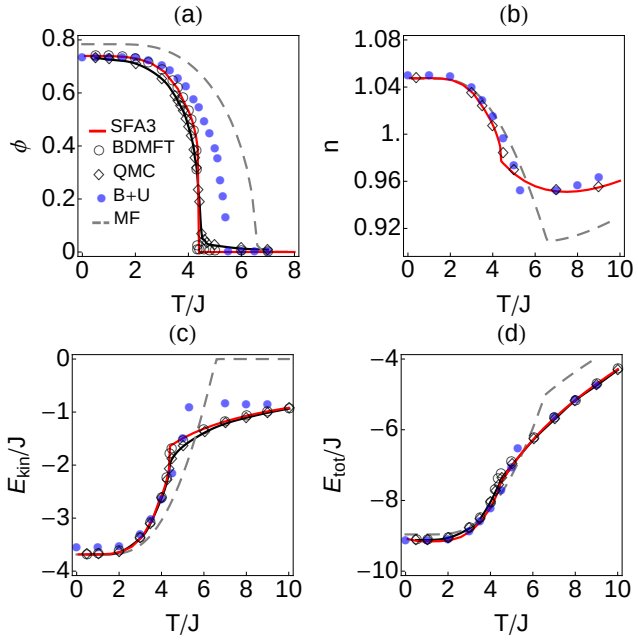

Figure 6.4.: Local observables and energies vs. temperature T for the Bose-Hubbard model on the three dimensional cubic lattice with $U/J = 20$ and $\mu/U = 0.4$ ($n \approx 1$). Panel (a): condensate order parameter ϕ, panel (b): local density n, panel (c): kinetic energy E_{kin}, and panel (d): total energy E_{tot}. Results for SFA3 (red line), MFT (dashed gray line), B+U (blue dots), QMC [87] (diamonds), and BDMFT [65, 67] (circles) are shown. The systematic errors are smaller than the marker size.

Fig. 6.4c it is evident that the major contribution to the kinetic energy in the normal phase is accounted for by the instantaneous SFA3 variational parameter Δ_{00}. This can be understood from the tremendous difference between SFA3 and the MFT result, where the latter contains zero variational parameters in the normal phase, and thereby produces the atomic limit with zero kinetic energy.

6.4.3. Stationary solutions and superfluid phase transition

In our SFA3 calculations on the Bose-Hubbard model we find several symmetry breaking stationary points with $F' \neq 0$. Most solutions can be discarded by requiring that the single-particle Green's function should fulfill the physical constraints $G_{00}(\mathbf{k}, i\omega_0) < 0$ and $\det \mathbf{G}(\mathbf{k}, i\omega_0) > 0$ at the zeroth Matsubara frequency $\omega_0 = 0$.

After discarding unphysical stationary points we still find two symmetry broken solutions in the deep superfluid phase. This occurs for temperatures $T/J < 3.7$ for $U/J = 20$ and $\mu/J = 0.4$. The two solutions are distinguished by the relative phases of the linear symmetry breaking field F' and the anomalous pairing field Δ_{01} variational parameters. One solution has the fields in-phase, $\arg \Delta_{01} = \arg F'$, and the other solution has the fields in anti-phase, $\arg \Delta_{01} = \arg F' + \pi$, see thin and thick lines respectively for $T < 3.7$ in the lower panel of Fig. 6.5.

The anti-phase solution disappears through a saddle-node bifurcation [138] with one of the unphysical stationary points at $T/J \approx 3.7$, while the in-phase solution prevails up to the normal-phase to superfluid phase transition temperature at $T_c \approx 4.39778$. However, when comparing free energies it turns out that the anti-phase solution, when present, has the lowest free energy. Thus within SFA3 when increasing temperature the system jumps from the anti-phase (deep superfluid) to the in-phase (weak) superfluid solution at $T \approx 3.7$. The jump between stationary

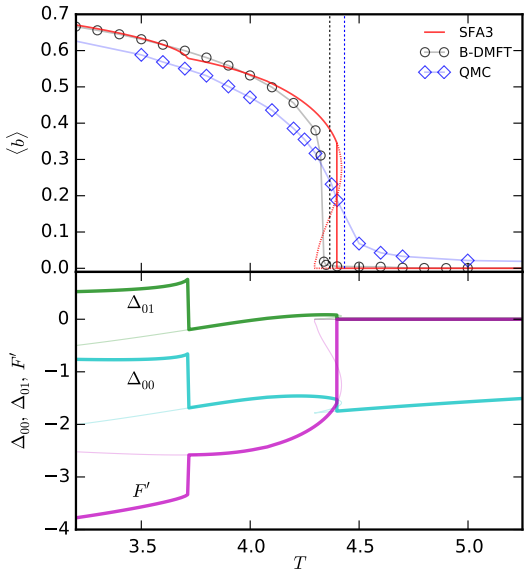

Figure 6.5.: Superfluid order parameter $\langle b \rangle$ from SFA3 (red line), B-DMFT (circles), and QMC (diamonds) [67] (upper panel) and SFA3 variational parameters Δ_{00}, Δ_{01} and F (lower panel) as a function of temperature T in the vicinity of the superfluid to normal phase transition for the 3d cubic lattice with $U/J = 20$ and $\mu/U = 0.4$, cf. Fig. 6.4. The location of the B-DMFT and QMC phase transitions are indicated (left and right vertical dotted line respectively). The QMC data were computed for a finite size system with 40^3 sites, leading to a crossover, while the phase transition line is calculated with finite-size scaling.

points causes weak discontinuities in observables, e.g., the superfluid order parameter $\phi = \langle b \rangle$, see the upper panel of Fig. 6.5.

The appearance of this spurious "phase-transition" in the SFA3 calculations might at first be considered a deficiency of the SFT scheme. However, rather than a general SFT issue it is the extremely simplistic SFA3 variational ansatz, with only three parameters that causes this behavior. In SFA3 the retarded hybridization is reduced to an instantaneous pairing field $\Delta_{01}(\tau) = \delta(\tau)\Delta_{01}$. This one parameter degree-of-freedom is simply not enough to interpolate between the two regimes and instead generates a discontinuity. As the SFA3 reference system is extended with additional bath sites the SFT calculation is expected to become continuous within the superfluid phase, as is the case for BDMFT.

At the stationary points of the SFT functional Γ_{SFT} [Eq. (6.9)], the free energy Ω is directly given by the value of the functional Γ_{SFT} itself, i.e., $\Omega = \Gamma_{\text{SFT}} : \delta\Gamma_{\text{SFT}} = 0$. The SFA3 free energy Ω as a function of temperature T for the same parameters as in Fig. 6.4 is shown in Fig. 6.6a. At low temperatures, SFA3 displays both superfluid and normal-phase stationary points, with the superfluid solution yielding the lowest free energy Ω. At the phase transition ($T_c \approx 4.39778$) the free energies of the two solutions cross, with the superfluid solution vanishing at slightly higher temperatures, whence the transition is weakly first order. While the phase transition in the Bose-Hubbard model is expected to be second order, the description of the symmetry breaking using a classical field F' is known to change the phase-transition order, see Ref. [139] for a discussion of the issue in the context of EDMFT.

The upper panel of Fig. 6.5 shows the detailed behavior of the order parameter $\phi = \langle b \rangle$ around the normal-phase to superfluid phase transition for SFA3, BDMFT, and QMC. The superfluid critical temperature within SFA3 is in quantitative agreement with BDMFT and QMC. As mentioned before, the phase transition, however, is weakly first order with an accompanying

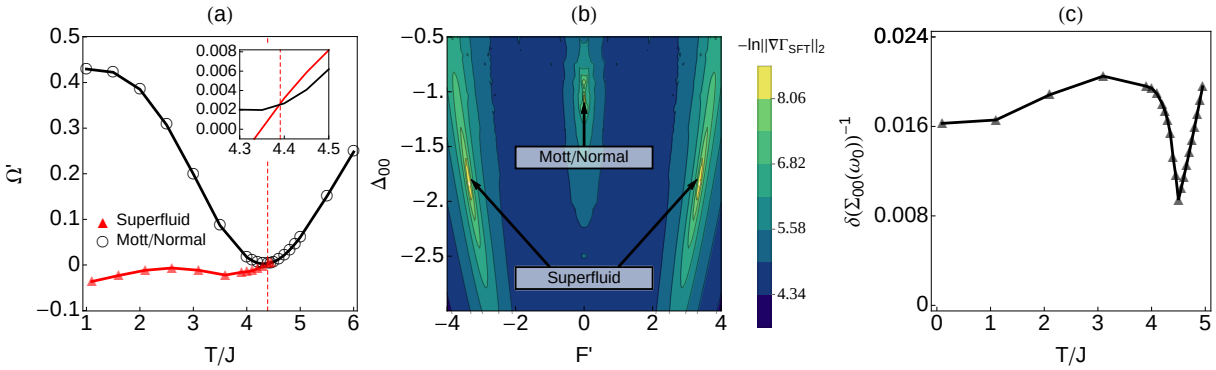

Figure 6.6.: Panel (a): Free energy Ω vs. temperature T of the Bose-Hubbard model on the three-dimensional cubic lattice at $U/J = 20$ and $\mu/U = 0.4$ ($n \approx 1$), showing the SFA3 normal-phase (circles) and superfluid (red triangles) stationary points. To discern the two solutions we subtract a fixed asymptotic model $f(T) = -T/2 - \sqrt{0.3 + (T - 4.3)^2/4} - 10.85$ from Ω and show $\tilde{\Omega} = \Omega - f(T)$. A detailed view of the crossing (dashed red line) of the free energies is shown in the inset. Panel (b): Gradient map of Γ_{SFT} as a function of Δ_{00} and F' with $\Delta_{01} = 0$ and $T/J = 1$ (deep in the superfluid phase). Panel (c): Relative breaking of the Hugenholtz-Pines relation $\delta/\Sigma_{00}(\mathbf{k} = 0, i\omega_0)$ vs. temperature T. The systematic error is smaller than the marker size.

narrow hysteresis region. The thermodynamical ground state solution is accompanied by an unstable superfluid solution that disappears through a saddle-node bifurcation with another stationary point (higher in free energy) that adiabatically connects the superfluid to the normal-phase solution (dotted red line). The phase transition within SFA3 is located between the BDMFT and QMC results (horizontal dotted lines), and is expected to shift to the BDMFT result as bath sites are added to the SFT reference system.

The existence of three solutions within a hysteresis region is a general feature of first order transitions, not limited to SFA3. It has also been observed e.g. in DMFT for the paramagnetic Mott to metal transition in the single-band Fermionic-Hubbard model [140], and for Gutzwiller variational calculations on two-band generalized Fermi-Hubbard models [141].

A map of the stationary points of the SFT functional Γ_{SFT} as a function of F' and Δ_{00} can be obtained from the gradient-two-norm-logarithm $-\log||\nabla\Gamma_{\text{SFT}}||_2$ which diverges at the stationary points where $\nabla\Gamma_{\text{SFT}} = \mathbf{0}$. As seen in Fig. 6.6b, deep in the superfluid phase ($T/J = 1$) Γ_{SFT} shows both a normal-phase stationary point (with $F' = 0$) and two symmetry-breaking superfluid stationary points. The symmetry breaking solutions are both part of the same class of $U(1)$ symmetry breaking solutions with $F' = |F'|e^{i\theta}$, where only $\theta = 0, \pi$ are seen in Fig. 6.6b, as F' is restricted to be real. Furthermore, the mirror symmetry $F' \to -F'$ in Fig. 6.6c is a direct result of the global $U(1)$ symmetry of Γ_{SFT}, $\Gamma_{\text{SFT}}[F'] = \Gamma_{\text{SFT}}[F'e^{i\theta}]$, $\forall\theta \in \Re$.

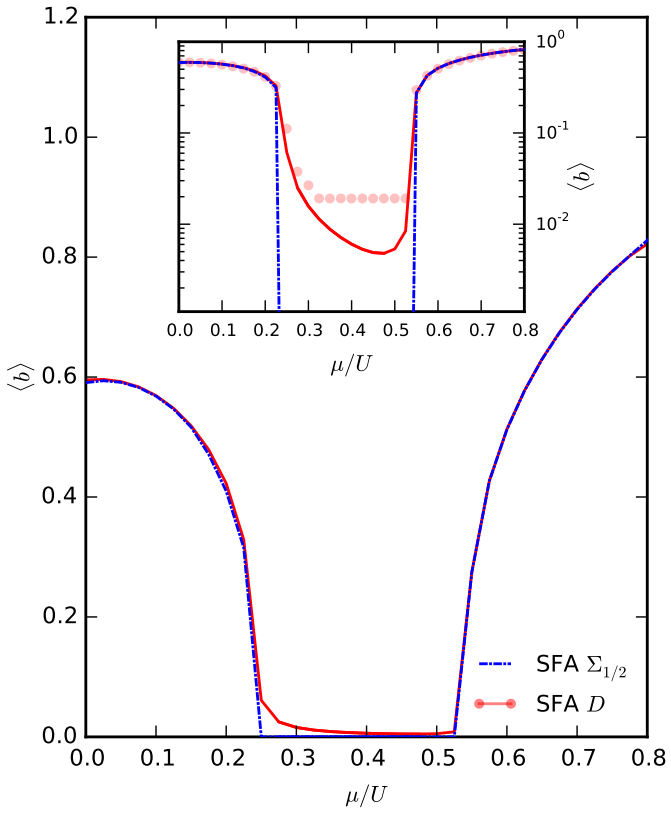

Figure 6.7.: Condensate order-parameter $\langle b \rangle$ of the 2d lattice as a function of chemical potential μ for $\beta = 6.4$ and $U = 20$. Both results using the SFT formalism presented here (blue dash-dotted line) and the formalism of Ref. [6] (solid red line) are shown. Inset: Logarithmic vertical axis with original data from Ref. [6] (red markers).

6.4.4. Hugenholtz-Pines relation

In the superfluid phase of the Bose-Hubbard model the broken $U(1)$ symmetry imposes a constraint on the zero-frequency single-particle Green's function, or equivalently the self-energy. In the continuum this constraint is the well known Hugenholtz-Pines relation [142, 143],

$$\mu = \Sigma_{00}(\mathbf{k} = 0, i\omega_0) - \Sigma_{01}(\mathbf{k} = 0, i\omega_0)\,,$$

valid in the symmetry-broken superfluid phase. On the lattice the Hugenholtz-Pines relation is shifted to $\mu = \Sigma_{00}(\mathbf{k} = 0, i\omega_0) - \Sigma_{01}(\mathbf{k} = 0, i\omega_0) - zJ$ [2], and is known to be weakly broken by local approximations such as MFT, SFT, and BDMFT [67]. The relative deviation $\delta/\Sigma_{00}(\mathbf{k} = 0, i\omega_0)$ of SFA3 from the shifted Hugenholtz-Pines relation is shown in Fig. 6.6c, where $\delta = \mu - \Sigma_{00}(\mathbf{k} = 0, i\omega_0) + \Sigma_{01}(\mathbf{k} = 0, i\omega_0) + zJ$. The deviation is small and comparable to BDMFT [67]; starting from the critical temperature T_c and going into the superfluid phase it shows an initial increase and then starts to decrease with temperature.

We note in passing that there are methods that obey the Hugenholtz-Pines relation exactly. One example is the nonperturbative renormalization group (NPRG) [136, 137], which approximately treats both local and critical fluctuations.

[2] Here specialized for lattices with cosine-dispersion, e.g., hypercubic lattices with nearest-neighbor hopping.

6.4.5. Comparison with Ref. [6]

As mentioned before, self-energy functional theory has already been applied to bosons including $U(1)$ symmetry breaking in Ref. [6]. In this section we show how the self-energy functional Γ_{SE} [Eq. (6.4)] derived in Section 6.1 differs from the result in Ref. [6].

The self-energy functional $\tilde{\Gamma}_{\text{SE}}$ of Ref. [6] is built around the Dyson equation ansatz

$$\mathbf{G}^{-1}\mathbf{\Phi} = \mathbf{F} - \mathbf{D}\,, \tag{6.43}$$

$$\mathbf{G}^{-1} = \mathbf{G}_0^{-1} - \mathbf{\Sigma}\,, \tag{6.44}$$

where the first-order tensor quantity $\mathbf{D}$ corresponds to a "self-energy like" object for the one-point propagator $\mathbf{\Phi}$. This ansatz differs from the one-point propagator Dyson equation, $\mathbf{G}_0^{-1}\mathbf{\Phi} = \mathbf{F} - \mathbf{\Sigma}_{1/2}$ [Eq. (4.31)] obtained from the stationarity of the Baym-Kadanoff functional Γ_{BK} in Eq. (4.26) and therefore contradicts Refs. [109, 110]. The difference being the appearance of the interacting propagator $\mathbf{G}$ in Eq. (6.43) instead of the non-interacting propagator $\mathbf{G}_0$.

Using the Dyson equation ansatz in Eqs. (6.43) and (6.44) the authors of Ref. [6] derive the self-energy effective action

$$\begin{aligned}\tilde{\Gamma}_{\text{SE}}[\mathbf{D},\mathbf{\Sigma}] = &\frac{1}{2}(\mathbf{F}-\mathbf{D})^\dagger(\mathbf{G}_0^{-1}-\mathbf{\Sigma})^{-1}(\mathbf{F}-\mathbf{D})\\ &+\frac{1}{2}\mathrm{Tr}\ln[-(\mathbf{G}_0^{-1}-\mathbf{\Sigma})] + \tilde{\mathcal{F}}[\mathbf{D},\mathbf{\Sigma}]\,,\end{aligned} \tag{6.45}$$

through a series of transforms of the free energy Ω, where the functional $\tilde{\mathcal{F}} \equiv \tilde{\mathcal{F}}[\mathbf{D},\mathbf{\Sigma}]$ is assumed to be a universal functional in $\mathbf{D}$ and $\mathbf{\Sigma}$ with variations $\delta_{\mathbf{D}}\tilde{\mathcal{F}} = \mathbf{\Phi}$ and $\delta_{\mathbf{\Sigma}}\tilde{\mathcal{F}} = [\mathbf{G} - \mathbf{\Phi}\mathbf{\Phi}^\dagger]/2$, such that the stationarity condition $\delta\tilde{\Gamma}_{\text{SE}} = 0$ reproduces the Dyson equation ansatz of Eqs. (6.43) and (6.44)

$$\frac{\delta\tilde{\Gamma}_{\text{SE}}}{\delta\mathbf{D}} = -\mathbf{G}(\mathbf{F}-\mathbf{D}) + \mathbf{\Phi} = 0\,, \tag{6.46}$$

$$\frac{\delta\tilde{\Gamma}_{\text{SE}}}{\delta\mathbf{\Sigma}} = -\frac{1}{2}(\mathbf{G}_0^{-1}-\mathbf{\Sigma})^{-1} + \frac{1}{2}\mathbf{G} = 0\,. \tag{6.47}$$

We have performed additional calculations employing the self-energy effective action $\tilde{\Gamma}_{\text{SE}}$ [Eq. (6.45)] in the construction of the SFT approximation [Eq. (6.9)] (here denoted by SFA-$\mathbf{D}$) comparing with the SFT results using the self-energy effective action Γ_{SE} [Eq. (6.4)] derived in this work (here denoted by SFA-$\mathbf{\Sigma}_{1/2}$), see Fig. 6.7. The system parameters are chosen to also enable comparison with numerical results published in Ref. [6] (Fig. 3b.2), see the inset in Fig. 6.7. The quantitative agreement indicates that our SFA-$\mathbf{D}$ calculations are consistent with Ref. [6].

When sweeping the chemical potential μ through the unit-filling Mott-lobe at finite temperature and studying the superfluid order parameter $\langle b\rangle$, we find that SFA-$\mathbf{\Sigma}_{1/2}$ displays a superfluid to normal-phase transition, while SFA-$\mathbf{D}$ only yields a crossover (in the range $0.25 < \mu/U < 0.52$). This is the result of the presence of a superfluid solution ($F' \neq 0$) with lower free-energy than the normal solution throughout the entire sweep in μ. In SFA-$\mathbf{D}$ the free energies of the two solutions therefore never cross, in contrast to SFA-$\mathbf{\Sigma}_{1/2}$ (see Fig. 6.6 a). The good agreement between the two methods deep in the superfluid phase can be understood from the fact that in this limit $\mathbf{G} \approx \mathbf{G}_0$, and therefore Eq. (6.43) is essentially equivalent to our symmetry-breaking Dyson equation (4.31). However, the absence of a finite temperature superfluid to normal-phase transition in SFA-$\mathbf{D}$ is unphysical.

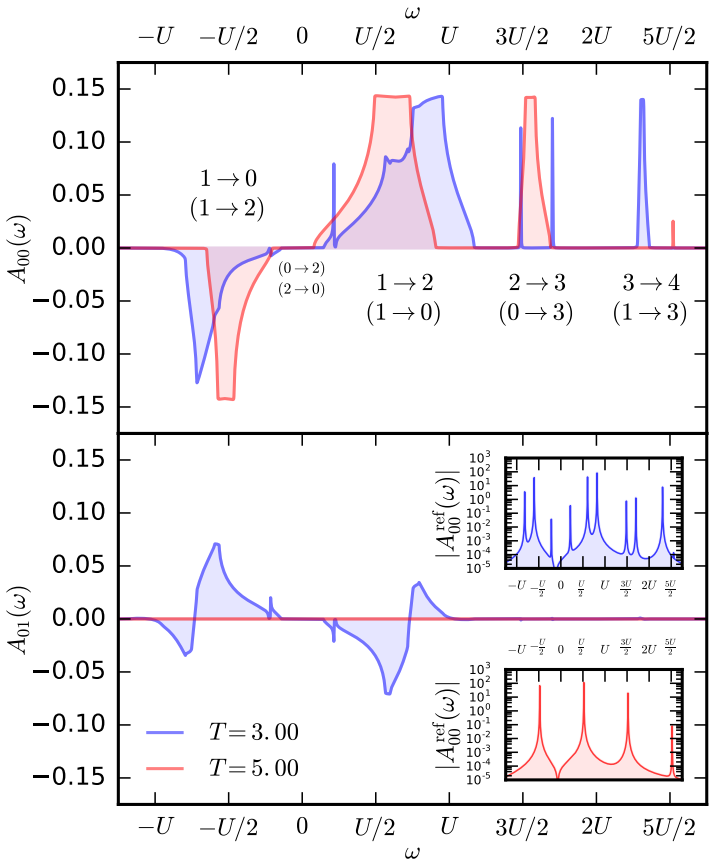

Figure 6.8.: Local spectral functions of the Bose-Hubbard model on the three dimensional cubic lattice on both sides of the temperature driven superfluid to normal-phase transition at $U/J = 20$, $\mu = 0.4U$, and $T/J = 3$ (blue), and $T/J = 5$ (red). Both the normal spectral functions $A_{00}(\omega)$ (upper panel) and the anomalous spectral functions $A_{01}(\omega)$ (lower panel) are shown as well as the SFA3 reference system spectral functions $A_{00}^{\mathrm{ref}}(\omega)$ (insets). The local transitions corresponding to each spectral feature are indicated, with the symmetry broken allowed transitions in parentheses (upper panel).

6.4.6. Spectral function

While lattice quantum Monte Carlo (QMC) provides numerically exact results for sign-problem-free interacting bosonic systems such as the Bose-Hubbard model with nearest-neighbor hopping [Eq. (6.22)], this is only true when it comes to thermodynamical expectation values. Dynamical properties, such as the single-particle spectral function, can only be obtained through numerical analytic continuation of imaginary-time results to the real-frequency axis [53, 54]. This is also an issue in local self-energy approximations such as BDMFT when using a Monte Carlo based reference-system solver, e.g. the continuous time quantum Monte Carlo (CT-QMC) method [65, 67, 144, 145]. Analytic continuation can resolve the low-energy spectral function but is limited when it comes to resolving high-energy features beyond the first Hubbard bands [54, 145]. Self energy functional theory combined with an exactly solvable reference system such as SFA3, on the other hand, gives direct access to the real-frequency spectral function without any restriction in frequency.

Here we report on the spectral function in the normal-phase using SFA3 and compare with previous results in the low-energy range from BDMFT and CT-QMC [145] and in the high-energy

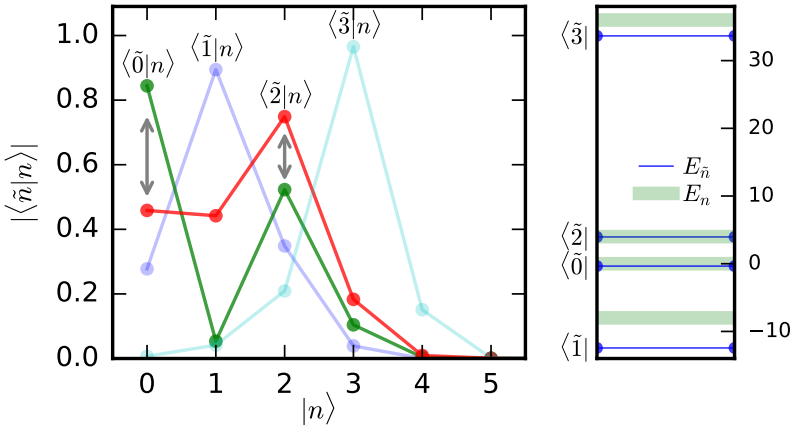

Figure 6.9.: SFA3 reference system eigenstate $|\tilde{n}\rangle$ overlap with the occupation number states $|n\rangle$ (left) in the superfluid phase with parameters identical to Fig. 6.8. The eigenstate energies $E_{\tilde{n}}$ and the zero-hopping limit energies E_n are also shown (right). The symmetry breaking and proximity in energy between $|\tilde{0}\rangle$ and $|\tilde{2}\rangle$ causes both eigenstates to have appreciable weights for both the $|0\rangle$ and $|2\rangle$ occupation number states (arrows in left panel).

range from BDMFT and the non-crossing approximation (NCA) [146]. We also study the finite temperature superfluid spectral function, previously studied in the low-energy range [54, 75], and make an extended analysis of its high-energy resonances. Entering from the normal phase into the superfluid we find that the high-energy resonances change character and fundamental behavior.

We choose to study the local spectral function in both phases of the temperature driven superfluid to normal-phase transition at $U/J = 20$ and $\mu = 0.4U$ ($\langle\hat{n}\rangle \approx 1$) previously discussed in Sec. 6.4.2 and Fig. 6.4. The normal and anomalous lattice spectral functions, A_{00} and A_{01} respectively, are shown in Fig. 6.8. The normal phase has been studied in detail elsewhere [146] using BDMFT+NCA and agrees qualitatively with the result we obtain using SFA3.

The features of the lattice spectral function can be understood by studying the corresponding SFA3 reference-system spectral function where the resonances can be understood in terms of transitions between local occupation number states. In the low energy range the normal phase exhibits a lower and upper Hubbard band, corresponding to singlon-holon ($1 \to 0$) and singlon-doublon ($1 \to 2$) transitions, respectively. The lower band has roughly half the spectral weight of the upper band due to boson prefactors, see Appendix A in Ref. [146]. Beyond the Hubbard bands resonances only occur at positive frequencies as the (local) bosonic states are not bound with respect to the addition of particles. The resonance at $\omega = 3U/2$ only occurs at elevated temperatures and corresponds to a thermally activated doublon-triplon transition ($2 \to 3$). Similarly, at $\omega = 5U/2$ we observe a much weaker resonance that, within the SFA3 reference system, is a thermally activated triplon-quadruplon transition ($3 \to 4$). However, when going beyond SFA3 and adding additional bath sites to the reference system (improving the description of kinetic fluctuations), we expect this resonance to persist down to zero temperature, where it turns into a pure lattice fluctuation of a singlon-triplon with a dispersing holon ($1 \to 3 \otimes h$), as shown in Ref. [146].

This picture is heavily modified when entering the superfluid phase. For $U/J = 20$ the superfluid is strongly correlated (i.e. $U \gg J, F', \Delta_{01}$) and on the SFA3 reference system level the eigenstates $|\tilde{n}\rangle$ maintain their main occupation number character $|\tilde{n}\rangle \approx |n\rangle$, whoose eigen energies $E_{\tilde{n}}$ are to first order given by the zero-hopping limit energies $E_{\tilde{n}} \approx E_n \equiv Un(n-1)/2 - \mu n$. However, the symmetry breaking terms F' and Δ_{01} in the reference-system Hamiltonian [Eq. (6.23)] cause the eigenstates to have small but finite admixtures of all other occupation-number

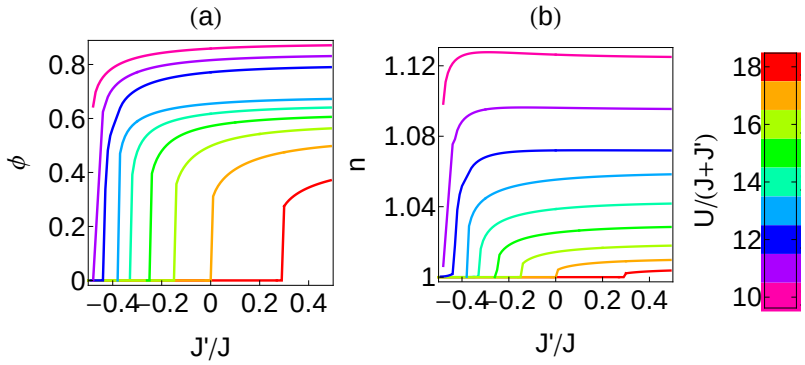

Figure 6.10.: Condensate ϕ (panel a) and density n (panel b) of the Bose-Hubbard model with next-nearest neighbor hopping J' for $J = 1$, $\mu/U = 0.4$, $U/(J+J') = 10, 11, 12, ...18$, and $T = 0.01$. The coloring indicates the respective $U/(J + J')$ values (see legend).

states, see Fig. 6.9. This turns many more overlaps for one-particle addition $\langle\tilde{n}|b|\tilde{n}'\rangle$ (and one-particle removal $\langle\tilde{n}|b^\dagger|\tilde{n}'\rangle$) non-zero in the symmetry broken phase, as compared to the normal phase where only $\langle n|b|n+1\rangle$ and $\langle n|b^\dagger|n-1\rangle$ contribute in Eq. (6.30).

On the reference system level, this causes the Green's function [Eq. (6.30)] and thus the spectral function, to exhibit an increased number of resonances in the superfluid phase, see insets in Fig. 6.8. One example are the two additional low energy resonances at $\pm U/4$, which correspond to the holon-doublon transition $(0 \to 2)$ upon adding *only one particle* and the doublon-holon transition $(2 \to 0)$ removing *only one particle*, respectively. The extra allowed transitions also split the reference system resonances at $\pm U/2$, causing a broadening of the upper and lower Hubbard bands of the lattice system. The thermally activated doublon-triplon transition at $\omega = 3U/2$ is also split into two separate resonances, that both diminish as the temperature is lowered (not shown). Studying the SFA3 eigenstate overlap with the occupation number states $\langle\tilde{n}|n\rangle$ in Fig. 6.9 we observe a substantial admixture of empty $|0\rangle$ and doubly occupied $|2\rangle$ states in the SFA3 eigenstates $|\tilde{0}\rangle$ and $|\tilde{2}\rangle$. This mixing causes the observed doubling of all resonances in the superfluid phase. In the normal phase on the other hand these resonances either start or end in a simple empty or doubly occupied state.

The high energy resonance at $\omega \approx 5U/2$ also undergoes drastic change, but is not split since no doubly occupied or empty states are involved in the transition. Instead of the thermally activated form found in the normal phase, the resonance carries much more spectral weight and persists down to low temperatures in the superfluid phase. At low temperatures this implies that we have non-zero overlaps $\langle\tilde{n}|b^\dagger|\mathrm{GS}\rangle$, where $|\mathrm{GS}\rangle = |\tilde{1}\rangle$ is the many-body groundstate of the SFA3 reference system. Thus, comparing eigenstate energies we can attribute this resonance to the direct singlon-triplon transition $(1 \to 3)$, which is clearly a forbidden one-particle transition of the SFA3 reference system in the normal phase.

Based on this result and the normal-phase results of Ref. [146] we predict that the singlon-triplon resonance is a fundamental quantum fluctuation of the Bose-Hubbard model, both in the normal and superfluid phase.

6.4.7. Frustration and next-nearest neighbor hopping

As an example of the broad applicability of SFT we go beyond previous works and investigate the effect of kinetic frustration on the superfluid to normal-phase transition, looking explicitly at effects that are beyond single-site mean-field and out-of-reach for QMC.

To this end we study the Bose-Hubbard model with additional diagonal next-nearest neighbor

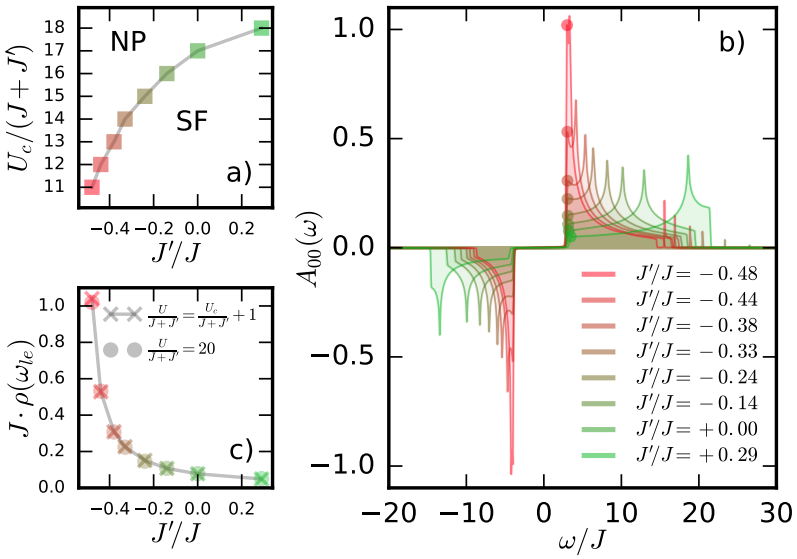

Figure 6.11.: Critical interaction $U_c/(J+J')$ for the superfluid (SF) to normal phase (NP) transition on the two dimensional lattice with nearest and next-nearest neighbor hopping (J and J') as a function of J'/J (panel a). The redistribution of spectral weight driven by J'/J in the spectral function $A_{00}(\omega)$ is shown in panel b for $U/(J+J') = 20$, $\mu/U = 0.4$, $T/J = 1$, and $J = 1$. The spectral weight $A_{00}(\omega)$ at the lower Hubbard-band edge anti-correlates with $U_c/(J+J')$ both for $U/(J+J') = 20$ (circles) and in the vicinity of the phase transtition at $U/(J+J') = U_c/(J+J')+1$ (crosses) (panel c).

hopping J' on the two dimensional square lattice, i.e.

$$H = H_{\mathrm{BH}} - J' \sum_{\langle\langle i,j \rangle\rangle} \left(b_i^\dagger b_j + b_j^\dagger b_i \right) , \tag{6.48}$$

where H_{BH} is the Bose-Hubbard Hamiltonian [Eq. (6.22)] and $\langle\langle i,j \rangle\rangle$ indicates summing over all next-nearest neighbors. For $J'/J < 0$ Eq. (6.48) exhibits frustration making it inaccessible for QMC, due to a strong sign-problem [49]. The standard mean-field approximation [9, 61] can be applied, but the symmetry-breaking mean-field F only depends on the total bandwidth $F = z\,(J+J')\,\langle b \rangle$, and does not account for the spectral weight distribution within the band. Hence, for fixed μ/U and $(J+J')/U$ mean-field yields constant results independent of the J'/J ratio. In other words for finite next-nearest-neighbor hopping J' mean-field is no longer expected to qualitatively describe the superfluid to normal phase transition, as was the case for only nearest-neighbor hopping J in Sec. 6.4.1.

Self-energy functional theory using the single-site reference system (SFA3) incorporates the spectral function and directly depends on the spectral distribution. In Fig. 6.10 we present SFA3 results for the condensate ϕ and local density n for fixed $\mu/U = 0.4$ and $U/(J+J') = 10, ..., 18$ as a function of J'/J. We find that both ϕ and n vary with J'/J and that the transition between the superfluid and the normal phase strongly depends on J'/J. The critical values of the interaction $U_c/(J+J')$ from the sweeps in Fig. 6.10 are shown in Fig. 6.11a revealing a drastic reduction of the critical coupling when moving into the frustrated regime $J'/J < 0$.

To understand this trend we study the local spectral function $A_{00}(\omega)$ in the normal phase at $U/(J+J') = 20$ and $\mu/U = 0.4$, see Fig. 6.11b. We see that fixing the bandwidth $z(J+J')/U$ and the chemical potential μ/U relative to the interaction U corresponds to fixing the gap in $A_{00}(\omega)$. However, tuning J'/J produces substantial spectral weight redistribution within the Hubbard bands, see Fig. 6.11b. In particular, the spectral density at the low frequency edges

of the Hubbard bands increases as J'/J is lowered. As can be seen in Fig. 6.11c, this effect prevails also when approaching the phase transition from the normal phase. Thus, we attribute the change in the critical coupling $U_c/(J + J')$ as a function of J'/J to this spectral weight redistribution. To conclude, we find that the enhancement of low energy kinetic fluctuations in the frustrated regime $J'/J < 0$ is detrimental for the superfluid and enhances the extent of the normal-phase.

7

Self-energy functional theory with disorder

The theoretical understanding of disordered and interacting lattice bosons has been primarily driven by numerical simulations. Exact diagonalization (ED) [147] can only be applied to relatively small finite system sizes, while the extension of the density matrix renormalization group (DMRG) [55, 56, 57, 58] to disorder [148] is restricted to low-dimensional systems. In higher dimensions the state of the art method is path integral quantum Monte Carlo (QMC) with worm updates [47, 48, 49, 15]. This algorithm provides numerically exact results for large but finite-sized bosonic lattice systems, while the disorder can be accounted for by averaging over many disorder realizations [15]. However, dynamical quantities such as the single-particle spectral function can only be determined by performing analytic continuation of imaginary-time propagators with stochastic noise [53, 54]. The continuation is an inherently illposed problem, and cannot resolve sharp resonances. While the methods mentioned above excel with a high numerical accuracy, they rely on finite system sizes, which can represent a problem when rare disorder-driven fluctuations play an important role, which can only be captured once one approaches the thermodynamical limit.

The available methods in the thermodynamical limit rely on approximations. The mean-field decoupling approximation [9] (see Sec. 4.2) can be applied to disordered systems using an arithmetically averaged condensate. However, this overestimates the phase coherence and the extent of the superfluid phases, as locally condensed bosons are mistaken for a global condensate [14]. In fact, in mean-field methods with position-space resolution the geometric percolation of condensed regions appears to be a more accurate quantity to evaluate the global superfluid response [149]. A more accurate mean-field approach is the stochastic mean-field theory [150, 16], where the condensate order parameter is treated as a disorder-dependent quantity. However, mean-field methods are self-consistent only in terms of the condensate (i.e. the one-point propagator). This severely hampers the ability to describe uncondensed phases, which are simply approximated by the zero hopping limit (i.e. the atomic limit).

A non-perturbative method which includes also a self-consistency in terms of the two-point propagator is the dynamical mean-field theory (DMFT), originally formulated for fermions [116, 117] and later generalized to bosons [62, 64, 63, 65, 67, 145] (see Sec. 4.5). For fermions the formalism has been extended to disordered systems [151, 152, 153, 154] averaging the systems propagators over all disorder configurations. While an arithmetic averaging in this framework works well for low disorder, it misses the essential physics in non-self-averaging phases. In such phases, like the Anderson-localized regime [155, 152], observables show broad tails in their disorder-distribution. An interesting idea for incorporating non-self-averaging effects is the typical medium theory [151, 152, 153, 154], where the arithmetic average is replaced by a geometrical mean. However, it is not clear what the range of validity is for this approach. We would like to point out that the works above employing disorder and DMFT all study fermionic systems. As of today we are not aware of any works applying DMFT to disordered *bosonic* systems.

A more general theoretical framework for constructing non-perturbative approximations for interacting many-body systems is the self-energy functional theory (SFT, see Chapter 6) [70, 71, 72, 73, 74, 75, 6], from which DMFT can be derived as a certain constriction of the variational space. Within SFT, non-perturbative approximations are readily constructed by restricting the self-energy domain of the original lattice system to the self-energies of a simpler exactly solvable *reference* system. This reduces the full complexity of the original problem to a search for stationary solutions in terms of the variational free propagators of the reference system. The generalization to systems with disorder of SFT has been developed for fermionis in Ref. [156] and applied in a variational cluster approximation to bosons in the absence of $U(1)$-symmetry-breaking in Ref. [157].

The aim of this paper is to extend the bosonic SFT formalism of Chapter 6 to disordered lattice bosons including the possibility of $U(1)$-symmetry-breaking. As argued for fermions in Ref. [156], the geometrical mean used in the context of DMFT [151, 152, 153, 154] is hard to reconcile with the variational SFT framework. We therefore derive an arithmetically averaged formalism, where, through the introduction of an appropriate $\hat{\mathcal{T}}_{PV}$ functional, the functional depends only on the self-energies of the arithmetically averaged propagators. Just as the version for clean systems (see Sec. 6.2.3), we find that SFT incorporates a disorder-averaged generalization of bosonic DMFT [62, 64, 63, 65, 67, 145] in a certain limit. The resulting functional is, however, more general than DMFT by being amenable to a more general variational space.

We apply SFT to the Bose-Hubbard model (BHm) with local box disorder (see Sec. 2.3) on the cubic lattice using the simplest imaginable reference system, comprising a single bosonic mode. This restriction to the minimal reference system produces a self-energy approximation with three variational degrees of freedom, which we will denote by SFA3. In the clean BHm the SFA3 approach has been shown to be in quantitative agreement with numerically exact QMC results in Chapter 6. In this work we investigate the disordered BHm in the vicinity of the superfluid finger, where the condensate density is extremely fragile, leading to a substantial shift in the phase boundaries even if the numerical error is very low. Nonetheless, we observe quantitative agreement of the thermodynamic quantities computed with SFT and the QMC reference results.

Since the SFA3 reference system can be solved exactly, we can also evaluate the lattice spectral function and thereby obtain spectroscopic information not readily avalable from QMC. By systematically analyzing the local excitations of the SFA3 spectral functions, we find that the strongly-interacting Bose glass is characterized by different regimes, depending on which local occupations n are activated as a function of the disorder strength Δ. While local observables are described well by the atomic limit, we find that the particles delocalize into isolated superfluid lakes over the strongly-localized background around highly-occupied sites whenever these sites are particularly rare. In particular, our results indicate that the transition from the strongly interacting Bose glass to the superfluid phase is driven by the percolation of superfluid lakes which form around doubly occupied sites. As Δ is further increased and the number of highly-occupied sites increases accordingly, the particles are localized by the increasing particle-number fluctuations and interaction energy, explaining the reentrant behavior of the superfluid finger at larger Δ. We also present results deeper in the superfluid phase (i.e. at weaker interactions), showing excellent agreement with QMC for thermodynamical quantities at low disorder. When the disorder dominates both over the bandwidth and the interaction, the restricted variational subspace of our SFA3 reference system is however insufficient, as we no-longer can stabilize a stationary solution. Whether this can be remedied by a more general reference system construction is an open question.

This chapter closely follows Ref. [5] and is organized as follows. In Sec. 7.1 we derive the self-energy functional theory for disordered lattice bosons: starting from the free-energy functional (Sec. 7.1.1), we generalize the bosonic Baym-Kadanoff functional to the case of disorder (Sec. 7.1.2), perform a Legendre transform to the self-energy effective action (Sec. 7.1.3), average the

effective action over all disorder configurations (Sec. 7.1.4), and finally arrive at the disorder-averaged self-energy functional (Sec. 7.1.5). We further specialize SFT to disorder-averaged BDMFT (Sec. 7.1.6) and the case of uncorrelated disorder (Sec. 7.1.7), and finally devise how to compute lattice observables in this approximation in Sec. 7.1.8. In Sec. 7.2 we introduce the disordered BHm, discussing the SFA3 reference system used in the SFT calculations (Sec. 7.2.1) and deriving analytic results in the atomic limit (Sec. 7.2.2). The numerical results are presented in Sec. 7.3, where we investigate the strongly-interacting Bose glass (Sec. 7.3.1), the strongly-interacting superfluid phase transition (Sec. 7.3.2), and the superfluid phase (Sec. 7.3.3).

7.1. Self-energy functional theory for disordered lattice bosons

In this section we derive the self-energy functional theory for disordered lattice bosons. In analogy to the formalism for clean systems derived in Chapter 6, we do so by a series of Legendre transformations starting from the free-energy functional and introduce a simpler exactly solvable reference system sharing the same local interaction and disorder distribution. As was done in a previous work on fermions [156], we average over all possible disorder configurations, arriving at a functional which only depends on the self-energies of the arithmetically averaged propagators of the system. In order to keep track of the various additional dependencies, we introduce a slightly more complex notation than in Chapter 6, where the explicit dependencies of the propagators and self-energies are denoted as subscripts. In particular, for notational purposes, we denote the one-point self-energy (formerly $\mathbf{\Sigma}_{1/2}$ in Chapters 4 and 6) by $\mathbf{S}$.

7.1.1. Free-energy functional

We start by generalizing the free-energy functional of Sec. 4.1 to the case of disorder. To this end, we consider a lattice system of bosons in the presence of quadratic disorder, with creation (annihilation) operator $b_i^\dagger$ (b_i) on site i. Using the Nambu operators $\mathbf{b}_\alpha^\dagger \equiv \mathbf{b}_{i\nu}^\dagger \equiv (b_i^\dagger, b_i)_\nu$ with commutator $[\mathbf{b}^\alpha, \mathbf{b}_\beta^\dagger] = (\mathbf{1} \otimes \sigma_z)_\beta^\alpha$, where α is a superindex spanning both the site index i and Nambu index ν, the Hamiltonian $\hat{H}$ of the system can be written as

$$\hat{H} = \mathbf{F}_\alpha^\dagger \mathbf{b}^\alpha + \frac{1}{2}\mathbf{b}_\alpha^\dagger \mathbf{t}_\beta^\alpha \mathbf{b}^\beta + \frac{1}{2}\mathbf{b}_\alpha^\dagger \boldsymbol{\eta}_\beta^\alpha \mathbf{b}^\beta + \hat{V}\,, \tag{7.1}$$

where repeated indices are summed over, $\mathbf{F}$ is an explicit symmetry-breaking field, $\mathbf{t}_\beta^\alpha = \mathbf{t}_{j\nu}^{i\eta} = t_{ij} \otimes \mathbf{1}$ is the hopping, the quadratic disorder $\boldsymbol{\eta}_\beta^\alpha = \boldsymbol{\eta}_{j\nu}^{i\eta} = \eta_{ij} \otimes \mathbf{1}$ has the probability distribution $P(\boldsymbol{\eta})$, and the general three and four-body interaction $\hat{V}$ can be expressed as $\hat{V} \equiv V^{(3)}_{\alpha\beta\gamma}\mathbf{b}^\alpha\mathbf{b}^\beta\mathbf{b}^\gamma + V^{(4)}_{\alpha\beta\gamma\delta}\mathbf{b}^\alpha\mathbf{b}^\beta\mathbf{b}^\gamma\mathbf{b}^\delta$. To keep the notation compact we will henceforth supress the lattice-Nambu superindices.

At finite temperature $T \equiv \beta^{-1}$ the free energy functional of the interacting system is given by

$$\hat{\Omega}_V[\mathbf{F}, \mathbf{G}_0^{-1}] = -\ln(\mathrm{Tr}[e^{-\mathcal{S}[\mathbf{F},\mathbf{G}_0^{-1}]}])/\beta\,, \tag{7.2}$$

where $\mathcal{S}$ is the imaginary-time action

$$\mathcal{S}[\mathbf{F}, \mathbf{G}_0^{-1}] \equiv \int_0^\beta d\tau\, \mathbf{F}^\dagger \mathbf{b}(\tau) + \int_0^\beta d\tau\, \hat{V}[\mathbf{b}(\tau)] - \frac{1}{2}\iint_0^\beta d\tau d\tau'\, \mathbf{b}^\dagger(\tau)\mathbf{G}_0^{-1}(\tau,\tau')\mathbf{b}(\tau')\,. \tag{7.3}$$

The free energy functional $\hat{\Omega}_V[\mathbf{F}, \mathbf{G}_0^{-1}]$ is equal to the free energy $\Omega_{\boldsymbol{\eta}}$ of the lattice system in Eq.

(7.1) with fix disorder configuration $\boldsymbol{\eta}$, when evaluated at the symmetry breaking field $\mathbf{F}$ and the free single-particle propagator $\mathbf{G}_{\mathbf{t}\boldsymbol{\eta}0}$, i.e.

$$\hat{\Omega}_V[\mathbf{F}, \mathbf{G}^{-1}_{\mathbf{t}\boldsymbol{\eta}0}] = \Omega_{\boldsymbol{\eta}}\,, \tag{7.4}$$

where the non-interacting ($\hat{V} = 0$) single-particle propagator of Eq. (7.1) is given by

$$\mathbf{G}^{-1}_{\mathbf{t}\boldsymbol{\eta}0}(\tau, \tau') = \delta(\tau - \tau')(-[\mathbf{1} \otimes \sigma_z]\partial_{\tau'} - \mathbf{t} - \boldsymbol{\eta})\,, \tag{7.5}$$

and the subscript means that it depends on the hopping $\mathbf{t}$ and the disorder configuration $\boldsymbol{\eta}$ only. By taking functional derivatives of the free energy functional $\hat{\Omega}_V$ with respect to $\mathbf{F}$ and $\mathbf{G}_0^{-1}$ we obtain the two functionals

$$\hat{\phi}_V[\mathbf{F}, \mathbf{G}_0^{-1}] \equiv \beta \frac{\delta \hat{\Omega}_V[\mathbf{F}, \mathbf{G}_0^{-1}]}{\delta \mathbf{F}^\dagger} \tag{7.6}$$

$$\hat{\mathcal{G}}_V[\mathbf{F}, \mathbf{G}_0^{-1}] \equiv 2\beta \frac{\delta \hat{\Omega}_V[\mathbf{F}, \mathbf{G}_0^{-1}]}{\delta \mathbf{G}_0^{-1}} + (\hat{\phi}_V \hat{\phi}_V^\dagger)[\mathbf{F}, \mathbf{G}_0^{-1}] \tag{7.7}$$

that reproduce the physical one- and two-point propagators (i.e. the condensate $\boldsymbol{\Phi}_{\mathbf{F}\mathbf{t}\boldsymbol{\eta}V}$ and the connected Green's function $\mathbf{G}_{\mathbf{F}\mathbf{t}\boldsymbol{\eta}V}$) of the disordered interacting system in Eq. (7.1) when evaluated at $\mathbf{F}$ and $\mathbf{G}^{-1}_{\mathbf{t}\boldsymbol{\eta}0}$, i.e.

$$\hat{\phi}_V[\mathbf{F}, \mathbf{G}^{-1}_{\mathbf{t}\boldsymbol{\eta}0}] = \boldsymbol{\Phi}_{\mathbf{F}\mathbf{t}\boldsymbol{\eta}V} = \langle \mathbf{b} \rangle\,, \tag{7.8}$$

$$\hat{\mathcal{G}}_V[\mathbf{F}, \mathbf{G}^{-1}_{\mathbf{t}\boldsymbol{\eta}0}] = \mathbf{G}_{\mathbf{F}\mathbf{t}\boldsymbol{\eta}V} = -\langle \mathbf{b}(\tau)\mathbf{b}^\dagger(0) \rangle + \langle \mathbf{b} \rangle \langle \mathbf{b}^\dagger \rangle\,. \tag{7.9}$$

7.1.2. Baym-Kadanoff functional

When exchanging the functional dependence of the free energy functional $\hat{\Omega}_V$ in Eq. (8.12), from $\mathbf{F}$ and $\mathbf{G}_0^{-1}$ to $\boldsymbol{\Phi}$ and $\mathbf{G}$ by means of a Legendre transformation, one obtains the bosonic Baym-Kadanoff functional [109, 110] (see also Sec. 4.4)

$$\Gamma_{\text{BK}}[\boldsymbol{\Phi}, \mathbf{G}] = \mathbf{F}^\dagger \boldsymbol{\Phi} - \frac{1}{2}\boldsymbol{\Phi}^\dagger \mathbf{G}^{-1}_{\mathbf{t}\boldsymbol{\eta}0}\boldsymbol{\Phi} + \frac{1}{2}\text{Tr}[\mathbf{G}^{-1}_{\mathbf{t}\boldsymbol{\eta}0}\mathbf{G}] + \frac{1}{2}\text{Tr}\ln[-\mathbf{G}^{-1}] + \Phi_{\text{LW}}[\boldsymbol{\Phi}, \mathbf{G}]\,. \tag{7.10}$$

At the physical interacting one and two-point propagators, the Baym-Kadanoff functional Γ_{BK} is stationary

$$\partial_{\boldsymbol{\Phi}} \Gamma_{\text{BK}}[\boldsymbol{\Phi}_{\mathbf{F}\mathbf{t}\boldsymbol{\eta}V}, \mathbf{G}_{\mathbf{F}\mathbf{t}\boldsymbol{\eta}V}] = 0\,, \tag{7.11}$$

$$\partial_{\mathbf{G}} \Gamma_{\text{BK}}[\boldsymbol{\Phi}_{\mathbf{F}\mathbf{t}\boldsymbol{\eta}V}, \mathbf{G}_{\mathbf{F}\mathbf{t}\boldsymbol{\eta}V}] = 0\,, \tag{7.12}$$

and equal to the free energy

$$\Gamma_{\text{BK}}[\boldsymbol{\Phi}_{\mathbf{F}\mathbf{t}\boldsymbol{\eta}V}, \mathbf{G}_{\mathbf{F}\mathbf{t}\boldsymbol{\eta}V}] = \Omega_{\boldsymbol{\eta}}\,. \tag{7.13}$$

The explicit functional derivatives take the form

$$\frac{\delta \Gamma_{\text{BK}}}{\delta \boldsymbol{\Phi}^\dagger} = \mathbf{F} - \mathbf{G}_0^{-1}\boldsymbol{\Phi} + \frac{\delta \Phi_{\text{LW}}}{\delta \boldsymbol{\Phi}^\dagger}\,, \tag{7.14}$$

$$2\frac{\delta \Gamma_{\text{BK}}}{\delta \mathbf{G}} = \mathbf{G}_0^{-1} - \mathbf{G}^{-1} + 2\frac{\delta \Phi_{\text{LW}}}{\delta \mathbf{G}}\,. \tag{7.15}$$

By identifying the variations with respect to the Luttinger-Ward functional Φ_{LW} as the one and two-point self-energies [109, 110]

$$\mathbf{S} = -\delta_{\boldsymbol{\Phi}^\dagger}\Phi_{\text{LW}}\,, \quad \boldsymbol{\Sigma} = -2\delta_{\mathbf{G}}\Phi_{\text{LW}}\,, \tag{7.16}$$

and applying the stationarity conditions [Eqs. (7.11) and (7.12)] we find that the interacting propagators fulfill the two Dyson equations

$$\mathbf{G}_0^{-1}\mathbf{\Phi} = \mathbf{F} - \mathbf{S}\,, \tag{7.17}$$

$$\mathbf{G}^{-1} = \mathbf{G}_0^{-1} - \mathbf{\Sigma}\,. \tag{7.18}$$

Consider now the result of substituting $\mathbf{F}$ and $\mathbf{G}_0^{-1}$ using Eqs. (7.17) and (7.18) in the functionals $\hat{\phi}_V$ and $\hat{\mathcal{G}}_V$ [Eqs. (7.6) and (7.7)]. This gives the highly non-linear coupled equations

$$\hat{\phi}_V[(\mathbf{G}^{-1} + \mathbf{\Sigma})\mathbf{\Phi} + \mathbf{S}, \mathbf{G}^{-1} + \mathbf{\Sigma}] = \mathbf{\Phi}\,, \tag{7.19}$$

$$\hat{\mathcal{G}}_V[(\mathbf{G}^{-1} + \mathbf{\Sigma})\mathbf{\Phi} + \mathbf{S}, \mathbf{G}^{-1} + \mathbf{\Sigma}] = \mathbf{G}\,. \tag{7.20}$$

For given self-energies $\mathbf{S}$ and $\mathbf{\Sigma}$ the concomitant solution of Eqs. (7.19) and (7.20) implicitly defines the functionals

$$\hat{\mathbf{\Phi}}_V[\mathbf{S}, \mathbf{\Sigma}] = \mathbf{\Phi}\,, \quad \hat{\mathbf{G}}_V[\mathbf{S}, \mathbf{\Sigma}] = \mathbf{G}, \tag{7.21}$$

depending solely on the self-energies $\mathbf{S}$ and $\mathbf{\Sigma}$ and the interaction $\hat{V}$, producing the physical interacting propagators when evaluated at the physical self-energies, i.e.

$$\hat{\mathbf{\Phi}}_V[\mathbf{S}_{\mathbf{F}t\eta V}, \mathbf{\Sigma}_{\mathbf{F}t\eta V}] = \mathbf{\Phi}_{\mathbf{F}t\eta V}\,, \tag{7.22}$$

$$\hat{\mathbf{G}}_V[\mathbf{S}_{\mathbf{F}t\eta V}, \mathbf{\Sigma}_{\mathbf{F}t\eta V}] = \mathbf{G}_{\mathbf{F}t\eta V}\,. \tag{7.23}$$

7.1.3. Bosonic self-energy effective action

By means of a further Legendre transform the Baym-Kadanoff functional Γ_{BK} with functional dependence on $\mathbf{F}$ and $\mathbf{G}$ can be transformed into the self-energy effective action

$$\Gamma_{\text{SE}}[\mathbf{S}, \mathbf{\Sigma}] = \frac{1}{2}(\mathbf{F} - \mathbf{S})^\dagger \mathbf{G}_{\mathbf{t}\eta 0}(\mathbf{F} - \mathbf{S}) + \frac{1}{2}\mathrm{Tr}\ln[-(\mathbf{G}_{\mathbf{t}\eta 0}^{-1} - \mathbf{\Sigma})] + \hat{\mathcal{F}}_V[\mathbf{S}, \mathbf{\Sigma}] \tag{7.24}$$

depending on the self-energies $\mathbf{S}$ and $\mathbf{\Sigma}$, where the universal functional $\hat{\mathcal{F}}_V[\mathbf{S}, \mathbf{\Sigma}]$ is the Legendre transform of the universal Luttinger-Ward functional $\Phi_{\text{LW}}[\mathbf{\Phi}, \mathbf{G}]$, with variations (see Chapter 6)

$$\delta_{\mathbf{S}}\hat{\mathcal{F}}_V = \mathbf{\Phi}\,, \quad \delta_{\mathbf{\Sigma}}\hat{\mathcal{F}}_V = \mathbf{G}. \tag{7.25}$$

The variations of the self-energy effective action give

$$\frac{\delta\Gamma_{\text{SE}}}{\delta\mathbf{S}} = -\mathbf{G}_{\mathbf{t}\eta 0}(\mathbf{F} - \mathbf{S}) + \mathbf{\Phi}\,, \tag{7.26}$$

$$\frac{\delta\Gamma_{\text{SE}}}{\delta\mathbf{\Sigma}} = -\left[\mathbf{G}_{\mathbf{t}\eta 0}^{-1} - \mathbf{\Sigma}\right]^{-1} + \mathbf{G}\,, \tag{7.27}$$

whence Γ_{SE} is stationary at the physical self-energies

$$\delta_{\mathbf{S}}\Gamma_{\text{SE}}[\mathbf{S}_{\mathbf{F}t\eta V}, \mathbf{\Sigma}_{\mathbf{F}t\eta V}] = 0\,, \tag{7.28}$$

$$\delta_{\mathbf{\Sigma}}\Gamma_{\text{SE}}[\mathbf{S}_{\mathbf{F}t\eta V}, \mathbf{\Sigma}_{\mathbf{F}t\eta V}] = 0\,. \tag{7.29}$$

and equal to the free energy

$$\Gamma_{\text{SE}}[\mathbf{S}_{\mathbf{F}t\eta V}, \mathbf{\Sigma}_{\mathbf{F}t\eta V}] = \Omega_\eta\,. \tag{7.30}$$

7.1.4. Disorder-averaged self-energy effective action

While we up till now have treated a system with a single disorder realization $\boldsymbol{\eta}$, we are interested in describing the averaged ensemble of systems with disorder probability distribution $P(\boldsymbol{\eta})$ and its ensemble averaged free-energy

$$\Omega_P \equiv \langle \Omega_{\boldsymbol{\eta}} \rangle_P \equiv \int d\boldsymbol{\eta} P(\boldsymbol{\eta}) \Omega_{\boldsymbol{\eta}} \,. \tag{7.31}$$

To this end we define the averaged self-energy effective action

$$\hat{\Gamma}^{(\mathrm{SE})}_{\mathbf{F}\mathbf{t}PV}[\{\mathbf{S}_{\boldsymbol{\eta}}, \boldsymbol{\Sigma}_{\boldsymbol{\eta}}\}] \equiv \langle \Gamma_{\mathrm{SE}}[\mathbf{S}_{\boldsymbol{\eta}}, \boldsymbol{\Sigma}_{\boldsymbol{\eta}}] \rangle_P \,. \tag{7.32}$$

where $\mathbf{S}_{\boldsymbol{\eta}}$ and $\boldsymbol{\Sigma}_{\boldsymbol{\eta}}$ denote the self-energies for the disorder configuration $\boldsymbol{\eta}$.

To describe the combined effect of disorder and interaction we rewrite $\hat{\Gamma}^{(\mathrm{SE})}_{\mathbf{F}\mathbf{t}PV}$ in terms of the universal averaged propagator functionals

$$\hat{\bar{\boldsymbol{\Phi}}} \equiv \hat{\bar{\boldsymbol{\Phi}}}_{P,V}[\{\mathbf{S}_{\boldsymbol{\eta}}, \boldsymbol{\Sigma}_{\boldsymbol{\eta}}\}] \equiv \left\langle \hat{\boldsymbol{\Phi}}_{\boldsymbol{\eta}} \right\rangle_P \,, \tag{7.33}$$

$$\hat{\bar{\mathbf{G}}} \equiv \hat{\bar{\mathbf{G}}}_{P,V}[\{\mathbf{S}_{\boldsymbol{\eta}}, \boldsymbol{\Sigma}_{\boldsymbol{\eta}}\}] \equiv \left\langle \hat{\mathbf{G}}_{\boldsymbol{\eta}} - \hat{\boldsymbol{\Phi}}_{\boldsymbol{\eta}} \hat{\boldsymbol{\Phi}}^{\dagger}_{\boldsymbol{\eta}} \right\rangle_P + \hat{\bar{\boldsymbol{\Phi}}} \hat{\bar{\boldsymbol{\Phi}}}^{\dagger} \,. \tag{7.34}$$

using the short-hand notation $\hat{\mathbf{G}}_{\boldsymbol{\eta}} \equiv \hat{\mathbf{G}}_V[\mathbf{S}_{\boldsymbol{\eta}}, \boldsymbol{\Sigma}_{\boldsymbol{\eta}}]$ and $\hat{\boldsymbol{\Phi}}_{\boldsymbol{\eta}} \equiv \hat{\boldsymbol{\Phi}}_V[\mathbf{S}_{\boldsymbol{\eta}}, \boldsymbol{\Sigma}_{\boldsymbol{\eta}}]$ [see Eqs. (7.22) and (7.23)]. The corresponding average self-energies $\bar{\mathbf{S}}$ and $\bar{\boldsymbol{\Sigma}}$ are defined through the Dyson equations

$$\bar{\mathbf{S}} = \mathbf{F} - \mathbf{G}^{-1}_{\mathbf{t}00} \bar{\boldsymbol{\Phi}} \,, \tag{7.35}$$

$$\bar{\boldsymbol{\Sigma}} = \mathbf{G}^{-1}_{\mathbf{t}00} - \bar{\mathbf{G}}^{-1} \,, \tag{7.36}$$

where $\mathbf{G}_{\mathbf{t}00}$ is the free propagator for the disorder-free system $\mathbf{G}_{\mathbf{t}00} \equiv \mathbf{G}_{\mathbf{t}\boldsymbol{\eta}0}|_{\boldsymbol{\eta}=\mathbf{0}}$, and $\bar{\boldsymbol{\Phi}}$ and $\bar{\mathbf{G}}$ are the disorder-avareged condensate and connected Green's function, respectively, computed by evaluating Eqs. (7.33) and (7.34) at the physical self-energies $\mathbf{S}_{\mathbf{F}\mathbf{t}\boldsymbol{\eta}V}$ and $\boldsymbol{\Sigma}_{\mathbf{F}\mathbf{t}\boldsymbol{\eta}V}$ for each disorder configuration $\boldsymbol{\eta}$.

The averaged self-energy effective action can now be expressed as

$$\begin{aligned} \hat{\Gamma}^{(\mathrm{SE})}_{\mathbf{F}\mathbf{t}PV}[\bar{\mathbf{S}}, \bar{\boldsymbol{\Sigma}}, \{\mathbf{S}_{\boldsymbol{\eta}}, \boldsymbol{\Sigma}_{\boldsymbol{\eta}}\}] =& \frac{1}{2}(\mathbf{F} - \bar{\mathbf{S}})^{\dagger} \mathbf{G}_{\mathbf{t}00} (\mathbf{F} - \bar{\mathbf{S}}) + \frac{1}{2} \mathrm{Tr} \ln[-(\mathbf{G}^{-1}_{\mathbf{t}00} - \bar{\boldsymbol{\Sigma}})] \\ &+ \hat{\mathcal{T}}_{P,V}[\bar{\mathbf{S}}, \bar{\boldsymbol{\Sigma}}, \{\mathbf{S}_{\boldsymbol{\eta}}, \boldsymbol{\Sigma}_{\boldsymbol{\eta}}\}] + \left\langle \hat{\mathcal{F}}_V[\mathbf{S}_{\boldsymbol{\eta}}, \boldsymbol{\Sigma}_{\boldsymbol{\eta}}] \right\rangle_P \,, \end{aligned} \tag{7.37}$$

where $\hat{\mathcal{T}}_{PV}$ is the universal functional for the averaged self-energies

$$\begin{aligned} \hat{\mathcal{T}}_{PV}[\bar{\mathbf{S}}, \bar{\boldsymbol{\Sigma}}, \{\mathbf{S}_{\boldsymbol{\eta}}, \boldsymbol{\Sigma}_{\boldsymbol{\eta}}\}] \equiv& -\frac{1}{2} \hat{\bar{\boldsymbol{\Phi}}}^{\dagger} (\hat{\bar{\mathbf{G}}}^{-1} + \bar{\boldsymbol{\Sigma}}) \hat{\bar{\boldsymbol{\Phi}}} + \frac{1}{2} \left\langle \hat{\bar{\boldsymbol{\Phi}}}^{\dagger}_{\boldsymbol{\eta}} (\hat{\bar{\mathbf{G}}}^{-1} + \bar{\boldsymbol{\Sigma}} - \boldsymbol{\eta})^{-1} \hat{\bar{\boldsymbol{\Phi}}}_{\boldsymbol{\eta}} \right\rangle_P \\ &- \frac{1}{2} \mathrm{Tr} \ln(-\hat{\bar{\mathbf{G}}}^{-1}) + \frac{1}{2} \left\langle \mathrm{Tr} \ln[-(\hat{\bar{\mathbf{G}}}^{-1} + \bar{\boldsymbol{\Sigma}} - \boldsymbol{\eta} - \boldsymbol{\Sigma}_{\boldsymbol{\eta}})] \right\rangle_P \,. \end{aligned} \tag{7.38}$$

Taking the variations of $\hat{\mathcal{T}}_{PV}$ with respect to $\bar{\mathbf{S}}$ and $\bar{\boldsymbol{\Sigma}}$ gives

$$\delta_{\bar{\mathbf{S}}} \hat{\mathcal{T}}_{PV} = \hat{\bar{\boldsymbol{\Phi}}} \,, \quad 2\delta_{\bar{\boldsymbol{\Sigma}}} \hat{\mathcal{T}}_{PV} = \hat{\bar{\mathbf{G}}} \,, \tag{7.39}$$

which shows that $\hat{\mathcal{T}}_{PV}$ is the analogue of the $\hat{\mathcal{F}}_V$ functional for the averaged self-energies, as by (7.25)

$$\delta_{\bar{\mathbf{S}}_{\boldsymbol{\eta}}} \hat{\mathcal{F}}_V = \hat{\boldsymbol{\Phi}}_{\boldsymbol{\eta}} \,, \quad 2\delta_{\bar{\boldsymbol{\Sigma}}_{\boldsymbol{\eta}}} \hat{\mathcal{F}}_V = \hat{\mathbf{G}}_{\boldsymbol{\eta}} \,. \tag{7.40}$$

The functional derivatives with respect to the self-energies at fixed disorder configuration $\boldsymbol{\eta}$ yield

$$\delta_{\mathbf{S}_\eta}\hat{\mathcal{T}}_{PV} = -P(\boldsymbol{\eta})\hat{\boldsymbol{\Phi}}_{\boldsymbol{\eta}}\,, \quad 2\delta_{\boldsymbol{\Sigma}_\eta}\hat{\mathcal{T}}_{PV} = -P(\boldsymbol{\eta})\hat{\mathbf{G}}_{\boldsymbol{\eta}}. \tag{7.41}$$

The variations of the averaged self-energy effective action $\hat{\Gamma}^{(\mathrm{SE})}_{\mathbf{Ft}PV}$ therefore give

$$\delta_{\bar{\mathbf{S}}}\hat{\Gamma}^{(\mathrm{SE})}_{\mathbf{Ft}PV} = -\mathbf{G}_{\mathbf{t}00}(\mathbf{F}-\bar{\mathbf{S}}) + \hat{\bar{\boldsymbol{\Phi}}} \tag{7.42}$$

$$2\delta_{\bar{\boldsymbol{\Sigma}}}\hat{\Gamma}^{(\mathrm{SE})}_{\mathbf{Ft}PV} = -[\mathbf{G}^{-1}_{\mathbf{t}00} - \bar{\boldsymbol{\Sigma}}]^{-1} + \hat{\bar{\mathbf{G}}} \tag{7.43}$$

$$\delta_{\mathbf{S}_\eta}\hat{\Gamma}^{(\mathrm{SE})}_{\mathbf{Ft}PV} = -P(\boldsymbol{\eta})\hat{\boldsymbol{\Phi}}_{\boldsymbol{\eta}} + \delta_{\mathbf{S}_\eta}\langle\hat{\mathcal{F}}_V[\mathbf{S}_{\boldsymbol{\eta}},\boldsymbol{\Sigma}_{\boldsymbol{\eta}}]\rangle_P \tag{7.44}$$

$$2\delta_{\boldsymbol{\Sigma}_\eta}\hat{\Gamma}^{(\mathrm{SE})}_{\mathbf{Ft}PV} = -P(\boldsymbol{\eta})\hat{\mathbf{G}}_{\boldsymbol{\eta}} + 2\delta_{\boldsymbol{\Sigma}_\eta}\langle\hat{\mathcal{F}}_V[\mathbf{S}_{\boldsymbol{\eta}},\boldsymbol{\Sigma}_{\boldsymbol{\eta}}]\rangle_P\,. \tag{7.45}$$

Hence, at the physical self-energies

$$\bar{\mathbf{S}},\bar{\boldsymbol{\Sigma}},\{\mathbf{S}_\eta,\boldsymbol{\Sigma}_\eta\} = \bar{\mathbf{S}}_{\mathbf{Ft}PV},\bar{\boldsymbol{\Sigma}}_{\mathbf{Ft}PV},\{\mathbf{S}_{\mathbf{Ft}\eta V},\boldsymbol{\Sigma}_{\mathbf{Ft}\eta V}\}\,, \tag{7.46}$$

the averaged self-energy effective action $\hat{\Gamma}^{(\mathrm{SE})}_{\mathbf{Ft}PV}$ is stationary

$$\delta_{\bar{\mathbf{S}}}\hat{\Gamma}^{(\mathrm{SE})}_{\mathbf{Ft}PV} = \delta_{\bar{\boldsymbol{\Sigma}}}\hat{\Gamma}^{(\mathrm{SE})}_{\mathbf{Ft}PV} = \delta_{\mathbf{S}_\eta}\hat{\Gamma}^{(\mathrm{SE})}_{\mathbf{Ft}PV} = \delta_{\boldsymbol{\Sigma}_\eta}\hat{\Gamma}^{(\mathrm{SE})}_{\mathbf{Ft}PV} = 0\,. \tag{7.47}$$

and equal to the average free energy

$$\hat{\Gamma}^{(\mathrm{SE})}_{\mathbf{Ft}PV}[\bar{\mathbf{S}}_{\mathbf{Ft}PV},\bar{\boldsymbol{\Sigma}}_{\mathbf{Ft}PV},\{\mathbf{S}_{\mathbf{Ft}\eta V},\boldsymbol{\Sigma}_{\mathbf{Ft}\eta V}\}] = \Omega_P\,. \tag{7.48}$$

The crucial part of the disorder-averaged self-energy effective action is that the functionals $\hat{\mathcal{T}}_{PV}$ and $\hat{\mathcal{F}}_V$ are universal, in the sense that they do not depend on the non-interacting propagator $\mathbf{G}_{\mathbf{t}00}$ or the symmetry-breaking field $\mathbf{F}$ (see Appendix A.5 for the explicit derivatives of $\hat{\mathcal{T}}_{PV}$). In fact, these functionals depend only on the interaction V, the disorder probability distribution $P(\boldsymbol{\eta})$, the set of disorder-dependent self-energies $\{\mathbf{S}_\eta,\boldsymbol{\Sigma}_\eta\}$, and the average self-energies $\bar{\mathbf{S}}$ and $\bar{\boldsymbol{\Sigma}}$. In the following we will make use of this property in order to derive consistent approximations of $\hat{\Gamma}^{(\mathrm{SE})}_{\mathbf{Ft}PV}$.

7.1.5. Disorder-averaged self-energy functional theory

We now consider the general interacting bosonic system with quadratic disorder of Eq. (7.1), and introduce a second *reference* system with the same interaction $\hat{V}$ and disorder $P(\boldsymbol{\eta})$ but with some arbitrary linear symmetry breaking field $\mathbf{F}'$, arbitrary free propagator

$$\mathbf{G}^{-1}_{\boldsymbol{\Delta}\eta 0}(\tau,\tau') = \delta(\tau-\tau')(-[\mathbf{1}\otimes\sigma_z]\partial_{\tau'} - \boldsymbol{\eta}) - \boldsymbol{\Delta}(\tau,\tau')\,, \tag{7.49}$$

and self-energy effective action $\hat{\Gamma}^{(\mathrm{SE})}_{\mathbf{F}'\boldsymbol{\Delta}PV}$. Here, the free propagator $\mathbf{G}_{\boldsymbol{\Delta}\eta 0}$ is parametrized by replacing the hopping $\mathbf{t}$ by a completely general matrix $\boldsymbol{\Delta}(\tau,\tau')$.

Now, since the self-energy effective actions of both systems contain the same universal functionals $\hat{\mathcal{F}}_{PV}$ and $\hat{\mathcal{T}}_{PV}$ we can evaluate $\hat{\Gamma}^{(\mathrm{SE})}_{\mathbf{Ft}PV}$ in terms of $\hat{\Gamma}^{(\mathrm{SE})}_{\mathbf{F}'\boldsymbol{\Delta}PV}$ as

$$\begin{aligned}\hat{\Gamma}^{(\mathrm{SE})}_{\mathbf{Ft}PV}[\bar{\mathbf{S}},\bar{\boldsymbol{\Sigma}}] =& \hat{\Gamma}^{(\mathrm{SE})}_{\mathbf{F}'\boldsymbol{\Delta}PV}[\bar{\mathbf{S}},\bar{\boldsymbol{\Sigma}}] + \frac{1}{2}\mathrm{Tr}\ln\left[\mathbf{G}^{-1}_{\mathbf{t}00} - \bar{\boldsymbol{\Sigma}}\right] - \frac{1}{2}\mathrm{Tr}\ln\left[\mathbf{G}^{-1}_{\boldsymbol{\Delta}00} - \bar{\boldsymbol{\Sigma}}\right] \\ &+ \frac{1}{2}(\mathbf{F}-\bar{\mathbf{S}})^\dagger\mathbf{G}_{\mathbf{t}00}(\mathbf{F}-\bar{\mathbf{S}}) - \frac{1}{2}(\mathbf{F}'-\bar{\mathbf{S}})^\dagger\mathbf{G}_{\boldsymbol{\Delta}00}(\mathbf{F}'-\bar{\mathbf{S}}).\end{aligned} \tag{7.50}$$

Note, that by replacing $\hat{\mathcal{F}}_{PV}$ and $\hat{\mathcal{T}}_{PV}$ we have now eliminated any dependence on the fixed-disorder self-energies $\{\mathbf{S}_\eta,\boldsymbol{\Sigma}_\eta\}$, such that the disorder-averaged self-energy effective action now

only depends on the average self-energies $\bar{\mathbf{S}}$ and $\bar{\mathbf{\Sigma}}$. The stationary condition (7.47) now translates into

$$\frac{\delta\hat{\Gamma}^{(\mathrm{SE})}_{\mathbf{F}\mathbf{t}PV}}{\delta\bar{\mathbf{S}}} = \mathbf{G}_{\mathbf{\Delta}00}(\mathbf{F}'-\bar{\mathbf{S}}) - \mathbf{G}_{\mathbf{t}00}(\mathbf{F}-\bar{\mathbf{S}}) = 0\,, \tag{7.51}$$

$$2\frac{\delta\hat{\Gamma}^{(\mathrm{SE})}_{\mathbf{F}\mathbf{t}PV}}{\delta\bar{\mathbf{\Sigma}}} = [\mathbf{G}^{-1}_{\mathbf{\Delta}00} - \bar{\mathbf{\Sigma}}]^{-1} - [\mathbf{G}^{-1}_{\mathbf{t}00} - \bar{\mathbf{\Sigma}}]^{-1} = 0\,. \tag{7.52}$$

If by an appropriate choice of $\mathbf{\Delta}$ and $\mathbf{F}'$ the reference system can be made simple enough to be exactly solvable, one can go one step further and evaluate the original systems functional $\hat{\Gamma}^{(\mathrm{SE})}_{\mathbf{F}\mathbf{t}PV}$ at the physical self-energies of the reference system $\bar{\mathbf{S}}_{\mathbf{F}'\mathbf{\Delta}} \equiv \bar{\mathbf{S}}_{\mathbf{F}'\mathbf{\Delta}PV}$ and $\bar{\mathbf{\Sigma}}_{\mathbf{F}'\mathbf{\Delta}} \equiv \bar{\mathbf{\Sigma}}_{\mathbf{F}'\mathbf{\Delta}PV}$. This produces the self-energy functional theory (SFT) approximation for the system and the SFT functional

$$\begin{aligned}\Gamma_{\mathrm{SFT}}[\bar{\mathbf{S}}_{\mathbf{F}'\mathbf{\Delta}},\bar{\mathbf{\Sigma}}_{\mathbf{F}'\mathbf{\Delta}}] =& \Omega_{\mathbf{F}'\mathbf{\Delta}PV} + \frac{1}{2}\mathrm{Tr}\ln\left[\mathbf{G}^{-1}_{\mathbf{t}00} - \bar{\mathbf{\Sigma}}_{\mathbf{F}'\mathbf{\Delta}}\right] - \frac{1}{2}\mathrm{Tr}\ln\left[\mathbf{G}^{-1}_{\mathbf{\Delta}00} - \bar{\mathbf{\Sigma}}_{\mathbf{F}'\mathbf{\Delta}}\right] \\ &+ \frac{1}{2}(\mathbf{F}-\bar{\mathbf{S}}_{\mathbf{F}'\mathbf{\Delta}})^{\dagger}\mathbf{G}_{\mathbf{t}00}(\mathbf{F}-\bar{\mathbf{S}}_{\mathbf{F}'\mathbf{\Delta}}) - \frac{1}{2}(\mathbf{F}'-\bar{\mathbf{S}}_{\mathbf{F}'\mathbf{\Delta}})^{\dagger}\mathbf{G}_{\mathbf{\Delta}00}(\mathbf{F}'-\bar{\mathbf{S}}_{\mathbf{F}'\mathbf{\Delta}})\,,\end{aligned} \tag{7.53}$$

where we have used that $\hat{\Gamma}^{(\mathrm{SE})}_{\mathbf{F}'\mathbf{\Delta}PV}[\bar{\mathbf{S}}_{\mathbf{F}'\mathbf{\Delta}},\bar{\mathbf{\Sigma}}_{\mathbf{F}'\mathbf{\Delta}}] = \Omega_{\mathbf{F}'\mathbf{\Delta}PV}$, and

$$\Gamma_{\mathrm{SFT}}[\bar{\mathbf{S}}_{\mathbf{F}'\mathbf{\Delta}},\bar{\mathbf{\Sigma}}_{\mathbf{F}'\mathbf{\Delta}}] \equiv \hat{\Gamma}^{(\mathrm{SE})}_{\mathbf{F}\mathbf{t}PV}[\bar{\mathbf{S}}_{\mathbf{F}'\mathbf{\Delta}},\bar{\mathbf{\Sigma}}_{\mathbf{F}'\mathbf{\Delta}}] \tag{7.54}$$

is the self-energy effective action of the original system $\hat{\Gamma}^{(\mathrm{SE})}_{\mathbf{F}\mathbf{t}PV}$ restricted to the domain of physical self-energies of the reference system.

The domain of Γ_{SFT} is therefore defined by the physical self-energies of the reference system ($\bar{\mathbf{S}}_{\mathbf{F}'\mathbf{\Delta}}$ and $\bar{\mathbf{\Sigma}}_{\mathbf{F}'\mathbf{\Delta}}$) and parametrized by $\mathbf{\Delta}$ and $\mathbf{F}'$. By generalizing the variational principle of Eq. (7.47) to the restricted domain we obtain a thermodynamically optimal approximation when the self-energy variations are zero on the domain, i.e. we seek $\mathbf{\Delta}$ and $\mathbf{F}'$ such that

$$\frac{\delta\Gamma_{\mathrm{SFT}}}{\delta\bar{\mathbf{S}}_{\mathbf{F}'\mathbf{\Delta}}} = \frac{\delta\Gamma_{\mathrm{SFT}}}{\delta\bar{\mathbf{\Sigma}}_{\mathbf{F}'\mathbf{\Delta}}} = 0, \tag{7.55}$$

which by

$$\begin{aligned}\frac{\delta\Gamma_{\mathrm{SFT}}}{\delta\bar{\mathbf{S}}_{\mathbf{F}'\mathbf{\Delta}}} &= \frac{\delta\Gamma_{\mathrm{SFT}}}{\delta\mathbf{F}'}\left[\frac{\delta\bar{\mathbf{S}}_{\mathbf{F}'\mathbf{\Delta}}}{\delta\mathbf{F}'}\right]^{-1} + \frac{\delta\Gamma_{\mathrm{SFT}}}{\delta\mathbf{\Delta}}\left[\frac{\delta\bar{\mathbf{S}}_{\mathbf{F}'\mathbf{\Delta}}}{\delta\mathbf{\Delta}}\right]^{-1}, \\ \frac{\delta\Gamma_{\mathrm{SFT}}}{\delta\bar{\mathbf{\Sigma}}_{\mathbf{F}'\mathbf{\Delta}}} &= \frac{\delta\Gamma_{\mathrm{SFT}}}{\delta\mathbf{F}'}\left[\frac{\delta\bar{\mathbf{\Sigma}}_{\mathbf{F}'\mathbf{\Delta}}}{\delta\mathbf{F}'}\right]^{-1} + \frac{\delta\Gamma_{\mathrm{SFT}}}{\delta\mathbf{\Delta}}\left[\frac{\delta\bar{\mathbf{\Sigma}}_{\mathbf{F}'\mathbf{\Delta}}}{\delta\mathbf{\Delta}}\right]^{-1},\end{aligned}$$

can be fulfilled if

$$\frac{\delta\Gamma_{\mathrm{SFT}}}{\delta\mathbf{F}'} = \frac{\delta\Gamma_{\mathrm{SFT}}}{\delta\mathbf{\Delta}} = 0. \tag{7.56}$$

By the SFT approximation, the entire complexity of the original lattice system has therefore been reduced to finding stationary solutions of the functional (7.53) in terms of the variational parameters $\mathbf{F}'$ and $\mathbf{\Delta}$.

7.1.6. Disorder-averaged bosonic dynamical mean-field theory limit

Disordered-averaged SFT for bosons has disorder-averaged bosonic dynamical mean-field theory (BDMFT, see Secs. 4.5 and 6.2.3) as a certain limit. In its simplest form, disorder-averaged BDMFT is restricted to site-local disorder $\boldsymbol{\eta}$ and site-local interaction $\hat{V}$.

In this case, disorder-averaged BDMFT is obtained from SFT by restricting the reference systems free propagator to be site-local, i.e.

$$\boldsymbol{\Delta}^{i\nu}_{j\nu'}(\tau,\tau') = \delta_{ij}[\boldsymbol{\Delta}_i]^{\nu}_{\nu'}(\tau,\tau')\,, \tag{7.57}$$

where i,j are the site-, and ν,ν' the Nambu indices. The imaginary time retardation in $\boldsymbol{\Delta}(\tau,\tau')$, however, remains completely general.

The reference systems local bare propagator $\mathbf{G}_{\boldsymbol{\Delta}\boldsymbol{\eta}0}$ and interaction give rise to a purely local self-energy

$$[\boldsymbol{\Sigma}_{\mathbf{F}'\boldsymbol{\Delta}\boldsymbol{\eta}V}]_{ij} = \delta_{ij}[\boldsymbol{\Sigma}_{\mathbf{F}'\boldsymbol{\Delta}\boldsymbol{\eta}V}]_{ii}\,, \tag{7.58}$$

$$[\bar{\boldsymbol{\Sigma}}_{\mathbf{F}'\boldsymbol{\Delta}PV}]_{ij} = \delta_{ij}[\bar{\boldsymbol{\Sigma}}_{\mathbf{F}'\boldsymbol{\Delta}PV}]_{ii}\,, \tag{7.59}$$

and the self-energy variations of Γ_{SFT} [Eqs. (7.51) and (7.52)] reduce to the disorder-averaged BDMFT self-consistency conditions

$$\mathbf{G}_{\boldsymbol{\Delta}00}(\mathbf{F}' - \bar{\mathbf{S}}_{\mathbf{F}'\boldsymbol{\Delta}}) - \mathbf{G}_{\mathbf{t}00}(\mathbf{F} - \bar{\mathbf{S}}_{\mathbf{F}'\boldsymbol{\Delta}}) = \mathbf{G}_{\mathbf{t}00}\left[(\mathbf{G}^{-1}_{\mathbf{t}00} - \mathbf{G}^{-1}_{\boldsymbol{\Delta}00})\bar{\boldsymbol{\Phi}}_{\mathbf{F}'\boldsymbol{\Delta}} + \mathbf{F}' - \mathbf{F}\right] = 0\,, \tag{7.60}$$

$$[(\mathbf{G}^{-1}_{\boldsymbol{\Delta}00})_{ii} - \bar{\boldsymbol{\Sigma}}_{\mathbf{F}'\boldsymbol{\Delta}}]^{-1} - [\mathbf{G}^{-1}_{\mathbf{t}00} - \bar{\boldsymbol{\Sigma}}_{\mathbf{F}'\boldsymbol{\Delta}}]^{-1}_{ii} = 0\,, \tag{7.61}$$

which can be fulfilled exactly by the retarded $\boldsymbol{\Delta}(\tau,\tau')$, and can be simplified to

$$\bar{\mathbf{G}}_{ii} = \bar{\mathbf{G}}_{\mathbf{F}'\boldsymbol{\Delta}PV}\,, \tag{7.62}$$

$$\bar{\boldsymbol{\Phi}} = \bar{\boldsymbol{\Phi}}_{\mathbf{F}'\boldsymbol{\Delta}PV}\,, \tag{7.63}$$

where $\bar{\boldsymbol{\Phi}}$ and $\bar{\mathbf{G}}_{ii}$ are the disorder-averaged condensate and local connected Green's function of the lattice, while $\bar{\boldsymbol{\Phi}}_{\mathbf{F}'\boldsymbol{\Delta}PV}$ and $\bar{\mathbf{G}}_{\mathbf{F}'\boldsymbol{\Delta}PV}$ are the disorder-averaged condensate and connected Green's function of the reference system. This is therefore the standard BDMFT self-consistency condition of clean systems [65, 67], where the propagators of the clean system have been replaced by their disorder-averaged counterparts.

7.1.7. Uncorrelated disorder: translational invariance of the arithmetic average

In the following we will specialize the formalism derived in Sec. 7.1.5 by assuming that the disorder is distributed according to an uncorrelated and translationally invariant probability distribution, i.e.

$$P(\boldsymbol{\eta}) = \prod_{ij} p_{i-j}(\eta_{ij}) \tag{7.64}$$

where the product goes over all site-indices i,j, and the distribution p_{i-j} depends only on the relative distance between the sites i and j. As we will see this enables us to simplify the reference system considerably due to the translational invariance of disorder-averaged observables.

The interacting propagators at a given disorder configuration $\boldsymbol{\eta}$ can be computed directly by

$$\mathbf{G}_{\mathbf{F}'\boldsymbol{\Delta}\boldsymbol{\eta}V}(\tau-\tau') = -\langle \mathcal{T}\mathbf{b}(\tau)\mathbf{b}^\dagger(\tau')\rangle_{\boldsymbol{\eta}} + \langle \mathbf{b}\rangle_{\boldsymbol{\eta}}\langle \mathbf{b}^\dagger\rangle_{\boldsymbol{\eta}} \tag{7.65}$$

$$\boldsymbol{\Phi}_{\mathbf{F}'\boldsymbol{\Delta}\boldsymbol{\eta}V} = \langle \mathbf{b}\rangle_{\boldsymbol{\eta}} \tag{7.66}$$

where $\mathcal{T}$ is the time-ordering operator and $\langle \dots \rangle_{\boldsymbol{\eta}}$ means taking the expectation value with respect to the reference system with disorder configuration $\boldsymbol{\eta}$.

Using Eqs. (7.65) and (7.66) further enables the computation of the fixed-disorder self-energies through Eqs. (7.17) and (7.18). The propagators $\mathbf{G}_{\mathbf{F}'\boldsymbol{\Delta}\boldsymbol{\eta}V}$, $\boldsymbol{\Phi}_{\mathbf{F}'\boldsymbol{\Delta}\boldsymbol{\eta}V}$, and the corresponding self-energies $\boldsymbol{\Sigma}_{\mathbf{F}'\boldsymbol{\Delta}\boldsymbol{\eta}V}$, $\mathbf{S}_{\mathbf{F}'\boldsymbol{\Delta}\boldsymbol{\eta}V}$, are not translationally invariant and can therefore be very hard to handle numerically.

If we now assume that we average over an infinite number of disorder configurations, the reference system's propagators will be translationally invariant, since due to the translational invariance of the uncorrelated disorder probability distribution of Eq. (7.64) all values η_{ij} will occur with the same weights for each pair of sites (i, j) with the same distance $i - j$, i.e.

$$\bar{\mathbf{G}}_{\mathbf{F}'\boldsymbol{\Delta}PV}(x_i, x_j, \tau - \tau') = \bar{\mathbf{G}}_{\mathbf{F}'\boldsymbol{\Delta}PV}(x_i - x_j, \tau - \tau') \tag{7.67}$$

with a translationally invariant condensate

$$\bar{\boldsymbol{\Phi}}_{\mathbf{F}'\boldsymbol{\Delta}PV}(x_i) = \bar{\boldsymbol{\Phi}}_{\mathbf{F}'\boldsymbol{\Delta}PV}(x_j) \tag{7.68}$$

According to Eqs. (7.17) and (7.18) this implies that also the average self-energies will be translationally invariant with

$$\bar{\boldsymbol{\Sigma}}_{\mathbf{F}'\boldsymbol{\Delta}}(i\omega_n, k) = \mathbf{G}^{-1}_{\boldsymbol{\Delta},0,0}(i\omega_n, k) - \bar{\mathbf{G}}^{-1}_{\mathbf{F}'\boldsymbol{\Delta}PV}(i\omega_n, k), \tag{7.69}$$

and

$$\begin{aligned} \bar{\mathbf{S}}_{\mathbf{F}'\boldsymbol{\Delta}}(x_i) &= \mathbf{F}'(x_i) - \mathbf{G}^{-1}_{\boldsymbol{\Delta},0,0}(i\omega_0, k = 0)\bar{\boldsymbol{\Phi}}_{\mathbf{F}'\boldsymbol{\Delta}PV}(x_i) \\ &= \bar{\mathbf{S}}_{\mathbf{F}'\boldsymbol{\Delta}}(x_j) \end{aligned} \tag{7.70}$$

Finally, $\Omega_{\mathbf{F}'\boldsymbol{\Delta}PV} = \langle \Omega_{\boldsymbol{\eta}} \rangle_P$ can be computed directly from averaging over the fixed-disorder systems.

As no fixed-disorder quantities are needed in order to evaluate the functional (7.53), the evaluation of the self-energy functional has now the same complexity as the disorder-free case of Chapter 6, where the self-energies and propagators were translationally invariant by definition. The only difference lies in the treatment of the reference system, which has to be averaged over all disorder configurations $\boldsymbol{\eta}$.

7.1.8. Lattice observables

Once a stationary solution fulfilling Eq. (7.56) has been found, the corresponding lattice observables can be computed using the self-energies

$$\boldsymbol{\Sigma}_{\boldsymbol{\eta}} \approx \boldsymbol{\Sigma}_{\mathbf{F}'\boldsymbol{\Delta}\boldsymbol{\eta}V}, \qquad \mathbf{S}_{\boldsymbol{\eta}} \approx \mathbf{S}_{\mathbf{F}'\boldsymbol{\Delta}\boldsymbol{\eta}V}, \tag{7.71}$$

$$\bar{\boldsymbol{\Sigma}} \approx \bar{\boldsymbol{\Sigma}}_{\mathbf{F}'\boldsymbol{\Delta}}, \qquad \bar{\mathbf{S}} \approx \bar{\mathbf{S}}_{\mathbf{F}'\boldsymbol{\Delta}}. \tag{7.72}$$

In particular, the disorder-averaged propagators $\bar{\mathbf{G}}$ and $\bar{\boldsymbol{\Phi}}$ can be computed using the self-energies $\bar{\boldsymbol{\Sigma}}$ and $\bar{\mathbf{S}}$ and the free propagator $\mathbf{G}_{\mathbf{t}00}$ in the Dyson equations (7.17) and (7.18). The fix-disorder propagators $\mathbf{G}_{\boldsymbol{\eta}}$ and $\boldsymbol{\Phi}_{\boldsymbol{\eta}}$, on the other hand, can be computed using $\boldsymbol{\Sigma}_{\boldsymbol{\eta}}$ and $\mathbf{S}_{\boldsymbol{\eta}}$ and the free propagator $\mathbf{G}_{\mathbf{t}\boldsymbol{\eta}0}$ in Eqs. (7.17) and (7.18). As the latter are not translational invariant, however, they can only be computed on a finite lattice-size, as Eqs. (7.17) and (7.18) now require the inversion of a matrix in position space. It is therefore preferable to use the translationally invariant averaged propagators $\bar{\mathbf{G}}$ and $\bar{\boldsymbol{\Phi}}$ in the thermodynamic limit.

As the arithmetic averaging is a linear operation, disorder-averaged observables of the lattice system which can be expressed as linear terms of one- and two-point quantities without any

disorder-dependent prefactors, can be directly evaluated from the average propagators $\bar{\mathbf{\Phi}}$ and $\bar{\mathbf{G}}$. This is trivially the case for the disorder-averaged condensate through Eq. (7.33), while for the particle density we have

$$n = \frac{1}{2\beta L}\left\langle \mathrm{Tr}[-\mathbf{G}_{\boldsymbol{\eta}}] + \mathbf{\Phi}^{\dagger}_{\boldsymbol{\eta}}\mathbf{\Phi}_{\boldsymbol{\eta}} \right\rangle_P = \frac{1}{2\beta L}\left(\mathrm{Tr}[-\langle \mathbf{G}_{\boldsymbol{\eta}}\rangle_P] + \langle \mathbf{\Phi}^{\dagger}_{\boldsymbol{\eta}}\mathbf{\Phi}_{\boldsymbol{\eta}}\rangle_P\right) = \frac{1}{2\beta L}\left(\mathrm{Tr}[-\bar{\mathbf{G}}] + \bar{\mathbf{\Phi}}^{\dagger}\bar{\mathbf{\Phi}}\right).$$

The same is true for the kinetic energy

$$E_{\mathrm{kin}} = \frac{1}{2\beta L}\left\langle \mathrm{Tr}\left[\mathbf{t}\left(\mathbf{G}_{\boldsymbol{\eta}} - \mathbf{\Phi}^{\dagger}_{\boldsymbol{\eta}}\mathbf{\Phi}_{\boldsymbol{\eta}}\right)\right]\right\rangle_P = \frac{1}{2\beta L}\mathrm{Tr}\left[\mathbf{t}\left(\bar{\mathbf{G}} - \bar{\mathbf{\Phi}}^{\dagger}\bar{\mathbf{\Phi}}\right)\right].$$

The interaction energy, on the other hand, cannot be directly evaluated from the averaged propagators as

$$E_{\mathrm{int}} = \frac{1}{L}\frac{U}{2}\sum_i \left\langle \langle n_i^2 - n_i\rangle_{\boldsymbol{\eta}} \right\rangle_P = -\frac{1}{4\beta L}\langle \mathrm{Tr}[\mathbf{\Sigma}_{\boldsymbol{\eta}}\mathbf{G}_{\boldsymbol{\eta}}]\rangle_P \neq -\frac{1}{4\beta L}\mathrm{Tr}[\bar{\mathbf{\Sigma}}\bar{\mathbf{G}}],$$

However, as the SFT functional is equal to the free-energy at stationarity, we have direct access to the disorder-averaged free energy of the lattice Ω_P, from which we can compute the interaction energy by the numerical derivative

$$E_{\mathrm{int}} = \frac{U}{L}\frac{\partial \Omega_P}{\partial U}. \tag{7.73}$$

7.2. Disordered Bose-Hubbard model

As a simple application of the formalism derived in Sec. 7.1 we study the disordered Bose-Hubbard model (BHm) [9, 14, 15, 16] on the cubic lattice with uncorrelated box disorder (see Sec. 2.3). The Hamiltonian has the form

$$H = -J\sum_{\langle i,j\rangle} b_i^{\dagger}b_j + \frac{U}{2}\sum_i b_i^{\dagger}b_i^{\dagger}b_i b_i + \sum_i (\eta_i - \mu)\,\hat{n}_i, \tag{7.74}$$

where $b_i^{(\dagger)}$ creates (annihilates) a boson at site i, $\hat{n}_i = b_i^{\dagger}b_i$ is the occupation number operator, $\langle i,j\rangle$ denotes summation over nearest neighbors, J is the hopping amplitude, U the on-site interaction, and μ the chemical potential. The local disorder potentials η_i are uncorrelated and are assumed to have a flat probability distribution

$$P(\boldsymbol{\eta}) = \prod_i p(\eta_i)\,,\ p(\eta) = \begin{cases} 1/(2\Delta) & \text{, if } |\eta| \leq \Delta \\ 0 & \text{, else} \end{cases} \tag{7.75}$$

where Δ is the disorder strength. Thus, the free propagator [Eq. (7.5)] is given by

$$\mathbf{G}^{-1}_{\mathbf{t}\boldsymbol{\eta}0}(\tau,\tau') = \delta(\tau-\tau')\left(-[\mathbf{1}\otimes\sigma_z]\partial_{\tau'} + \left[\left(J\delta_{\langle i,j\rangle} + [\mu-\eta_i]\delta_{ij}\right)\otimes\mathbf{1}\right]\right), \tag{7.76}$$

where $\delta_{\langle ij\rangle}$ is non-zero only for nearest neighbors $\langle i,j\rangle$.

7.2.1. Minimal reference system

In this first application of SFT with symmetry breaking to the disordered BHm, we will make use of the simplest possible reference system, comprising a single bosonic mode per site. In this case the reference system Hamiltonian reads

$$H'_{\boldsymbol{\eta}}\left[\mathbf{F}', \boldsymbol{\Delta}\right] = \sum_i \tilde{H}'_{i,\eta_i}\left[\mathbf{F}', \boldsymbol{\Delta}\right], \tag{7.77}$$

with independent single-site Hamiltonians

$$\tilde{H}'_{i,\eta_i} = \frac{U}{2} b_i^\dagger b_i^\dagger b_i b_i + (\eta_i - \mu)\,\hat{n}_i + \mathbf{b}_i^\dagger \mathbf{F}' + \mathbf{b}_i^\dagger \frac{\boldsymbol{\Delta}}{2} \mathbf{b}_i, \tag{7.78}$$

The reference system is parametrized by three real translationally-invariant parameters F', Δ_{00}, and Δ_{01}, where $\mathbf{F}' = (F', F')$ and $\boldsymbol{\Delta}(\tau - \tau') = \delta(\tau - \tau')\boldsymbol{\Delta}$ is instantaneous in imaginary time and site-local as

$$\boldsymbol{\Delta}(\tau - \tau') = \delta(\tau - \tau')[\delta_{ij} \otimes (\Delta_{00}\mathbf{1} + \Delta_{01}\sigma_x)]\,. \tag{7.79}$$

This reference system is therefore the disordered equivalent of the SFA3 reference system (Sec. 6.3), which yields quantitatively correct results for the clean BHm comparing with numerically exact QMC results (see Chapter 6).

In the case of uncorrelated disorder considered here, the disorder-averaging of observables [Eq. (7.31)] gives translationally invariant results, see Sec. 7.1.7. The disorder-averaged free energy of the SFA3 reference system is therefore given by

$$\Omega_{\mathbf{F}'\boldsymbol{\Delta}PU} = N\langle \Omega_{i,\mathbf{F}'\boldsymbol{\Delta}\eta_i U}\rangle_p \tag{7.80}$$

where N is the number of lattice sites, $\Omega_{i,\mathbf{F}'\boldsymbol{\Delta}\eta_i U}$ is the free energy of a single site in the reference system, and $\langle f(\eta)\rangle_p \equiv \int d\eta\, p(\eta) f(\eta)$. Analogously, the propagators are obtained as

$$\bar{\mathbf{G}}_{\mathbf{F}'\boldsymbol{\Delta}PU}(\tau - \tau') = \delta_{ij} \otimes \langle \mathbf{G}_{ii,\mathbf{F}'\boldsymbol{\Delta}\eta_i U}(\tau - \tau')\rangle_p\,, \tag{7.81}$$

$$\bar{\boldsymbol{\Phi}}_{\mathbf{F}'\boldsymbol{\Delta}PU} = \langle \boldsymbol{\Phi}_{i,\mathbf{F}'\boldsymbol{\Delta}\eta_i U}\rangle_p\,. \tag{7.82}$$

Hence, to evaluate the disorder-averaged quantities of the reference system it suffices to solve the single-site Hamiltonian of Eq. (7.78) for all possible values of η_i and then average the result over the probability distribution $p(\eta)$. The corresponding average self-energies $\bar{\mathbf{S}}_{\mathbf{F}'\Delta PU}$ and $\bar{\boldsymbol{\Sigma}}_{\mathbf{F}'\Delta PU}$ of the reference system are then obtained from Eqs. (7.35) and (7.36).

Physical solutions of the lattice system can be found by searching for stationary values of the SFT functional in Eq. (7.53) fulfilling Eq. (7.56) using a standard root solver to find the point with zero gradient. This procedure is identical to the algorithm detailed in Sec. 6.3.3.

7.2.2. Atomic limit

As in this work we mainly analyze the behavior of the disordered BHm at large interactions $U/J \gg 1$, we want to compare to the analytic atomic limit of having decoupled sites, i.e. $J = 0$. In this section we analyze the properties of the infinite system in this limit.

Local occupations

We start by analyzing the local occupations as a function of disorder in the atomic limit. For $J = 0$, we can have a local occupation $n_i = \langle \hat{n}_i \rangle$ at zero temperature if the local potential η_i takes values $\eta_{\min}(n_i) < \eta_i < \eta_{\max}(n_i)$. In order to derive this, we turn to the local energy of the

decoupled site i with occupation number n_i and local potential η_i, i.e.

$$E_{\mathrm{SS}}(n_i, \eta_i) = \frac{U}{2} n_i \left(n_i - 1\right) + \left(\eta_i - \mu\right) n_i, \tag{7.83}$$

The groundstate will have local occupation larger than $n_i - 1$ if $E_{\mathrm{SS}}(n_i, \eta_i) < E_{\mathrm{SS}}(n_i - 1, \eta_i)$, i.e. if

$$\eta_i < \eta_{\max}(n_i) = \begin{cases} \mu - U(n_i - 1) & \text{if } n_i > 0, \\ \infty & \text{if } n_i = 0, \end{cases} \tag{7.84}$$

where we used that the local occupation n_i is bounded from below by zero, and therefore $\eta_{\min}(0) = \infty$. Additionally, in order to have a local occupation of n_i we need to fulfill the condition $E_{\mathrm{SS}}(n_i, \eta_i) < E_{\mathrm{SS}}(n_i + 1, \eta_i)$, resulting in

$$\eta_i > \eta_{\min}(n_i) = \mu - U n_i. \tag{7.85}$$

As the minimum possible value of η_i is $-\Delta$ [see Eq. (7.75)], this implies that the maximal possible local occupation $n_{\max}$ is given by

$$n_{\max} = \left\lfloor \frac{\Delta + \mu}{U} + 1 \right\rfloor. \tag{7.86}$$

Furthermore, as the maximum value of η_i is Δ and the local occupation is bounded from below by $n_i = 0$, we have a minimal possible local occupation of

$$n_{\min} = \mathrm{Max}\left\{ \left\lceil \frac{\mu - \Delta}{U} \right\rceil, 0 \right\}. \tag{7.87}$$

We can use the information above to derive the probability of sites with occupation n in the infinite system. We denote this quantity by r_n, defined as the number of sites with local occupation n divided by the total number of sites, which can be computed by

$$r_n = \begin{cases} 0 \text{ if } n < n_{\min} \text{ or } n > n_{\max}, \\ \frac{1}{2\Delta} \left(\mathrm{Min}\left\{\Delta, \eta_{\max}(n)\right\} - \mathrm{Max}\left\{-\Delta, \eta_{\min}(n)\right\}\right) \text{ else.} \end{cases}$$

We can use the probabilities r_n in order to derive an expression for the total density n, given by

$$n = \sum_{m=0}^{\infty} r_m m, \tag{7.88}$$

and the interaction energy given by,

$$E_{\mathrm{int}} = \frac{U}{2} \sum_{m=0}^{\infty} r_m \left(m^2 - m\right). \tag{7.89}$$

Note that, while the values of r_n depend on the disorder distribution $P(\boldsymbol{\eta})$, the values of Δ where they become non-zero [and therefore the maximal and minimal possible occupations for a given disorder strength in Eqs. (7.86) and (7.87)] depend only on the maximal and minimal values of the local potential $\pm\Delta$ (and the global parameters μ and U). These are therefore universal, in the sense that they do not depend on the disorder distribution $P(\boldsymbol{\eta})$ as long as it is uncorrelated and bounded [i.e. with $p\left(|\eta_i| > \Delta\right) = 0$].

Local Excitations

On a single-site level, the process $(n_i \to n_i + 1)$ on site i leads to the energy difference

$$\Delta E\left[n_i \to n_i + 1\right] = U n_i - \mu + \eta_i. \tag{7.90}$$

As discussed in Sec. 7.2.2, in the groundstate we can have a local occupation of n_i only if $\eta_{\min}(n_i) \leq \eta_i \leq \eta_{\max}(n_i)$, see Eqs. (7.84) and (7.85). If we average over all sites i, we therefore find, that the local processes $(n_l \to n_l + 1)$, with local groundstate occupations n_l, span over the energy range given by

$$\Delta E\left[n_l \to n_l + 1\right] \geq \mathrm{Max}\left\{0, U n_l - \mu - \Delta\right\}, \tag{7.91}$$

and

$$\Delta E\left[n_l \to n_l + 1\right] \leq \begin{cases} \Delta - \mu \text{ if } n_l = 0, \\ \mathrm{Min}\left\{U, U n_l - \mu + \Delta\right\} \text{ else.} \end{cases} \tag{7.92}$$

We can further derive the energy difference for the opposite process in the same way, yielding

$$\Delta E\left[n_l + 1 \to n_l\right] \geq \mathrm{Max}\left\{0, \mu - \Delta - U n_l\right\}, \tag{7.93}$$

and

$$\Delta E\left[n_l + 1 \to n_l\right] \leq \mathrm{Min}\left\{U, \mu + \Delta - U n_l\right\}. \tag{7.94}$$

The disorder-averaged local spectral function is defined as

$$A_{\mathrm{loc}}(\omega) = -\frac{1}{N\pi} \sum_i \mathrm{Im}\left[\bar{G}_{ii}(\omega)\right]. \tag{7.95}$$

At zero temperature we have

$$G_{ii,\boldsymbol{\eta}}(\omega) = \sum_{n \neq \mathrm{GS}} \left(\frac{\left|\left\langle n \left| b_i^\dagger \right| \mathrm{GS} \right\rangle\right|^2}{E_{\mathrm{GS}} - E_n + \omega^+} + \frac{\left|\left\langle n \left| b_i \right| \mathrm{GS} \right\rangle\right|^2}{E_{\mathrm{GS}} - E_n - \omega^+} \right),$$

where GS is the groundstate, the sum runs over all other eigenstates, E_n is the energy of eigenstate n, and $\omega^+ = \omega + i\epsilon$ with a small broadening parameter ϵ. Disorder-averaging over infinite configurations therefore yields a translational invariant local Green's function

$$\bar{G}_{ii}(\omega) = \int_{-\Delta}^{\Delta} d\eta p(\eta) \left(\frac{\tilde{n}(\eta) + 1}{\omega^+ - \Delta E\left[\tilde{n}(\eta) \to \tilde{n}(\eta) + 1\right]} + \frac{\tilde{n}(\eta)}{\Delta E\left[\tilde{n}(\eta) - 1 \to \tilde{n}(\eta)\right] - \omega^+} \right), \tag{7.96}$$

where

$$\tilde{n}\left(\eta_{\min}(n) < \eta < \eta_{\max}(n)\right) = n. \tag{7.97}$$

Using Eqs. (7.91-7.97) we therefore find that the resonances of the spectral function for the processes $(n \to n+1)$ are bounded by Eqs. (7.91) and (7.92), while the processes $(n+1 \to n)$ are bounded by Eqs. (7.93) and (7.94). Therefore, the effect of the disorder strength Δ on the spectral function in the atomic limit – which in the absence of disorder consists of sharp delta peaks – is to broaden the peaks to a width which is proportional to Δ. A consequence of this is that, apart from the process $(0 \to 1)$, all local resonances are bounded by $-U \leq \omega \leq U$. Further, it can easily be shown that for $\Delta \geq mU/2$, with integer m, we have $\omega_{\max}(n \to n+1) > \omega_{\min}(n+m \to n+m+1)$, leading to an overlap of the processes $(n \to n+1)$ and $(n+m \to n+m+1)$ (and equivalently for the reversed particle-removal processes).

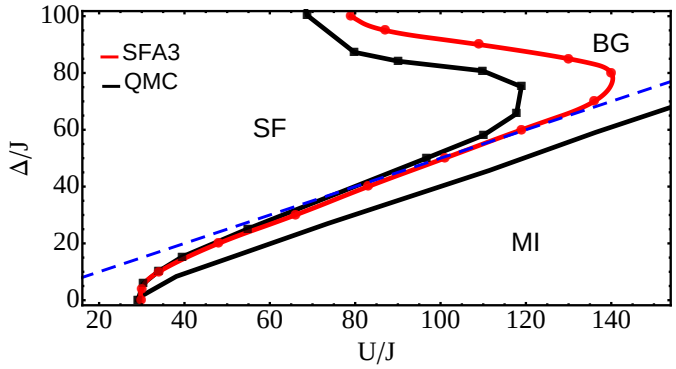

Figure 7.1.: Groundstate phase diagram of the disordered BHm with box disorder at fixed density $n = 1$ and large interaction strength U/J. The SFA3 results on the superfluid to Bose glass transition are shown in red, while the QMC results (black squares) are taken from Ref. [15]. The blue dashed line indicates the point where doubly occupied sites are activated in the atomic limit. See Fig. 2.2 for the full groundstate phase diagram.

7.3. Results

We analyze the BHm with box disorder using SFT with an SFA3 reference system, see Sec. 7.2.1. The calculations are compared to disorder-averaged path integral quantum Monte Carlo (QMC) [49, 87, 15] simulations on a finite cubic lattice of 8^3 sites. In the strongly-interacting case we further compare to analytic results in the atomic limit (i.e. the limit of zero hopping $J = 0$), detailed in Sec. 7.2.2. The resulting groundstate phase diagram computed with SFA3 at large interactions for fixed density $n = 1$ is shown in Fig. 7.1 together with the QMC results of Ref. [15]. The groundstate phases exhibited by the system are the superfluid, the Mott insulator, and the Bose glass. For the ordered BHm ($\boldsymbol{\eta} = \mathbf{0}$), the SFA3 approximation showed remarkable agreement with exact QMC results (see Chapter 6). The phase diagram in Fig. 7.1 shows that this remains true also for weak disorder $\Delta/J \lesssim 30$, where the SFA3 superfluid to Bose glass transition line shows excellent agreement with the QMC result.

For stronger disorder the situation changes, in particular in the so-called *superfluid finger*, i.e., the narrow region of the superfluid phase extending to large values of the interaction strength U/J. In the finger, the condensate density $\rho_c = \frac{1}{2}\bar{\Phi}^\dagger\bar{\Phi}$ is extremely low, and therefore very hard to resolve experimentaly [15]. Small deviations from numerically exact results in the SFA3 calculations therefore lead to a notable shift in the phase boundaries and an overestimation of the extent of the superfluid finger, as seen in Fig. 7.1. At even larger disorder when leaving the superfluid finger, the discrepancy between SFA3 and QMC results is reduced. The Mott insulator to Bose glass transition at fixed density $n = 1$ is very hard to resolve numerically (unlike the transition at fixed chemical potential discussed later), as the finite compressibility in the Bose glass close to the phase boundary is exponentially small [15]. Instead, in Fig. 7.1 we show analytic results on the phase boundary from Ref. [15].

7.3.1. Strongly-interacting Bose glass phase

Using the local occupation probabilities r_n of Sec. 7.2.2, it is possible to distinguish different regimes of the Bose glass in the atomic limit: coming from the Mott-insulating groundstate at density $n = 1$ (where $r_{n\neq 1} = 0$) and increasing the disorder strength Δ, as we enter the Bose glass either r_0 or r_2 become non-zero, as either empty or doubly-occupied sites are activated by the disorder depending on the value of the chemical potential. When the disorder is increased

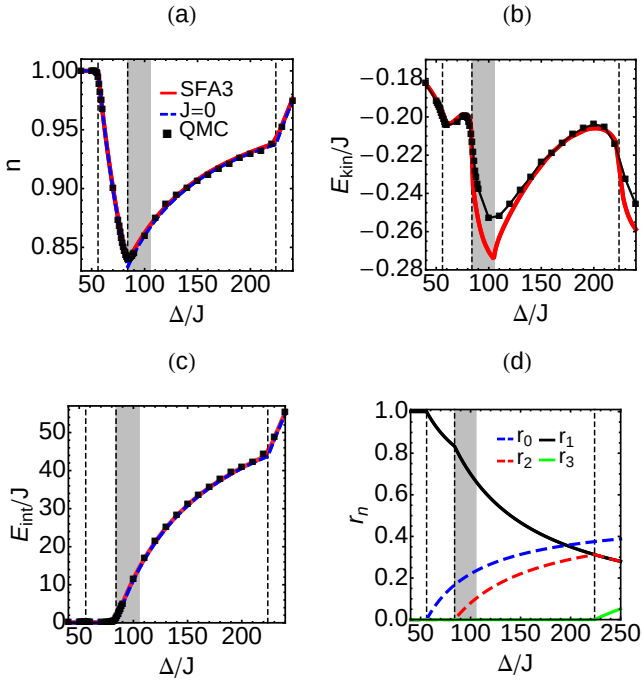

Figure 7.2.: Observables of the disordered BHm as a function of disorder strength Δ/J for $U/J = 140$, $\mu/U = 0.4$ and $T/J = 0.1$. (a) Density n computed with SFA3 (red), QMC (black squares), and in the atomic limit ($J = 0$, blue dashed). (b) Kinetic energy per site E_{kin}/J computed with SFA3 (red), and QMC (black squares). (c) Interaction energy per site E_{int}/J computed with SFA3 (red), QMC (black squares), and in the atomic limit ($J = 0$, blue dashed). (d) Probabilities of having sites with local occupation 0 (r_0, blue dashed), 1 (r_1, black), 2 (r_2, red dashed), and 3 (r_3, green), as computed in the atomic limit. The vertical dashed lines show the transitions between the different regimes in the atomic limit, while the grey area is where the non-local Green's function of SFA3 develops a pole, indicating the presence of isolated quasi-condensates.

further, also higher occupancies are activated and other probabilities r_n become non-zero.

While the atomic limit shows sharp transitions between the different regimes (see the values of r_n in Fig. 7.2d), for finite hopping J or temperature T, the kinetic fluctuations turn the transitions into crossovers. Nonetheless, for the sweep in disorder strength of Fig. 7.2 the results for local quantities such as the density (Fig. 7.2a) and the interaction energy (Fig. 7.2c) show perfect agreement between the analytic results in the atomic limit and both SFA3 and QMC results, except right at the transition/crossover between the different regimes. In fact, the kinetic energy (Fig. 7.2b) – which is the dominating additional contribution of the finite hopping in SFA3 and QMC, as compared to the atomic limit – is orders of magnitude smaller than the interaction energy at large disorder. In the following we will discuss these different strongly-interacting regimes in more detail, analyzing the qualitative behavior of the observables in Fig. 7.2 and extracting additional information from the corresponding local spectral functions $A_{\text{loc}}(\omega)$ shown in Fig. 7.3.

We start at $\Delta = 0$, i.e., in the non-disordered Mott insulator. As every site has the same local occupation $n_i = 1$, the local spectral function (Fig. 7.3b) is characterized by the two Hubbard bands corresponding to the transitions $(1 \to 0)$ at negative frequencies and $(1 \to 2)$ at positive frequencies. While in the atomic limit these resonances would correspond to delta-peaks, at finite hopping the shape of the spectral function depends on the non-interacting dispersion and

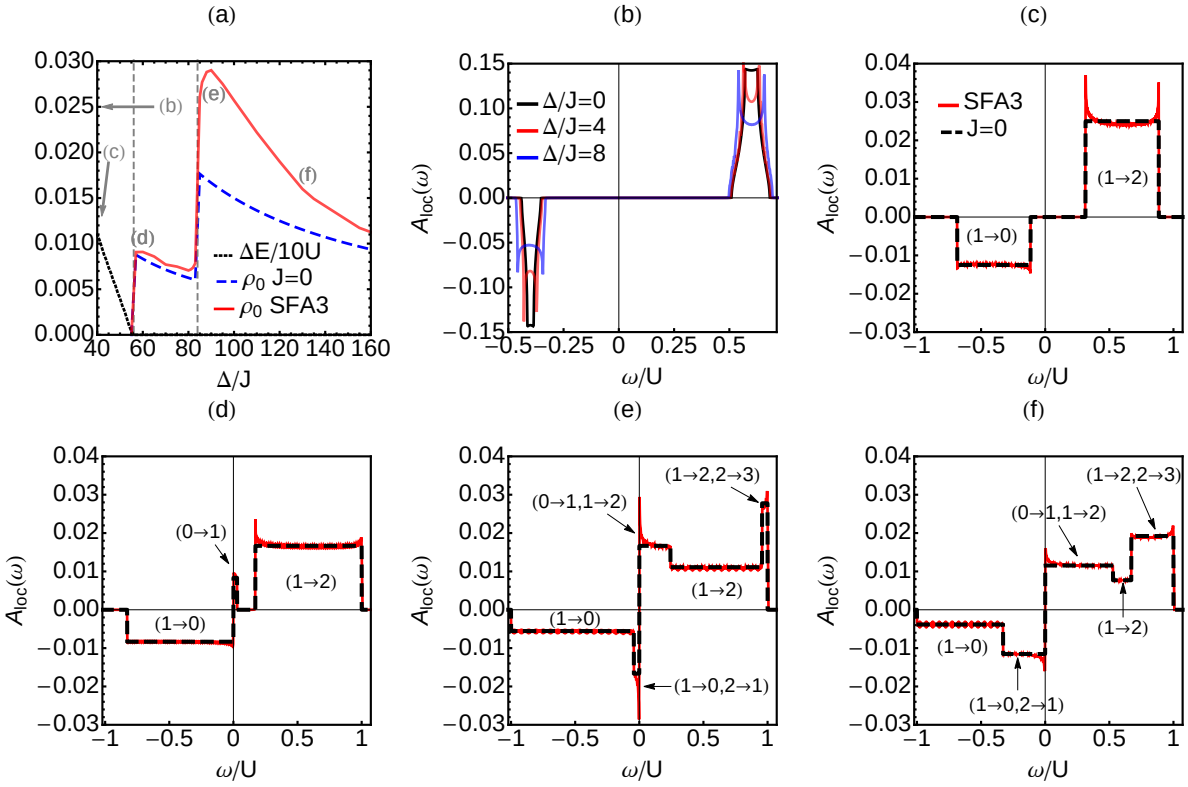

Figure 7.3.: Properties of the local spectral function of the disordered BHm as a function of disorder strength Δ/J for $U/J = 140$, $\mu/U = 0.4$ and $T/J = 0.1$. (a) Mott gap [black dotted, renormalized as $\Delta E/(10U)$ for plotting purposes], and spectral weight around $\omega = 0$, ρ_0 [see Eq. (7.98)] computed with SFA3 (red) and in the atomic limit (blue dashed). (b) Local spectral function for $\Delta/J = 0$ (black), $\Delta/J = 4$ (red), and $\Delta/J = 8$ (blue). (c-f) Local spectral functions computed with SFA3 (red) and in the atomic limit (black dashed) for $\Delta/J = 40$ (c), $\Delta/J = 60$ (d), $\Delta/J = 90$ (e), and $\Delta/J = 130$ (f). The involved transitions from local occupation x to local occupation y are denoted as $(x \to y)$.

its bandwidth $W = 2zJ$, where $z = 6$ is the coordination number of the lattice. In particular, the unit filling Mott insulator lower and upper Hubbard bands have the bandwidths W and $2W$ respectively, see Ref. [146] for a derivation. For weak disorder $\Delta < W$ the qualitative behavior remains the same. However, the Hubbard bands are broadened by the finite disorder strength Δ and the spectral weight at the center of the bands is reduced, see Fig. 7.3b.

The situation changes when $\Delta > W$ (see Fig. 7.3c), where the spectral function is more similar to the one predicted by the atomic limit: as discussed in Sec. 7.2.2, the width of the Hubbard bands now is fully determined by the disorder strength Δ, and the dispersive features of the spectral function are lost. As we are still in the Mott phase, the spectral function shows a finite gap, defined as the minimal distance between the Hubbard bands and $\omega = 0$. As the disorder strength Δ is increased, so does the kinetic energy (see Fig. 7.2b), due to increasing kinetic fluctuations, while the gap of the spectral function decreases (see Fig. 7.3a).

At $\Delta \approx \mu$ ($\Delta/J \approx 56$) the gap goes to zero, and we enter the Bose glass phase. The disorder activates empty sites (i.e. $r_0 > 0$, see Fig. 7.2d), and as a consequence the density drops (Fig. 7.2a), while the kinetic fluctuations decrease (Fig. 7.2b). The lower Hubbard band now extends to $\omega = 0$, and we find a finite spectral weight at small positive frequencies corresponding to the local excitation $(0 \to 1)$ of the unoccupied sites (see Fig. 7.3d). In order to study trends in the

spectral weight at zero frequency $\omega = 0$, we introduce the spectral weight measure

$$\rho_0 \equiv \frac{1}{2}\left(|A_{\mathrm{loc}}(\omega = \delta)| + |A_{\mathrm{loc}}(\omega = -\delta)|\right), \tag{7.98}$$

where $\delta = 0.002U$. As shown in Fig. 7.3a, in this first regime of the Bose glass, the spectral weight ρ_0 for finite hopping is very close to the atomic limit result. In fact, the spectral function (Fig. 7.3d) only differs from the atomic limit result at the edges of the upper Hubbard band, corresponding to the excitation $(1 \to 2)$, indicating a strong localization around empty sites with large values of η_i.

The situation changes abruptly for $\Delta \gtrsim U - \mu$ ($\Delta/J \gtrsim 84$). As doubly occupied sites are activated by the disorder (see Fig. 7.2d), the density increases (Fig. 7.2a), and so does the kinetic energy (Fig. 7.2b), indicating an increase of non-local kinetic processes. The additional doublons lead to a substantail increase in interaction energy (Fig. 7.2c), which dominates over the kinetic energy. One would therefore naively expect a better agreement between the spectral functions computed with SFA3 and in the atomic limit. This is however not the case for the spectral weight around zero frequency ρ_0 which increases abruptly at $\Delta/J \approx 84$, see Fig. 7.3a, deviating markedly from the atomic limit prediction. The appearance of doubly-occupied sites in the atomic limit drives additional excitations $(2 \to 1)$ and $(2 \to 3)$ in the spectral function (Fig. 7.3e), which overlap with other excitations, leading to additional "bands" composed of multiple resonating excitations, see e.g. $(1 \to 0, 2 \to 1)$ at low negative frequencies in Fig. 7.3e.

It is at the edges of these new "bands" that the spectral function is strongly peaked showing a considerable difference with respect to the atomic-limit spectral function, indicating delocalization of quasi-particles and quasi-holes in the vicinity of the rare sites with occupation $n > 1$ (i.e. occupation 2 in the atomic limit). However, in the Bose glass discussed here, there is no global superfluid response, as the sites contributing to these peaks are rare. Instead the physics are described by the notion of isolated superfluid lakes [15] around rare sites with particularly low local potential.

In this regime (denoted by the grey area in Fig. 7.2), the non-local Green's function of SFA3 develops a simple pole at zero Matsubara frequency, which can be integrated out when computing local quantities such as the local Green's function, see Appendix A.6 for details. Whence, the self-energy functional and local observables can still be evaluated in this regime. In a homogeneous system, such a pole would indicate an instability towards spontaneous $U(1)$-symmetry-breaking and the particles would condense. Here, however, it is only the rare sites with $n > 1$ that contribute to the pole, not allowing for a global condensate. The pole therefore implies the presence of isolated quasi-condensates on the lattice, which can have different $U(1)$ phases and therefore do not allow for global phase-coherence (i.e. a finite superfluid response). These highly non-local processes in the vicinity of a superfluid phase transition cannot be expected to be fully captured by the self-energies of a local reference system with translationally invariant variational parameters, leading to a deviation in the SFA3 kinetic energy with respect to the numerically exact QMC data in Fig. 7.2b. This was also the case in close proximity to phase transitions in SFT (see Chapter 6) and BDMFT [65, 67] calculations in the clean BHm.

For even stronger disorder, the situation changes when the number of doubly occupied sites in the atomic limit (proportional to r_2 in Fig. 7.2d) increases further: the background containing more and more strongly interacting doublons (see the increase of interaction energy in Fig. 7.2c) makes it harder for particles to delocalize. This can be observed in the kinetic energy of Fig. 7.2b, which decreases again as the particles localize. The same behavior can also be seen in the spectral function of Fig. 7.3f, where the bands involving highly occupied sites increase in width, but are much closer to the atomic limit results. The zero frequency spectral weight ρ_0 decreases accordingly, as shown in Fig. 7.3a.

When the disorder is strong enough to activate triplon occupancies, the behaviour changes once

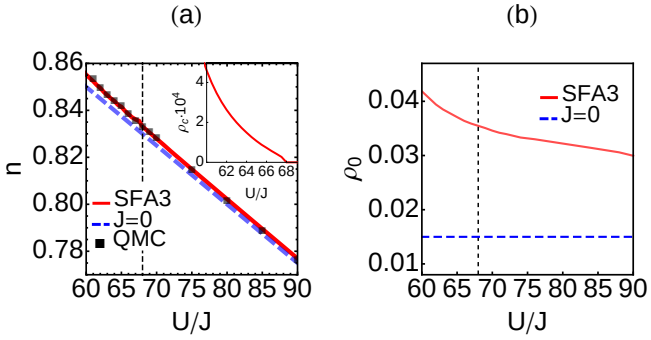

Figure 7.4.: Strongly-interacting superfluid to Bose glass phase transition at $\Delta/J = 100$, $\mu/U = 0.25$ and $T/J = 0.1$. (a) Density n and condensate-density ρ_c (inset, rescaled by 10^4) as a function of U/J computed with SFA3 (red), QMC (black squares) and in the atomic limit (blue dashed). (b) Spectral weight around $\omega = 0$, ρ_0 [see Eq. (7.98)], as a function of U/J computed with SFA3 (red) and in the atomic limit (blue dashed). The vertical dashed line indicates the phase transition between the superfluid and the Bose glass phase in SFA3.

more. The kinetic energy (Fig. 7.2b) increases as the particles delocalize around the rare triply occupied sites, and so does the interaction energy (Fig. 7.2c). The number of doubly occupied sites on the other hand decreases and $r_2 = r_1$ (see Fig. 7.2d). This behavior arises naturally from the probabilities r_n of Sec. 7.2.2: while the number of unoccupied sites is unbounded, once $\Delta > \eta_{\max}(n)$ and $\Delta > -\eta_{\min}(n)$, the probability of finding a site with local occupation $n > 0$ is given by the particle-number-independent value $r_n = U/2\Delta$.

In summary, our results show that at fixed interaction U/J (and chemical potential μ/U) the strongly interacting Bose glass as a function of Δ is described by the subsequent activation of local occupations n. As these occupations accumulate, the interaction energy increases, driving the phase towards the atomic limit. This is however not the case every time these sites are very rare (i.e. if $0 < r_n \ll 1$ for some local occupation $n > 0$): in this case the particles tend to delocalize and form superfluid lakes [15] around the rare highly occupied sites.

7.3.2. Strongly-interacting phase transition

The regime where the Bose glass exhibits superfluid lakes around doubly occupied sites surrounds the superfluid finger at large interactions in the phase diagram of Fig. 7.1. In fact, the lower edge of the superfluid finger strongly correlates with the line where doubly-occupied sites are activated in the atomic limit (see blue dashed line in Fig. 7.1). The strongly-interacting phase transition at fixed chemical potential is illustrated in Fig. 7.4, where we show the superfluid to Bose glass phase transition as a function of U/J at fixed chemical potential $\mu/U = 0.25$ and disorder strength $\Delta/J = 100$. With decreasing interaction U/J, these superfluid lakes percolate and resonances between the low-energy excitations $(0 \to 1)$ and $(1 \to 2)$ on neighboring sites (and between the corresponding particle-removal processes, see e.g. Fig. 7.3e) favour the spontaneous breaking of $U(1)$-symmetry through a homogeneous condensate. The particles therefore eventually condense, driving the transition to the superfluid phase. As the sites contributing to the resonating low-energy excitations remain relatively rare, the condensate fraction and the correction of the density with respect to the atomic limit close to the phase transition are extremely low (with a condensate density on the order of 10^{-4}, see inset of Fig. 7.4a).

At density $n \approx 1$ and larger disorder strength, the increase of highly occupied sites is compensated by a proliferation of empty sites (see e.g. Fig. 7.2d). Thus, the probability of having neighboring sites with occupations n and $n + 1$ [and thereby of having resonances between the

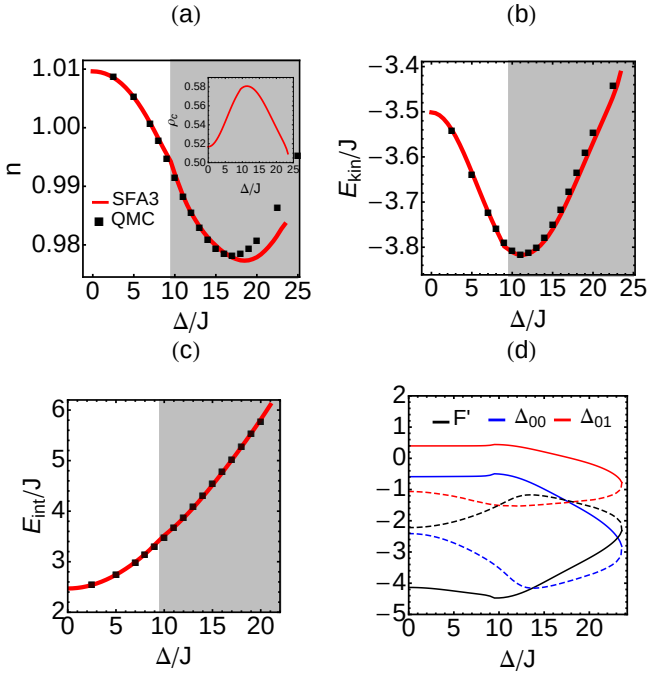

Figure 7.5.: (a-c) Observables of the disordered BHm in the superfluid phase for $U/J = 20$, $\mu/U = 0.35$ and $T/J = 0.1$, computed with SFA3 (red) and QMC (black squares). (a) Density n and condensate density ρ_c (inset) as a function of disorder strength Δ/J. (b) Kinetic energy per site E_{kin}/J as a function of disorder strength Δ/J. (c) Interaction energy per site E_{int}/J as a function of disorder strength Δ/J. The grey area indicates the region where the non-local Green's function of SFA3 develops a pole. (d) Variational parameters of the SFA3 calculation, F' (black), Δ_{00} (blue) and Δ_{01} (red), as a function of disorder strength Δ/J. The solid lines indicate the stationary solution corresponding to panels (a-c), while the dashed line shows a metastable solution.

processes $(n \to n+1)$ and $(n+1 \to n+2)$] decreases, making the spontaneous breaking of $U(1)$-symmetry less likely. The increased interaction energy and particle number fluctuations therefore suppress the superfluid phase, explaining the reentrant behavior of the superfluid finger at larger disorder (see Figs. 7.1 and 2.2).

7.3.3. Superfluid phase

We now turn to lower interactions, i.e. deeper into the superfluid phase away from the superfluid finger. If U/J is lower than the critical value of the clean system, the condensate density is much larger than in the superfluid finger, and the uncondensed background is no longer well described by the atomic limit.

In Fig. 7.5 we show a sweep of the thermodynamical observables as a function of Δ/J deep in the superfluid phase at $U/J = 20$ and $\mu/U = 0.35$. At low disorder SFA3 shows excellent agreement with QMC, as the condensate density increases and the density decreases as a function of disorder (Fig. 7.5a). As a consequence of the larger condensate fraction, the magnitude of the kinetic energy increases as well (Fig. 7.5b). The interaction energy increases throughout the entire parameter range $0 \leq \Delta/J \leq 25$, indicating increasing spatial particle number fluctuations (Fig. 7.5c).

When the disorder becomes comparable to the single-particle bandwidth $W = 2zJ$, these

fluctuations reverse the trend of the condensate density which starts to decrease as a function of Δ/J. It is at this point that also the kinetic energy starts to decrease and the non-local connected Green's function develops a pole at zero Matsubara frequency (see Appendix A.6). As in the Bose glass (see Sec. 7.3.1), the pole indicates the appearance of additional isolated quasi-condensates in the system: this is most likely related to the disorder inducing rare regions, explaining the decrease in condensate density and kinetic energy, and leading to a glassy behavior in the superfluid.

Eventually, deeper in the glassy regime of the superfluid where the disorder dominates over both the interaction and the single-particle bandwidth, our SFA3 approach of having translationally-invariant variational parameters on the reference system becomes too simple to fully capture the groundstate behavior. In fact, the SFA3 results start to deviate from the QMC results, see Fig. 7.5a. As shown in Fig. 7.5d, eventually at $\Delta/J \approx 2W$ the variational parameters of the stationary SFA3 solution join with a metastable solution with higher free energy through a saddle-node bifurcation [138], vanishing for larger disorder.

A possibility to get around this problem, may be the introduction of a spatially modulated symmetry-breaking field on the reference system, as was also done in stochastic mean-field theory [150, 16]. In SFT, this would however involve the inversion of a non-translationally-invariant connected Green's function, limiting us to very small system sizes, while we here want to analyze the thermodynamic limit.

Part III.

Reciprocal cluster mean-field theory

8

Derivation and benchmarking

The cluster Gutzwiller mean-field method (CGMF) [77, 104] discussed in Sec. 4.3 enables the (perturbative) treatment of systems with non-trivial unit-cells by treating short-distance non-local correlations within a given cluster size exactly. However, as argued in Sec. 4.3, it breaks the translational invariance of the lattice by applying the mean-field decoupling approximation only to the hopping-terms at the boundary of the cluster, while the hopping terms within the cluster are treated exactly. The simplest case where this can be observed is when the symmetry-breaking field is zero, reducing the lattice to a set of decoupled clusters with open boundaries. This violation of translational invariance breaks the symmetries of the dispersion and thereby e.g. its topological properties. In order to mitigate such artifacts we develop a mean-field decoupling based on the concept of momentum coarse-graining, introduced in the context of the dynamical cluster approximation [79].

We term this method as "reciprocal cluster mean field" (RCMF). It is defined in the thermodynamic limit and variationally approaches both condensed and uncondensed phases in models with multiorbital unit-cells and non-trivial dispersions, while preserving the translational symmetry of the lattice. For topologically trivial translationally-invariant systems it yields more accurate results than the previous mean-field methods discussed in Chapter 4, and it is well-suited for cases where the underlying symmetries of the dispersion are indispensable to understand the physical properties, such as, e.g., topological insulators. See Appendix B.1 for a detailed comparison between RCMF and CGMF. This chapter closely follows Ref. [3] and is organized as follows. In Sec. 8.1 we derive the effective RCMF Hamiltonian, while the self-consistency is discussed in Sec. 8.2. Finally, in Sec. 8.3 we benchmark the method.

8.1. Effective Hamiltonian

In this section we will illustrate the procedure to derive RCMF for a two-dimensional system, although the same procedure can also be applied to Hamiltonians of different dimensions. Within RCMF, a locally interacting bosonic lattice Hamiltonian in the thermodynamic limit is decoupled into a set of identical clusters with size $N_c \times M_c$ through a combination of momentum coarse-graining [79] and the mean-field decoupling approximation [9] (see Sec. 4.2).

To illustrate our procedure let us first start from a general non-interacting hopping Hamiltonian

$$H_0 = \sum_{x',y'} \sum_{x,y} t_{(x',\,y'),(x,\,y)} b^\dagger_{\mathrm{x'},\mathrm{y'}} b_{\mathrm{x},\mathrm{y}} = \sum_{k,q} \epsilon_{\mathrm{k},\mathrm{q}} b^\dagger_{\mathrm{k},\mathrm{q}} b_{\mathrm{k},\mathrm{q}} \tag{8.1}$$

with hopping amplitudes $t_{(x',\,y'),(x,\,y)}$ in position-space and dispersion $\epsilon_{\mathrm{k},\mathrm{q}}$ in reciprocal space. As in the dynamical cluster approximation [79], the main idea of RCMF consists in projecting the $N \times M$ lattice system onto a lattice of $N_c \times M_c$ clusters (later we will take $N, M \to \infty$, but the method is also well-defined for finite systems). Each cluster is spanned by the internal cluster

coordinates X and Y, such that we can decompose the position coordinates x and y on the lattice into

$$x = X + \tilde{x},\ y = Y + \tilde{y},$$

where $\tilde{x}$ and $\tilde{y}$ are inter-cluster coordinates. In the same way the momenta in x and y-direction – k and q, respectively – are decomposed as

$$k = K + \tilde{k},\ q = Q + \tilde{q},$$

where K and Q are the cluster momenta in reciprocal space. Through a partial Fourier transform, the creation and annihilation operators in reciprocal space can be written in the mixed representation

$$b_{K+\tilde{k},Q+\tilde{q}} = \frac{\sqrt{N_c M_c}}{\sqrt{NM}} \sum_{\tilde{x},\tilde{y}} e^{-i(\tilde{k}\tilde{x}+\tilde{q}\tilde{y})} b_{\mathrm{K,Q}}(\tilde{x},\tilde{y}), \tag{8.2}$$

where $b_{\mathrm{K,Q}}(\tilde{x},\tilde{y})$ annihilates a boson with cluster-momenta K and Q on the cluster located at $(\tilde{x},\tilde{y})$ [79].

The central idea of the momentum coarse-graining consists of projecting the dispersion of the lattice $\epsilon_{\mathrm{k,q}}$ onto the clusters in reciprocal space. This can be done by a partial Fourier transform of the dispersion onto the subspace of cluster-local hopping processes, giving the intra-cluster dispersion $\bar{\epsilon}_{\mathrm{K,Q}}$ as

$$\bar{\epsilon}_{\mathrm{K,Q}} = \frac{N_c M_c}{NM} \sum_{\tilde{k},\tilde{q}} \epsilon_{K+\tilde{k},Q+\tilde{q}}, \tag{8.3}$$

representing hopping processes within the cluster, while the remainder $\delta\epsilon_{\mathrm{K},\,\tilde{k},\mathrm{Q},\,\tilde{q}} = \epsilon_{K+\tilde{k},Q+\tilde{q}} - \bar{\epsilon}_{\mathrm{K,Q}}$ represents all other hopping processes between different clusters [79].

Now we can decompose the Hamiltonian of Eq. (8.1) into

$$H_0 = H_{\mathrm{c}} + \Delta H, \tag{8.4}$$

where, using Eq. (8.2), the part H_{c} is cluster-local,

$$H_{\mathrm{c}} = \sum_{\tilde{k},\tilde{q}} \sum_{K,Q} \bar{\epsilon}_{\mathrm{K,Q}} b^{\dagger}_{\mathrm{K}+\tilde{k},\mathrm{Q}+\tilde{q}} b_{\mathrm{K}+\tilde{k},\mathrm{Q}+\tilde{q}} = \sum_{\tilde{x},\tilde{y}} \sum_{K,Q} \bar{\epsilon}_{\mathrm{K,Q}} b^{\dagger}_{\mathrm{K,Q}}(\tilde{x},\tilde{y}) b_{\mathrm{K,Q}}(\tilde{x},\tilde{y}),$$

while ΔH contains the coupling between different clusters

$$\begin{aligned} \Delta H &= \sum_{\tilde{k},\tilde{q}} \sum_{K,Q} \delta\epsilon_{\mathrm{K},\,\tilde{k},\mathrm{Q},\,\tilde{q}} b^{\dagger}_{K+\tilde{k},Q+\tilde{q}} b_{K+\tilde{k},Q+\tilde{q}} \\ &= \sum_{K,Q} \sum_{\tilde{x},\tilde{y}} \sum_{\tilde{x}',\tilde{y}'} \delta\epsilon_{\mathrm{K,Q}}(\tilde{x}-\tilde{x}',\tilde{y}-\tilde{y}') b^{\dagger}_{\mathrm{K,Q}}(\tilde{x},\tilde{y}) b_{\mathrm{K,Q}}(\tilde{x}',\tilde{y}'), \end{aligned} \tag{8.5}$$

where in the second line we introduced the mixed representation of $\delta\epsilon_{\mathrm{K},\,\tilde{k},\mathrm{Q},\,\tilde{q}}$,

$$\delta\epsilon_{\mathrm{K,Q}}(\tilde{x},\tilde{y}) = \sum_{\tilde{k},\tilde{q}} e^{i(\tilde{k}\tilde{x}+\tilde{q}\tilde{y})} \delta\epsilon_{\mathrm{K},\,\tilde{k},\mathrm{Q},\,\tilde{q}}.$$

Our goal is to derive an effective Hamiltonian which is cluster local through a mean-field decoupling approximation of ΔH. To this end we decompose the creation/annihilation operators into their static expectation values $\phi_{\mathrm{K,Q}}(\tilde{x},\tilde{y}) = \langle b_{\mathrm{K,Q}}(\tilde{x},\tilde{y})\rangle$ and fluctuations δb, i.e.

$$b_{\mathrm{K,Q}}(\tilde{x},\tilde{y}) = \phi_{\mathrm{K,Q}}(\tilde{x},\tilde{y}) + \delta b_{\mathrm{K,Q}}(\tilde{x},\tilde{y}). \tag{8.6}$$

This approach decomposes ΔH into three separate parts

$$\Delta H = \Delta H_\phi + H_\phi + H_\delta,$$

where ΔH_ϕ is linear in b, and $b^\dagger$,

$$\Delta H_\phi = \sum_{K,Q} \sum_{\tilde{x},\tilde{y}} \sum_{\tilde{x}',\tilde{y}'} \delta\epsilon_{\mathrm{K,Q}}(\tilde{x}-\tilde{x}',\tilde{y}-\tilde{y}') \left(b^\dagger_{\mathrm{K,Q}}(\tilde{x},\tilde{y})\phi_{\mathrm{K,Q}}(\tilde{x}',\tilde{y}') + \phi^*_{\mathrm{K,Q}}(\tilde{x},\tilde{y}) b_{\mathrm{K,Q}}(\tilde{x}',\tilde{y}') \right),$$

H_ϕ is the constant contribution

$$H_\phi = -\sum_{K,Q} \sum_{\tilde{x},\tilde{y}} \sum_{\tilde{x}',\tilde{y}'} \delta\epsilon_{\mathrm{K,Q}}(\tilde{x}-\tilde{x}',\tilde{y}-\tilde{y}') \phi^*_{\mathrm{K,Q}}(\tilde{x},\tilde{y}) \phi_{\mathrm{K,Q}}(\tilde{x}',\tilde{y}'),$$

and H_δ contains all quadratic fluctuations

$$H_\delta = \sum_{K,Q} \sum_{\tilde{x},\tilde{y}} \sum_{\tilde{x}',\tilde{y}'} \delta\epsilon_{\mathrm{K,Q}}(\tilde{x}-\tilde{x}',\tilde{y}-\tilde{y}') \delta b^\dagger_{\mathrm{K,Q}}(\tilde{x},\tilde{y}) \delta b_{\mathrm{K,Q}}(\tilde{x}',\tilde{y}').$$

The standard procedure of the mean-field decoupling approximation consists in neglecting quadratic fluctuations (see Sec. 4.2), i.e. $H_\delta \approx 0$. Furthermore, we assume translational invariance between the different clusters

$$\phi_{\mathrm{K,Q}}(\tilde{x},\tilde{y}) = \phi_{\mathrm{K,Q}}. \tag{8.7}$$

By $\sum_{\tilde{x},\tilde{y}} \delta\epsilon_{\mathrm{K,Q}}(\tilde{x},\tilde{y}) = \delta\epsilon_{\mathrm{K,\,0,Q,\,0}}$, this reduces the cluster-coupling part of the Hamiltonian to

$$\begin{aligned}
\Delta H &\approx \sum_{\tilde{x},\tilde{y}} \left(\Delta H_{\tilde{x},\tilde{y}} + C_\phi \right), \\
\Delta H_{\tilde{x},\tilde{y}} &= \sum_{K,Q} \delta\epsilon_{\mathrm{K,\,0,Q,\,0}} \left(b^\dagger_{K,Q}(\tilde{x},\tilde{y}) \phi_{K,Q} + \phi^*_{K,Q} b_{K,Q}(\tilde{x},\tilde{y}) \right),
\end{aligned}$$

with a constant scalar shift C_ϕ, which for simplicity in the following will be omitted in the Hamiltonian (but has to be taken into account for the free energy), given by

$$C_\phi = -\sum_{K,Q} \delta\epsilon_{\mathrm{K,\,0,Q,\,0}} \left| \phi_{K,Q} \right|^2. \tag{8.8}$$

The system now consists of $(NM)\,/\,(N_c M_c)$ identical decoupled clusters with individual Hamiltonians

$$H_{\tilde{x},\tilde{y}} = \sum_{K,Q} \bar{\epsilon}_{\mathrm{K,Q}} b^\dagger_{\mathrm{K,Q}}(\tilde{x},\tilde{y}) b_{\mathrm{K,Q}}(\tilde{x},\tilde{y}) + \Delta H_{\tilde{x},\tilde{y}},$$

which, after a Fourier transform to position space, and dropping the $(\tilde{x},\tilde{y})$-notation, yields the effective mean-field Hamiltonian

$$H_{\mathrm{eff}} = \sum_{X',Y'} \sum_{X,Y} \bar{t}_{(X',Y'),(X,Y)} b^\dagger_{X',\,Y'} b_{X,\,Y} + \sum_{X,Y} \left(b^\dagger_{X,\,Y} F_{X,\,Y} + F^*_{X,\,Y} b_{X,\,Y} \right),$$

where the symmetry breaking field $F_{X,\,Y}$ is given by

$$F_{X,\,Y} = \sum_{X',Y'} \delta t_{(X,Y),(X',Y')} \phi_{X',\,Y'} \tag{8.9}$$

and

$$\bar{t}_{(X',Y'),(X,Y)} = \frac{1}{N_c M_c} \sum_{K,Q} e^{i\left(K\left(X'-X\right)+Q\left(Y'-Y\right)\right)} \bar{\epsilon}_{K,Q},$$
$$\delta t_{(X',Y'),(X,Y)} = t_{(X',Y'),(X,Y)} - \bar{t}_{(X',Y'),(X,Y)}. \tag{8.10}$$

If instead of a pure hopping Hamiltonian, the Hamiltonian also includes local (interaction) terms, e.g.

$$H^{'} = H_0 + H_{\text{int}} = H_0 + \frac{U}{2} \sum_{x,y} n_{x,y} \left(n_{x,y} - 1\right) - \mu \sum_{x,y} n_{x,y},$$

the local part H_{int} is already inherently cluster-local and can be absorbed into H_{c} in Eq. (8.4), such that the effective Hamiltonian becomes

$$H^{'}_{\text{eff}} = H_{\text{eff}} + H_{\text{int}}. \tag{8.11}$$

Taking into account the constant shift of Eq. (8.8), the free-energy of the full lattice system under the mean-field decoupling approximation can now be expressed as

$$\Omega = \Omega^{'} - \frac{1}{2} \sum_{X,Y} \left(\phi^{*}_{X,Y} F_{X,Y} + F^{*}_{X,Y} \phi_{X,Y}\right), \tag{8.12}$$

where $\Omega^{'}$ is the free energy of the cluster with the Hamiltonian of Eq. (8.11). Note that Eq. (8.12) is consistent with the standard lattice free-energy within the single-site mean-field approximation discussed in Sec. 6.2.4.

It should be noted that, in order for the assumption (8.7) which was used to decouple the clusters to be physical, it is indispensable that the cluster is both an integer multiple of the unit cell and that the groundstate momenta of the non-interacting model (i.e. the momenta where condensation can occur in a locally interacting model) can be reproduced exactly by the grid of cluster momenta spanned by K and Q. This is a direct consequence of Eq. (8.7), which in reciprocal space implies $\phi_{\text{K}+\tilde{k},\text{Q}+\tilde{k}} = \phi_{\text{K,Q}} \delta_{\tilde{k},0} \delta_{\tilde{q},0}$. In other words, the approximation can be expected to work as long as the minima of the non-interacting dispersion can be reproduced by the quasi-momenta of the $N_c \times M_c$ clusters [i.e. $\mathbf{K}_{n,m} = (2n\pi/N_c, 2m\pi/M_c)$].

As the approximation neglects quadratic fluctuations between particles on neighboring clusters (which we know matter at this level of accuracy, cf. Sec. 4.5 and Part II), RCMF tends to systematically overestimate the condensate order parameter at the expense of gapped phases. If the RCMF cluster is as large as the full system (i.e. $N_c \times M_c = N \times M$), we have $\bar{\epsilon}_{K,Q} = \epsilon_{K,Q}$ and $F_{X,Y} = 0$, such that the Hamiltonian in Eq. (8.11) becomes identical to the one of the original lattice. RCMF therefore becomes exact in the limit of infinite cluster sizes. Furthermore, RCMF reduces to exact diagonalization (up to a renormalization of the hopping parameters originating from coarse graining in momentum space) where it finds gapped phases: It is thus well equipped to find non-trivial gapped phases and only approaches the thermodynamic limit in a non-conventional but mathematically sound way. Since conventional exact diagonalization lacks $U(1)$-symmetry-breaking, regions of the phase diagram where both methods agree are therefore a strong indication of trustworthiness.

8.2. Self-consistency

The effective Hamiltonian we have derived in Sec. 8.1 is cluster local and given by

$$H'_{\text{eff}} = \sum_{X',Y'} \sum_{X,Y} \bar{t}_{(X',Y'),(X,Y)} b^\dagger_{X',\,Y'} b_{X,\,Y} - \mu \sum_{X,Y} n_{X,\,Y} + \frac{U}{2} \sum_{X,Y} n_{X,\,Y} \left(n_{X,\,Y} - 1\right) + \sum_{X,Y} \left(b^\dagger_{X,\,Y} F_{X,\,Y} + F^*_{X,\,Y} b_{X,\,Y} \right), \tag{8.13}$$

which can be solved by exact diagonalization in Fock space using the definition of the symmetry-breaking field F (8.9). The only unknown therefore is the condensate $\phi_{X,\,Y}$.

Requiring stationarity in the symmetry breaking field $F_{X,\,Y}$,

$$\frac{\delta\Omega}{\delta F_{X,\,Y}} = \frac{\delta\Omega}{\delta F^*_{X,\,Y}} = 0,$$

taking into account Eq. (8.9), reproduces the standard mean-field self-consistency condition

$$\phi_{X,\,Y} = \langle b_{X,\,Y} \rangle. \tag{8.14}$$

Here, $\langle \dots \rangle$ means taking the expectation value with respect to the RCMF Hamiltonian [Eq. (8.13)]. It should be noted that, while the kinetic term (and thereby the energy balance) is treated differently in RCMF by preserving the translational invariance through Eq. (8.9), the self-consistency condition for the condensate of Eq. (8.14) is identical to that of previous cluster mean-field methods [77, 78] (see Sec. 4.3). We note in passing that the treatment of the symmetry-breaking field F is identical to the way it should be implemented in a dynamical cluster approximation extension of bosonic dynamical mean-field theory (see Sec. 4.5).

Just as in standard single-site mean-field (see Sec. 4.2), the self-consistency condition (8.14) can be solved iteratively by starting from an initial guess for $\phi_{X,\,Y}$, plugging it into the Hamiltonian (8.13), and computing a new value of the condensate through (8.14) until the algorithm converges. Due to the position-dependence of $\phi_{X,\,Y}$ different stationary solutions fulfilling (8.14) can be found, corresponding to different competing phases of the system. In order to find all solutions, we start from different translational-invariant initial guesses consisting of all linear combinations of finite/zero condensates $\phi_{K,\,Q}$ for all possible values of K, Q. We also start from random initial conditions without translational invariance in order to make sure we do not miss any important solutions. However, in all computations we have performed, this does not increase the number of stationary solutions.

8.3. Benchmarking on topologically trivial lattices

In order to benchmark RCMF we turn to the Bose-Hubbard model with hard-core bosons on a two-dimensional square lattice with different hopping amplitudes in x- and y-direction ($J = t_{x/y}$, respectively), using a 4×4 cluster Hamiltonian. In Fig. 8.1a we show RCMF results for the condensate density $\rho_c = \sum_{X,Y} |\phi_{X,\,Y}|^2$ as a function of chemical potential for $t_x = t_y = 1$ and compare with standard single-site mean field, CGMF (see Sec. 4.3) on a 4×4 cluster, and numerically exact path integral quantum Monte Carlo (QMC) [87, 160] results. As expected, RCMF shows better agreement with QMC than the two other mean-field methods. In contrast to CGMF, which due to the breaking of translational invariance converges towards a weakly position-dependent (unphysical) condensate $\phi_{X,\,Y}$, the condensate in RCMF is completely

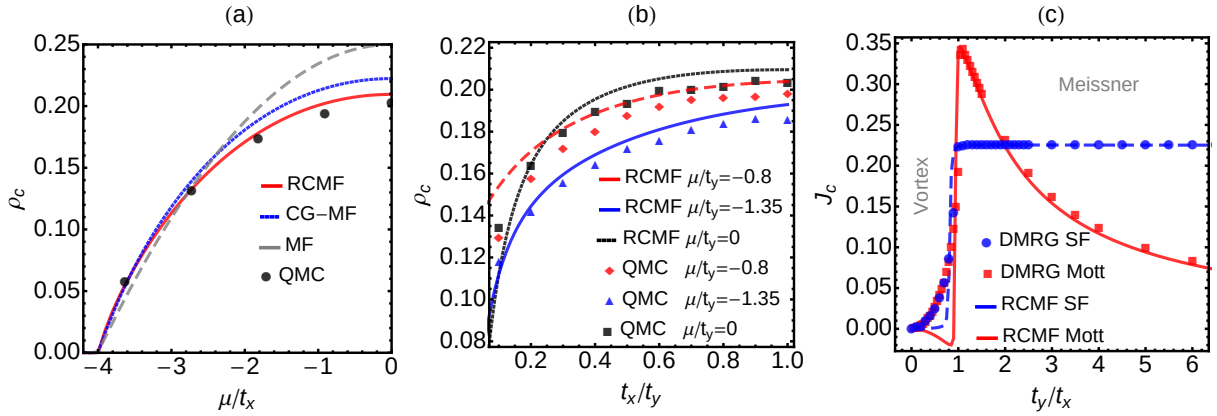

Figure 8.1.: (a) Sweep of the condensate density ρ_c in chemical potential μ for the Bose-Hubbard model with hard-core bosons on a 2d square lattice for $t_x = t_y = 1$. The data are computed with QMC (black dots), RCMF on a 4×4 cluster (red), CGMF on the same cluster (blue dotted) and standard single-site mean field (gray dashed). (b) Sweep of the condensate density ρ_c of the Bose-Hubbard model with hard-core bosons on a 2d square lattice as a function of t_x/t_y, for fixed chemical potentials $\mu/t_y = 0$ (black), $\mu/t_y = -0.8$ (red) and $\mu/t_y = -1.35$ (blue). RCMF data are shown as lines, while QMC data are shown as dots. (c) Chiral current J_c [equation (8.15)] of the chiral ladder of Refs. [158] and [159] with hard-core bosons for $\Phi = \pi/2$ as a function of anisotropy t_x/t_y. Results for $n = 0.5$ (Mott) are shown in red, while results for $n = 0.25$ (superfluid) are shown in blue. The RCMF results are shown as lines, while DMRG results [158] are shown as dots.

homogeneous.

We also compare RCMF results with QMC for anisotropic systems in Fig. 8.1b, observing stronger deviations with increasing anisotropy $|t_x - t_y|$. This is related to the use of a square symmetric 4×4 cluster, while the bandwidths in k- and q-direction are no longer equal. As the one-dimensional limit ($t_x = 0$) is approached, mean-field methods are always expected to behave worse, since quantum fluctuations play a bigger role. However, the results are still qualitatively correct, and we conclude that RCMF works reasonably well also for anisotropic systems.

In order to ensure that RCMF can properly treat artificial gauge fields, we simulate the two-leg ladder of Refs. [159] and [158] with a magnetic flux of $\Phi = \pi/2$ per plaquette and hard-core bosons using a 2×8 cluster. This ladder corresponds to the Harper-Hofstadter-Mott model (see Sec. 2.4) where the x-direction is restricted to just two sites. It shows Mott phases at density $n = 0.5$ and superfluid phases otherwise, with both phases exhibiting Meissner and vortex current-patterns depending on the anisotropy [158]. The Meissner phases can be found for anisotropies where for the gauge of Ref. [159] the non-interacting groundstate momenta – i.e. the momenta where the dispersion has (degenerate) global minima – are $k_{\mathrm{gs}} = \pm\pi/4$. These momenta are fully captured by the 2×8 cluster with cluster-momenta $K = m\pi/4$, where $m = 0, 1, 2, ..., 7$. On the other hand, in the anisotropy-region where the vortex phases appear, k_{gs} varies as a function of the hopping-anisotropy [159] and can no longer be represented within a 2×8 cluster. This is shown in Fig. 8.1c, where the chiral current

$$J_{\mathrm{c}} = \frac{1}{N} \sum_{y} \left(J_{\mathrm{y}}(0, y) - J_{\mathrm{y}}(1, y) \right) \tag{8.15}$$

computed with RCMF is compared to DMRG results [158] both in the Mott ($n = 0.5$) and superfluid ($n = 0.25$) regime. Here, $J_{\mathrm{y}}(l, y)$ is the current in y-direction on the yth site of the

ladder-leg l. The RCMF results agree very well in the Meissner phases, while they cannot capture the vortex phases. This is a good example of what RCMF can do and what not: as discussed in Sec. 8.1, for RCMF to work it is indispensable that the cluster is both an integer multiple of the unit cell and that the groundstate momenta of the non-interacting model can be reproduced exactly by the grid of cluster momenta spanned by K and Q. If this is the case, as seen in Fig. 8.1c, the deviation from the DMRG results on the chiral current [158] is below 1%.

9

Anisotropic Harper-Hofstadter-Mott model

Since the discovery of the quantum Hall effect [27, 30, 31], the lattice geometry's influence on charged particles in magnetic fields has been the subject of extensive research. Prototypical models such as the non-interacting Harper-Hofstadter model (HHm, see Sec. 2.4.2) [20, 21] exhibit fractionalization of the Bloch bands with non-trivial topology, manifesting in quantum (spin) Hall phases [161, 162, 35]. Ultracold atomic gases with artificial magnetic fields [40, 41, 12, 42, 43] (see Sec. 3.3) enabled the experimental study of the non-interacting model [35, 163, 164, 165], while the effect of strong interactions on the band properties remains an open problem. While heating processes in the regime of strong interactions still represent a problem for cold atom experiments with artificial magnetic fields, recent experimental progress gives hope that this can be controlled in the near future [45, 46].

For bosons in the HHm with local interaction, i.e. the Harper-Hofstadter-Mott model (HHMm, see Sec. 2.4.3), previous theoretical studies found fractional quantum Hall (fQH) phases, which have no counterpart in the continuum for strong fields [81], using exact diagonalization (ED) [33, 80, 81], composite fermion theory [81], and the density matrix renormalization group (DMRG) on cylinder [82, 83], and (for lower fields) square geometries [84]. Composite fermion studies also found evidence of a bosonic integer quantum Hall phase in bands with Chern number two [166], also observed with ED [85] in the presence of next-neighbor hopping. In a recent DMRG study [82] a bosonic integer quantum Hall groundstate was also observed in the standard HHMm at filling $\nu = 2$. However, the composite fermion approach is biased by the choice of the wavefunction [81, 166], while ED on small finite systems suffers from strong finite-size effects [33, 80, 85].

The issue becomes especially challenging when going to strong fluxes, where extrapolation to the thermodynamic limit is impossible [167] and the overlap of the finite-size groundstate with Laughlin [33, 80] or composite fermion [81] wavefunctions quickly decreases. DMRG, on the other hand, is restricted to cylinder geometries [82, 83, 29, 59] or small finite systems [84], and condensed or critical phases are out of reach due to long range entanglement. Variational Gutzwiller mean field studies also found evidence of fQH phases [168, 169, 170], as well as striped vortex-lattice phases [168], but the variational basis is restricted by construction. The results of a recent cluster Gutzwiller mean field (CGMF) study [104] are likewise hard to interpret since the method breaks the translational invariance and the topology of the system (see Sec. 4.3).

To overcome these problems, we developed the reciprocal cluster mean field (RCMF) method (see Chapter 8), directly defined in the thermodynamic limit, which preserves the topology of the lattice, and yields excellent agreement with numerically exact results for the Bose-Hubbard model. Further, we introduce an observable for the measure of topological properties in the presence of interactions.

We systematically map out the phase diagram of the strongly interacting HHMm as a function of the chemical potential and the hopping anisotropy. The phase diagram features band insulating,

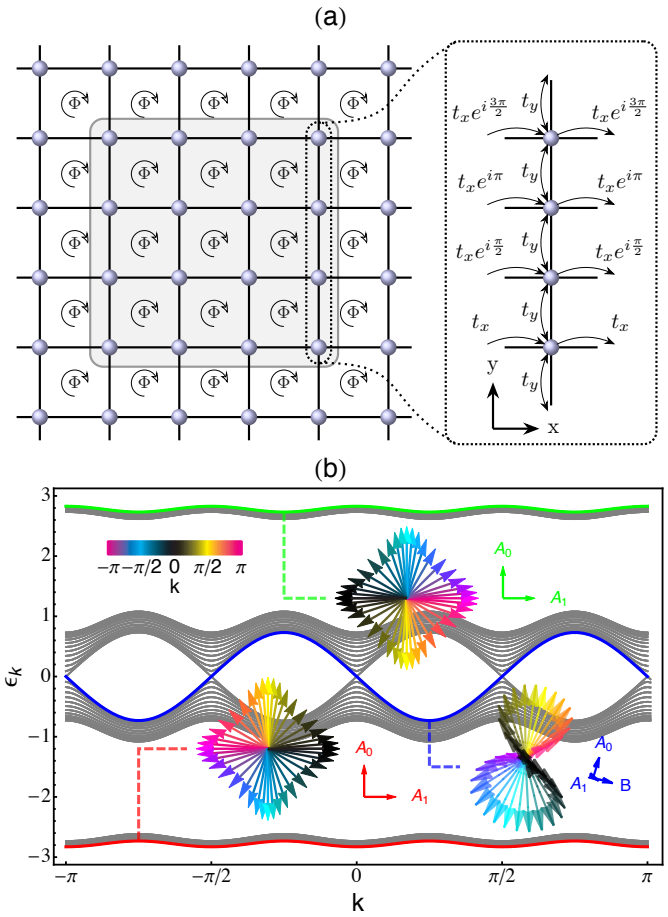

Figure 9.1.: Harper-Hofstadter model. (a) Setup of the single-particle hopping where each plaquette is pierced by a flux of Φ. The 4×1 unit cell for $\Phi = \pi/2$ is shown (dotted lines), where the arrows indicate the direction of the corresponding hopping processes. The 4×4 cluster employed in the RCMF approach is also shown (gray shaded area). (b) Single-particle dispersion for $\Phi = \pi/2$ and $t_x = t_y = 1$. The precession of the $\hat{h}_{k,q}$ vector [Eq. (9.6)] is shown for three states (red, blue and green) when varying k. The vector-colors indicate the values of k (see colorbar).

striped superfluid, and supersolid phases. At integer fillings we further observe highly anisotropic gapless uncondensed liquid phases, which are analyzed using exact diagonalization. For fractional filling, we find incompressible metastable states, indicating competing fQH phases. We define the respective order parameters, and present spatially resolved density, condensate-density, and current patterns.

This chapter closely follows Ref. [3] and is organized as follows. In Sec. 9.1 we discuss the anisotropic HHm, while the HHMm is discussed in Sec. 9.2, where the method for measuring non-trivial topological properties is introduced. In Sec. 9.3 we specialize RCMF to the treatment of the HHMm. Finally, the results for the HHMm are presented and discussed in Sec. 9.4.

9.1. Harper-Hofstadter model

To facilitate the discussion for the strongly-interacting system, we first review the non-interacting HHm, introduced in Sec. 2.4.2, on the square lattice. The Hamiltonian is given by

$$H_\Phi = -\sum_{x,y}\left(t_x e^{iy\Phi} b^\dagger_{x+1,y} b_{x,y} + t_y b^\dagger_{x,y+1} b_{x,y}\right) + h.c. \tag{9.1}$$

with hopping amplitudes $t_{x/y}$ and annihilation (creation) operators $b^{(\dagger)}_{x,y}$. Each plaquette is pierced by a flux such that a phase Φ is picked up when going around it, as illustrated in Fig. 9.1a. For $\Phi = 2\pi/N_\Phi$ the unit cell can be chosen as N_Φ sites in the y-direction.

Eq. (9.1) is diagonalized by the transform $b_l(k,q) = (2\pi)^{-1}\sum_{x,j} e^{-i(kx+q(l+jN_\Phi))} b_{x,l+jN_\Phi}$, where $l \in [0, N_\Phi - 1]$ and $k(q)$ are the momenta in $x(y)$-direction. For even N_Φ the Hamiltonian reduces to $H_\Phi = \sum_{k,q} H_{k,q}$, with

$$H_{k,q} = -\sum_{l=0}^{N_\phi/2-1} 2t_x \cos\left(k - l\Phi\right) A_l(k,q) - 2t_y \cos(q) B(k,q), \tag{9.2}$$

and

$$A_l(k,q) = n_l(k,q) - n_{l+N_\phi/2}(k,q)\,, \tag{9.3}$$

$$B(k,q) = \frac{e^{-iq}}{2\cos(q)} \sum_l b^\dagger_{l+1}(k,q) b_l(k,q) + h.c. \tag{9.4}$$

For $\Phi = \pi/2$, used below, the system has three isolated topologically non-trivial bands, see Fig 9.1b. Here we use the notation of Ref. [165] where the central (super)band contains twice the number of states as compared to the two other bands.

Both the topological properties and the location of the four minima of the dispersion at $q = 0$ and $k = 0, \pm\pi/2, \pi$ are independent of the anisotropy between the hopping amplitudes t_x and t_y. The bandwidths of the three bands, on the other hand, are affected by the ratio t_x/t_y. In order to analyze this, we introduce the quantities ΔE_k and ΔE_q for the lowest band, where ΔE_k is the bandwidth in k-direction, i.e.

$$\Delta E_k = \max_q \Delta\tilde{E}_k(q),$$

where

$$\Delta\tilde{E}_k(q) = \max_k \epsilon^0(k,q) - \min_k \epsilon^0(k,q),$$

$\epsilon^0(k,q)$ is the dispersion of the lowest band, and $\max_{k/q}$ corresponds to taking the maximum with respect to k and q, respectively. The bandwidth in q-direction, ΔE_q is defined analogously. As shown in the upper panel of Fig. 9.6a, for $t_x \ll t_y$ the lowest band is particularly flat in the k-direction ($\Delta E_k \ll 1$), while for $t_y \ll t_x$ it is particularly flat in the q-direction ($\Delta E_q \ll 1$). Note that this is not to be confused with the "flatness" of the bands that typically supports fractional quantum Hall effects, which would consist in $\max\left[\Delta E_k, \Delta E_q\right] \ll 1$ (in fact this quantity is low in the region of low hopping anisotropy). Instead, having only $\Delta E_k \ll 1$ or $\Delta E_q \ll 1$ will result simply in suppressing the condensation of bosons in the minima of the dispersion.

Another quantity affected by the anisotropy is the gap between the lowest and the central band. The simplest many-body problem where this plays a role is the case of spinless non-interacting fermions, which exhibit an integer quantum Hall phase for integer filling of the lowest band (see Sec. 2.4.2), i.e. if the chemical potential μ lies within the (anisotropy-dependent) gap, see Fig. 9.6a.

The Hamiltonian H_Φ and Eq. (9.2) can be rewritten in the compact notation

$$H_\Phi = \int dkdq \left(\boldsymbol{v}_{k,q} \cdot \boldsymbol{h}_{k,q} \right), \tag{9.5}$$

where $\boldsymbol{v}_{k,q}$ is a vector of scalars and $\boldsymbol{h}_{k,q}$ is a vector of operators

$$\boldsymbol{v}_{k,q} = \begin{pmatrix} -2t_x \cos(k) \\ -2t_x \cos\left(k - \frac{\pi}{2}\right) \\ -2t_y \cos(q) \end{pmatrix}, \quad \boldsymbol{h}_{k,q} = \begin{pmatrix} A_0(k,q) \\ A_1(k,q) \\ B(k,q) \end{pmatrix}.$$

The operator $\boldsymbol{h}_{k,q}$ fully determines the momentum dependence of the non-interacting system, and we can apply the concept of parallel transport [171]. The local Berry curvature at the point (k,q) is proportional to the rotation of the unit-vector

$$\hat{h}_{k,q} = \langle \boldsymbol{h}_{k,q} \rangle / |\langle \boldsymbol{h}_{k,q} \rangle| \tag{9.6}$$

under an infinitesimal momentum shift. In fact, if $\hat{h}_{k,q}$ shows a non-trivial winding under transport on a closed path through the Brillouin zone, the Berry-curvature cannot be continuously deformed to a trivial one and the system is topologically non-trivial. The Chern number of the nth band is given by the number and direction of closed loops of $\hat{h}_{k,q}$, i.e.

$$c_n = \frac{\gamma_n}{2\pi},$$

where γ_n is the solid angle subtended by $\hat{h}_{k,q}$ when taking the expectation value with respect to the single-particle eigenstates of the nth band and sweeping the momenta through the Brillouin zone. This is shown in Fig. 9.1b. For the lowest band $\langle A_0(k,0) \rangle$ and $\langle A_1(k,0) \rangle$ are shown while $\langle B(k,0) \rangle$ varies only slightly: $\hat{h}_{k,q}$ performs one anti-clockwise loop, corresponding to a Chern number of $c_0 = -1$. Equivalently, for the central band $\hat{h}_{k,q}$ performs a double clockwise loop ($c_1 = 2$), while the highest band again has $c_2 = -1$.

The connection between the winding of $\hat{h}_{k,q}$ and the Hall conductivity can be seen from the example of the integer quantum Hall effect, i.e. the lowest band being completely filled with non-interacting fermions (see Sec. 2.4.2). Adding a magnetic flux Φ_y piercing a torus of size $L_x \times L_y$ in y-direction can be achieved by transforming the hopping amplitudes as $t_x \to t_x e^{i\Phi_\mathrm{y}/L_x}$ for hopping processes in $+\hat{x}$, while taking the complex-conjugate in the opposite direction. The effect of this transform on the Hamiltonian (9.5) amounts to

$$\boldsymbol{v}_{k,q} \to \boldsymbol{v}_{k-\Phi_\mathrm{y}/L_x,q},$$

which is manifested in a translation of the vector $\boldsymbol{h}_{k,q}$ with respect to the case without flux *at each* momentum (k,q), i.e.

$$\langle \Psi(\Phi_\mathrm{y}) | \boldsymbol{h}_{k,q} | \Psi(\Phi_\mathrm{y}) \rangle = \left\langle \Psi(0) \middle| \boldsymbol{h}_{k+\Phi_\mathrm{y}/L_x,q} \middle| \Psi(0) \right\rangle, \tag{9.7}$$

where $|\Psi(\Phi_\mathrm{y})\rangle$ is the many-body groundstate under the flux Φ_y.

The sole effect of Φ_y is therefore a transform of the many-body groundstate such that at each momentum (k,q) Eq. (9.7) is fulfilled, resulting in a rotation of $\hat{h}_{k,q}$. Inserting a flux of $\Phi_\mathrm{y} = 2\pi L_x/4$ yields the transform $A_0(k,q) \to A_1(k,q)$, $A_1(k,q) \to -A_0(k,q)$, and therefore $n_l(k,q) \to n_{l+1}(k,q)$. Adding a magnetic flux of $\Phi_\mathrm{y} = 2\pi L_x/4$ is therefore equivalent to translating the manybody groundstate by one site in the y-direction.

If the lowest band is completely filled, the total number of particles on the torus is $L_x L_y/4$. Therefore adiabatically inserting a flux of $\Phi_\mathrm{y} = 2\pi L_x/4$ results in $L_x L_y/4$ particles being

translated by one site in y-direction, or equivalently a total number of $L_x/4$ particles being transported once around the periodic boundary in the y-direction. Consequently, adiabatically inserting a flux of $\Phi_y = 2\pi$ results in a quantized total transverse transport of a single particle around the periodic boundary.

9.2. Harper-Hofstadter-Mott model

We proceed with the study of the HHMm with interaction U, chemical potential μ, and magnetic flux $\Phi = \pi/2$,

$$H = H_\Phi + \lim_{U\to\infty} \frac{U}{2} \sum_{x,y} n_{x,y}(n_{x,y} - 1) - \mu \sum_{x,y} n_{x,y}, \tag{9.8}$$

in the hard-core limit $U \to \infty$.

For hard-core bosons a particle-hole transform (i.e. simultaneous $b^\dagger \to b$ and $b \to b^\dagger$) is equivalent to an inversion of the flux in the Hamiltonian of Eq. (9.8), i.e. $\Phi \to -\Phi$. A direct consequence of this, is that the manybody groundstates at densities n and $1-n$ are related by the $\mathcal{CT}$ operation, where $\mathcal{C}$ is the particle-hole transform, and $\mathcal{T}$ the complex conjugation operator. This implies that the Hall conductivity σ_{xy} is anti-symmetric under the transform $n \to 1-n$ [172], i.e.

$$\sigma_{xy}(n) = -\sigma_{xy}(1-n). \tag{9.9}$$

This effect is known as the charge conjugation symmetry of hard-core bosons [172].

In contrast to the non-interacting case, for a finite interacting system the Berry curvature is defined with respect to boundary twisting angles (see Sec. 2.4.2), i.e.,

$$C = \frac{1}{2\pi} \int_0^{2\pi} d\theta_x \int_0^{2\pi} d\theta_y \left(\partial_{\theta_x} \mathcal{A}_y - \partial_{\theta_y} \mathcal{A}_x \right), \tag{9.10}$$

where $\mathcal{A}_j(\theta_x, \theta_y) = i\langle \Psi(\theta_x, \theta_y) | \partial_{\theta_j} | \Psi(\theta_x, \theta_y) \rangle$ is the Berry connection, Ψ is the many-body groundstate, and θ_x, and θ_y are twisting angles of the boundary conditions in x- and y-direction, respectively (i.e. $T_{x/y}\Psi(\theta_x, \theta_y) = e^{i\theta_{x/y}}\Psi(\theta_x, \theta_y)$, where $T_{x/y}$ is a translation by the system size $L_{x/y}$ in x-, and y-direction, respectively).

The twisted boundary conditions can be implemented in the same way as the magnetic flux discussed in Sec. 9.1 by transforming the hopping as $t_x \to t_x e^{i\theta_x/L_x}$ and $t_y \to t_y e^{i\theta_y/L_y}$ for hopping processes in $+\hat{x}$, and $+\hat{y}$-direction, respectively, while taking the complex-conjugate in the opposite directions. The interaction and chemical potential terms in Eq. (9.8) remain unchanged. The only effect of adding the twisting angles (θ_x, θ_y) to the infinite system is, as in Sec. 9.1,

$$\boldsymbol{v}_{k,q} \to \boldsymbol{v}_{k-\theta_x/L_x, q-\theta_y/L_y}.$$

In other words, if T_{θ_x,θ_y} is the momentum-space translation operator which transforms each momentum as $k \to k + \theta_x/L_x$, and $q \to q + \theta_y/L_y$, we have

$$|\Psi(\theta_x, \theta_y)\rangle = T_{\theta_x,\theta_y} |\Psi(0,0)\rangle .$$

For the Berry-curvature

$$\mathcal{B}(\theta_x, \theta_y) = \partial_{\theta_x}\mathcal{A}_y - \partial_{\theta_y}\mathcal{A}_x = i\left(\langle \partial_{\theta_x}\Psi(\theta_x,\theta_y)| \, \partial_{\theta_y}\Psi(\theta_x,\theta_y)\rangle - \left\langle \partial_{\theta_y}\Psi(\theta_x,\theta_y)\right| \partial_{\theta_x}\Psi(\theta_x,\theta_y)\rangle \right),$$

we therefore have

$$\langle \partial_{\theta_i}\Psi(\theta_x,\theta_y)| \, \partial_{\theta_j}\Psi(\theta_x,\theta_y)\rangle = \left[\langle \Psi(0,0)| \, \partial_{\theta_i} T^\dagger_{\theta_x,\theta_y}\right] \left[\partial_{\theta_j} T_{\theta_x,\theta_y} |\Psi(0,0)\rangle\right].$$

The Berry curvature is therefore fully determined by the response of the periodic-boundary many-body groundstate $\Psi(0,0)$ to a translation in momentum.

If we define $P_{\text{h.c.}}$ as the projector onto the Hilbert space of hard-core bosons (where multiple occupancy in position space is forbidden), the interacting many-body Hamiltonian [Eq. (9.8)] can be written as

$$H = P_{\text{h.c.}} \left(H_\Phi - \mu N\right) P_{\text{h.c.}} = \int dk dq \boldsymbol{v}_{k,q} \cdot P_{\text{h.c.}} \boldsymbol{h}_{k,q} P_{\text{h.c.}} - \mu P_{\text{h.c.}} N P_{\text{h.c.}},$$

with particle-number operator N. The full momentum dependence of the hard-core bosons is therefore contained in the term $P_{\text{h.c.}} \boldsymbol{h}_{k,q} P_{\text{h.c.}}$. Furthermore, for any hard-core boson many-body eigenstate Ψ we have $P_{\text{h.c.}} |\Psi\rangle = |\Psi\rangle$. As in the non-interacting case therefore a non-trivial winding of $\langle \Psi(0,0) | \boldsymbol{h}_{k,q} | \Psi(0,0) \rangle$ in momentum space indicates a non-trivial topology of the many-body groundstate. It should be emphasized that this measure is different from summing over the individual single-particle Chern numbers of the occupied bands, since no projection onto non-interacting bands is involved.

For a further discussion of the measurement of topological properties with the $\hat{h}_{k,q}$-vector, see Appendix B.2.

9.3. Reciprocal cluster mean-field approach

The HHm has groundstate momenta $k_{\text{gs}} = 0, \pm\pi/2, \pi$ and $q_{\text{gs}} = 0$. Since the momenta of the groundstate are independent of the anisotropy, we do not encounter the difficulties described in Sec. 8.3 for the vortex phases of the chiral ladder when using apropriate cluster-sizes in our RCMF approach. In order to fulfill Eq. (8.7) by reproducing the minima of the dispersion (see Sec. 8.1) a multiple of 4 sites in X direction is needed, since for 4 sites K is a multiple of $\pi/2$. We also need a multiple of 4 sites in Y direction in order to fully capture the 1×4 unit cell. See Appendix B.3 for a further discussion of constraints on the cluster size. In this chapter we restrict ourselves to the minimal cluster, i.e. 4×4.

Since the mean-field decoupling is performed in the thermodynamic limit, the sum over $\tilde{k}$ and $\tilde{q}$ in (8.3) can be replaced by an integral and computed analytically. In this configuration the coarse-graining described in Sec. 8.1 leads to the cluster-hopping

$$\bar{t}_{(X',Y'),(X,Y)} = \frac{2\sqrt{2}}{\pi} t_{(X',Y'),(X,Y)}, \tag{9.11}$$

where $t_{(X',Y'),(X,Y)}$ is the original hopping of the HHm [Eq. (9.1)] with periodic boundary conditions, which plugged into the results of Sec. 8.1 yields the effective RCMF Hamiltonian for the Harper-Hofstadter-Mott model on a 4×4 cluster.

The free energy Ω of Eq. (8.12) represents the free energy of the lattice system in the thermodynamic limit within the RCMF approximation. Using functional derivatives of Eq. (8.12) we can compute expectation values with respect to the full lattice system. According to the self-consistency condition [Eq. (8.14)], this is trivial for the condensate

$$\phi_{X,Y} = \langle b_{X,Y} \rangle.$$

Accordingly, we get for the condensate density

$$\rho_c(X,Y) = |\phi_{X,Y}|^2,$$

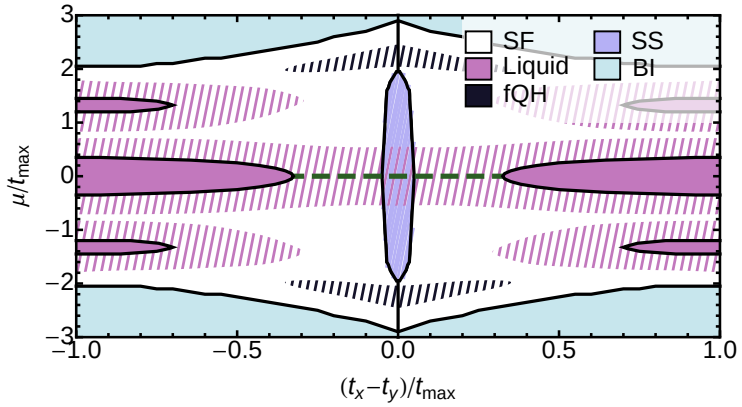

Figure 9.2.: Groundstate phase diagram of the HHMm in two dimensions with hard-core bosons and flux $\Phi = \pi/2$ in terms of $\mu/t_{\max}$ and $(t_x - t_y)/t_{\max}$. The observed phases are band insulating (BI, light blue), supersolid (SS, dark blue), striped superfluid (SF, white), gapless uncondensed liquid (Liquid, pink), and fractional quantum Hall (fQH, dark gray). The dashed regions indicate where the RCMF groundstate has a non-zero condensate order parameter but is very close in energy ($< 3\%$) to metastable uncondensed states. At zero anisotropy the striped superfluid undergoes phase separation between vertically (for $t_x > t_y$) and horizontally (for $t_x < t_y$) striped order (black vertical line), while for $\mu = 0$ the density is homogeneous and fixed to $n = 1/2$ in all phases (green dashed line).

and the total condensate density per site

$$n_c = \frac{1}{N_c M_c} \sum_{X,Y} \rho_c(X,Y).$$

Also for the particle density we get an equivalence between the full lattice and the 4×4 cluster, since

$$\rho(X,Y) = -\frac{\delta\Omega}{\delta\mu_{\mathrm{X,Y}}} = \langle n_{X,\,Y} \rangle,$$

and, accordingly, for the total particle density per site

$$n = \frac{1}{N_c M_c} \sum_{X,Y} \rho(X,Y).$$

The current $J_{\mathrm{x}}(x,y)$ in x-direction between the sites (x,y) and $(x+1,y)$ is defined as

$$J_{\mathrm{x}}(x,y) = -i \left(t_{(x+1,\,y),\,(x,\,y)} \langle b^\dagger_{x+1,\,y} b_{x,\,y} \rangle_{\mathrm{latt}} - t_{(x,\,y),\,(x+1,\,y)} \langle b^\dagger_{x,\,y} b_{x+1,\,y} \rangle_{\mathrm{latt}} \right), \tag{9.12}$$

where $\langle \dots \rangle_{\mathrm{latt}}$ is the lattice-system expectation value. However, by

$$\begin{aligned} \langle b^\dagger_{x',\,y'} b_{x,\,y} \rangle_{\mathrm{latt}} &= \frac{\partial\Omega}{\partial t_{(x',\,y'),\,(x,\,y)}} \\ &= \frac{\partial \bar{t}_{(x',\,y'),\,(x,\,y)}}{\partial t_{(x',\,y'),\,(x,\,y)}} \langle b^\dagger_{x',\,y'} b_{x,\,y} \rangle + \frac{1}{2} \frac{\partial \delta t_{(x',\,y'),\,(x,\,y)}}{\partial t_{(x',\,y'),\,(x,\,y)}} \left(\langle b^\dagger_{x',\,y'} \rangle \phi_{x,\,y} + \phi^*_{x',\,y'} \langle b_{x,\,y} \rangle \right), \end{aligned} \tag{9.13}$$

we can express the lattice quantities in terms of expectation values with respect to the RCMF Hamiltonian.

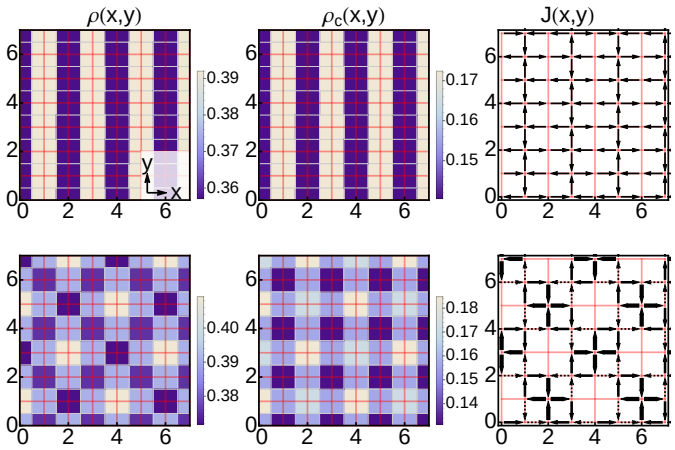

Figure 9.3.: Density (left column), condensate-density (central column), and current patterns (right column) for the VS-SF at $\mu/t_{\max} = -0.8$, $(t_x - t_y)/t_{\max} = 0.2$ (upper row), and the SS at $\mu/t_{\max} = -0.8$, $(t_x - t_y)/t_{\max} = 0$ (lower row). The arrow-thickness indicates the magnitude of the currents.

By Eq. (9.13) we can also compute the current in the y-direction given by

$$J_{\mathrm{y}}(x,y) = -i\left(t_{(x,\,y+1),\,(x,\,y)}\langle b^{\dagger}_{x,\,y+1} b_{x,\,y}\rangle_{\mathrm{latt}} - t_{(x,\,y),\,(x,\,y+1)}\langle b^{\dagger}_{x,\,y} b_{x,\,y+1}\rangle_{\mathrm{latt}}\right), \tag{9.14}$$

and by Fourier transform also the occupation in momentum space

$$\langle n_{K,\,Q}\rangle_{\mathrm{latt}} = \sum_{X,Y} e^{i\,(KX+QY)}\langle b^{\dagger}_{X,\,Y} b_{0,\,0}\rangle_{\mathrm{latt}}.$$

9.4. Results

In Fig. 9.2 we present the groundstate phase diagram in terms of the chemical potential $\mu/t_{\max}$ and the hopping-anisotropy $(t_x - t_y)/t_{\max}$, where $t_{\max} = \max[\{t_x, t_y\}]$. The phases at densities n and $1-n$ are related by a $\mathcal{CT}$-transformation consisting of a particle-hole transform combined with complex-conjugation (see Sec. 9.2). The symmetry around the $(t_x - t_y) = 0$ axis corresponds to gauge invariance, since t_x and t_y can be exchanged in combination with a lattice-rotation of $\pi/2$. At $n = 0$ and $n = 1$ we find topologically trivial band insulators (BI). Below we discuss the other resulting phases in more detail.

9.4.1. Condensed phases

At moderate values of μ we observe superfluid phases with striped density and condensate density modulation. For $t_x > t_y$ this is a vertically striped superfluid (VS-SF), with vertically striped density distribution $\rho(x,y)$ and condensate-density distribution $\rho_c(x,y) = |\phi_{x,y}|^2$, as shown in Fig. 9.3 together with the spatially resolved particle current $\boldsymbol{J}(x,y)$. The net current is zero, as expected for an infinite system. Locally, however, there are chiral currents around two plaquettes in the horizontal direction. We therefore introduce the striped-superfluid order parameter $J_{\mathrm{str}} = \sum_{x,y}\left[\cos\left(\frac{\pi}{2}(x+2y)\right) J_{\mathrm{x}}(x,y) - \cos\left(\frac{\pi}{2}(2x+y)\right) J_{\mathrm{y}}(x,y)\right]$, where $J_{\mathrm{x(y)}}(x,y)$ is the groundstate expectation value of the current in x (y) direction. For $t_x < t_y$ the superfluid phase is horizontally striped (HS-SF), with the patterns of Fig. 9.3 rotated by $\pi/2$ compared to the VS-SF. Since at $t_x = t_y$ the system is invariant under a $\pi/2$-rotation, for $|\mu|/t_{\max} \gtrsim 2$ the VS-SF and HS-SF undergo phase separation.

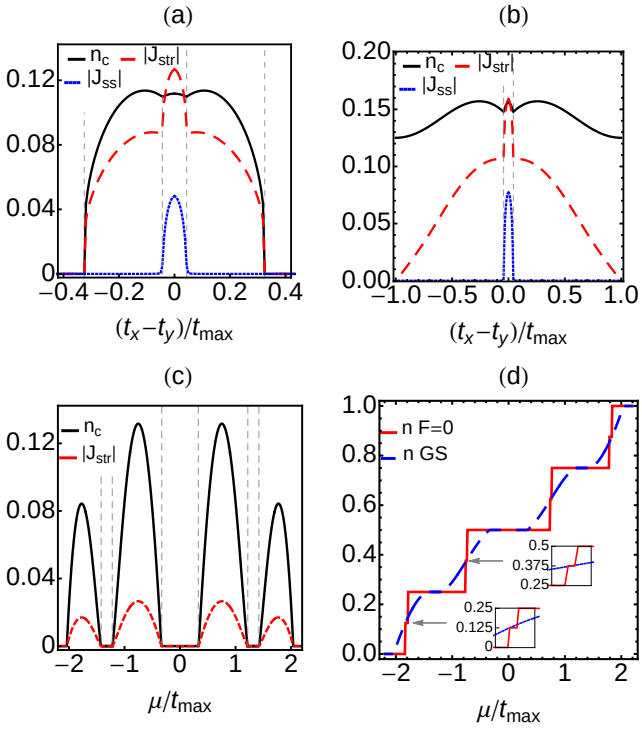

Figure 9.4.: Order parameters and densities. (a) and (b) Sweep in anisotropy at fixed $\mu/t_{\max}$. In (a) the average condensate density n_c (black), and the order parameters J_{str} (red, dashed), and J_{ss} (blue, dotted) are shown for $\mu/t_{\max} = 0$. In (b) the same quantities are shown for $\mu/t_{\max} = -0.8$. (c) and (d) Sweep in μ at fixed $(t_x - t_y)/t_{\max} = -0.8$. In (c) n_c (black) and J_{str} (red, dashed) are shown. In (d) the average density n is shown in the groundstate (blue dashed) and for the stationary solution with zero symmetry-breaking field F (red). The insets indicate the regions where the $F = 0$ solution shows plateaus at fractional filling $\nu = 1/2$ ($n = 1/8$) and $\nu = 3/2$ ($n = 3/8$), respectively. In (a), (b), and (c) the vertical dashed lines indicate phase transitions.

At $|\mu|/t_{\max} \lesssim 2$ and for low anisotropy we find a supersolid phase (SS) with lower free energy than the striped phases. The density distributions ρ and ρ_c spontaneously break translational invariance, having a period larger than the unit cell (see Fig. 9.3). A similar spontaneous breaking of translational invariance has already been observed in the staggered-flux bosonic Harper-Mott model [173] and the bosonic Hofstadter model on a dice lattice [174], and has recently been measured experimentally in spin-orbit coupled Bose-Einstein condensates [175]. The SS exhibits chiral currents around single plaquettes, with position-dependent amplitudes, as captured by the order parameter $J_{\text{ss}} = \sum_{x,y} \cos\left(\frac{\pi}{2}(x+y)\right)\left(J_{\text{x}}(x,y) - J_{\text{y}}(x,y)\right)$. In all phases, at $\mu = 0$ the density distribution is homogeneous, $\rho(x,y) = 1/2$, while $\rho_c(x,y)$ remains modulated.

The phase transition between the striped superfluids and the SS phase is characterized by a kink in the average condensate density n_c, see Figures 9.4a and 9.4b. For $n_c > 0$, the striped superfluid order parameter J_{str} is only zero at $|t_x - t_y|/t_{\max} = 1$ (where the lattice is a set of trivial one-dimensional chains), exhibiting a kink at the phase transition to the SS, where also J_{ss} becomes non-zero.

9.4.2. Uncondensed phases

At density $n = 1/2$ (Fig. 9.4a) and stronger anisotropy we find a phase with zero condensate density ($n_c = 0$). In Figs. 9.4c and 9.4d we show a sweep in μ for $(t_x - t_y)/t_{\max} = -0.8$, where we

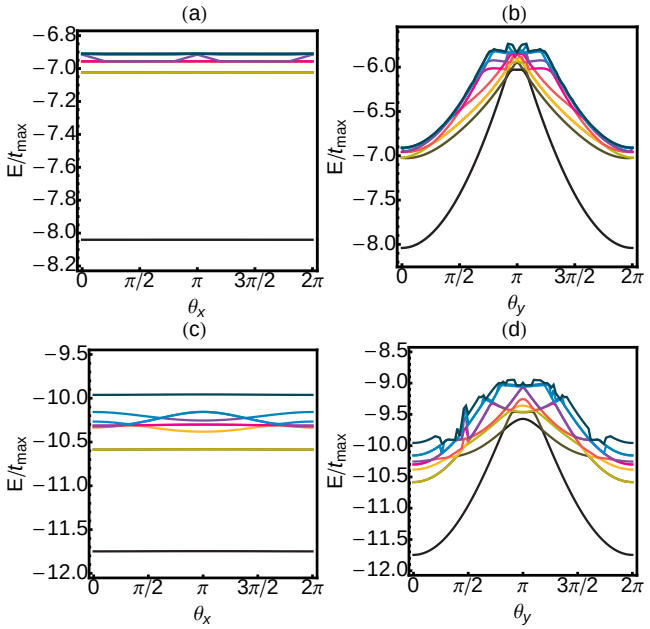

Figure 9.5.: Response of the lowest 10 eigenvalues of a 4×4 system to twisted boundary conditions. (a) and (b): For 4 particles ($\nu = 1$), $t_x = 0.2$, $t_y = 1$, and fixed twisting angles $\theta_y = 0$ (a) and $\theta_x = 0$ (b). (c) and (d): For 8 particles ($\nu = 2$), $t_x = 0.5$, $t_y = 1$, and fixed twisting angles $\theta_y = 0$ (c) and $\theta_x = \pi$ (d).

observe plateaus with zero n_c, zero current, and homogeneous density distribtution $\rho(x, y) = \nu/4$, with fillings $\nu = 1, 2, 3$. In these phases, since $F_{x,y} = 0$, the RCMF Hamiltonian of Eq. (8.13) reduces to a finite 4×4 torus without any external variational parameter. In order to further analyze these phases we therefore turn to ED using twisted boundary conditions in order to analyze finite-size effects (see Sec. 9.2). If the phases are gapped, one expects the manybody gap to stay finite for all twisting angles (θ_x, θ_y), while in gapless phases the groundstate mixes with excited states.

As can be seen in Fig. 9.5 for $t_x < t_y$ the groundstate remains gapped with respect to boundary twisting in the x-direction with $\theta_y = 0$, while it mixes with the excited states for twisting in the y-direction. For $t_y < t_x$ the behavior is reversed. Apart from the response to twisted boundaries, the anisotropic gapless nature of the two-dimensional uncondensed phases can also be observed in the scaling of the many-body gap as a function of L_x while keeping $L_y = 4$ fixed. As shown in Fig. 9.8b the manybody gaps remain essentially constant if t_x is (sufficiently) smaller than t_y, while it decreases in a non-monotonous way if t_x is larger than t_y. If the same scaling is done in y-direction the situation is reversed. The same behavior can also be observed in the correlations $|\langle b^\dagger_{x,y} b_{0,y}\rangle|$ in a system with $L_y = 4$ and $L_x = 8$, shown in Fig. 9.8c, which quickly drop to zero as a function of x for $t_x < t_y$. For $t_x > t_y$ on the other hand, the correlations stay finite throughout the whole system hinting at the anisotropic gapless nature of the phase in two dimensions.

In contrast to the two-dimensional Bose-Hubbard model without magnetic flux, which in the superfluid groundstate always shows condensation as long as both hopping amplitudes are finite [160], the HHMm therefore shows a transition at finite t_x/t_y to a highly anisotropic uncondensed gapless liquid. The fact that these phases are adiabatically connected to the one-dimensional limit ($t_x = 0$ or $t_y = 0$), where hard-core bosons are in a superfluid phase, as well as the highly anisotropic correlations $|\langle b^\dagger_{x,y} b_{0,y}\rangle|$, possibly point to an unconventional one-dimensional superfluid order.

As a function of the hopping anisotropy, the liquid phases occur where the lowest band is

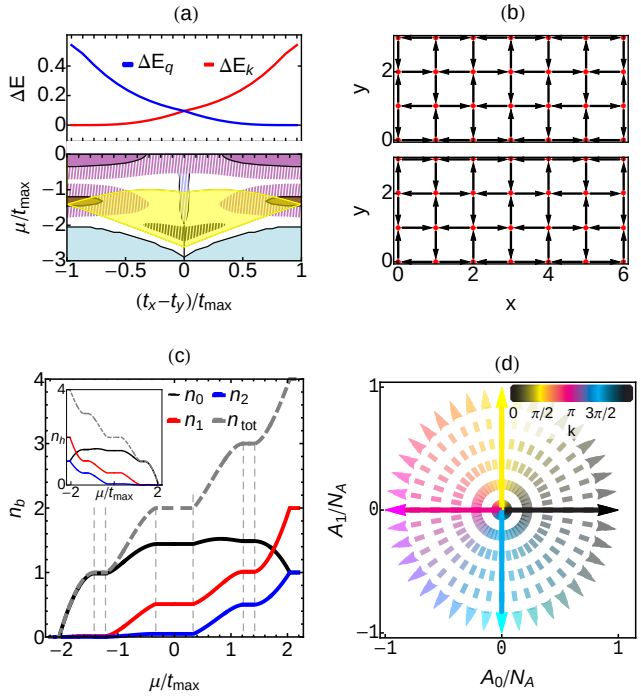

Figure 9.6.: Uncondensed phases. (a) top: Bandwidths of the lowest band in k-, and q-direction, ΔE_k (red) and ΔE_q (blue), as a function of $(t_x - t_y)/t_{\max}$; (a) bottom: quantum Hall plateau for non-interacting fermions (yellow) compared to the hard-core boson phase diagram. (b) Two counter-propagating current patterns (upper and lower panel, respectively) whose sum gives zero net current, resulting from current-current correlations. (c) Occupations of the lowest (n_0, black), central (n_1, red), highest (n_2, blue) band, and total occupation $n_{\text{tot}} = n_0 + n_1 + n_2$ (gray dashed), for $(t_x - t_y)/t_{\max} = -0.8$ as a function of μ. The phase transitions between condensed and uncondensed phases are indicated with dashed vertical lines. In the inset the corresponding hole occupations ($n_h = \langle bb^\dagger \rangle$) are shown in the same colors. (d) A_0 and A_1 components of the $\hat{h}_{k,q}$ vector [Eq. (9.6)] for $(t_x - t_y)/t_{\max} = -0.8$ as a function of k (see coloring) in the single-particle case (dashed arrows), and for hard-core bosons with $\mu/t_{\max} = 0$ (full arrows). A_0 and A_1 are normalized by $N_A = \sqrt{A_0^2 + A_1^2}$, while the B-component varies only slightly (not shown).

particularly flat either in k- or q-direction, suppressing condensation in the minima of the dispersion (see Fig. 9.6a and Sec. 9.1). While the system has zero current everywhere (due to the periodic boundaries), a signature of the response of the liquid to the magnetic field is found by analyzing current-current correlations (see Appendix B.4), resulting in two counter-propagating currents which cancel each other, shown in Fig. 9.6b.

In Fig. 9.6c we show the projection of the groundstate onto the three non-interacting bands n_0, n_1, and n_2, for the same parameters as in Figs. 9.4c and 9.4d. At $\nu = 1$ the lowest band shows unit filling. As shown in Fig. 9.6a, this phase appears in the same regions of μ as the integer quantum Hall plateau of non-interacting spinless fermions. At $\nu = 3$ the holes show unit filling in the lowest band, due to the $\mathcal{CT}$ transform discussed in Sec. 9.2.

As can be seen in Fig. 9.6d, the vector $\hat{h}_{k,q}$ shows the same behavior as for the lowest non-interacting band in all three liquid phases (shown for $\nu = 2$), in contrast to the trivial BI at $n = 0, 1$ and the one-dimensional superfluid at $t_x = 0$ or $t_y = 0$. For $\nu = 1$, as in the case of non-interacting fermions discussed in Sec. 9.1, this winding indicates the transverse transport of

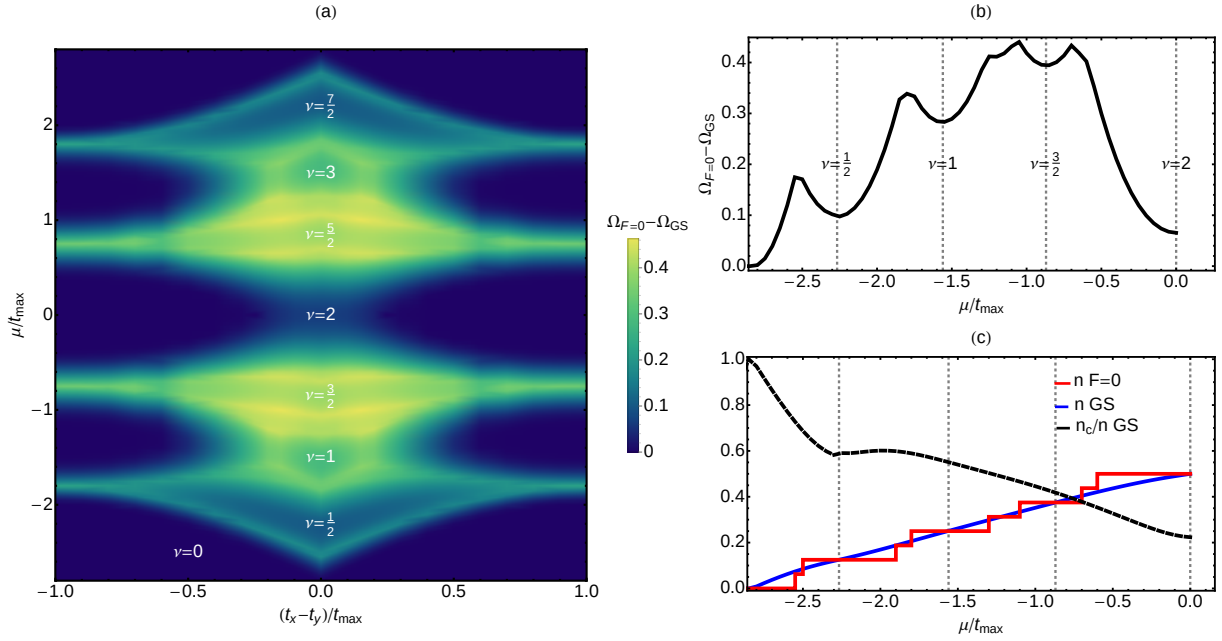

Figure 9.7.: Analysis of metastable phases. (a) and (b) Difference in free energy between the solution with zero symmetry-breaking field ($\Omega_{F=0}$) and the groundstate (Ω_{GS}) (a) as a function of anisotropy and chemical potential, (b) as a function of chemical potential at $t_x = t_y$. (c) Condensate fraction n_c/n (blacked, dashed) and density (blue) of the groundstate compared to the density of the $F = 0$ solution (red) as a function of chemical potential and $t_x = t_y$. In panels (b) and (c) the vertical dotted lines show the locations of the metastable plateaus, while in panel (a) they are indicated with white labels.

a single particle if a magnetic flux of $\Phi_{\mathrm{y}} = 2\pi$ is inserted. At $\nu = 3$, the transverse transport consists of a single hole. This is consistent with the band fillings in Fig. 9.6c and the $\mathcal{CT}$ transform discussed in Sec. 9.2, i.e. the reversal of the Hall conductivity $\sigma_{xy}(\nu = 3) = -\sigma_{xy}(\nu = 1)$. As these phases are gapless in the two-dimensional thermodynamic limit, the quantization of the Hall conductivity is not topologically protected by edge modes and therefore sensitive to disorder, as is the case for metallic Fermi-liquid-like phases of hard-core bosons [85, 97, 176].

By contrast, in the case of a cylindrical geometry, i.e. $L_y = 4$ and $L_x \to \infty$, the response to the twisted boundaries in x-direction while $\theta_y = 0$, shown in Figs. 9.5a and 9.5c, indicates that all three plateaus are gapped. As a function of θ_x the vector $\hat{h}_{k,q}$ shows a complete loop and appears to be robust against local perturbations (see Appendix B.2). What the nature of the phases at $\nu = 1, 3$ is in such a quasi-one-dimensional setup will be investigated in Chapter 10: the non-trivial winding indicates a gapped phase with odd Hall conductivity, which is expected to show intrinsic topological order and fractional quasiparticle excitations for bosons in two dimensions [28, 177]. The non-degenerate groundstate we observe (which for bosons is only expected at even Hall conductivities, see Sec. 2.4.3) apparently is at odds with this prediction.

At $\nu = 2$ ($n = 1/2$), the Hamiltonian of Eq. (9.8) is $\mathcal{CT}$-symmetric. It directly follows that $\sigma_{xy}(\nu = 2) = 0$. This is consistent with the bands being equally filled with particles and holes (see Fig. 9.6b), resulting in a zero net Hall conductivity. In two-dimensional systems such a $\mathcal{CT}$-symmetric phase is expected to be topologically trivial [22, 23, 24], in line with the gaplessness observed in Figs. 9.5c and 9.5d.

Whereas away from integer fillings the groundstate is always symmetry-broken, it is always possible within RCMF to find (metastable) stationary solutions with zero symmetry-breaking

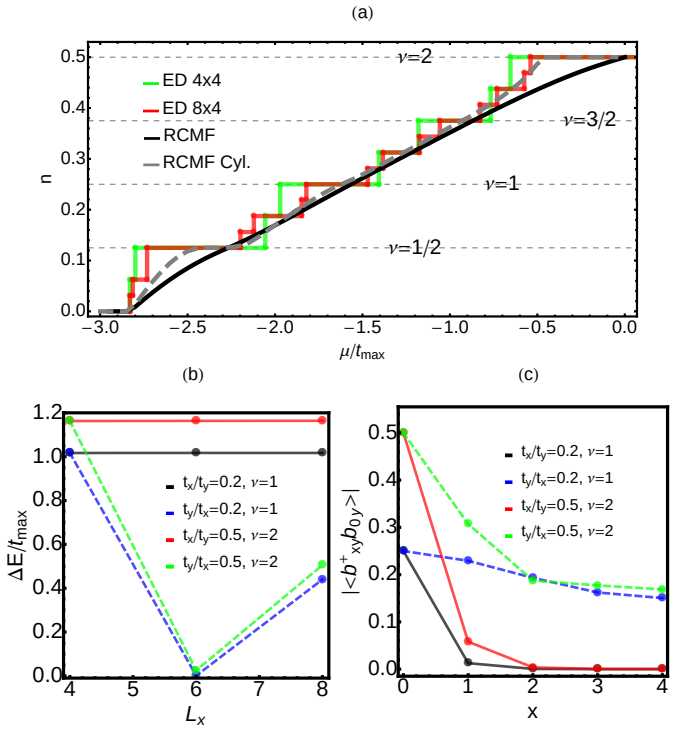

Figure 9.8.: (a) Density n as a function of μ at $t_x = t_y$ computed with ED on a 4×4 (green) and 8×4 (red) system, compared to RCMF results on the square lattice ("RCMF", black) and on a cylinder with 4 sites and periodic boundaries in the y-direction ("RCMF Cyl.", gray dashed). (b) Manybody gap for periodic boundaries and $L_y = 4$ as a function of L_x for $\nu = 1$ and $t_x/t_y = 0.2$ (black), $t_y/t_x = 0.2$ (blue, dashed), and for $\nu = 2$ and $t_x/t_y = 0.5$ (red), $t_y/t_x = 0.5$ (green, dashed). (c) Correlations $\left|\langle b^\dagger_{x,y} b_{0,y}\rangle\right|$ as a function of x on a system with periodic boundaries, $L_x = 8$, and $L_y = 4$ for the same values and colors as in (b).

field ($F = 0$) and therefore $n_c = 0$, as shown in Fig. 9.4d. While at large hopping anisotropy fractional fillings are largely suppressed, at low anisotropy the $F = 0$ solution shows plateaus at any filling commensurate with the 4×4 cluster, i.e. $\nu = m/4$ with integer m, as shown in Fig. 9.7c.

As mean-field approaches such as RCMF tend to overestimate the stability of symmetry-broken phases (see Secs. 4.2 and 8.1), we critically analyze the difference in free energy between the groundstate and the metastable plateaus in Fig. 9.7. As can be seen, this quantity shows local minima at integer ($\nu = 1, 2, 3$) and half-integer ($\nu = 1/2, 3/2, 5/2, 7/2$) fillings, while quarter fillings correspond to local maxima. This is consistent with the argument that without long-range interactions it costs a negligible energy to compress the $\nu = 1/4$ to the $\nu = 1/2$ Laughlin liquid [80]. The energy difference is particularly low in the vicinity of the liquid phases indicating that these might extend to lower values of hopping anisotropy. Furthermore, at low anisotropy (where the lowest band is particularly flat, see Fig. 9.6c and Sec. 9.1) the metastable plateau at $\nu = 1/2$ (and $\nu = 7/2$) is very close in free energy to the groundstate. This plateau has been shown to correspond to a fQH phase in ED [33, 80, 81], variational Gutzwiller mean field [170], and DMRG [82, 83] studies. As shown in Fig. 9.7c, at zero anisotropy, the condensate fraction of the groundstate shows a local minimum at both $\nu = 1/2$ and $\nu = 2$, further indicating that it might converge to zero with increasing cluster size.

In Fig. 9.8a we compare our RCMF results with ED results on finite systems with periodic

boundaries (see Appendix B.3). The 4×4 ED system differs from the $F = 0$ solution of RCMF by a renormalization of the hopping according to Eq. (9.11), resulting in a shift in chemical potential of the plateaus. We present a sweep of the density in chemical potential without hopping anisotropy (i.e. $t_x = t_y$). As can be seen the only regions where we see a large discrepancy with respect to ED are around fillings $\nu = 1/2$ and $\nu = 2$. These are the fillings where the metastable plateaus are particularly close in energy to the symmetry-broken groundstate (see Fig. 9.7).

We further compare the ED results with RCMF results on a cylinder with just 4 sites and periodic boundary conditions in y-direction. This can easily been done by modyfying the coarse-graining procedure of Eq. (8.3), which is now only integrated over k. This results in a new cluster-hopping

$$\bar{t}_{(X \pm 1, Y),(X,Y)} = \frac{2\sqrt{2}}{\pi} t_{(X \pm 1, Y),(X,Y)},$$
$$\bar{t}_{(X, Y \pm 1),(X,Y)} = t_{(X, Y \pm 1),(X,Y)}.$$

As can be seen in Fig. 9.8a, in this case also RCMF shows a fractional plateau at $\nu = 1/2$ and a plateau at $\nu = 2$, indicating that at zero anisotropy these phases are much more robust in the cylinder geometry than they are on the infinite square lattice. This will be investigated in more detail in Chapter 10.

To conclude, there are regions of the phase diagram, where the symmetry-broken groundstate and the metastable plateaus are too close in free energy to dismiss finite size effects. We denote these regions (identified by the condition $|\Omega_{\mathrm{GS}} - \Omega_{F=0}| < 3\%$ of the groundstate energy) as dashed areas in the phase diagram of Fig. 9.2.

10

Quasi-one-dimensional Harper-Hofstadter-Mott model

After studying the general Harper-Hofstadter-Mott model (HHMm) in Chapter 9, here we analyze the properties of the HHMm on a quasi-one-dimensional lattice, consisting of just a single flux quantum along the y-direction, while the x-direction is treated in the thermodynamical limit. For the flux of $\Phi = \pi/2$ considered here, this consists of 4 plaquettes in y-direction with periodic boundaries. Such a thin-torus limit has been previously investigated in fermionic systems in the lowest Landau level, where one-dimensional analogues of quantum Hall states were observed, which are predicted to continuously develop into their two-dimensional counterparts for increasing y-direction [178, 179, 180]. For interacting bosons an effective ladder model realizing the thin-torus limit with 2 sites in y-direction has been proposed, predicting a charge density wave analogue of the two-dimensional $\nu = 1/2$ fractional quantum Hall (fQH) phase [181].

As anticipated in Chapter 9, the quasi-one-dimensional limit in combination with anisotropic hopping amplitudes leads to larger many-body gaps due to the finite size in y-direction, and therefore to more stable topological phases than in in the fully two-dimensional limit. This can be a useful insight in the experimental search for bosonic topologically non-trivial phases, where robustness against the expected strong heating processes is of great importance [44]. Equally important, fillings which are expected to be always gapless in the fully two-dimensional limit [28, 177] can become gapped as a consequence of the finite size, leading to unexpected new groundstates. Another feature of the quasi-one-dimensional geometry lies in its low number of sites in y-direction, which makes it possible to map the spatial y-direction onto a finite number of internal degrees of freedom (in this case 4), rewriting the system as a one-dimensional multi-component system, which in the future could be simulated by cold atoms in the synthetic dimensions concept [182, 183, 184, 185], or by using microwave cavities [186].

While both exact diagonalization (ED) and the density matrix renormalization group (DMRG) have provided great insight in models such as the HHMm, they rely on finite system sizes. In two dimensions, these may be too small for ED whereas DMRG has difficulties converging for gapless phases due to rapid entanglement growth; ie, there is a preference for gapped, low entanglement phases. The reciprocal cluster mean-field method (RCMF, see Chapter 8) on the other hand tends to favor the opposite: it is defined in the thermodynamic limit and favors condensed phases (although it certainly can find topologically non-trivial phases as we will see). A systematic comparison of the two approaches therefore provides a promising path towards understanding the groundstate properties of the system in question. The restriction of the y-direction to four sites enables us to benchmark our RCMF results against ED, where it suffices to scale the system-size in the x-direction only.

While at other fillings our groundstate phase diagram features superfluid phases with striped or checkerboard order, at integer and half filling we observe a number of gapped phases in agreement with ED results. At $\nu = 1/2$ and $3/2$ we find that the quasi-one-dimensional geometry in combination with hopping anisotropy stabilizes gapped degenerate groundstates, which are quasi-

one-dimensional analogues of fQH phases with a quantized fractional Hall response, differing from their two-dimensional counterparts in the continuum through a weak charge density wave order. At integer fillings – where for the flux considered here the uncondensed phases are always gapless in the two-dimensional setup (see Chapter 9) – we see that the anisotropic setup introduces new phases with surprising properties: We observe gapped non-degenerate groundstates, which at $\nu = 1$ feature a "fermionic" Hall conductance of $\sigma_{xy} = 1$, while at $\nu = 2$ the Hall response consists of the quantized transport of a single particle-hole pair with total conductance of $\sigma_{xy} = 0$.

This chapter closely follows Ref. [4] and is organized as follows. The HHMm on a cylinder is introduced in Sec. 10.1. We present some preliminary ED results in Sec. 10.2, which will later be compared to RCMF. The RCMF approach to this specific problem is discussed in Sec. 10.3, while finally, in Sec. 10.4 we present our results on the groundstate phase diagram and discuss the individual phases.

10.1. Harper-Hofstadter-Mott model on a cylinder

The Hamiltonian of the HHMm (see Sec. 2.4.3) can be written as

$$H = -\sum_{x,y} \left(t_x e^{iy\Phi} b^\dagger_{x+1,y} b_{x,y} + t_y b^\dagger_{x,y+1} b_{x,y} + \text{h.c.} \right) + \frac{U}{2} \sum_{x,y} n_{x,y} \left(n_{x,y} - 1 \right) - \mu \sum_{x,y} n_{x,y}, \quad (10.1)$$

where the coordinates (x, y) parameterize a system of size $L_x \times L_y$, with periodic boundary conditions. The operators $b^{(\dagger)}_{x,y}$ are the annihilation (creation) operators at site (x, y), and $n_{x,y} = b^\dagger_{x,y} b_{x,y}$ is the occupation number operator. The hopping amplitudes in x- and y-direction are t_x and t_y, respectively, Φ is the flux through each plaquette, U is the strength of the on-site interaction, and μ is the chemical potential. Throughout our analysis we focus on the hard-core boson limit, $U \to \infty$, and the flux $\Phi = \pi/2$. We are left with two dimensionless parameters, the hopping anisotropy $(t_x - t_y)/t_{\max}$, and the chemical potential $\mu/t_{\max}$, where $t_{\max} = \max\{t_x, t_y\}$.

Furthermore, we focus on the cylinder-geometry in the thermodynamic limit, with $L_x \to \infty$ and $L_y = 4$. In the case $\Phi = \pi/2$ the magnetic unit-cell is of the size 1×4 for the Landau gauge used in Eq. (10.1). This choice of the lattice size therefore makes the cylinder quasi-one-dimensional, as only one unit-cell is present in the y-direction, and different groundstate phases than those of the fully two-dimensional HHMm (see Chapter 9) can be expected. Note that even though the magnetic unit cell can be chosen to consist of less than 4 sites in y-direction, e.g. of size 2×2 [166], the particles would still need to perform a (gauge-invariant) loop around 4 plaquettes in y-direction in order to pick up a trivial phase of 2π. Having just two plaquettes in y-direction on the other hand, would correspond to just half of the flux quantum 2π. In this sense our approach to quasi-one-dimensionality is different to the one of Refs. [181, 159, 158], where there is just one plaquette in y-direction on a ladder geometry.

The Hamiltonian (10.1) can be block-diagonalized in the hard-core boson limit with the Fourier transform $d_y(k) = \sqrt{L_x}^{-1} \sum_x e^{-ikx} d_{x,y}$, where $k \in \{ \frac{2\pi m}{L_x} \mid m \in \{0, \dots, L_x - 1\} \}$ is the quasi-momentum in the x-direction, and $d_{x,y}$ is the annihilation operator of a hard-core boson at site (x, y) with $\left(d_{x,y}\right)^2 = \left(d^\dagger_{x,y}\right)^2 = 0$. In this basis Eq. (10.1) for the case $\Phi = \pi/2$ can be rewritten as $H = \sum_k H_k$, where

$$H_k = -\sum_{y=0}^{3} \left(t_x e^{i(\frac{\pi}{2} y - k)} d^\dagger_y(k) d_y(k) + t_y d^\dagger_{y+1}(k) d_y(k) \right) + \text{H.c.} \quad (10.2)$$

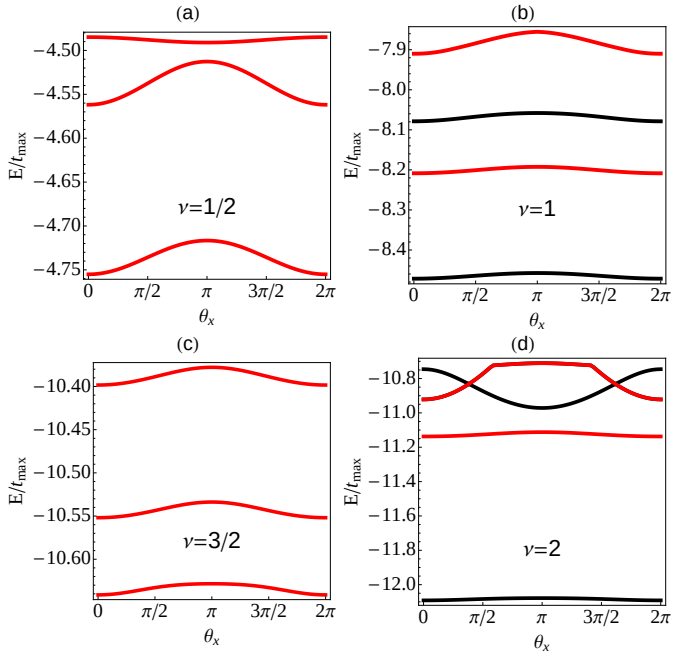

Figure 10.1.: Lowest 6 ED eigenvalues of a 4×4 system as a function of the twisted boundary angle θ_x for hopping anisotropy $(t_x - t_y)/t_{\max} = -0.35$, and fillings $\nu = 1/2$ (a), $\nu = 1$ (b), $\nu = 3/2$ (c), and $\nu = 2$ (d). Non-degenerate eigenstates are shown in black, doubly-degenerate ones in red.

Note that the Hamiltonian (10.1) in the hard-core boson case is invariant – up to a constant – under the charge-conjugation transformation (see also Sec. 9.2)

$$d_{x,y} \leftrightarrow d^\dagger_{x,y}, \quad \Phi \mapsto -\Phi, \quad \mu \mapsto -\mu. \tag{10.3}$$

This implies that the groundstates at positive and negative chemical potentials (or equivalently at densities n and $1 - n$), are related by the holes taking on the role of particles and the Hall response changing sign ($\sigma_{xy} \mapsto -\sigma_{xy}$) [172]. In the following we will therefore restrict ourselves to the case of $\mu \leq 0$ (i.e. $n \leq 1/2$), with the phases at positive chemical potentials related to the ones discussed in this work by Eq. (10.3).

10.2. Analysis using exact diagonalization

By examining the spectrum on a finite system, twisted boundaries offer a reasonable tool to compensate for finite-size effects in ED calculations regarding the robustness of spectral gaps. In our calculations on the 4×4 torus, the y-direction is treated exactly (as $L_y = 4$). We can therefore only introduce a twisted boundary angle in the x-direction, θ_x, defined as

$$\Psi(x + L_x) = e^{i\theta_x}\Psi(x). \tag{10.4}$$

Figs. 10.1 and 10.2 show the dependency of the spectrum on the twisting angle θ_x for fillings $\nu = \frac{1}{2}$, 1, $\frac{3}{2}$ and 2 at $(t_x - t_y)/t_{\max} = -0.35$ and $(t_x - t_y)/t_{\max} = 0.35$, respectively. The six lowest eigenvalues are shown, as computed with ED on the 4×4 lattice. When the spectrum mixes, the many-body groundstate on the lattice in the thermodynamic limit can be assumed to be gapless.

In Figs. 10.1 and 10.2 we see that the groundstate at fractional fillings is 2-fold degenerate.

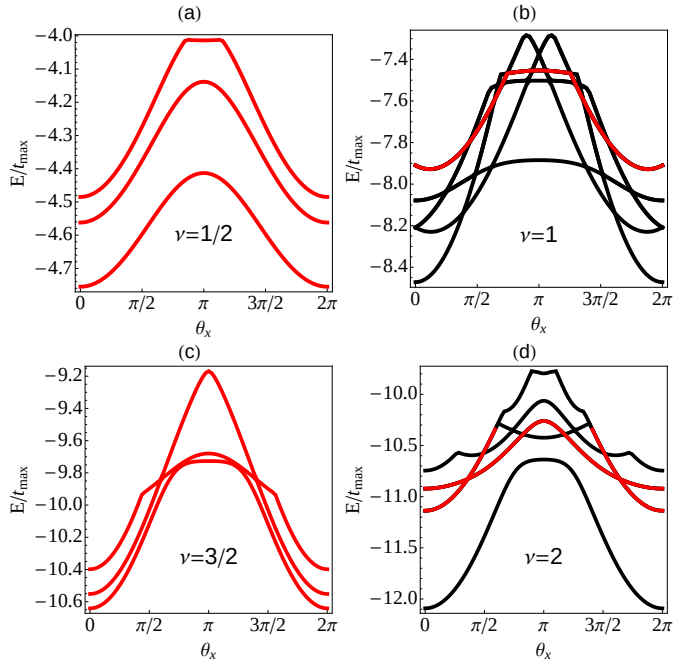

Figure 10.2.: Lowest 6 ED eigenvalues of a 4×4 system as a function of the twisted boundary angle θ_x for hopping anisotropy $(t_x - t_y)/t_{\max} = 0.35$, and fillings $\nu = 1/2$ (a), $\nu = 1$ (b), $\nu = 3/2$ (c), and $\nu = 2$ (d). Non-degenerate eigenstates are shown in black, doubly-degenerate ones in red.

Furthermore, we observe how the groundstates mix with the excited ones as a function of θ_x at $(t_x - t_y)/t_{\max} = 0.35$ and fillings $\nu = 1$ and $\nu = 3/2$, while the other cases shown (i.e., $\nu = 1/2$ and $\nu = 2$ in Fig. 10.2 and all negative values of $(t_x - t_y)/t_{\max} = -0.35$ in Fig. 10.1) appear to be gapped.

Let us now rewrite the Hamiltonian (10.2) into the form used in Sec. 9.1 suited to introduce the $\hat{h}$-vector. To this end, we define

$$A_y(k) = d_y^\dagger(k) d_y(k) - d_{y+2}^\dagger(k) d_{y+2}(k), \tag{10.5}$$

$$B(k) = \frac{1}{2} \sum_y d_{y+1}^\dagger(k) d_y(k) + \text{H.c.}, \tag{10.6}$$

the Hamiltonian (10.2) now reads

$$H = \sum_k \boldsymbol{v}_k \cdot \boldsymbol{h}_k, \tag{10.7}$$

where

$$\boldsymbol{v}_k = \begin{pmatrix} -2t_x \cos(k) \\ -2t_x \sin(k) \\ -2t_y \end{pmatrix}, \quad \boldsymbol{h}_k = \begin{pmatrix} A_0(k) \\ A_1(k) \\ B(k) \end{pmatrix}. \tag{10.8}$$

As discussed in more detail in Sec. 9.1, the expectation value $\left\langle \hat{h} \right\rangle = \frac{\langle \boldsymbol{h} \rangle}{|\langle \boldsymbol{h} \rangle|}$ can be used to measure the Hall response. The twisting angle θ_x can be seen as a magnetic flux piercing the system in y-direction and can be implemented by the transform

$$t_x \mapsto e^{i\theta_x / L_x} t_x, \tag{10.9}$$

transforming $\boldsymbol{v}_k \mapsto \boldsymbol{v}_{k-\theta_x/L_x}$, or equivalently - as long as the groundstate stays gapped -

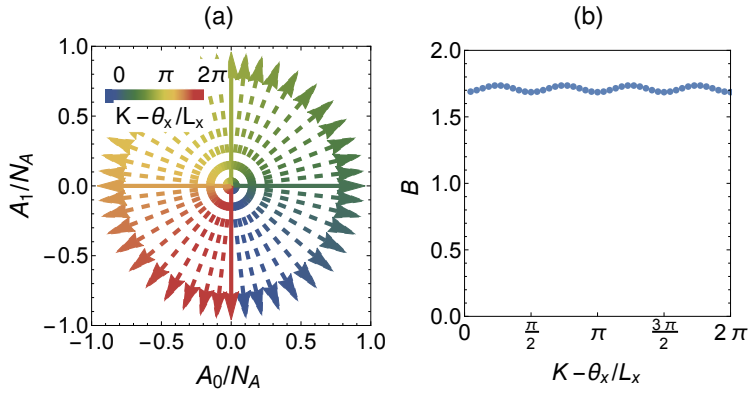

Figure 10.3.: Winding of the $\langle \hat{h} \rangle$-vector as a function of momentum K and twisting angle θ_x at filling $\nu = 1/2$ and hopping anisotropy $(t_x - t_y)/t_{\max} = -0.35$. (a) Projection of $\langle \hat{h} \rangle$ onto the (A_0, A_1)-plane. The components A_0 and A_1 are normalized with $N_A = \sqrt{A_0^2 + A_1^2}$, while the coloring corresponds to different values of $K - \theta_x/L_x$. (b) z-component of $\langle \hat{h} \rangle$, i.e. $\langle B \rangle$, as a function of $K - \theta_x/L_x$.

$\langle \hat{h}_k \rangle \mapsto \langle \hat{h}_{k+\theta_x/L_x} \rangle$.

As shown in Fig. 10.3, this causes the rotation of $\langle \hat{h} \rangle$ in response to the twisting angle in the (A_0, A_1)-plane. During $L_x/4$ subsequent charge-pumping processes (i.e. $\theta_x : 0 \to 2\pi \cdot L_x/4$) the many-body groundstate transforms as $A_0 \mapsto A_1$ and $A_1 \mapsto -A_0$, and therefore $\langle d_y^\dagger(k) d_y(k) \rangle \mapsto \langle d_{y+1}^\dagger(k) d_{y+1}(k) \rangle$. This means that the many-body groundstate is adiabatically translated by a single site in y-direction. For a single charge-pump process ($\theta_x : 0 \to 2\pi$) and filling ν (i.e. total number of particles $N = \nu L_x$ for $L_y = 4$) this amounts to the transverse transport of $N = \nu 4$ particles by one site, or equivalently ν particles through the full system (i.e. by $L_y = 4$ sites) in y-direction.

The winding shown in Fig. 10.3 for $\nu = 1/2$ therefore implies a Hall conductance of $\sigma_{xy} = 1/2$. Similarly, $\nu = 1$ and $\nu = 3/2$ correspond to $\sigma_{xy} = 1$, and $\sigma_{xy} = 3/2$, respectively. The winding in the $\nu = 2$ case is special, due to the charge-conjugation symmetry at $n = 1/2$ [see Eq. (10.3)]. For each particle being transported there is also a hole being transported, resulting in a total quantized transport of a particle-hole pair, and zero Hall conductivity.

For the integer filling phases – as their many-body gap is a direct consequence of the anisotropic geometry – the Hall conductance is highly anisotropic, in the sense that it is quantized for charge-pump processes in the x-direction only. As the groundstate mixes with the excited states as a function of twisting in y-direction (as seen in Chapter 9), $\sigma_{yx} \neq \sigma_{xy}$ is not quantized, emphasizing the quasi-one-dimensional nature of these phases.

Finally, it should be noted that if the y-direction is mapped onto four different species/internal states, such that $\langle d_y^\dagger(k) d_y(k) \rangle$ and $\langle d_{y+1}^\dagger(k) d_{y+1}(k) \rangle$ can be resolved separately in time-of-flight measurements (see Chapter 3), $\langle \hat{h} \rangle$ could be computed in experiment, providing a direct measurement of the Hall response in equilibrium. For more details on the measurement of topological properties through the $\langle \hat{h} \rangle$-vector see Appendix B.2.

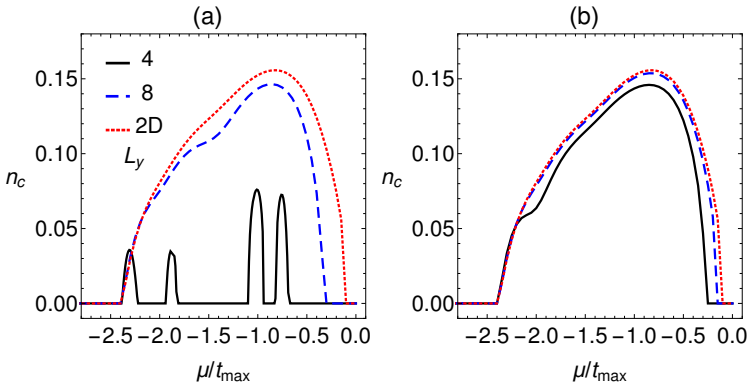

Figure 10.4.: Condensate density n_c as a function of chemical potential $\mu/t_{\max}$ for different lattices, i.e. $L_y = 4$ (solid, black), $L_y = 8$ (dashed, blue) and $L_y \to \infty$ (dotted, red). In (a) the hopping anisotropy is $(t_x - t_y)/t_{\max} = -0.35$ and in (b) $(t_x - t_y)/t_{\max} = 0.35$.

10.3. Reciprocal cluster mean-field approach

10.3.1. Quasi-one-dimensional vs two-dimensional geometry

The quantity which differentiates between the different lattice geometries in RCMF is the coarse-grained dispersion on the 4×4 cluster, i.e.

$$\bar{\epsilon}_{\mathbf{K}} = \frac{C_x C_y}{L_x L_y} \sum_{\tilde{\mathbf{k}}} \epsilon_{\mathbf{K}+\tilde{\mathbf{k}}}, \tag{10.10}$$

where $\mathbf{K} = \{(0,0), (0,\pi/2), (0,\pi), (0,3\pi/2)\}$ are the quasi-momenta of the 4×4 cluster (see Chapter 8 for details).

The general two-dimensional system can be written as $H = \sum_{\mathbf{k}} H_{\mathbf{k}}$ (see Chapter 9), where $\mathbf{k} = (k, q)$, k is the quasi-momentum in x-direction, q the quasi-momentum in y-direction, and

$$H_{\mathbf{k}} = -\sum_{y=0}^{3} \left(t_x e^{i(\frac{\pi}{2}y - k)} d_y^\dagger(\mathbf{k}) d_y(\mathbf{k}) + t_y e^{-iq} d_{y+1}^\dagger(\mathbf{k}) d_y(\mathbf{k}) \right) + \text{H.c.}. \tag{10.11}$$

In the thermodynamic limit in x-direction assumed for all geometries ($L_x \to \infty$), $k \in [0, 2\pi]$ is continuous. For $L_y = 4$ considered in this chapter, $q = 0$, such that the coarse-grained dispersion is given by a one-dimensional integral $\bar{\epsilon}_{\mathbf{K}} = \frac{C_x}{L_x} \int \mathrm{d}\tilde{k}\ \epsilon_{K+\tilde{k}}$, resulting in the effective hopping amplitudes

$$\bar{t}_{\mathbf{R}+\mathbf{e}_x,\mathbf{R}} = \frac{2\sqrt{2}}{\pi}\, t_x\, e^{iY\frac{\pi}{2}}, \tag{10.12}$$

$$\bar{t}_{\mathbf{R}+\mathbf{e}_y,\mathbf{R}} = t_y, \tag{10.13}$$

with cluster coordinates $\mathbf{R} = (X, Y)$.

In a system with arbitrary finite size in y-direction, $q = n2\pi/L_y$ with $n = 0, 1, \ldots, L_y/4$. For a cylinder with $L_y = 8$ (and therefore two flux quanta in y-direction) Eq. (10.10) yields the effective hopping amplitudes

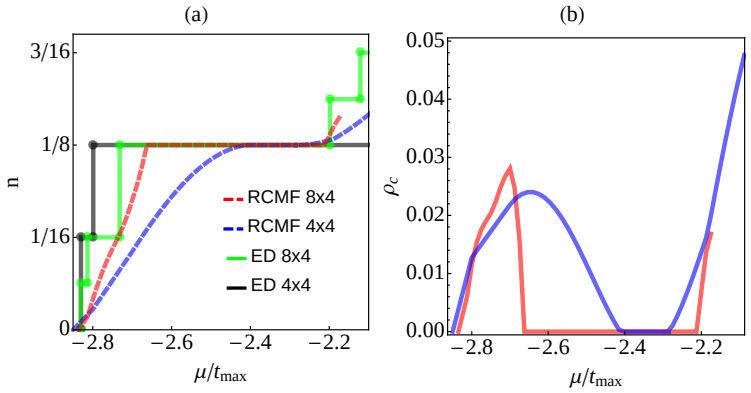

Figure 10.5.: Comparison of particle density (a) and condensate density (b) as a function of chemical potential for $t_x = t_y$ computed with ED on a 4×4 torus (black), ED on an 8×4 torus (green), RCMF with a 4×4 cluster impurity (blue) and RCMF with an 8×4 cluster impurity (red).

$$\bar{t}_{\mathbf{R}+\mathbf{e}_x,\mathbf{R}} = \frac{2\sqrt{2}}{\pi}\, t_x\, e^{iY\frac{\pi}{2}}, \tag{10.14}$$

$$\bar{t}_{\mathbf{R}+\mathbf{e}_y,\mathbf{R}} = \frac{\sqrt{2+\sqrt{2}}}{2}\, t_y. \tag{10.15}$$

Finally, in the case $L_y \to \infty$ also $q \in [0, \pi/2]$ becomes continuous, and the integral $\bar{\epsilon}_{\mathbf{K}} = \frac{C_x C_y}{L_x L_y} \int \mathrm{d}\tilde{k}\mathrm{d}\tilde{q}\, \epsilon_{\mathbf{K}+\tilde{\mathbf{k}}}$ yields the effective hopping amplitudes used in Chapter 9

$$\bar{t}_{\mathbf{R}+\mathbf{e}_x,\mathbf{R}} = \frac{2\sqrt{2}}{\pi}\, t_x\, e^{iY\frac{\pi}{2}}, \tag{10.16}$$

$$\bar{t}_{\mathbf{R}+\mathbf{e}_y,\mathbf{R}} = \frac{2\sqrt{2}}{\pi}\, t_y. \tag{10.17}$$

In Fig. 10.4 we compare the three geometries ($L_y = 4$, $L_y = 8$ and $L_y \to \infty$). We show the condensate density $n_c = \frac{1}{C_x C_y} \sum_{\mathbf{R}} |\phi_{\mathbf{R}}|^2$ for the three different lattices as a function of chemical potential, illustrating how the $L_y = 8$ cylinder with just two unit-cells in y-direction already shows much better agreement with the gapless two-dimensional results of Chapter 9, further indicating the exclusive quasi-one-dimensional nature of the $L_y = 4$ cylinder.

10.3.2. Scaling at low densities

As mentioned in Chapter 8, for the RCMF approximation to work, it is indispensable that the momentum values of the four minima of the non-interacting dispersion at $k = 0, \pi, \pm\pi/2$ can be represented within the $C_x \times 4$ cluster impurity. After the 4×4 cluster employed in this work the next cluster size which is consistent with this approach would be therefore 8×4, which in the absence of particle number conservation is computationally out of reach.

In the case of low density however we can restrict the basis of the 8×4 cluster to the particle number sectors $N = 0, 1, 2, ..., 6$, making the search for a symmetry-broken groundstate numerically accessible. The resulting hopping amplitudes with respect to the 4×4 cluster change accordingly to

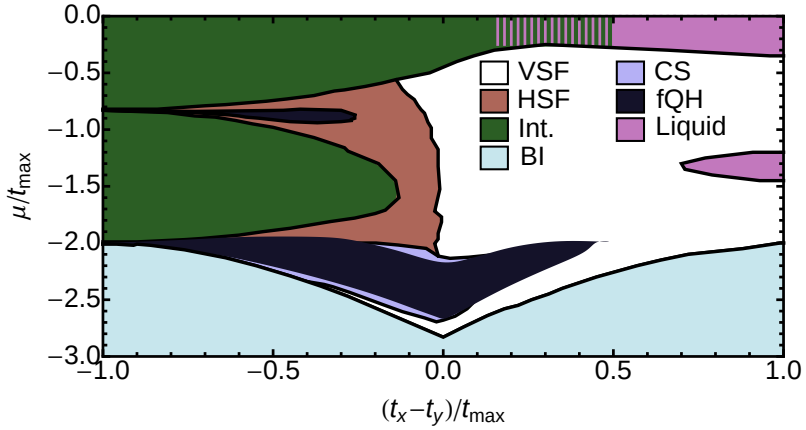

Figure 10.6.: Groundstate phase diagram of the HHMm on the $L_y = 4$ cylinder as computed with RCMF as a function of chemical potential $\mu/t_{\max}$ and hopping anisotropy $(t_x - t_y)/t_{\max}$. The observed phases are: band insulator (BI, light blue), gapped phases at integer fillings $\nu = 1, 2$ (Int., green), quasi-one-dimensional analogues of fractional quantum Hall phases at fillings $\nu = 1/2, 3/2$ (fQH, dark grey), gapless liquid (Liquid, pink), and superfluid phases with different patterns: vertically striped (VSF, white), horizontally striped (HSF, brown) or with checkerboard order (CS, dark blue). The phases in the purely one-dimensional case are an uncondensed superfluid at $(t_x - t_y)/t_{max} = 1$, and gapped decoupled 4-site rings at $(t_x - t_y)/t_{\max} = -1$ (except for the band-insulator at density $n = 0$). In the dashed region around zero chemical potential the results are inconclusive whether the phase is gapped (Int.) or gapless (Liquid). The fractional plateau at $\nu = 1/2$ was computed using an 8×4 cluster, unlike the results for higher chemical potentials/densities which were computed using a 4×4 cluster, see also Sec. 10.3.2. The plateau at $\nu = 3/2$ is most likely larger than the one found here (see Fig 10.11c), however both RCMF and ED are inconclusive on the exact phase boundaries within the accessible cluster-/system-sizes.

$$\bar{t}_{\mathbf{R}+\mathbf{e}_x,\mathbf{R}} = \frac{8}{\pi} \sin\left(\frac{\pi}{8}\right) t_x \, e^{iY\frac{\pi}{2}}, \tag{10.18}$$

$$\bar{t}_{\mathbf{R}+\mathbf{e}_y,\mathbf{R}} = t_y. \tag{10.19}$$

In Fig. 10.5 we compare results computed with such a restricted basis using an 8×4 cluster in the vicinity of density $n = 1/8$ (i.e. $\nu = 1/2$), where such an approach is still controlled. We see how ED and RCMF scale differently with cluster size, converging towards each other: since ED prefers gapped phases, the fractional plateau at $\nu = 1/2$ shrinks with cluster size. As RCMF prefers gapless phases, the fractional plateau increases with cluster size (see also Fig. 10.11a).

10.4. Results

The groundstate phase diagram of the quasi-one-dimensional model computed with RCMF is shown in Fig. 10.6 in terms of the hopping anisotropy $(t_x - t_y)/t_{\max}$ and the chemical potential $\mu/t_{\max}$. In the limit $(t_x - t_y)/t_{\max} = 1$ (i.e. $t_y = 0$), the system consists of four decoupled infinite chains each exhibiting an uncondensed one-dimensional superfluid (or band-insulating) groundstate. At $(t_x - t_y)/t_{\max} = -1$ (i.e. $t_x = 0$), instead, the cylinder reduces to an infinite

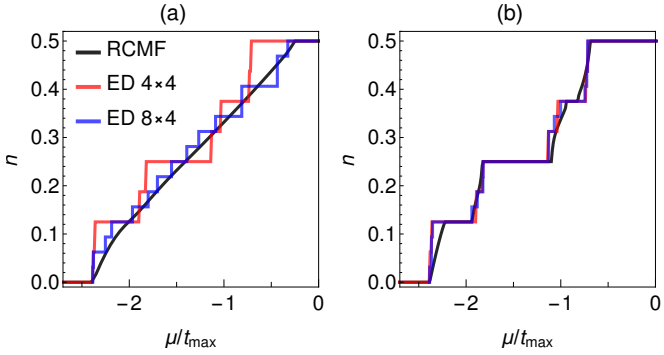

Figure 10.7.: Comparison between results computed with RCMF (black) and ED on system sizes 4×4 (red) and 8×4 (blue) with periodic boundary conditions. Particle density n as a function of chemical potential $\mu/t_{\max}$ at hopping anisotropy $(t_x - t_y)/t_{\max} = 0.35$ (a) and $(t_x - t_y)/t_{\max} = -0.35$ (b).

set of decoupled 4-site rings which – depending on the filling – can exhibit gapped phases. The phase diagram therefore strongly differs at negative anisotropies from the one observed in the fully two-dimensional model in Chapter 9. The fact that the phases discussed in the following are in part entirely related to the quasi-one-dimensional geometry of the lattice is further evidenced by the fact that the situation changes drastically as soon as L_y is changed from 4 to 8 with two unit cells in the y-direction, as discussed in Sec. 10.3.1, where the $L_y = 8$ results are much closer to the fully two-dimensional results than the ones for $L_y = 4$.

Before discussing the different phases in more detail, let us illustrate the role of sign asymmetry in the hopping anisotropy as well as perform a benchmarking of RCMF against ED by studying the density as a function of chemical potential, shown in Fig. 10.7. If μ is sufficiently negative the model is in a trivial band-insulating (BI) phase with zero particles for either anisotropy. For hopping anisotropy $(t_x - t_y)/t_{\max} = 0.35$ (Fig. 10.7a), RCMF always finds a condensed groundstate except in a narrow region at density $n = 1/2$. The ED results (which can only exhibit plateaus at densities commensurable with the system size) tend towards the continuous RCMF results as L_x is increased, as all observed plateaus quickly shrink with system size (again excluding the narrow region at density $n = 1/2$, which remains gapped in either method). For hopping anisotropy $(t_x - t_y)/t_{\max} = -0.35$ (Fig. 10.7b), the agreement between RCMF and ED increases further, as the RCMF groundstate now also shows plateaus at integer ($\nu = 1, 2$, i.e. $n = 1/4, 1/2$) and fractional ($\nu = 1/2, 3/2$, i.e. $n = 1/8, 3/8$) fillings. The fractional plateaus, which look almost system size independent in ED, are however smaller in RCMF. In the limit of low densities however, we are able to extend the RCMF cluster from a size of 4×4 to 8×4 (see Sec. 10.3.2). As can be seen in Figs. 10.5 and 10.11a for the plateau at $\nu = 1/2$ this increases the accuracy substantially, finding excellent agreement with ED.

10.4.1. Symmetry-broken phases

The groundstate away from integer ($\nu = 1, 2$) and half-integer ($\nu = 1/2, 3/2$) filling is always condensed, exhibiting different density and condensate modulations as a function of chemical potential and hopping anisotropy. The three resulting phases we will discuss in the following exhibit first order phase transitions.

At positive anisotropy a large part of the phase diagram is occupied by the vertically striped superfluid (VSF) where both the total and the condensate density exhibit vertical stripes (see Fig. 10.8a). With increasing negative anisotropy, these patterns are rotated by $\pi/2$ and the superfluid becomes horizontally striped (HSF). Finally, in the vicinity of filling $\nu = 1/2$ the

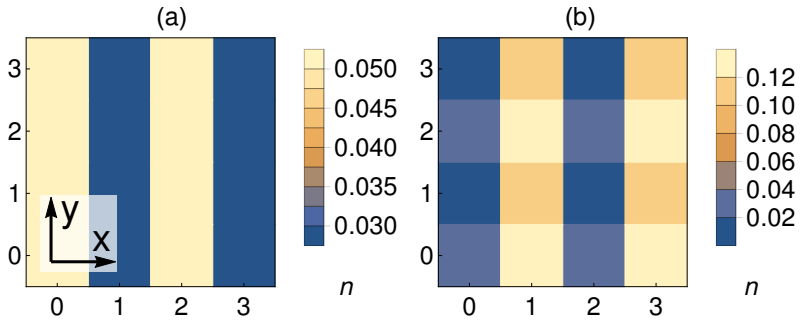

Figure 10.8.: Patterns of the particle density n in two different superfluid groundstate phases: (a) The vertically striped superfluid (VSF) at $(t_x - t_y)/t_{\max} = 0.35$ and $\mu/t_{\max} = -2.3$; (b) The checkerboard superfluid (CS) at $(t_x - t_y)/t_{\max} = -0.35$ and $\mu/t_{\max} = -2.3$.

groundstate exhibits a checkerboard superfluid pattern, apparently due to doping mechanisms on top of the degenerate groundstate (CS, see Fig. 10.8b).

10.4.2. $U(1)$-symmetry preserving phases

In the absence of a finite condensate order parameter $\phi_{\mathbf{R}}$, the RCMF Hamiltonian reduces to a finite $U(1)$-symmetry-preserving 4×4 torus with periodic boundaries. We can therefore turn to ED in order to further analyze the properties of $U(1)$-symmetry preserving phases (the only difference is a rescaling of the energy unit).

In order to extrapolate to the thermodynamic limit $L_x \to \infty$ we apply the twisted boundary conditions $\Psi(x + L_x) = e^{i\theta_x}\Psi(x)$. This allows us to estimate the many-body gap as

$$\Delta E = \min_{\theta_x}(\varepsilon_1(\theta_x) - \varepsilon_{\mathrm{GS}}(\theta_x)), \tag{10.20}$$

where $\varepsilon_{\mathrm{GS}}$ and ε_1 are the energies of the groundstate(s) and the first excited state, respectively. In addition, by analyzing the behavior of the quasi-one-dimensional h-vector as a function of the twisting angle θ_x we can extrapolate the topological properties of the system (see Sec. 10.2). If the h-vector shows a closed-loop as a function of θ_x, and the groundstate does not mix with the excited states such that (10.20) stays finite, it implies that the many-body groundstate is adiabatically translated in y-direction during one charge-pump cycle, resulting in different quantized Hall conductances depending on the filling.

Integer filing

At (low enough) negative hopping anisotropy we observe non-degenerate groundstates at integer fillings $\nu = 1$, and 2 (see "Int." in Fig. 10.6). In Figs. 10.9b and 10.9d we show the many-body gap computed with ED for these fillings as a function of hopping anisotropy. The gap computed with (10.20) on a 4×4 system, as well as the scaling when going from $L_x = 4$ to $L_x = 8$ clearly indicate a gapped groundstate. Furthermore, as shown in Figs. 10.11b and 10.11d, the single-particle gap computed with ED agrees perfectly with the region where we observe the gapped integer filling phases in RCMF.

For $\nu = 2$ a known candidate for gapped non-trivial many-body states in the HHMm is the bosonic integer quantum Hall (biQH) phase with transverse conductance $\sigma_{xy} = 2$ [187, 28, 166, 188, 82, 189]. While this phase has been found in the HHMm with hard-core bosons at lower fluxes [82], the case of $\Phi = \pi/2$ is special, as filling $\nu = 2$ corresponds to a density of $n = 1/2$, where hard-core bosons show a $\mathcal{CT}$-symmetry (as discussed in Sec. 10.1). We checked numerically

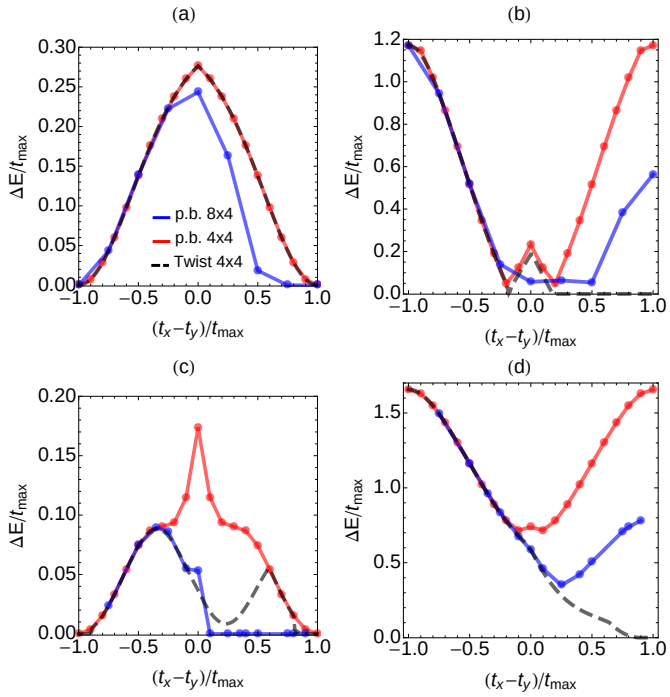

Figure 10.9.: Many-body gaps $\Delta E/t_{\max}$ as a function of hopping anisotropy $(t_x - t_y)/t_{\max}$ computed using twisted boundaries on a 4×4 system (black dashed), periodic boundaries on a 4×4 system (red), and periodic boundaries on a 8×4 system (blue) for fillings $\nu = 1/2$ (a), $\nu = 1$ (b), $\nu = 3/2$ (c), and $\nu = 2$ (d).

that this symmetry is not spontaneously broken, by computing the overlap of the ED groundstate with its $\mathcal{CT}$-transform (i.e. the complex-conjugated groundstate after a particle-hole transform), yielding always 1. The Hall conductance of this groundstate can therefore only be $\sigma_{xy} = 0$.

At filling $\nu = 1$, a biQH phase can only be expected in the presence of two different bosonic species [190] (i.e. filling $\nu = 1 + 1$). Another candidate for gapped phases is the non-abelian Moore-Read state [191, 192], which however is characterized by a degenerate groundstate, not observed here.

As discussed in Sec. 10.2, the h-vector winds once around the origin as a function of the twisting angle for both fillings. For $\nu = 2$ this implies the quantized transverse transport of a single particle-hole pair during one charge-pumping cycle, resulting in a total Hall conductance of $\sigma_{xy} = 0$, consistent with the charge conjugation-symmetry of (10.3). For $\nu = 1$ on the other hand this implies the transport of a single particle, and thereby a Hall conductance of $\sigma_{xy} = 1$, as would be observed in a fermionic integer quantum Hall effect [27].

Especially the latter phase may seem surprising, as such a bosonic phase with odd Hall conductance is expected to be either gapless, or show intrinsic topological order and thereby a degenerate groundstate [28, 177]. However, while in the two-dimensional lattice phases with $\phi = 0$ at these fillings are found to be always gapless liquids (see Chapter 9), in the quasi-one-dimensional setup these are connected to the limit of decoupled 4-site rings at $t_x = 0$, where hard-core bosons behave as free fermions gapped by the finite size of the rings, providing an intuitive explanation for the "fermionic" behavior of the $\nu = 1$ phase. In fact, the argument of Ref. [28] relies on the fact that the quasiparticle excitations need to behave as fermions under exchange in such an odd Hall conductivity phase.

As discussed in Chapter 9, in two-dimensional systems a $\mathcal{CT}$-symmetric phase such as the one observed at $\nu = 2$ is expected to be topologically trivial [22, 23, 24]. On a cylinder, however, this

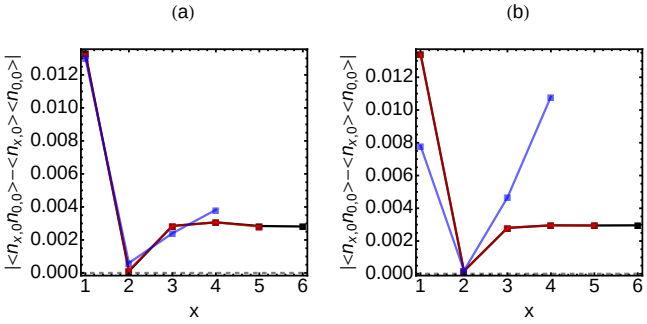

Figure 10.10.: Density-density correlations $|\langle n_{x,0}n_{0,0}\rangle - \langle n_{x,0}\rangle\langle n_{0,0}\rangle|$ as a function of x for filling $\nu = 1/2$ and $t_x = t_y$ on a cylinder with $L_y = 4$ and $L_x = 8$ (blue), $L_x = 10$ (red), and $L_x = 12$ (black). Panels (a) and (b) show the two degenerate groundstates at momentum sectors $K = 0$ and $K = \pi$, respectively. Due to the periodic boundary conditions, the correlations are only shown up to the center of the cylinder at $L_x/2$.

phase is gapped as the one-dimensional limit is approached, where $\mathcal{CT}$-symmetric phases can have a non-zero topological $\mathbb{Z}$ invariant for non-interacting fermions [22]. Wether the quantized particle-hole transport is a consequence of topologically protected edge modes on the cylinder remains to be investigated on larger system sizes, possibly using DMRG [82, 29, 59].

Eventually, when going to positive hopping anisotropies, the gaps computed with (10.20) and the strongly size-dependent scaling of the gaps with periodic boundaries shown in Figs. 10.9b and 10.9d indicate a gapless groundstate for both fillings. These phases are equivalent to the anisotropic gapless liquid observed in the fully two-dimensional model (see Chapter 9). In fact, at positive anisotropies, those phases are connected to the limit of decoupled infinite chains at $t_y = 0$, where the hard-core bosons are in a superfluid groundstate.

Fractional filling

In the region of negative hopping anisotropies we observe commensurate phases at fillings $\nu = 1/2$, and $3/2$. For both fillings the system is characterized by a two-fold degenerate groundstate, and is gapped for negative (and low positive) anisotropies, as evidenced by the ED results shown in Figs. 10.9a and 10.9c.

As for the integer filling phases, the h-vector shows a closed loop as a function of the twisting angle (see Sec. 10.2) indicating Hall conductances of $\sigma_{xy} = 1/2$, and $3/2$, respectively. In the two-dimensional case a fQH phase at filling $\nu = 1/2$ has already been observed in previous ED [33, 81, 80], variational Gutzwiller mean field [170], and DMRG [82, 83] studies, while the one at $\nu = 3/2$ has not been observed in the two-dimensional limit. As for the integer phases, which are only gapped on the cylinder, the fractional phases therefore appear to be much more stable on a quasi-one-dimensional geometry.

In order to fully classify the gapped phases at fractional filling, we turn to the density-density correlations in x-direction $|\langle n_{x,y}n_{0,y}\rangle - \langle n_{x,y}\rangle\langle n_{0,y}\rangle|$. As shown in Fig. 10.10 for the two degenerate groundstates at filling $\nu = 1/2$ and $t_x = t_y$ for $y = 0$, these correlations indicate a charge density wave order: after decreasing for short distances they quickly saturate to a small finite value as a function of x and appear to be converged in the system size L_x for $L_x = 10$ and 12. A similar behavior is also observed for other values of y and at filling $\nu = 3/2$.However, while for the integer filling phases the many-body gap closes for twisting in the y-direction and $\sigma_{yx} \neq \sigma_{xy}$ is not quantized, the fractional phases stay gapped for twisting in both directions, and therefore show a truly two-dimensional Hall response $\sigma_{yx} = \sigma_{xy}$. We conclude that these

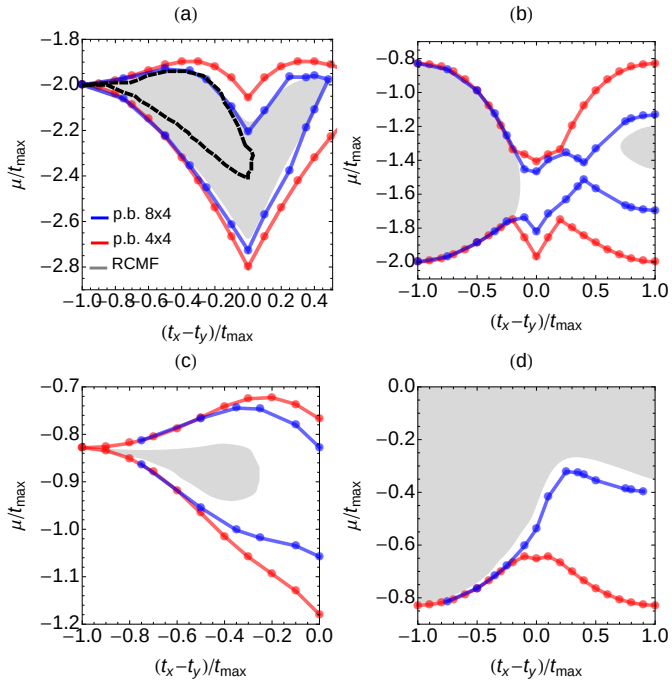

Figure 10.11.: Regions of the groundstate phase diagram computed with RCMF where we observe non-trivial phases with $\phi = 0$ (grey), compared with the single particle gaps measured with ED using periodic boundaries on system sizes 4×4 (red) and 8×4 (blue) for fillings $\nu = 1/2$ (a), $\nu = 1$ (b), $\nu = 3/2$ (c), and $\nu = 2$ (d). In panel (a) the RCMF plateau is computed using an 8×4 cluster, while the RCMF results using a 4×4 cluster (which is employed for all other fillings) are shown as a black dashed line.

phases are quasi-one-dimensional analogues of fQH phases, which continuously develop into their two-dimensional counterparts as the circumference of the cylinder is increased [178, 179, 180, 181]. A similar case has been discussed in the $1 + 1$-dimensional two-leg ladder with an additional external parameter in Ref. [181].

While showing the same general trend, the single particle gaps predicted by ED for the fractional phases in Figs. 10.11a and 10.11c are significantly larger than the ones predicted by RCMF using a 4×4 cluster, which tends to underestimate long-range-entangled phases. However, when employing an 8×4 cluster for low densities (see Sec. 10.3.2), the results on the $\nu = 1/2$ plateau show excellent agreement with ED. Unfortunately, for the $\nu = 3/2$ plateau such a cluster size is out of reach for RCMF, and also ED appears to not be converged with system size, such that we can only conclude that the phase boundaries of the fractional phase at $\nu = 3/2$ lie in between the ones found with ED and RCMF.

In the isotropic two-dimensional system, the fQH phase at filling $\nu = 1/2$ predicted by other methods [33, 81, 80, 82, 83, 170] is found to be slightly metastable in RCMF (see Chapter 9). However, seeing the scaling when increasing C_x to 8, we expect that an 8×8 cluster would be needed to fully capture the groundstate behavior at $\nu = 1/2$ in the two-dimensional case. Finally, we note that both our RCMF results and our ED results do not point to a gapped phase at filling $\nu = 2/3$ claimed in Ref. [82] (see Appendix B.5).

11

Conclusion

In this thesis, we derived and benchmarked several different self-consistent schemes for the numerical treatment of interacting bosonic lattice systems. As these methods are – although approximate – highly flexible and numerically simple, the aim is to apply them to systems where path integral quantum Monte Carlo (QMC) simulations [47, 48, 49] are subject to a sign-problem (e.g. in the presence of gauge fields [37, 38, 39] or spin-orbit coupling [50, 51, 52]) and the density matrix renormalization group (DMRG) [55, 56, 57, 58, 59] cannot be applied (i.e. in high dimensions or in the presence of critical phases). The main concept that the self-consistent methods presented in this work have in common, relies on the solution of the full lattice problem in the thermodynamical limit by means of an exactly solvable auxiliary system, dubbed *reference system*, sharing the same interaction (and disorder distribution).

In order to filter out the essential degrees of freedom such a reference system should have to yield a good accuracy, we developed the *Bogoliubov+U theory* (B+U). B+U uses a single-site Hamiltonian as reference system, which contains just three variational parameters, controlling the condensate, the particle density, and the pair creation/annihilation of depleted particles, respectively. We were able to reproduce the zero-temperature phase diagram and thermodynamic observables of the three- and two-dimensional Bose-Hubbard model (BHm) [9, 11] in excellent agreement with numerically exact QMC data [47, 48, 49, 87], while at finite temperature the method looses accuracy.

Next, we turned to the *self-energy functional theory* (SFT), a non-perturbative framework previously developed for fermions [70, 71, 72, 73]. We systematically extended SFT to include the possibility of a broken $U(1)$-symmetry, deriving a functional which depends on the self-energies of the one- and two-point propagators, i.e. the condensate and the connected Green's function. The SFT approximation then consists of replacing the self-energies of the lattice system by their counterparts from the reference system. While we showed that SFT reduces to bosonic dynamical mean-field theory (BDMFT) [62, 63, 64, 65, 66, 67] in a certain limit, it represents a more general variational scheme where the reference system can be parametrized freely (as long as it shares the same interaction and disorder distribution of the lattice), allowing for the construction of diagrammatically sound approximations that are quantitatively precise and controlled, but remain computable by modest means.

By using the same reference system as in B+U, we were able to accurately reproduce QMC data both at zero and finite temperature in the BHm. We also investigated the frustrated BHm with additional diagonal next-nearest-neighbor hopping, which is beyond the reach of QMC due to the sign-problem. Furthermore, we computed the high-energy features of spectral functions, which also cannot be computed in QMC as it is restricted to the imaginary-frequency axis and has to resort to analytic continuation for real-frequency quantities [53, 54].

We then extended SFT to the case of disordered lattice systems, deriving a functional that depends only on the self-energies of the disorder-averaged interacting propagators. By using the same reference system as in the clean model, we investigated the BHm in the presence of local uncorrelated disorder on a cubic lattice [9, 14, 15, 16]. We showed that the method remains

very accurate for low disorder, and in the case of strong interactions. If the disorder dominates over both the interaction and the non-interacting bandwidth, however, the restricted variational subspace of the reference system is no-longer general enough to stabilize a stationary solution. By systematically studying local spectral functions and comparing to analytic results in the atomic limit, we showed that the strongly-interacting Bose glass phase of the disordered BHm is characterized by different regimes as a function of the disorder strength Δ. With increasing Δ, sites with local occupations $n \neq 1$ appear as predicted by the atomic limit, leading to crossovers between different regimes whenever a new local occupation n is activated. Furthermore, we showed that the phase transition from the Bose glass to the superfluid at strong interactions is driven by the percolation of superfluid lakes which form around doubly occupied sites, leading to a small condensate fraction over an atomic-limit background.

In order to be able to treat also systems with unit cells larger then a single site, we further derived the *reciprocal cluster mean-field* method (RCMF). In this method, the reference system consists of a cluster of sites which is decoupled by the mean-field decoupling approximation [9, 60, 61] in reciprocal space. Unlike previous cluster mean-field methods [77, 78], it does not break the translational-invariance of the lattice, leading to more accurate results and crucially preserving the topological features and symmetries of the non-interacting dispersion. We benchmarked the method on the BHm with hard-core bosons and on a two-leg ladder in the presence of artificial gauge fields [159, 158], showing excellent agreement with numerically exact data.

We then proceeded to investigate the strongly-interacting Harper-Hofstadter-Mott model (HHMm) [18, 19, 20, 21] by combining RCMF and exact diagonalization (ED) [33, 80, 81]. For the two-dimensional model with hopping-anisotropy we observed a groundstate phase diagram featuring band insulating, striped superfluid, and supersolid phases. At finite anisotropy and integer filling we further found anisotropic gapless uncondensed liquid groundstates. At fractional filling we observed metastable fractional quantum Hall (fQH) phases, predicted as the groundstate by other methods [33, 80, 81, 82, 83, 84]. As RCMF tends to overestimate condensed phases this is most likely related to the finite size of the reference system.

Finally, we turned to the strongly-interacting HHMm on a quasi-one-dimensional lattice consisting of a single magnetic-flux-quantum in one direction. We found that the quasi-one-dimensional geometry stabilizes gapped phases, whose topological features are analyzed through a newly introduced *topological* vector $h_{k,q}$. We found quasi-one-dimensional analogues of fQH phases at fillings 1/2 and 3/2 and unconventional gapped non-degenerate groundstates at filling 1 (characterized by a quantized odd "fermionic" Hall conductance) and filling 2 (with total zero Hall conductance, but characterized by the quantized transverse transport of a single particle-hole pair as Hall response). By systematically comparing RCMF and ED, which approach the thermodynamical limit from opposite sides (the first method favours gapless, the second one gapped phases), we were able to give conclusive quantitative answers on the phase boundaries of the gapped phases.

In the future, SFT could also be used in combination with cluster reference systems. This can be done in the spirit of the variational cluster approximation used in SFT for fermions [76] and $U(1)$-symmetric bosons [75], while RCMF provides insight on how to treat the $U(1)$-symmetry-breaking field on clusters. This would enable the study of systems with non-trivial unit cells (such as the HHMm) in the thermodynamic limit with higher accuracy. It further would allow for the systematic study of spectral functions and the effect of finite temperature or disorder in such systems. The bosonic version of SFT could further be extended to the study of out-of-equilibrium problems. Here, however, it would most likely encounter the same technical difficulties as recently observed in the fermionic version [129, 130]. While being (slightly) less accurate, RCMF is numerically extremely simple. As it systematically overestimates condensed phases, while ED does the opposite, the combination of RCMF and ED provides a promising

venue for the numerical simulation of bosonic lattice systems with larger unit cells. Where the two methods agree, the results can be considered to be under control. Another interesting venue for RCMF is its extention to out-of-equilibrium following the time-dependent variational Gutzwiller framework [193, 194, 195], enabling the study of short-time and steady-state dynamics of systems with non-trivial unit cells.

Appendix

A

Tensor traces: notation and high-frequency tails

A.1. Imaginary time tensor products

The effective action formalism involves imaginary-time first and second order tensors, such as $\mathbf{F}$ and $\mathbf{G}_0$. The product $\mathbf{C}^{\alpha}_{\beta}(\tau,\tau')$ of two second-order tensors $\mathbf{A}^{\beta}_{\alpha}(\tau,\tau')$ and $\mathbf{B}^{\beta}_{\alpha}(\tau,\tau')$, $\mathbf{C}=\mathbf{AB}$, is defined as the sum over one super-index and an integration in imaginary time

$$\mathbf{C}^{\alpha}_{\beta}(\tau,\tau') = \sum_{\gamma}\int_0^{\beta} d\bar{\tau}\, \mathbf{A}^{\alpha}_{\gamma}(\tau,\bar{\tau})\mathbf{B}^{\gamma}_{\beta}(\bar{\tau},\tau')\,, \tag{A.1}$$

while the product $\mathbf{R}^{\alpha}(\tau)$ of a first-order tensor $\mathbf{F}^{\alpha}(\tau)$ and a second order tensor $\mathbf{A}^{\beta}_{\alpha}(\tau,\tau')$, $\mathbf{R}=\mathbf{AF}$, is defined as

$$\mathbf{R}^{\alpha}(\tau) = \sum_{\gamma}\int_0^{\beta} d\bar{\tau}\, \mathbf{A}^{\alpha}_{\gamma}(\tau,\bar{\tau})\mathbf{F}^{\gamma}(\bar{\tau})\,. \tag{A.2}$$

Hence, the scalar S, given by the sandwiched product $S=\mathbf{R}^{\dagger}\mathbf{AF}$ of two first-order tensors $\mathbf{R}^{\dagger}_{\alpha}(\tau)$ and $\mathbf{F}^{\alpha}(\tau)$ with a second order tensor $\mathbf{A}^{\alpha}_{\beta}(\tau,\tau')$, becomes

$$S=\mathbf{R}^{\dagger}\mathbf{AF} = \sum_{\alpha\beta}\iint_0^{\beta} d\tau d\tau'\, \mathbf{R}^{\dagger}_{\alpha}(\tau)\mathbf{A}^{\alpha}_{\beta}(\tau,\tau')\mathbf{F}^{\beta}(\tau')\,. \tag{A.3}$$

In equilibrium first-order tensors are time independent, $\mathbf{F}^{\alpha}(\tau)=\mathbf{F}^{\alpha}$, while second-order tensors are time-translation invariant, $\mathbf{A}(\tau,\tau')=\mathbf{A}(\tau-\tau')$. Thus, second-order tensors can be transformed to Matsubara frequency space using the relations [196, 134, 95]

$$\mathbf{A}^{\alpha}_{\beta}(i\omega_n) = \int_0^{\beta} d\tau e^{i\omega_n\tau}\mathbf{A}^{\alpha}_{\beta}(\tau)\,, \tag{A.4}$$

$$\mathbf{A}^{\alpha}_{\beta}(\tau) = \frac{1}{\beta}\sum_{n=-\infty}^{\infty} e^{-i\omega_n\tau}\mathbf{A}^{\alpha}_{\beta}(i\omega_n)\,, \tag{A.5}$$

where $\omega_n=\frac{\pi}{\beta}(2n+\vartheta)$ with $\vartheta=(1-\xi)/2$ and $\xi=\pm 1$ for bosons and fermions, respectively [197]. Correspondingly first-order tensors transform like second-quantization operators [198]

$$\mathbf{F}^{\alpha}(i\omega_n) = \frac{1}{\sqrt{\beta}}\int_0^{\beta} d\tau e^{i\omega_n\tau}\mathbf{F}^{\alpha}(\tau)\,, \tag{A.6}$$

$$\mathbf{F}^{\alpha}(\tau) = \frac{1}{\sqrt{\beta}}\sum_{n=-\infty}^{\infty} e^{-i\omega_n\tau}\mathbf{F}^{\alpha}(i\omega_n)\,, \tag{A.7}$$

which simplifies to $\mathbf{F}^\alpha(\tau) = \mathbf{F}^\alpha$ and $\mathbf{F}^\alpha(i\omega_n) = \sqrt{\beta}\delta_{n,0}\mathbf{F}^\alpha$.

For spatially translation-invariant systems, first-order tensors are position independent, $\mathbf{F}^\alpha(\tau) = \mathbf{F}^{\mathbf{r}_i,\eta}(\tau) \equiv \mathbf{F}^\eta(\tau)$, while second-order tensors are invariant under simultaneous translations of the lattice vectors $\mathbf{r}_i$ and $\mathbf{r}_j$

$$\mathbf{A}^\alpha_\beta(\tau - \tau') = \mathbf{A}^{\mathbf{r}_i,\eta}_{\mathbf{r}_j,\nu}(\tau - \tau') = \mathbf{A}^\eta_\nu(\mathbf{r}_i - \mathbf{r}_j, \tau - \tau')\,. \tag{A.8}$$

Hence, in momentum space, $\mathbf{A}$ is diagonal and given by the transforms

$$\mathbf{A}^\eta_\nu(\mathbf{k}, \tau) = \sum_{\mathbf{r}} e^{-i\mathbf{k}\cdot\mathbf{r}}\mathbf{A}^\eta_\nu(\mathbf{r}, \tau)\,, \tag{A.9}$$

$$\mathbf{A}^\eta_\nu(\mathbf{r}, \tau) = \frac{1}{N}\sum_{\mathbf{k}} e^{i\mathbf{k}\cdot\mathbf{r}}\mathbf{A}^\eta_\nu(\mathbf{k}, \tau)\,, \tag{A.10}$$

where N is the number of lattice sites. Accordingly, first-order tensors only contribute at zero momentum

$$\mathbf{F}^\eta(\mathbf{k}, \tau) = \delta_{\mathbf{k},\mathbf{0}}\sqrt{N}\mathbf{F}^\eta(\tau)\,, \tag{A.11}$$

as they again transform as [198]

$$\mathbf{F}^\eta(\mathbf{k}, \tau) = \frac{1}{\sqrt{N}}\sum_{\mathbf{r}} e^{-i\mathbf{k}\cdot\mathbf{r}}\mathbf{F}^\eta(\mathbf{r}, \tau)\,, \tag{A.12}$$

$$\mathbf{F}^\eta(\mathbf{r}, \tau) = \frac{1}{\sqrt{N}}\sum_{\mathbf{k}} e^{i\mathbf{k}\cdot\mathbf{r}}\mathbf{F}^\eta(\mathbf{k}, \tau)\,. \tag{A.13}$$

Thus, in momentum- and Matsubara frequency-space the product relations [Eqs. (A.1), (A.2) and (A.3)] simplify to

$$\mathbf{C}^\eta_\nu(\mathbf{k}, i\omega_n) = \sum_\mu \mathbf{A}^\eta_\mu(\mathbf{k}, i\omega_n)\mathbf{B}^\mu_\nu(\mathbf{k}, i\omega_n)\,, \tag{A.14}$$

$$\mathbf{R}^\eta = \sum_\mu \mathbf{A}^\eta_\mu(\mathbf{k} = \mathbf{0}, i\omega_0)\mathbf{F}^\mu\,, \tag{A.15}$$

$$S = \beta N \sum_{\eta\nu} \mathbf{R}^\dagger_\eta \mathbf{A}^\eta_\nu(\mathbf{k} = \mathbf{0}, i\omega_0)\mathbf{F}^\nu\,. \tag{A.16}$$

A.2. Imaginary time tensor traces

Also the trace of a second-order tensor appears in the Baym-Kadanoff effective action and can be defined as the trace over super-indices and a double integral in imaginary time

$$\mathrm{Tr}[\mathbf{A}] = \sum_\gamma \iint_0^\beta d\tau d\tau'\, \delta_\gamma(\tau - \tau')\mathbf{A}^\gamma_\gamma(\tau, \tau')\,, \tag{A.17}$$

where $\delta_\gamma(\tau)$ is the Nambu kernel $\delta_\alpha(\tau) = \delta_{\mathbf{r}_i,\eta}(\tau) = \delta(\tau - (-1)^\eta 0^+)$ enforcing normal ordering (with Nambu index $\eta = 0, 1$). Imposing time- and spatial-translational invariance in Eq. (A.17) yields

$$\mathrm{Tr}[\mathbf{A}] = \beta N \sum_\mu \mathbf{A}^\mu_\mu(\mathbf{r} = \mathbf{0}, \tau = (-1)^\mu 0^-) = \sum_{\mu\mathbf{k}n} e^{i\omega_n(-1)^\mu 0^+}\mathbf{A}^\mu_\mu(\mathbf{k}, i\omega_n)\,. \tag{A.18}$$

Note that the trace definition obeys the cyclicity conditions $\mathrm{Tr}[\mathbf{AB}] = \mathrm{Tr}[\mathbf{BA}]$ and $S = \mathbf{R}^\dagger\mathbf{AF} = \mathrm{Tr}[\mathbf{AFR}^\dagger]$.

The fact that the Nambu-kernel $\delta(\tau - (-1)^\eta 0^+)$ is necessary to yield normal ordering can be understood by taking the trace of a Nambu Green's function $\mathbf{G}$, given by the time-ordered

expectation value $\mathbf{G}^{\eta}_{\nu}(\tau) = -\langle \mathbf{b}^{\eta}(\tau)\mathbf{b}^{\dagger}_{\nu}\rangle$,

$$\mathrm{Tr}[\mathbf{G}] = -\beta \sum_{\mu} \langle \mathbf{b}^{\mu}((-1)^{\mu}0^{-})\mathbf{b}^{\dagger}_{\mu}\rangle = -2\beta\langle b^{\dagger}b\rangle\,. \tag{A.19}$$

Here the factor β comes from the integrals over imaginary time, see Eq. (A.17), and the factor of two comes from the sum over Nambu indices. Thus, the Nambu kernel $\delta_{\gamma}(\tau - \tau')$ in the imagnary-time trace $\mathrm{Tr}[\cdot]$ is normal-ordering both diagonal Nambu components of $\mathbf{G}$, producing the second quantization normal ordered result. This property is central for obtaining the correct free energy contribution from the $\frac{1}{2}\mathrm{Tr}\ln[-\mathbf{G}^{-1}]$ terms in the Baym-Kadanoff functional [Eq. (4.26)], as will be shown in Appendix A.3.

A.2.1. Reformulation using Matsubara asymptotic form

One possible route for the numerical evaluation of the trace is to compute the sum over Matsubara frequencies in Eq. (A.18)

$$\mathrm{Tr}[\mathbf{A}] = \sum_{\mu\mathbf{k},n} e^{i\omega_n(-1)^{\mu}0^{+}} \mathbf{A}^{\mu}_{\mu}(\mathbf{k}, i\omega_n)\,. \tag{A.20}$$

However, in general, second-order tensors decay slowly with respect to $|\omega_n|$, with the asymptotic behavior $\mathbf{A}^{\mu}_{\mu} \sim (i\omega_n)^{-1}$ whenever $\mathbf{A}$ has a discontinuity at $\tau = 0$. For a Green's function $\mathbf{G} = -\langle \mathbf{b}(\tau)\mathbf{b}^{\dagger}\rangle$ this is generated by the time-ordering operator $\mathcal{T}$ in the expectation value $\langle\cdot\rangle = \mathcal{Z}^{-1}\mathrm{Tr}[\mathcal{T}e^{-S}\cdot]$ and the (equal time) commutation relation $[\mathbf{b}, \mathbf{b}^{\dagger}] = \sigma_z$.

To improve the convergence properties of the Matsubara frequency sum we introduce $\mathcal{A}$, the Nth order high-frequency expansion of $\mathbf{A}(i\omega_n) = \mathcal{A}(i\omega_n) + \mathcal{O}([i\omega_n]^{-(N+1)})$ given by

$$\mathcal{A}(i\omega_n) = \sum_{p=1}^{N} \mathbf{a}_p Q_p(i\omega_n)\,, \tag{A.21}$$

where $\mathbf{a}_p$ are the high-frequency expansion coefficients of $\mathbf{A}$ and $Q_p(i\omega_n)$ are the high frequency basis functions

$$Q_p(i\omega_n) = \begin{cases} (i\omega_n)^{-p}, & \omega_n \neq 0 \\ 0, & \omega_n = 0 \end{cases}\,, \tag{A.22}$$

with the zeroth frequency mode removed.

Given $\mathcal{A}$ the trace of $\mathbf{A}$ can be written as

$$\mathrm{Tr}[\mathbf{A}] = \sum_{\mu\mathbf{k}} \Big(\sum_{n} [\mathbf{A}(\mathbf{k}, i\omega_n) - \mathcal{A}(\mathbf{k}, i\omega_n)]^{\mu}_{\mu} + \beta \mathcal{A}^{\mu}_{\mu}(\mathbf{k}, \tau = (-1)^{\mu}0^{-}) \Big)\,, \tag{A.23}$$

where the summand in Matsubara frequency sum on the first row now decays as $[\mathbf{A} - \mathcal{A}]^{\mu}_{\mu} \sim (i\omega_n)^{-N}$. Hence, the regularizing exponent factor $\exp(i\omega_n(-1)^{\mu}0^{+})$ is no longer needed. The improved decay in the sum comes at the price of having to evaluate $\mathcal{A}$ in imaginary time

$$\mathcal{A}^{\mu}_{\mu}(\mathbf{k}, \tau = (-1)^{\mu}0^{-}) = \sum_{p=1}^{N} [\mathbf{a}_p(\mathbf{k})]^{\mu}_{\mu} Q_p(\tau = (-1)^{\mu}0^{-})\,, \tag{A.24}$$

which can be done analytically using the imaginary time form of Q_p derived in Appendix A.2.2, see Eq. (A.33).

The asymptotic form can be used for constructing numerical approximants and to derive alternate analytic formulas for the trace. For the latter, only the first-order term of the expansion

is needed. Given $\mathbf{A}(\mathbf{k}, i\omega_n)$ and the first expansion coefficient $\mathbf{a}_1(\mathbf{k})$, Eq. (A.23) gives

$$\mathrm{Tr}[\mathbf{A}] = \sum_{\mu\mathbf{k}} \Big(\sum_n \mathbf{A}^\mu_\mu(\mathbf{k}, i\omega_n) + \frac{\beta}{2}[\mathbf{a}_1(\mathbf{k})\sigma_z]^\mu_\mu \Big) , \tag{A.25}$$

where we have used that the Matsubara sum over the asymptotic form including only the first order term is zero, $\sum_n \mathcal{A}(\mathbf{k}, i\omega_n) = \mathbf{a}_1(\mathbf{k}) \sum_n Q_1(i\omega_n) = \mathbf{0}$, and that $\mathbf{a}_1(\mathbf{k})$ is diagonal, which gives $[\mathbf{a}_1(\mathbf{k})]^\mu_\mu Q_1(\tau = (-1)^\mu 0^-) = [\mathbf{a}_1(\mathbf{k})\sigma_z/2]^\mu_\mu$, see Eq. (A.33).

To numerically calculate tensor traces given $\mathbf{A}(i\omega_n)$ at a finite number N_ω of Matsubara frequencies and N high-frequency expansion coefficients $\mathbf{a}_p$, the trace is readily approximated as the finite frequency sum

$$\begin{aligned} \mathrm{Tr}[\mathbf{A}] \approx \sum_{\mu\mathbf{k}} \Bigg(& \mathbf{A}^\mu_\mu(\mathbf{k}, i\omega_0) + \sum_{n=-N_\omega}^{N_\omega{}'} \Big[\mathbf{A}(\mathbf{k}, i\omega_n) - \sum_{p=1}^{N} \frac{\mathbf{a}_p(\mathbf{k})}{(i\omega_n)^p} \Big]^\mu_\mu \\ & + \beta \sum_{p=1}^{N} [\mathbf{a}_p(\mathbf{k})]^\mu_\mu Q_p(\tau = (-1)^\mu 0^-) \Bigg) , \end{aligned} \tag{A.26}$$

which converges asymptotically as $\sim 1/N_\omega^{N+1}$ and where the primed sum excludes the zeroth term ($n = 0$). For the SFA3 calculations presented in Chapters 6 and 7 we use second order tail corrections ($N = 2$) see Appendix A.3.

A.2.2. High-frequency basis functions in imaginary time

The imaginary time form of the high-frequency basis functions Q_p in Eq. (A.22) is given by the Fourier transform [Eq. (A.5)]

$$Q_p(\tau) = \frac{1}{\beta} \sum_{n=-\infty}^{\infty{}'} \frac{e^{-i\omega_n \tau}}{(i\omega_n)^p} = \sum_{n=-\infty}^{\infty{}'} \mathrm{Res} \left[\frac{e^{(\beta-\tau)z}}{z^p} f(z), i\omega_n \right] ,$$

where the summand has been rewritten as a residue and $f(z)$ is the distribution function $f(z) = (e^{\beta z} - \xi)^{-1}$. The sum of residues is related to the contour integral

$$0 = \oint_C \frac{dz}{2\pi i} \frac{\xi e^{(\beta-\tau)z}}{z^p} f(z) = \sum_{n=-\infty}^{\infty} \mathrm{Res} \left[\frac{\xi e^{(\beta-\tau)z}}{z^p} f(z), i\omega_n \right] ,$$

whence Q_p is given by the $n = 0$ term

$$Q_p(\tau) = -\mathrm{Res} \left[\frac{e^{(\beta-\tau)z}}{z^p} f(z), 0 \right] . \tag{A.27}$$

To evaluate the residue, bosons and fermions must be separated, as $f(z)$ contains a simple pole in the Bosonic case. For Fermions (with $\xi = -1$) Eq. (A.27) becomes

$$Q_p(\tau) = -\frac{1}{(p-1)!} \left(\frac{d}{dz} \right)^{p-1} e^{(\beta-\tau)z} f(z) \Big|_{z\to 0} , \tag{A.28}$$

whose first orders are $Q_1(\tau) = -1/2$, $Q_2(\tau) = (2\tau - \beta)/4$, and $Q_3(\tau) = \tau(\beta - \tau)/4$ for $\tau \in (0, \beta]$. While on $\tau \in [-\beta, \beta]$ the functions are anti-periodic, and the first order is a step function, see

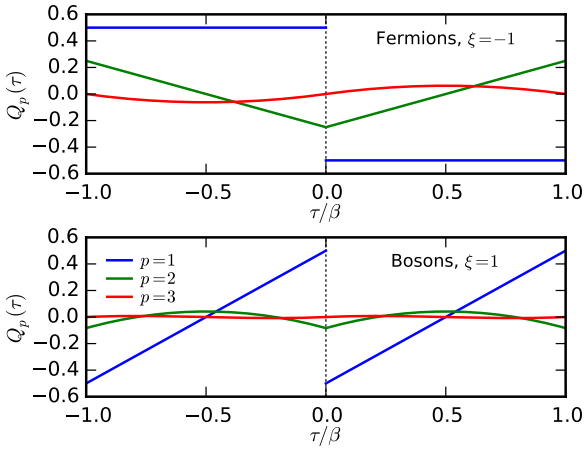

Figure A.1.: High-frequency basis functions $Q_p(\tau)$ for Fermions (upper panel) and Bosons (lower panel).

the upper panel in Fig. A.1. For bosons one obtains

$$Q_p(\tau) = -\frac{1}{p!}\left(\frac{d}{dz}\right)^p z e^{(\beta-\tau)z} f(z)\Big|_{z\to 0}\,, \tag{A.29}$$

yielding the first order terms

$$Q_1(\tau) = (-\beta + 2\tau)/(2\beta)\,, \tag{A.30}$$
$$Q_2(\tau) = (-\beta^2 + 6\beta\tau - 6\tau^2)/(12\beta)\,, \tag{A.31}$$
$$Q_3(\tau) = \tau(\beta^2 - 3\beta\tau + 2\tau^2)/(12\beta)\,. \tag{A.32}$$

The bosonic functions are periodic on $\tau \in [-\beta, \beta]$ and the first order term is a saw-tooth function, see lower panel in Fig. A.1. From the bosonic basis functions $Q_p(\tau)$ we readily obtain the zero-time limits

$$\begin{aligned} Q_1(\tau = (-1)^\eta 0^-) &= (-1)^\eta/2\,, \\ Q_2(\tau = (-1)^\eta 0^-) &= -\beta/12\,, \\ Q_3(\tau = (-1)^\eta 0^-) &= 0\,, \end{aligned} \tag{A.33}$$

which are used in the Matsubara sum asymptotic expansion in Eqs. (A.23), (A.24), and (A.26).

A.3. Matsubara trace logarithm

Apart from direct traces of second order tensors, the Baym-Kadanoff functional in Eq. (4.26) also contains the term $\mathrm{Tr}\ln[-\mathbf{G}^{-1}]$, i.e., the trace of the functional logarithm of the interacting Green's function. In the non-interacting limit only this term remains and yields the free energy up to an infinite regularization factor.

To derive a closed formula for the trace log and the regularization factor reproducing the non-interacting limit we introduce the trace log functional $\Lambda[\mathbf{G}]$,

$$\beta\Lambda[\mathbf{G}] = \frac{1}{2}\mathrm{Tr}\ln[-\mathbf{G}^{-1}] - C_\infty\,, \tag{A.34}$$

where C_∞ is an infinite constant, $C_\infty = \frac{1}{2}\mathrm{Tr}\ln[-\mathbf{R}^{-1}]$, defined in terms of the regularizing

second-order tensor

$$\mathbf{R}(i\omega_n) = \begin{cases} -\beta\mathbf{1}, & \omega_n = 0 \\ \dfrac{\sigma_z}{i\omega_n}, & \omega_n \neq 0 \end{cases} . \tag{A.35}$$

As we will see (Eq. (A.41)), this definition of C_∞ imposes that the trace log functional $\Lambda[\mathbf{G}]$ correctly yields the free energy in the non-interacting case. Since C_∞ is constant it will have no effect on the variations of the SFT functional.

Using Eq. (A.18) to write the logarithm trace in momentum- and Matsubara-frequency-space gives

$$\begin{aligned} \beta\Lambda[\mathbf{G}] &= -\frac{1}{2}\sum_{\mu\mathbf{k}n} e^{i\omega_n(-1)^\mu 0^+} \Big(\ln[\mathbf{R}^{-1}(i\omega_n)\mathbf{G}(\mathbf{k}, i\omega_n)] \Big)_\mu^\mu \\ &= -\frac{1}{2}\sum_{\mu\mathbf{k}} \Big(\ln[-\mathbf{G}(\mathbf{k}, i\omega_0)/\beta] + \sum_n{}' e^{i\omega_n(-1)^\mu 0^+} \ln[(\sigma_z i\omega_n)\mathbf{G}(\mathbf{k}, i\omega_n)] \Big)_\mu^\mu . \end{aligned} \tag{A.36}$$

To get rid of the exponential convergence factor we use the high-frequency expansion of the logarithm

$$\ln[(\sigma_z i\omega_n)\mathbf{G}(\mathbf{k}, i\omega_n)] = \frac{\sigma_z \mathbf{c}_2(\mathbf{k})}{i\omega_n} + \frac{\sigma_z \mathbf{c}_3 - (\sigma_z \mathbf{c}_2)^2/2}{(i\omega_n)^2} + \mathcal{O}([i\omega_n]^{-3}) , \tag{A.37}$$

where $\mathbf{c}_1 = \sigma_z$, $\mathbf{c}_2$ and $\mathbf{c}_3$ are the three first coefficients in the high-frequency expansion of $\mathbf{G}$ [Eq. (A.21)].

Using the first order correction and Eq. (A.25) therefore yields $\Lambda[\mathbf{G}]$ as

$$\beta\Lambda[\mathbf{G}] = -\frac{1}{2}\sum_{\mu\mathbf{k}} \Big(\ln[-\mathbf{G}(\mathbf{k}, i\omega_0)/\beta] + \sum_n{}' \ln[(\sigma_z i\omega_n)\mathbf{G}(\mathbf{k}, i\omega_n)] + \mathbf{c}_2(\mathbf{k})\frac{\beta}{2} \Big)_\mu^\mu . \tag{A.38}$$

To show that the trace log functional $\beta\Lambda[\mathbf{G}]$ is correctly regularized as to reproduce the non-interacting limit we consider the free Green's function $\mathbf{G}_0(i\omega_n) = [\sigma_z i\omega_n - \mathbf{1}\epsilon_\mathbf{k}]^{-1}$, and its high-frequency expansion

$$\mathbf{G}_0(i\omega_n) = \frac{\sigma_z}{i\omega_n} + \frac{\mathbf{1}\epsilon_\mathbf{k}}{(i\omega_n)^2} + \mathcal{O}([i\omega_n]^{-3}) . \tag{A.39}$$

Hence, $\mathbf{G}_0$ yields $\mathbf{c_2}(\mathbf{k}) = \mathbf{1}\epsilon_\mathbf{k}$ and $\mathbf{G}_0(\mathbf{k}, i\omega_0) = -\mathbf{1}/\epsilon_\mathbf{k}$ which inserted in Eq. (A.38) gives

$$\begin{aligned} \beta\Lambda[\mathbf{G}] &= -\sum_\mathbf{k} \Big(-\ln[\beta\epsilon_\mathbf{k}] + \sum_n{}' \ln\left[\frac{i\omega_n}{i\omega_n - \epsilon_\mathbf{k}}\right] + \frac{\beta\epsilon_\mathbf{k}}{2} \Big) \\ &= -\sum_\mathbf{k} \ln\left[\frac{e^{\frac{\beta\epsilon_\mathbf{k}}{2}}}{\beta\epsilon_\mathbf{k}} \prod_n{}' \frac{i\omega_n}{i\omega_n - \epsilon_\mathbf{k}} \right] = \sum_\mathbf{k} \ln(1 - e^{-\beta\epsilon_\mathbf{k}}) , \end{aligned} \tag{A.40}$$

where in the last step we have used the relation $(\beta\epsilon)^{-1}\prod_n' \frac{i\omega_n}{i\omega_n - \epsilon} = [2\sinh(\beta\epsilon/2)]^{-1}$, see e.g. Ref. [199]. Thus, for a free Green's function $\mathbf{G}_0$ the regularized trace log functional $\Lambda[\mathbf{G}_0]$ is equal to the non-interacting bosonic free energy Ω_0 [134]

$$\beta\Lambda[\mathbf{G}_0] = \sum_\mathbf{k} \ln(1 - e^{-\beta\epsilon_\mathbf{k}}) = \beta\Omega_0 , \tag{A.41}$$

confirming the ansatz in Eq. (A.35) for the regularizing tensor $\mathbf{R}$. An intuitive understanding of

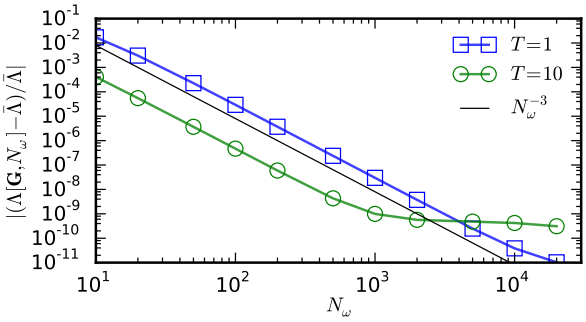

Figure A.2.: Convergence of the lattice Green's function trace log $\Lambda[\mathbf{G}, N_\omega]$ in N_ω at $U = 20$ and $\mu/U = 0.4$ (with baseline $\bar{\Lambda} = \Lambda[\mathbf{G}, N_\omega]$ with $N_\omega = 5 \cdot 10^4$) for both the superfluid at $T/J = 1$ (blue squares) and the normal phase at $T/J = 10$ (green circles), for reference N_ω^{-3} is also shown (black line).

$\mathbf{R}$ can be obtained by rewriting $\beta\Lambda[\mathbf{G}]$ in Eq. (A.34) using functional determinants

$$\beta\Lambda[\mathbf{G}] = \ln\left[\frac{\det\sqrt{-\mathbf{G}^{-1}}}{\det\sqrt{-\mathbf{R}^{-1}}}\right] = \ln\left[\frac{\det\sqrt{-\mathbf{G}^{-1}}}{\beta^{-1}\det'\sqrt{\sigma_z\partial_\tau}}\right].$$

I.e., the regularization $\det\sqrt{-\mathbf{R}^{-1}}$ corresponds to the functional determinant of the free inverse propagator, $\det\sqrt{-\mathbf{R}^{-1}} = \beta^{-1}\det'\sqrt{\sigma_z\partial_\tau}$, where the primed determinant indicates removal of all nullspace-eigenmodes of the argument.

In the SFT calculations presented here we use a second order high-frequency expansion and a finite number N_ω of Matsubara frequencies [Eq. (A.26)] which from Eq. (A.38) gives the trace log functional $\Lambda[\mathbf{G}]$ as

$$\begin{aligned}\beta\Lambda[\mathbf{G}] \approx -\frac{1}{2}\sum_{\mu\mathbf{k}}\Big(&\ln[-\mathbf{G}(\mathbf{k},i\omega_0)/\beta] + \frac{\beta}{2}\mathbf{c}_2(\mathbf{k}) - \frac{\beta^2}{12}\mathbf{q}_2(\mathbf{k}) \\ &+ \sum_{n=-N_\omega}^{N_\omega}{}' \left[\ln[(\sigma_z i\omega_n)\mathbf{G}(\mathbf{k},i\omega_n)] - \frac{\mathbf{q}_2(\mathbf{k})}{(i\omega_n)^2}\right]\Big)_\mu^\mu,\end{aligned} \tag{A.42}$$

where $\mathbf{q}_2$ is the second-order coefficient in Eq. (A.37), $\mathbf{q}_2 = \sigma_z\mathbf{c}_3 - (\sigma_z\mathbf{c}_2)^2/2$. Equation (A.42) converges cubically with N_ω^{-3}, such that for the lattice Green's function trace log in both the normal and super-fluid phase at the parameters used in Fig. 6.4 we reach a precision of 10^{-9} with $N_\omega = 10^3$ and 10^4 respectively, see Fig. A.2.

A.4. High frequency tail expansions

To evaluate the self-energy functional to high precision we use tail-corrected Matsubara traces as described in Appendix A.2. This procedure requires the high-frequency tail coefficients of all Green's functions and self-energies. The details on how to obtain these coefficients for the reference system and the lattice system are detailed in this Appendix.

A.4.1. Hamiltonian reference system

For a reference system which is given by a finite-dimensional Hamiltonian the expansion can be calculated exactly. Formally, the high frequency tail of a Matsubara Green's function, i.e. the $1/(i\omega_n)^k$ expansion, can be obtained from the imaginary-time Green's function by partial

integration of the Fourier transform expression

$$\mathbf{G}(i\omega_n) = \int_0^\beta d\tau\, \mathbf{G}(\tau) e^{i\omega_n \tau} = \sum_{k=0}^{\infty} (-1)^k \frac{\xi \partial_\tau^k \mathbf{G}(\beta^-) - \partial_\tau^k \mathbf{G}(0^+)}{(i\omega_n)^{k+1}} = \sum_{k=0}^{\infty} \frac{\mathbf{c}_{k+1}}{(i\omega_n)^{k+1}}\,, \tag{A.43}$$

where the c_k are the high-frequency tail expansion coefficients. Derivatives of the Green's function can be obtained directly from the imaginary-time expression

$$\mathbf{G}(\tau) = -\langle \mathbf{b}(\tau)\mathbf{b}^\dagger(0)\rangle = -\frac{1}{\mathcal{Z}} \mathrm{Tr}[e^{-\beta H} e^{\tau H} \mathbf{b} e^{-\tau H} \mathbf{b}^\dagger]\,, \tag{A.44}$$

or, equivalently, from the equation of motion of the operator $\mathbf{b}(\tau)$, $\partial_\tau \mathbf{b}(\tau) = [H, \mathbf{b}(\tau)]$. The first and kth order derivatives take the form

$$\begin{aligned} \partial_\tau \mathbf{G}(\tau) &= -\langle [H, \mathbf{b}(\tau)], \mathbf{b}^\dagger \rangle\,, \\ \partial_\tau^k \mathbf{G}(\tau) &= -\langle [[H, \mathbf{b}(\tau)]]^{(k)}, \mathbf{b}^\dagger \rangle\,, \end{aligned} \tag{A.45}$$

where $[[H, \mathbf{b}(\tau)]]^{(k)} = [H, ...[H, [H, \mathbf{b}(\tau)]]$ is the kth order left side commutator of H with $\mathbf{b}(\tau)$. For the specific imaginary times $\tau = 0^+$ and β^- the time ordering can be made explicit yielding the static expectation values

$$\begin{aligned} \partial_\tau^k \mathbf{G}(0^+) &= -\langle [[H, \mathbf{b}]]^{(k)} \mathbf{b}^\dagger \rangle\,, \\ \partial_\tau^k \mathbf{G}(\beta^-) &= -\langle \mathbf{b}^\dagger [[H, \mathbf{b}]]^{(k)} \rangle\,. \end{aligned} \tag{A.46}$$

Combining these two relations the coefficients c_k of the high-frequency tail expansion can be written in terms of the static expectation value

$$\mathbf{c}_{k+1} = (-1)^k [\xi \partial_\tau^k \mathbf{G}(\beta^-) - \partial_\tau^k \mathbf{G}(0^+)] = (-1)^{k+1} \langle [\,[[H, \mathbf{b}]]^{(k)}, \mathbf{b}^\dagger]_{-\xi} \rangle\,. \tag{A.47}$$

A.4.2. Lattice system

Consider the free Nambu Green's function $\mathbf{G}_0^{-1}(z) = \sigma_z z - \mathbf{1}h$ (with $z = i\omega_n$, for brevity). Inversion and Taylor expansion give

$$\begin{aligned} \mathbf{G}_0(z) =& \left[\mathbf{1} - \frac{\sigma_z h}{z}\right]^{-1} \frac{\sigma_z}{z} = \left[\sum_{p=0}^{\infty} \left(\frac{\sigma_z h}{z}\right)^p\right] \frac{\sigma_z}{z} \\ =& \frac{\sigma_z}{z} + \frac{\sigma_z h \sigma_z}{z^2} + \frac{\sigma_z h \sigma_z h \sigma_z}{z^3} + \mathcal{O}(z^{-4})\,. \end{aligned} \tag{A.48}$$

Similarly, for a general Nambu Green's function $\mathbf{G}$ with high frequency expansion $\mathbf{G}(z) = \sum_{p=1}^{\infty} \frac{\mathbf{c}_p}{z^p}$, the inverse is given by

$$\begin{aligned} \mathbf{G}^{-1}(z) =& \left[\mathbf{1} + \sigma_z z \sum_{p=2}^{\infty} \frac{\mathbf{c}_p}{z^p}\right]^{-1} \sigma_z z \\ =& \sigma_z z - \sigma_z \mathbf{c}_2 \sigma_z + \frac{1}{z}\left(-\sigma_z \mathbf{c}_3 \sigma_z + (\sigma_z \mathbf{c}_2)^2 \sigma_z\right) \\ &+ \frac{1}{z^2}\left(-\sigma_z \mathbf{c}_4 \sigma_z + \sigma_z \mathbf{c}_2 \sigma_z \mathbf{c}_3 \sigma_z + \sigma_z \mathbf{c}_3 \sigma_z \mathbf{c}_2 \sigma_z - (\sigma_z \mathbf{c}_2)^3 \sigma_z\right) + \mathcal{O}(z^{-3})\,, \end{aligned} \tag{A.49}$$

where we have used the fact that $\mathbf{c}_1 = \sigma_z$. Combining these relations allows us to write down the high-frequency expansion of the self energy, $\mathbf{\Sigma}(z) = \sum_{p=0}^{\infty} \frac{\mathbf{s}_p}{z^p}$, in terms of the high-frequency

expansion coefficients $\mathbf{c}_p$ of the Green's function

$$\begin{aligned}\boldsymbol{\Sigma}(z) = \mathbf{G}_0^{-1}(z) - \mathbf{G}^{-1}(z) &= -h - \left[\sum_{q=1}^{\infty}\left(-\sigma_z z \sum_{p=2}^{\infty}\frac{\mathbf{c}_p}{z^p}\right)^q\right]\sigma_z z \\ &= -h + \sigma_z \mathbf{c}_2 \sigma_z - \frac{1}{z}\left(-\sigma_z \mathbf{c}_3 \sigma_z + [\sigma_z \mathbf{c}_2]^2 \sigma_z\right) + \mathcal{O}(z^{-2})\,. \end{aligned} \tag{A.50}$$

Hence, the lattice Green's function $\mathbf{G}(\mathbf{k}, z)$ with a momentum independent self energy $\boldsymbol{\Sigma}$, $\mathbf{G}^{-1}(\mathbf{k}, z) = \sigma_z z - E_{\mathbf{k}} - \boldsymbol{\Sigma}(z)$, has the tail expansion

$$\mathbf{G}(\mathbf{k}, z) = \frac{\sigma_z}{z} + \frac{\sigma_z(E_{\mathbf{k}} + \mathbf{s}_0)\sigma_z}{z^2} + \frac{1}{z^3}\left(\sigma_z \mathbf{s}_1 \sigma_z + [\sigma_z(E_{\mathbf{k}} + \mathbf{s}_0)]^2 \sigma_z\right) + \mathcal{O}(z^{-4})\,, \tag{A.51}$$

where $E_{\mathbf{k}} = \mathbf{1}(\epsilon_{\mathbf{k}} - \mu)$.

A.5. Canceling functional derivatives of $\hat{\mathcal{T}}_{PV}$

In order to check that there are not any implicit dependencies of the functional $\hat{\mathcal{T}}_{PV}$ on $\mathbf{G}_{\mathbf{t},0,0}$ or $\mathbf{F}$, we rewrite Eq. (7.38) in terms of $\mathbf{G}_{\mathbf{t},0,0}$ and $\mathbf{F}$ as

$$\begin{aligned}\hat{\mathcal{T}}_{PV}[\bar{\mathbf{S}}, \bar{\boldsymbol{\Sigma}}, \{\mathbf{S}_{\boldsymbol{\eta}}, \boldsymbol{\Sigma}_{\boldsymbol{\eta}}\}] =& \frac{1}{2}\left\langle \mathrm{Tr}\ln\left[-\left(\mathbf{G}_{\mathbf{t},0,0}^{-1} - \boldsymbol{\eta} - \boldsymbol{\Sigma}_{\boldsymbol{\eta}}\right)\right]\right\rangle_P + \frac{1}{2}\left\langle (\mathbf{F} - \mathbf{S}_{\boldsymbol{\eta}})^\dagger \left[\mathbf{G}_{\mathbf{t},0,0}^{-1} - \boldsymbol{\eta}\right]^{-1}(\mathbf{F} - \mathbf{S}_{\boldsymbol{\eta}})\right\rangle_P \\ &- \frac{1}{2}\mathrm{Tr}\ln\left[-\left(\mathbf{G}_{\mathbf{t},0,0}^{-1} - \bar{\boldsymbol{\Sigma}}\right)\right] - \frac{1}{2}(\mathbf{F} - \bar{\mathbf{S}})^\dagger \mathbf{G}_{\mathbf{t},0,0}(\mathbf{F} - \bar{\mathbf{S}}). \end{aligned} \tag{A.52}$$

The variation in $\mathbf{G}_{\mathbf{t},0,0}^{-1}$ yields

$$\begin{aligned}\frac{\delta\hat{\mathcal{T}}_{PV}[\bar{\mathbf{S}}, \bar{\boldsymbol{\Sigma}}, \{\mathbf{S}_{\boldsymbol{\eta}}, \boldsymbol{\Sigma}_{\boldsymbol{\eta}}\}]}{\delta\mathbf{G}_{\mathbf{t},0,0}^{-1}} =& \frac{1}{2}\left\langle \mathrm{Tr}\left[\mathbf{G}_{\mathbf{t},\boldsymbol{\eta},0}^{-1} - \boldsymbol{\Sigma}_{\boldsymbol{\eta}}\right]^{-1}\right\rangle_P - \frac{1}{2}\left\langle (\mathbf{F} - \mathbf{S}_{\boldsymbol{\eta}})^\dagger \left[\mathbf{G}_{\mathbf{t},\boldsymbol{\eta},0}\right]^2 (\mathbf{F} - \mathbf{S}_{\boldsymbol{\eta}})\right\rangle_P \\ &- \frac{1}{2}\mathrm{Tr}\left[\mathbf{G}_{\mathbf{t},0,0}^{-1} - \bar{\boldsymbol{\Sigma}}\right]^{-1} + \frac{1}{2}(\mathbf{F} - \bar{\mathbf{S}})^\dagger \left[\mathbf{G}_{\mathbf{t},0,0}\right]^2 (\mathbf{F} - \bar{\mathbf{S}}), \end{aligned} \tag{A.53}$$

which by the short-hand notations introduced in Eqs. (7.33), and (7.34) can be rewritten as

$$\frac{\delta\hat{\mathcal{T}}_{PV}[\bar{\mathbf{S}}, \bar{\boldsymbol{\Sigma}}, \{\mathbf{S}_{\boldsymbol{\eta}}, \boldsymbol{\Sigma}_{\boldsymbol{\eta}}\}]}{\delta\mathbf{G}_{\mathbf{t},0,0}^{-1}} = \frac{1}{2}\mathrm{Tr}\left\langle \hat{\mathbf{G}}_{\boldsymbol{\eta}}\right\rangle_P - \frac{1}{2}\left\langle \hat{\boldsymbol{\Phi}}_{\boldsymbol{\eta}}^\dagger \hat{\boldsymbol{\Phi}}_{\boldsymbol{\eta}}\right\rangle_P - \frac{1}{2}\mathrm{Tr}\hat{\bar{\mathbf{G}}} + \frac{1}{2}\hat{\bar{\boldsymbol{\Phi}}}^\dagger \hat{\bar{\boldsymbol{\Phi}}} = 0, \tag{A.54}$$

where we have used that the trace and the arithmetic average commute, i.e. $\frac{1}{2}\left\langle \mathrm{Tr}\hat{\mathbf{G}}_{\boldsymbol{\eta}}\right\rangle_P = \frac{1}{2}\mathrm{Tr}\left\langle \hat{\mathbf{G}}_{\boldsymbol{\eta}}\right\rangle_P$. Note that - as opposed to the arithmetical average - the geometrical average used in the context of fermionic DMFT [151, 152, 153, 154] would not commute with the trace operator Tr in Eq. (A.54) and therefore break the universality of the functional $\hat{\mathcal{T}}_{PV}$. As pointed out in Ref. [156] for fermions, the geometrical average introduced in DMFT, therefore appears to be incompatible with SFT. The variation of $\hat{\mathcal{T}}_{PV}$ in $\mathbf{F}$ yields

$$\frac{\delta\hat{\mathcal{T}}_{PV}[\bar{\mathbf{S}}, \bar{\boldsymbol{\Sigma}}, \{\mathbf{S}_{\boldsymbol{\eta}}, \boldsymbol{\Sigma}_{\boldsymbol{\eta}}\}]}{\delta\mathbf{F}^\dagger} = \mathbf{G}_{\mathbf{t},0,0}(\mathbf{F} - \bar{\mathbf{S}}) - \left\langle \mathbf{G}_{\mathbf{t},\boldsymbol{\eta},0}(\mathbf{F} - \mathbf{S}_{\boldsymbol{\eta}})\right\rangle_P, \tag{A.55}$$

which using Eq. (7.33) can be rewritten as

$$\frac{\delta\hat{\mathcal{T}}_{PV}[\bar{\mathbf{S}}, \bar{\boldsymbol{\Sigma}}, \{\mathbf{S}_{\boldsymbol{\eta}}, \boldsymbol{\Sigma}_{\boldsymbol{\eta}}\}]}{\delta\mathbf{F}^\dagger} = \hat{\bar{\boldsymbol{\Phi}}} - \left\langle \hat{\boldsymbol{\Phi}}_{\boldsymbol{\eta}}\right\rangle_P = 0. \tag{A.56}$$

A.6. Poles in the connected Green's function

The arithmetically averaged connected Green's function of the lattice, $\bar{\mathbf{G}}$, depends on momentum k only through the non-interacting dispersion ϵ_k and can thus be parametrized in the single-particle energy ϵ as $\bar{\mathbf{G}}(i\omega_n, \epsilon) = \bar{\mathbf{G}}(i\omega_n, \epsilon = \epsilon_k)$. In terms of a local disorder-averaged self-energy $\bar{\mathbf{\Sigma}}$ (such as the one used in the SFA3 reference system) it can be written as

$$\bar{\mathbf{G}}(i\omega_n, \epsilon) = \left[\sigma_z i\omega_n + (\mu - \epsilon)\,\mathbf{1} - \bar{\mathbf{\Sigma}}(i\omega_n)\right]^{-1} . \tag{A.57}$$

The inversion in Eq. (A.57) results in simple poles of $\bar{\mathbf{G}}$ whenever $\det\left[\bar{\mathbf{G}}^{-1}(i\omega_n, \epsilon)\right] = 0$, i.e., when

$$\epsilon = \mu - \mathrm{Re}\left[\bar{\mathbf{\Sigma}}_{00}(i\omega_n)\right] \pm A\left[\bar{\mathbf{\Sigma}}, i\omega_n\right] \equiv \epsilon^p_{\pm}(i\omega_n)\,, \tag{A.58}$$

where $A\left[\bar{\mathbf{\Sigma}}, i\omega_n\right] = \sqrt{\left|\bar{\mathbf{\Sigma}}_{01}(i\omega_n)\right|^2 - \omega_n^2 - \mathrm{Im}\left[\bar{\mathbf{\Sigma}}_{00}(i\omega_n)\right]^2}$ and $\bar{\mathbf{\Sigma}}_{\nu\nu'}$ are the Nambu-components of the 2×2 local self-energy. In other words, the lattice Green's function $\bar{\mathbf{G}}$ develops a pole if for some $i\omega_n$

$$\min_k \epsilon_k \leq \epsilon^p_{\pm}(i\omega_n) \leq \max_k \epsilon_k\,, \tag{A.59}$$

while the determinant of $\bar{\mathbf{G}}$ can be expressed as

$$\det\left[\bar{\mathbf{G}}^{-1}(\epsilon, i\omega_n)\right] = \left(\epsilon - \epsilon^p_+(i\omega_n)\right)\left(\epsilon - \epsilon^p_-(i\omega_n)\right) . \tag{A.60}$$

In the absence of $U(1)$ symmetry-breaking $\bar{\mathbf{\Sigma}}_{01}(i\omega_n) = 0$, and $\bar{\mathbf{G}}$ can only have a simple pole at $i\omega_0 = 0$, since $\epsilon^p_+(i\omega_0) = \epsilon^p_-(i\omega_0)$ and $A\left[\bar{\mathbf{\Sigma}}, i\omega_n \neq 0\right]$ is always imaginary. In the superfluid phase, where $\left|\bar{\mathbf{\Sigma}}_{01}(i\omega_n)\right| > 0$, the poles $\epsilon^p_{\pm}$ of $\bar{\mathbf{G}}$ can be located at any Matsubara frequency.

However, the superfluid SFT groundstates we observe only develop simple poles at zero frequency (in specific parameter ranges). This happens in the superfluid phase for strong disorder $\Delta \gtrsim W$ and in the Bose glass phase close to the superfluid phase boundary, see the grey regions in Figs. 7.2 and 7.5. In the clean system, such a pole arises only in the $U(1)$-symmetry-preserving solution (i.e. the Mott insulator) when this solution is metastable (i.e. when the groundstate is superfluid), signaling an instability towards $U(1)$-symmetry breaking. In the case studied here, which is no-longer homogeneous, as discussed in Sec. 10.4, the pole is related to the appearance of isolated quasi-condensates on the lattice.

Remarkably, although the poles make non-local quantities such as, e.g., $n_k = -\sum_n \mathrm{Tr}\bar{\mathbf{G}}(i\omega_n, k)/2\beta$ diverge at certain values of k, the pole can be treated semi-analytically in the computation of local quantities, as we will show in the following.

The central quantity where the lattice Green's function enters in the SFT functional of Eq. (7.53) is the trace-log term $\mathrm{Tr}\ln\left[-\bar{\mathbf{G}}^{-1}\right]$, which – as shown in Appendix A.3 – is only defined up to a regularization factor C_∞ and can be evaluated as

$$\frac{1}{2}\mathrm{Tr}\ln\left[-\bar{\mathbf{G}}^{-1}\right] - C_\infty = \ln\left[\frac{\det\sqrt{-\bar{\mathbf{G}}^{-1}}}{\det\sqrt{-\mathbf{R}^{-1}}}\right] \tag{A.61}$$

where $\mathbf{R}$ is the regularization function

$$\mathbf{R}(i\omega_n) = \begin{cases} -i\sigma_\mathbf{z}/\omega_n, & n \neq 0, \\ -\beta\mathbf{1}, & n = 0. \end{cases} \tag{A.62}$$

By $\mathrm{Tr}\ln\left[-\bar{\mathbf{G}}^{-1}\right] = \mathrm{Tr}\ln\left[-\bar{\mathbf{G}}^{-4}\right]/4$, we therefore can evaluate the trace-log term as

$$\frac{1}{2}\mathrm{Tr}\ln\left[-\bar{\mathbf{G}}^{-1}\right] - C_\infty = \frac{1}{4}\sum_n \int d\epsilon\, \mathcal{D}(\epsilon) \ln\left[Q(i\omega_n)\det\left[\bar{\mathbf{G}}^{-1}(\epsilon, i\omega_n)\right]^2\right], \tag{A.63}$$

where $\mathcal{D}(\epsilon)$ is the single-particle density of states, and $Q(i\omega_n)$ is the reguarlization function

$$Q(i\omega_n) = \begin{cases} \omega_n^4, & n \neq 0, \\ \beta^{-4}, & n = 0. \end{cases} \tag{A.64}$$

In order to evaluate the integral in Eq. (A.63) numerically, the dispersion is discretized on the energy grid $\epsilon = \epsilon_m$. Using the linear interpolation

$$\tilde{D}_m(\epsilon) = \frac{\mathcal{D}(\epsilon_{m+1}) - \mathcal{D}(\epsilon_m)}{\epsilon_{m+1} - \epsilon_m}\epsilon + \mathcal{D}(\epsilon_m) \tag{A.65}$$

of the density of states, and inserting the explicit expression for the determinant from Eq. (A.60) gives

$$\int d\epsilon\, \mathcal{D}(\epsilon) \ln\left[Q(i\omega_n)\det\left[\bar{\mathbf{G}}^{-1}(\epsilon, i\omega_n)\right]^2\right] \approx \sum_m \int_{\epsilon_m}^{\epsilon_{m+1}} d\epsilon\, I_m(\epsilon, i\omega_n), \tag{A.66}$$

where the integrand is given by

$$I_m(\epsilon, i\omega_n) \equiv \tilde{D}_m(\epsilon) \ln\left[Q(i\omega_n)\left(\epsilon - \epsilon_+^p(i\omega_n)\right)^2\left(\epsilon - \epsilon_-^p(i\omega_n)\right)^2\right]. \tag{A.67}$$

If the interval $[\epsilon_m, \epsilon_{m+1}]$ does not contain the poles $\epsilon_\pm^p(i\omega_n)$, the mth summand of Eq. (A.66) can be straight-forwardly integrated analytically. Also in the presence of a pole, $\epsilon_m < \epsilon^p < \epsilon_{m+1}$, this term is integrable, and can be computed analytically by dividing up the interval into two pieces as

$$\int_{\epsilon_m}^{\epsilon_{m+1}} d\epsilon\, I_m = \int_{\epsilon_m}^{\epsilon^p} d\epsilon\, I_m + \int_{\epsilon^p}^{\epsilon_{m+1}} d\epsilon\, I_m. \tag{A.68}$$

Also in the presence of poles (i.e. quasi-condensates) in the connected Green's function, the SFT functional therefore remains well-defined.

A central local observable that is directly computed from $\bar{\mathbf{G}}$ is the density per site n, given by Eq. (7.73) and thereby by the sum

$$n = -\frac{1}{\beta}\sum_n \int d\epsilon\, \mathcal{D}(\epsilon)\bar{\mathbf{G}}_{00}(i\omega_n, \epsilon) \approx -\frac{1}{\beta}\sum_{n,m}\int_{\epsilon_m}^{\epsilon_{m+1}} d\epsilon\, \tilde{D}_m(\epsilon)\bar{\mathbf{G}}_{00}(i\omega_n, \epsilon), \tag{A.69}$$

where in the last step we have used Eq. (A.65). Using Eq. (A.60) the Green's function component $\bar{\mathbf{G}}_{00}$ can be expressed as

$$\bar{\mathbf{G}}_{00}(i\omega_n, \epsilon) = \frac{i\omega_n - \epsilon + \mu - \bar{\mathbf{\Sigma}}_{00}(i\omega_n)}{\left(\epsilon - \epsilon_+^p(i\omega_n)\right)\left(\epsilon - \epsilon_-^p(i\omega_n)\right)}. \tag{A.70}$$

Again, if $[\epsilon_m, \epsilon_{m+1}]$ does not contain $\epsilon_\pm^p(i\omega_n)$, the mth summand of Eq. (A.69) can be integrated analytically. If a pole ϵ^p is present, the expression (A.69) is an integral over a simple pole, which however can be integrated analytically using the limit

$$\int_{\epsilon_m}^{\epsilon_{m+1}} d\epsilon\, \tilde{D}_m(\epsilon)\bar{\mathbf{G}}_{00}(\epsilon, i\omega_n) = \lim_{\gamma\to 0}\left(\int_{\epsilon^p+\gamma}^{\epsilon_{m+1}} + \int_{\epsilon_m}^{\epsilon^p-\gamma}\right) d\epsilon \tilde{D}_m(\epsilon)\bar{\mathbf{G}}_{00}(\epsilon, i\omega_n), \tag{A.71}$$

which ensures that the two divergent parts of the integrals cancel each other out, giving a finite

result.

The same procedure can also be applied when computing the kinetic energy, which by Eq. (7.73) is given by

$$E_{\text{kin}} = -\frac{1}{\beta}\sum_n \int d\epsilon \mathcal{D}(\epsilon)\epsilon \bar{\mathbf{G}}_{00}(i\omega_n, \epsilon)\,. \tag{A.72}$$

B

Harper-Hofstadter-Mott model

B.1. Comparison of reciprocal cluster and cluster Gutzwiller mean-field methods

In Fig. B.1 we compare the density, condensate density, and free energy of the Harper-Hofstadter-Mott model (HHMm) for $t_x = t_y$ as a function of the chemical potential μ computed with RCMF and CGMF [77]. While the densities appear to agree nicely, there are strong deviations on the level of the condensate density, due to the different treatment of the symmetry-breaking field. In fact the condensate and density modulations within CGMF feel a strong influence of the boundaries and show no translational invariance or periodicity within the cluster. Furthermore, while the condensate density found with RCMF shows a kink at density $n = 1/8$ - indicative of the close proximity in energy of the fractional quantum Hall state at $\nu = 1/2$ - CGMF seems to miss this feature. Throughout the simulation the free energy found with RCMF is lower than the one found with CGMF. As both methods are variational - in the sense that the exact groundstate energy is approached from above - RCMF appears therefore to converge to a more precise solution.

This discrepancy in the variational energy becomes much more pronounced for increasing hopping anisotropy, as RCMF preserves translational invariance, while CGMF treats sites differently depending if they lie on the boundary or not. In the case of very low hopping in one direction (e.g. $t_x \ll 1$) the CGMF cluster reduces to weakly coupled chains which are treated on different levels: the ones that lie on the "boundary" couple to the symmetry-breaking field on each site, while the ones which are not on the boundary couple to the field only on the open ends.

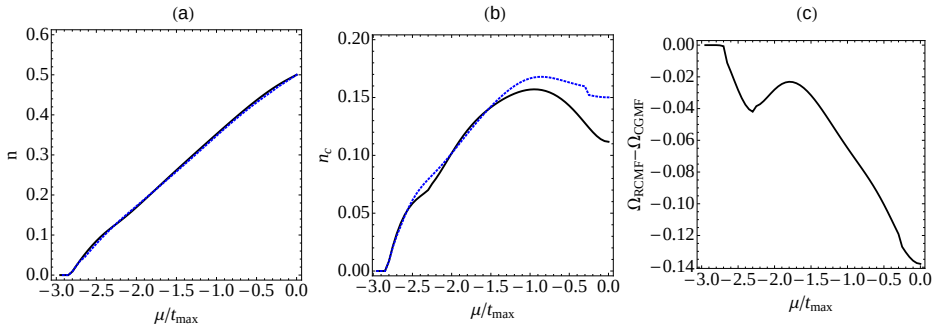

Figure B.1.: (a-b): Density (a), and condensate density (b), of the HHMm for $t_x = t_y$ as a function of the chemical potential μ. The results were computed with RCMF (black) and CGMF (blue, dotted). (c) Difference in free energy between the RCMF and CGMF solutions $\Omega_{\mathrm{RCMF}} - \Omega_{\mathrm{CGMF}}$.

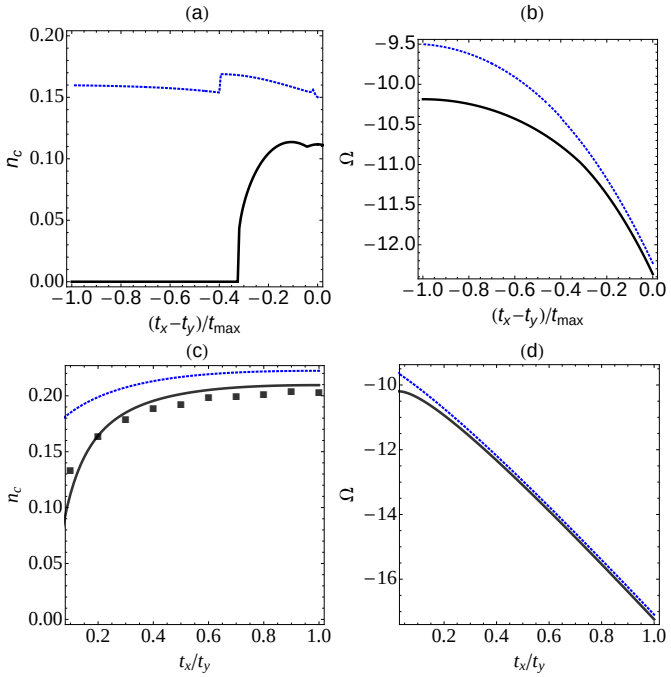

Figure B.2.: (a-b): Condensate density (a), and free energy (b), of the Harper-Hofstadter-Mott model for $\mu = 0$ as a function of hopping anisotropy. (c-d): Condensate density (a), and free energy (b), of the Bose-Hubbard model for $\mu = 0$ as a function of hopping anisotropy. The results were computed with QMC (black squares), RCMF (black line) and CGMF (blue dotted line).

This leads to increasing artificial density and condensate-density modulations and a decrease in precision. RCMF on the other hand does not run into this problem.

This can be seen in Fig. B.2, where we show how the difference between the RCMF and CGMF results increases with hopping anisotropy. Both in the HHMm and the Bose-Hubbard model the free energy found with RCMF is considerably lower than the one found with CGMF. Further the RCMF results agree better with the quantum Monte Carlo (QMC) data in the Bose-Hubbard model.

B.2. Topological properties of the Harper-Hofstadter-Mott model

Since RCMF does not give direct access to the many-body groundstate of the infinite lattice, nor to dynamical quantities, there is no way to directly compute the many-body Chern number of the system. Instead, we make use of the properties of the lattice to indirectly measure the topology of the groundstate using the $\hat{h}_{k,q}$ vector introduced in Sec. 9.1.

In our RCMF approach Eq. (8.12) reduces to $\Omega = \Omega'$ in the absence of $U(1)$ symmetry-breaking. Computing $\hat{h}_{k,q}$ in the phases with $F = 0$ by taking expectation values for the discrete momentum values of the cluster (K and Q) then is equivalent to taking the same expectation values with respect to the infinite lattice. By looking at the values of $\hat{h}_{K,Q}$ at these discrete momenta and extrapolating its rotation on the infinite lattice, we are thereby able to measure the topology of the infinite lattice in a way that is not limited by finite-size effects. This is shown in Fig. B.3a, where the $\hat{h}_{k,q}$ vector is compared in a 4×4 and 8×4 periodic system, respectively, for filling $\nu = 2$ and $(t_x - t_y)/t_{\max} = -0.5$, yielding excellent agreement. In Figs. B.3b and B.3c we

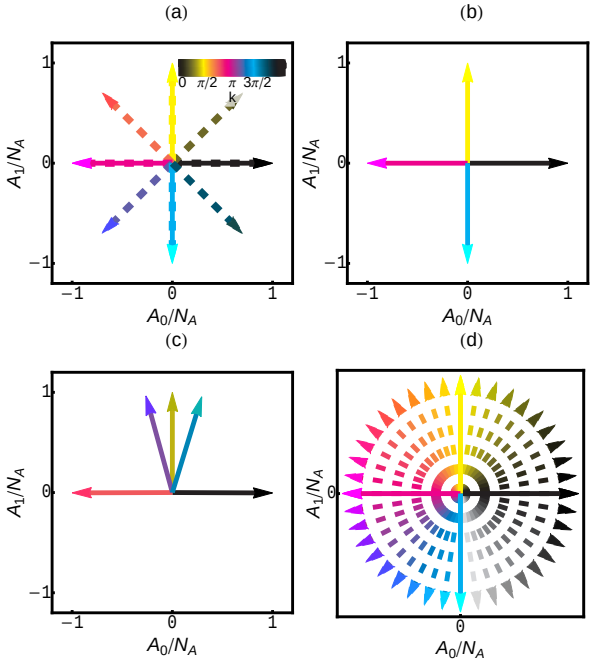

Figure B.3.: (a) Values of the $\boldsymbol{h}$ vector as a function of momentum for $t_x/t_y = 0.5$ and $\nu = 2$, on a 4×4 (full lines) and 8×4 (dashed lines) system. (b) Values of the $\boldsymbol{h}$ vector as a function of momentum for $t_y/t_x = 0.2$ and $\nu = 1/2$, on a 4×4 system. (c) Values of the $\boldsymbol{h}$ vector as a function of momentum for $t_y/t_x = 0.2$ and $\nu = 3/5$ on a 5×4 system. (d) Response of the momentum-values of $\boldsymbol{h}_{k,q}$ to the boundary twisting angle $\theta_x \in [0, 2\pi]$ on a cylinder geometry ($\theta_y = 0$) for $t_x/t_y = 0.2$ and $\nu = 1$ on a 4×4 system, where the dashed lines indicate $\theta_x \neq 0$, while the coloring indicates the value of $k + \theta_x/L_x$.

show the precession of $\hat{h}_{k,q}$ for filling $\nu = 1/2$ on a 4×4 system, and $\nu = 3/5$ on a 5×4 system. At $\nu = 1/2$ the system is in a fQH phase showing a topological winding. At $\nu = 3/5$, where for bosons no fQH phase is possible, the vector does not show any closed loop and has a net geometric angle of zero.

By using twisted boundaries in x-direction (i.e. varying θ_x), while keeping $\theta_y = 0$, we measure the response of the vector $\hat{h}_{k,q}$ on a cylinder to a magnetic flux piercing the system in y-direction in Fig. B.3d. As discussed in Secs. 9.1 and 10.2, under the insertion of a flux of $\Phi_\mathrm{y} = \theta_x = 2\pi$, the winding of the vector indicates an adiabatic translation of the manybody groundstate by one site in y-direction. For $\nu = 1$ (shown in Fig. B.3d) this translates into a quantized transverse transport of a single particle around the periodic boundaries in y-direction, while for $\nu = 3$ a single hole is being transported. In the case of $\nu = 2$ the total charge transport is zero, as a particle-hole pair is transported.

We further analyze the stability of the winding number against local perturbations. To that end we introduce a local shift in chemical potential Δ, such that the chemical potential is shifted on site $(X, Y) = (0, 0)$ on the cluster, i.e.

$$\mu_{\mathrm{X,Y}} = \mu - \Delta\delta_{\mathrm{X},0}\delta_{\mathrm{Y},0}. \tag{B.1}$$

In Fig. B.4 we show the response of the uncondensed phases on a 4×4 system at $\nu = 2$ to this local perturbation. As can be seen in Fig. B.4a, while the individual momentum values of the $\boldsymbol{h}_{k,q}$-vector change with the strength of the perturbation Δ, the total winding of the vector around the origin remains stable even at such large values as $\Delta \approx t_\mathrm{max}$, while the single-particle

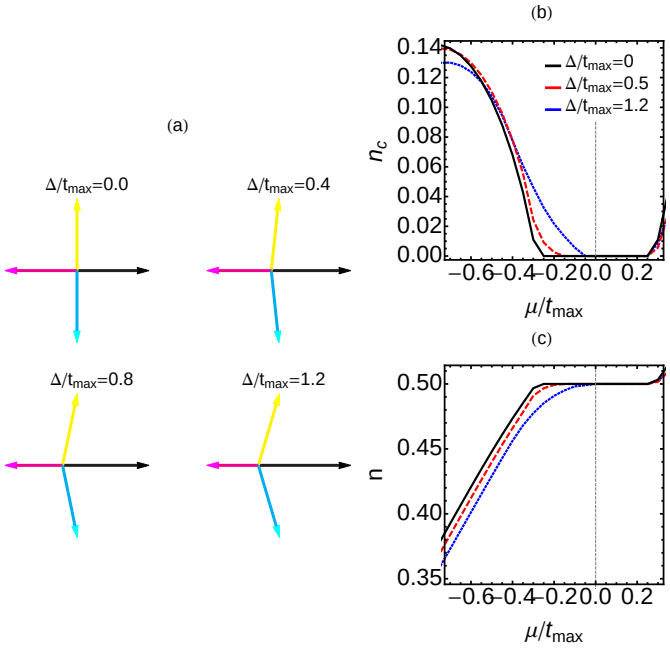

Figure B.4.: Stability of the winding against local perturbations. (a) Winding of the $\boldsymbol{h}_{k,q}$-vector for $\nu = 2$ at $t_x/t_y = 0.4$ and $\mu = 0$ for different perturbation strengths Δ [see Eq. (B.1)]. (b) and (c) Sweeps in chemical potential of the condensate density n_c and the total density n at $(t_x - t_y)/t_{\max} = -0.6$ and $\Delta/t_{\max} = 0$ (black), $\Delta/t_{\max} = 0.5$ (red dashed), and $\Delta/t_{\max} = 1.2$ (blue).

gap (i.e. the size of the plateau) decreases (see Figs. B.4b and B.4c). At larger values of Δ the phase has a non-zero condensate order parameter. A similar behavior can also be observed in the $\nu = 1, 3$ phases. In the full two-dimensional system we expect this robustness to vanish as the system-size is increased and the manybody gap goes to zero. In the cylindrical geometry however this points to a stability of the winding against disorder, indicative of topological protection.

B.3. Periodic boundary conditions vs. finite size clusters

As we want to project the full lattice system of Fig. 9.1a onto a finite cluster with periodic boundaries, i.e. with $\Psi(x + L_x, y) = \Psi(x, y + L_y) = \Psi(x, y)$, we are restricted to cluster sizes of $L_x \times L_y = m4 \times n4$ with integers n and m. This can easily be seen from the following effect: On a cluster of size $L_x \times L_y$ under the gauge of Fig. 9.1a, a particle hopping along the periodic boundary in x-direction, i.e. $(x, y) \to (x + L_x, y)$ will pick up a phase of $\phi_x(y) = L_x \Phi y$. For a flux of $\Phi = 2\pi/N_\Phi$ this will be equivalent to a global phase in $x-$direction of $\phi_x = 2\pi m$ only if $L_x = mN_\Phi$, while any other choice of L_x would introduce some additional artificial magnetic fields in the finite system, which cannot be gauged away through an additional boundary-phase, i.e.

$$\Psi(x + L_x, y) = e^{i\phi_x(y)} \Psi(x, y). \tag{B.2}$$

Another way to look at the same effect is the following: the dispersion for $\Phi = \pi/2$ shown in Fig. 9.1b, has 4 minima in k-direction. Any lattice with $L_x \neq m4$ would therefore break this 4-fold degeneracy of the non-interacting groundstate. In the y-direction any value of $L_y \neq n4$ would split up the 1×4 unit cell. A more general discussion of this effect can be found in Ref.

[200].

In the limit of large finite systems (or in the continuum limit $\Phi \ll 1$) this effect can be neglected, as a weak perturbation would not affect the system, especially in the case of topologically robust phases. In the system sizes which are accessible to us, however, such strong boundary effects will heavily affect the eigenstates for system sizes different from $m4 \times n4$. In fact in such "incommensurate" cluster sizes, gauge invariance is suddendly lost leading to different results for different gauges. In commensurate lattice sizes, on the other hand, the Hofstadter model retains its gauge invariance.

B.4. Current-current correlations

In the uncondensed phases which we discuss in Sec. 9.4 the current within the system is zero. However, as the system is not band insulating and the kinetic energy is non-zero this must result from two counter-propagating modes which cancel each other out. We can analyze these modes by measuring current-current correlations between neighboring bonds. By Eq. (9.13) we can write the currents on the full lattice $J_{\mathrm{x/y}}$ as expectation values of lattice-operators $\hat{J}_{\mathrm{x/y}}$ with respect to the RCMF Hamiltonian, i.e.

$$J_{\mathrm{x/y}}(x,y) = \langle \hat{J}_{\mathrm{x/y}}(x,y) \rangle$$

with $\hat{J}_{\mathrm{x/y}}(x,y)$ defined according to Eqs. (9.12)-(9.14). We now can look at the following current-current correlations:

$$\begin{aligned}
\Delta J_{\mathrm{x,x}}(x,y) &= \left\langle \hat{J}_{\mathrm{x}}(x,y)\hat{J}_{\mathrm{x}}(x+1,y) \right\rangle \\
\Delta J_{\mathrm{x,y}}(x,y) &= \left\langle \hat{J}_{\mathrm{x}}(x,y)\hat{J}_{\mathrm{y}}(x,y) \right\rangle \\
\Delta J_{\mathrm{x,y\text{-}1}}(x,y) &= \left\langle \hat{J}_{\mathrm{x}}(x,y)\hat{J}_{\mathrm{y}}(x,y-1) \right\rangle
\end{aligned}$$

These three quantities are enough to describe the current patterns depicted in Fig. 9.6d: if $\Delta J_{\mathrm{x,x}}(x,y)$ is positive the currents $J_{\mathrm{x}}(x,y)$ and $J_{\mathrm{x}}(x+1,y)$ point in the same direction, if it is negative they point in opposite directions. The same is also true for $\Delta J_{\mathrm{x,y}}(x,y)$ and $\Delta J_{\mathrm{x,y\text{-}1}}(x,y)$. Assuming a finite current in $+x$ direction on a given site (x,y) and extracting the sign of the currents on the neighboring bonds through the correlations introduced above, one can therefore easily draw one of the two counter-propagating current patterns. The other pattern results from simply inverting the direction of all currents.

B.5. Filling $\nu = 2/3$

Jain's sequence [32], a composite fermion approach to the HHMm (see Sec. 2.4.3) predicts a series of gapped phases at fillings $\nu = p/(p+1)$ for integer p. In this picture the fQH phase at filling $\nu = 1/2$ is equivalent to the first state of Jain's sequence at $p = 1$. The bosonic quantum Hall phase at $\nu = 2$ with $\sigma_{xy} = 2$ is equivalent to $p = -2$. Note that it does not exist for $\Phi = \pi/2$ with hard-core bosons (the charge-conjugation symmetry of Eq. (10.3) imposes $\sigma_{xy} = 0$ at $\nu = 2$), but was measured for lower fluxes in Ref. [82].

Ref. [82] further reports on a gapped phase at filling $\nu = 2/3$ and no hopping anisotropy at flux $\Phi = \pi/2$, equivalent to the next state in Jain's sequence after the $\nu = 1/2$ fQH (i.e. $p = 2$), i.e. Halperin's (211) state, which we do not observe in RCMF. We therefore turn to the ED spectrum of system sizes $L_x \times 4$ with $L_x = 6$, 9 and 12 to look for signatures of a gapped phase at filling $\nu = 2/3$ in Fig. B.5a. As can be seen for both $L_x = 6$ and $L_x = 12$ we do not observe

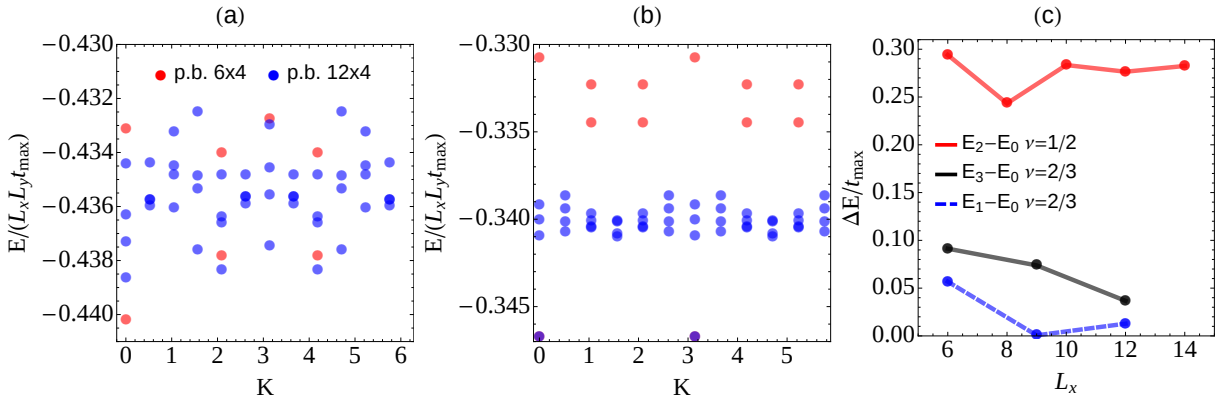

Figure B.5.: Comparison of the ED spectra at fillings $\nu = 2/3$ and $\nu = 1/2$. (a) and (b): Eigenvalues as a function of momentum sector K at $t_x = t_y$ and system sizes 6×4 (red) and 12×4 for fillings $\nu = 2/3$ (a) and $\nu = 1/2$ (b). (c) Many-body gap of the fractional phase at $\nu = 1/2$ (red) and gaps at $\nu = 2/3$ between the lowest and the first excited state (blue, dashed) and between the lowest and the third excited state (black) as a function of L_x.

a clear indication of a three-fold degeneracy of the ground-state expected for Halperin's (211) state.

In Fig. B.5c the distance between the lowest and the degenerate second and third eigenstate is shown as a function of L_x. While it generally decreases (and goes almost to zero at $L_x = 9$), so does the gap between the third and the lowest eigenstate (which would be the many-body gap in case the ground-state were truly three-fold degenerate). For comparison, we show in Fig. B.5b the spectrum for $\nu = 1/2$ for the same system sizes. Here, as expected, the ground-state is two-fold degenerate, and the many-body gap to the first excited state is considerably larger (around 1/4 of the hopping). In line with RCMF, the ED results do not seem to point toward the existence of a gapped state at filling $\nu = 2/3$.

Bibliography

[1] Hügel D and Pollet L 2015 *Phys. Rev. B* **9**1 224510

[2] Hügel D, Werner P, Pollet L and Strand H U R 2016 *Phys. Rev. B* **9**4 195119

[3] Hügel D, Strand H U R, Werner P and Pollet L 2017 *Phys. Rev. B* **9**6(5) 054431

[4] Kozarski F, Hügel D and Pollet L 2018 *New J. Phys.* **h**ttps://doi.org/10.1088/1367-2630/aab081

[5] Hügel D, Strand H U R and Pollet L 2018 *arXiv:1801.07274*

[6] Arrigoni E, Knap M and von der Linden W 2011 *Phys. Rev. B* **8**4 014535

[7] Wheatley J C 1975 *Rev. Mod. Phys.* **4**7 415

[8] Anderson P W 1966 *Rev. Mod. Phys.* **3**8 298

[9] Fisher M P A, Weichman P B, Grinstein G and Fisher D S 1989 *Phys. Rev. B* **4**0 546

[10] Ashcroft N W and Mermin D 1976 *Solid State Physics* (Sanders College Publishing)

[11] Jacksch D, Bruder C, Cirac J I, Gardiner C W and Zoller P 1998 *Phys. Rev. Lett.* **8**1 3108

[12] Bloch I, Dalibard J and Zwerger W 2008 *Rev. Mod. Phys.* **8**0 885–964

[13] Stoof H T C, Gubbels K B and Dickerscheid D B M 2009 *Ultracold Quantum Fields* (Springer Science+Buisness Media B. V., P.O. Box 17, 3300 AA Dordrecht, Netherlands)

[14] Krutitsky K V, Pelster A and Graham R 2006 *New J. Phys.* **8**

[15] Gurarie V, Pollet L, Prokof'ev N, Svistunov B and Troyer M 2009 *Phys. Rev. B* **8**0 214519

[16] Bissbort U, Thomale R and Hofstetter W 2010 *Phys. Rev. A* **8**1 063643

[17] Aidelsburger M 2016 *Artificial Gauge Fields with Ultracold Atoms in Optical Lattices* (Springer International Publishing Switzerland)

[18] He L, Ji A and Hofstetter W 2015 *Phys. Rev. A* **9**2 023630

[19] He L, Li Y, Altman E and Hofstetter W 2012 *Phys. Rev. A* **8**6 043620

[20] Harper P G 1955 *Proc. Phys. Soc. A* **6**8 Section A

[21] Hofstadter D R 1976 *Phys. Rev. B* **1**4 2239

[22] Ryu S, Schnyder A P, Furusaki A and Ludwig A W W 2010 *New J. Phys.* **1**2 065010

[23] Chen X, Gu Z C, Liu Z X and Wen X G 2012 *Science* **3**38 1604–1606 ISSN 0036-8075

[24] Lu Y M and Vishwanath A 2012 *Phys. Rev. B* **8**6 125119

[25] Kohmoto M 1985 *Annals of Physics* **1**60 343–354

[26] Hatsugai Y 1993 *Phys. Rev. Lett.* **7**1 3697–3700

[27] von Klitzing K, Dorda G and Pepper M 1980 *Phys. Rev. Lett.* **4**5 494

[28] Senthil T and Levin M 2013 *Phys. Rev. Lett.* **1**10 046801

[29] He Y C, Bhattacharjee S, Moessner R and Pollmann F 2015 *Phys. Rev. Lett.* **1**15 116803

[30] Tsui D C, Stormer H L and Gossard A C 1982 *Phys. Rev. Lett.* **4**8 1559

[31] Laughlin R B 1983 *Phys. Rev. Lett.* **5**0 1395

[32] Jain J K 1989 *Phys. Rev. Lett.* **6**3 199–202

[33] Sørensen A S, Demler E and Lukin M D 2005 *Phys. Rev. Lett.* **9**4 086803

[34] Morsch O and Oberthaler M 2006 *Rev. Mod. Phys.* **7**8 179

[35] Aidelsburger M, Atala M, Lohse M, Barreiro J T, Paredes B and Bloch I 2013 *Phys. Rev. Lett.* **1**1 185301

[36] Tiesinga E, Verhaar B J and Stoof H T C 1993 *Phys. Rev. A* **4**7 4114

[37] Struck J, Ölschläger C, Weinberg M, Hauke P, Simonet J, Eckardt A, Lewenstein M, Sengstock K and Windpassinger P 2012 *Phys. Rev. Lett.* **1**08 225304

[38] Greschner S, Sun G, Poletti D and Santos L 2014 *Phys. Rev. Lett.* **1**13 215303

[39] Goldman N and Dalibard J 2014 *Phys. Rev. X* **4** 031027

[40] Madison K W, Chevy F, Wohlleben W and Dalibard J 2000 *Phys. Rev. Lett.* **8**4 806

[41] Abo-Shaeer J R, Raman C, Vogels J M and Ketterle W 2001 *Science* **2**92 476–479 ISSN 0036-8075

[42] Lin Y J, Compton R L, Jiménez-García K, Porto J V and Spielman I B 2009 *Nature* **4**62 628

[43] Dalibard J, Gerbier F, Juzeliūnas G and Öhberg P 2011 *Rev. Mod. Phys.* **8**3 1523

[44] Bilitewski T and Cooper N R 2015 *Phys. Rev. A* **9**1(3) 033601

[45] Kennedy C J, Burton W C, Chung W C and Ketterle W 2015 *Nature Physics* **1**1 859–864

[46] Tai M E, Lukin A, Rispoli M, Schittko R, Menke T, Borgnia D, Preiss P M, Grusdt F, Kaufman A M and Greiner M 2017 *Nature* **5**46 519–523

[47] Prokof'ev N, Svistunov B and Tupitsyn I 1998 *J. Exp. Theor. Phys.* **8**7 310

[48] Trotzky S, Pollet L, Gerbier F, Schnorrberger U, Bloch I, Prokof'ev N, Svistunov B and Troyer M 2010 *Nat. Phys.* **6** 998–1004

[49] Pollet L 2012 *Rep. Prog. Phys.* **7**5 094501

[50] Lin Y J, Jiménez-García K and Spielman I B 2011 *Nature* **4**71 83

[51] Struck J, Simonet J and Sengstock K 2014 *Phys. Rev. A* **9**0 031601

[52] Jiménez-García K, LeBlanc L J, Williams R A, Beeler M C, Qu C, Gong M, Zhang C and Spielman I B 2015 *Phys. Rev. Lett.* **1**14 125301

[53] Jarrell M and Gubernatis J E 1996 *Physics Reports* **2**69

[54] Pippan P, Evertz H G and Hohenadler M 2009 *Phys. Rev. A* **8**0 033612

[55] Kühner T D and Monien H 1998 *Phys. Rev. B* **5**8

[56] Rapsch S, Schollwöck U, von Delft J and Zwerger W 1999 *Europhys. Lett.* **4**6

[57] Kollath C, Schollwöck U, von Delft J and Zwerger W 2004 *Phys. Rev. A* **6**9

[58] Kollath C, Läuchli A M and Altman E 2007 *Phys. Rev. Lett.* **9**8 180601

[59] Motruk J, Zaletel M P, Mong R S K and Pollmann F 2016 *Phys. Rev. B* **9**3 155139

[60] Chaikin P M and Lubensky T C 1995 *Principles of Condensed Matter Physics* (Cambridge University Press, the Edinburgh Building, Cambridge CB2 8RU, UK)

[61] Sachdev S 1999 *Quantum Phase Transitions* (Cambridge University Press, the Edinburgh Building, Cambridge CB2 2RU, UK)

[62] Byczuk K and Vollhardt D 2008 *Phys. Rev. B* **7**7 235106

[63] Hubener A, Snoek M and Hofstetter W 2009 *Phys. Rev. B* **8**0 245109

[64] Hu W J and Tong N H 2009 *Phys. Rev. B* **8**0 245110

[65] Anders P, Gull E, Pollet L, Troyer M and Werner P 2011 *New J. Phys.* **1**3 075013

[66] Snoek M and Hofstetter W 2013 *Quantum Gases: Finite Temperature and Non-Equilibrium Dynamics (Vol. 1 Cold Atoms Series)* (Imperial College Press, London, 2013)

[67] Anders P, Gull E, Pollet L, Troyer M and Werner P 2010 *Phys. Rev. Lett.* **1**05 096402

[68] Werner P, Comanac A, de Medici L, Troyer M and Millis A J 2006 *Phys. Rev. Lett.* **9**7 076405

[69] Gull E, Millis A J, Lichtenstein A I, Rubtsov A N, Troyer M and Werner P 2011 *Rev. Mod. Phys.* **8**3

[70] Potthoff M 2003 *The European Physical Journal B - Condensed Matter and Complex Systems* **3**2 429

[71] Potthoff M 2003 *The European Physical Journal B - Condensed Matter and Complex Systems* **3**6 335

[72] Potthoff M 2006 *Cond. Mat. Phys* **9** 557

[73] Potthoff M 2012 *Strongly Correlated Systems* (*Springer Series Solid State Physics* vol 171) (Berlin, Heidelberg: Springer)

[74] Koller W and Dupuis N 2006 *Journal of Physics: Condensed Matter* **1**8 9525

[75] Knap M, Arrigoni E and von der Linden W 2010 *Phys. Rev. B* **8**1 024301

[76] Potthoff M, Aichhorn M and Dahnken C 2003 *Phys. Rev. Lett.* **9**1 206402

[77] Lühmann D S 2013 *Phys. Rev. A* **8**7 043619

[78] Huerga D, Dukelsky J and Scuseria G E 2013 *Phys. Rev. Lett.* **1**11

[79] Maier T, Jarrell M, Pruschke T and Hettler M H 2005 *Rev. Mod. Phys.* **7**7 1027

[80] Hafezi M, Sørensen A S, Demler E and Lukin M D 2007 *Phys. Rev. A* **7**6 023613

[81] Möller G and Cooper N R 2009 *Phys. Rev. Lett.* **1**03 105303

[82] He Y C, Grusdt F, Kaufman A, Greiner M and Vishwanath A 2017 *Phys. Rev. B* **9**6 201103

[83] Motruk J and Pollmann F 2017 *Phys. Rev. B* **9**6 165107

[84] Gerster M, Rizzi M, Silvi P, Dalmonte M and Montangero S 2017 *Phys. Rev. B* **9**6 195123

[85] Zeng T S, Zhu W and Sheng D N 2016 *Phys. Rev. B* **9**3 195121

[86] Auerbach A 1994 *Interacting electrons and quantum magnetism* (Springer-Verlag New York)

[87] Capogrosso-Sansone B, Prokof'ev N and Svistunov B 2007 *Phys. Rev. B* **7**5 134302

[88] Kuehner T D, White S R and Monien H 2000 *Phys. Rev. B* **6**1 12474

[89] Mermin N D and Wagner H 1966 *Phys. Rev. Lett.* **1**7 1133

[90] Fisher M E, Barber M N and Jasnow D 1973 *Phys. Rev. A* 1111

[91] Kosterlitz J M and Thouless D J 1973 *J. Phys. C: Solid State Phys.* **6** 1181

[92] Cardy J 1996 *Scaling and Renormalization in Statistical Physics* (Cambridge University, Cambridge) ISBN 9780521499590

[93] Pollet L, Prokof'ev N, Svistunov B V and Troyer M 2009 *Phys. Rev. Lett.* **1**03 140402

[94] Shen S Q 2012 *Topological Insulators - Dirac Equation in Condensed Matter* (Springer-Verlag Berlin Heidelberg)

[95] Mahan G D 2000 *Many-Particle Physics* (Kluwer Academic/Plenum Publishers, 233 Spring Street, New York, New York 10013)

[96] Kitaev A Y 2003 *Annals of Physics* **3**03 2

[97] Read N 1998 *Phys. Rev. B* **5**8 16262

[98] Grimm R, Weidemüller M and Ovchinnikov Y B 2000 *Adv. At. Mol. Opt. Phys.* **4**2 95

[99] Goodman J W 1998 *Speckle phenomena in optics* (Roberts)

[100] Chen Y P, Hitchcock J, Dries D, Junker M, Welford C and Hulet R G 2008 *Phys. Rev. A* **7**7 033632

[101] Lye J E, Fallani L, Modugno M, Wiersma D S, Fort C and Inguscio M 2005 *Phys. Rev. Lett.* **9**5 070401

[102] Pasienski M, McKay D, White M and DeMarco B 2010 *Nat. Phys.* **6** 677

[103] Capogrosso-Sansone B, Giorgini S, Pilati S, Pollet L, Prokof'ev N, Svistunov B and Troyer M 2010 *New J. Phys.* **1**2 043010

[104] Natu S S, Mueller E J and Sarma S D 2016 *Phys. Rev. A* **9**3 063610

[105] Kleinert H 1982 *Fortschritte der Physik* **3**0 187

[106] Berges J, Borsanyi S, Reinosa U and Serrau J 2005 *Annals of Physics* **3**20 344

[107] Baym G and Kadanoff L P 1961 *Phys. Rev.* **1**24 287

[108] Baym G 1962 *Phys. Rev.* **1**27 1391

[109] Dominicis C D and Martin P C 1964 *Journal of Mathematical Physics* **5** 14

[110] Dominicis C D and Martin P C 1964 *Journal of Mathematical Physics* **5** 31

[111] Cornwall J M, Jackiw R and Tomboulis E 1974 *Phys. Rev. D* **1**0 2428

[112] Luttinger J M and Ward J C 1960 *Phys. Rev.* **1**18

[113] Kleinert H and Schulte-Frohlinde V 2001 *Critical properties of ϕ^4 theories* (World Scientific Publishing Co. Pte. Ltd., Singapore)

[114] Kozik E, Ferrero M and Georges A 2015 *Phys. Rev. Lett.* **1**14 156402

[115] Stan A, Romaniello P, Rigamonti S, Reining L and Berger J A 2015 *New J. Phys.* **1**7 093045

[116] Metzner W and Vollhardt D 1989 *Phys. Rev. Lett.* **6**2 324

[117] Georges A, Kotliar G, Krauth W and Rozenberg M J 1996 *Rev. Mod. Phys.* **6**8 13

[118] Akerlund O and de Forcrand P 2013 *arXiv:1311.4440*

[119] Akerlund O, de Forcrand P, Georges A and Werner P 2014 *Phys. Rev. D* **9**0 065008

[120] Knap M, Arrigoni E and von der Linden W 2011 *Phys. Rev. B* **8**3 134507

[121] Kleinert H, Narzikulov Z and Rakhimov A 2014 *J. Stat. Mech.* P01003

[122] Dawson J F, Cooper F, Chien C C and Mihaila B 2013 *Phys. Rev. A* **8**8 023607

[123] Cooper F, Chien C C, Mihaila B, Dawson J F and Timmermans E 2012 *Phys. Rev. A* **8**5 023631

[124] Mihaila B, Cooper F, Dawson J, Chien C C and Timmermans E 2011 *Phys. Rev. A* **8**4 023603

[125] Trefzger C and Sengupta K 2011 *Phys. Rev. Lett.* **1**06 095702

[126] Duchon E, Loh Y L and Trivedi N 2013 *Novel Superfluids* vol 2 (Oxford, UK: Oxford University Press)

[127] Kotliar G, Savrasov S Y, Haule K, Oudovenko V S, Parcollet O and Marianetti C A 2006 *Rev. Mod. Phys.* **7**8 865

[128] Potthoff M and Balzer M 2007 *Phys. Rev. B* **7**5 125112

[129] Hofmann F, Eckstein M, Arrigoni E and Potthoff M 2013 *Phys. Rev. B* **8**8 165124

[130] Hofmann F, Eckstein M and Potthoff M 2016 *J. Phys.: Conf. Ser.* **6**96 012002

[131] Aoki H, Tsuji N, Eckstein M, Kollar M, Oka T and Werner P 2014 *Rev. Mod. Phys.* **8**6 779

[132] Strand H U R, Eckstein M and Werner P 2015 *Phys. Rev. X* **5** 011038

[133] Boyd S and Vandenberghe L 2004 *Convex Optimization* (Cambridge University Press, the Edinburgh Building, Cambridge CB2 8RU, UKRU, UK)

[134] Negele J W and Orland H 1998 *Quantum Many-Particle Systems* (Westview Press)

[135] Jones E, Oliphant T and Petersen P 2001- Scipy: Open source scientific tools for python

[136] Rancon A and Dupuis N 2011 *Phys. Rev. B* **8**3 172501

[137] Rancon A and Dupuis N 2011 *Phys. Rev. B* **8**4 174513

[138] Crawford J D 1991 *Rev. Mod. Phys.* **6**3 991

[139] Pankov S, Kotliar G and Motome Y 2002 *Phys. Rev. B* **6**6 045117

[140] Strand H U R, Sabashvili A, Granath M, Hellsing B and Östlund S 2011 *Phys. Rev. B* **8**3 205136

[141] Lanata N, Strand H U R, Dai X and Hellsing B 2012 *Phys. Rev. B* **8**5 035133

[142] Hugenholtz N M and Pines D 1959 *Phys. Rev.* **1**16 489

[143] Rickayzen G 1980 *Green's functions and condensed matter* (Academic Press Inc.)

[144] Anders P, Werner P, Troyer M, Sigrist M and Pollet L 2012 *Phys. Rev. Lett.* **1**09 206401

[145] Panas J, Kauch A, Kunes J, Vollhardt D and Byczuk K 2015 *Phys. Rev. B* **9**2 045102

[146] Strand H U R, Eckstein M and Werner P 2015 *Phys. Rev. A* **9**2 063602

[147] Runge K J 1992 *Phys. Rev. B* **4**5 13136

[148] Rapscha S, Schollwoeck U and Zwerger W 1999 *Eur. Phys. Lett.* **4**6 559

[149] Niederle A and Rieger H 2013 *New J. Phys.* **1**5 075029

[150] Bissbort U and Hofstetter W 2009 *Eur. Phys. Lett.* **5**0007

[151] Dobrosavljević V and Kotliar G 1997 *Phys. Rev. Lett.* **7**8 3943

[152] Dobrosavljević V, Pastor A A and Nikolić B K 2003 *Europhys. Lett.* **6**2 76

[153] Byczuk K, Hofstetter W and Vollhardt D 2005 *Phys. Rev. Lett.* **9**4 056404

[154] Byczuk K 2005 *Phys. Rev. B* **7**1 205105

[155] Anderson P W 1958 *Phys. Rev.* **1**09 1492

[156] Potthoff M and Balzer M 2007 *Phys. Rev. B* **7**5 125112

[157] Knap M, Arrigoni E and von der Linden W 2010 *Phys. Rev. A* **8**2 053628

[158] Piraud M, Heidrich-Meisner F, McCulloch I P, Greschner S, Vekua T and Schollwoeck U 2015 *Phys. Rev. B* **9**1 140406

[159] Hügel D and Paredes B 2014 *Phys. Rev. A* **8**9 023619

[160] Schönmeier-Kromer J and Pollet L 2014 *Phys. Rev. A* **8**9 023605

[161] Bernevig B A and Zhang S C 2006 *Phys. Rev. Lett.* **9**6 106802

[162] Goldman N, Satija I, Nikolic P, Bermudez A, Martin-Delgado M A, Lewenstein M and Spielman I B 2010 *Phys. Rev. Lett.* **1**05 255302

[163] Miyake H, Siviloglu G A, Kennedy C J, Burton W C and Ketterle W 2013 *Phys. Rev. Lett.* **1**11 185302

[164] Atala M, Aidelsburger M, Lohse M, Barreiro J T, Paredes B and Bloch I 2014 *Nature Physics* **1**0 588

[165] Aidelsburger M, Lohse M, Schweizer M, Atala M, Barreiro J T, Nascimbéne S, Cooper N, Bloch I and Goldman N 2015 *Nature Physics* **1**1 162

[166] Möller G and Cooper N R 2015 *Phys. Rev. Lett.* **1**15 126401

[167] Hafezi M, Sørensen A S, Lukin M D and Demler E 2008 *Eur. Phys. Lett.* **8**1 10005

[168] Palmer R N, Klein A and Jaksch D 2008 *Phys. Rev. A* **7**8 013609

[169] Umucalilar R O and Oktel M Ö 2007 *Phys. Rev. A* **7**6 055601

[170] Umucalilar R O and Mueller E J 2010 *Phys. Rev. A* **8**1 053628

[171] Qi X L, Hughes T L and Zhang S C 2008 *Phys. Rev. B* **7**8 195424

[172] Lindner N, Auerbach A and Arovas D P 2010 *Phys. Rev. B* **8**2 134510

[173] Möller G and Cooper N R 2010 *Phys. Rev. A* **8**2 063625

[174] Möller G and Cooper N R 2012 *Phys. Rev. Lett.* **1**08 045306

[175] Li J R, Lee J, Huang W, Burchesky S, Shteynas B, Top F C, Jamison A O and Ketterle W 2017 *Nature* **5**43 91–94

[176] Sheng D N, Wan X, Rezayi E H, Yang K, Bhatt R N and Haldane F D M 2003 *Phys. Rev. Lett.* **9**0 256802

[177] Lu Y M 2017 *arXiv:1705.04691*

[178] Bergholtz E J and Karlhede A 2005 *Phys. Rev. Lett.* **9**4 026802

[179] Bergholtz E J and Karlhede A 2006 *Journal of Statistical Mechanics: Theory and Experiment* **L**04001

[180] Bernevig B A and Regnault N 2012 *arXiv:1204.5682*

[181] Grusdt F and Höning M 2014 *Phys. Rev. A* **9**0 053623

[182] Boada O, Celi A, Latorre J I and Lewenstein M 2012 *Phys. Rev. Lett.* **1**08(13) 133001

[183] Celi A, Massignan P, Ruseckas J, Goldman N, Spielman I B, Juzeliūnas G and Lewenstein M 2014 *Phys. Rev. Lett.* **1**12(4) 043001

[184] Mancini M, Pagano G, Cappellini G, Livi L, Rider M, Catani J, Sias C, Zoller P, Inguscio M, Dalmonte M and Fallani L 2015 *Science* **3**49 1510–1513 ISSN 0036-8075

[185] Stuhl B K, Lu H I, Aycock L M, Genkina D and Spielman I B 2015 *Science* **3**49 1514–1518 ISSN 0036-8075

[186] Anderson B M, Ma R, Owens C, Schuster D I and Simon J 2016 *Phys. Rev. X* **6**(4) 041043

[187] Kol A and Read N 1993 *Phys. Rev. B* **4**8 8890

[188] Sterdyniak A, Bernevig B A, Cooper N R and Regnault N 2015 *Phys. Rev. B* **9**1 035115

[189] Andrews B and Moeller G 2018 *Phys. Rev. B* **9**7 035159

[190] Furukawa S and Ueda M 2013 *Phys. Rev. Lett.* **1**11 090401

[191] Moore G and Read N 1991 *Nuclear Physics B* **3**60 362

[192] Sterdyniak A, Regnault N and Möller G 2012 *Phys. Rev. B* **8**6 165314

[193] Schiro M and Fabrizio M 2010 *Phys. Rev. Lett.* **1**05 076401

[194] Lanata N 2010 *Phys. Rev. B* **8**2 195326

[195] Lanata N and Strand H U R 2012 *Phys. Rev. B* **8**6 115310

[196] Fetter A L and Walecka J D 2003 *Quantum Theory of Many-Particle Systems* (Dover Publications Inc., 31 East 2nd Street, Mineloa, New York 11501)

[197] Matsubara T 1955 *Prog. Theor. Phys.* **1**4 351

[198] Altland A and Simons B 2010 *Condensed Matter Field Theory* (Cambridge University Press, the Edinburgh Building, Cambridge CB2 8RU, UK)

[199] Kleinert H 2009 *Path Integrals in Quantum Mechanics, Statistics, Polymer Physics, and Financial Markets* (World Scientific Publishing Co. Pte. Ltd., Singapore)

[200] Fremling M 2013 *J. Phys. A: Math. Theor.* **4**6 275302

Acknowledgements

This work wouldn't have been possible without the support of the people I list below, to which I want to direct my deepest gratitude:

... my supervisor **Lode Pollet** for making this thesis possible, always being available for help and discussions, guiding me throughout this thesis, while also giving me the freedom to develop my own ideas, and supporting my work in innumerable other ways. It's been a great and highly valued experience!

... **Frank Pollmann** for examining this thesis, valuable discussions, sharing unpublished data on the HHMm, and being part of my PhD commission.

... **Alexander Högele** and **Ivo Sachs** for being part of my PhD commission.

... **Hugo U. R. Strand** for great support, the many Skype meetings and several very pleasant and fruitful collaborations. We were a great team!

... **Filip Kozarski** for his valuable contributions to this work during his excellent Masters thesis.

... **Philipp Werner** for very fruitful collaborations and a pleasant time in Fribourg.

... **Tobias Pfeffer** for proof reading part of this thesis, and being a great office mate. I will always remember our many discussions, ranging from physics, global politics and art to football and gangster rap.

... **Sebastian Schulteß** for proof reading part of this thesis, and a memorable trip from Chicago to Montreal. Our daily work breaks were the perfect way to refresh and reorder my thoughts.

... **Peter Kroiss** for a warm welcome into the office as the "senior" group member, providing a light and fun atmosphere for everyone, and for a great time hanging out in the Canadian outbacks.

... **Jens Grimm** for his refreshing blend of irrational humour and rational seriousness, making my first year in the group a really fun (and confusing) time.

... **Jacopo Nespolo** and **Alessio Recati** for the daily coffee breaks and bringing a very welcome part of my second home into our group.

... the **Lo Studente** and **El Gusto** crew, for providing the great food for fun and interesting lunches with the people mentioned above, **Andrew Hayward**, **Jan Stolpp**, **Carlos Velasco**, and many others. Our lunch breaks were the highlights of any workday.

... **Cordula Weber** for all the perfect administrative support and always being patient, even though I forgot to hand in my time-sheet in time almost every month.

... **Marin Bukov**, **Ines de Vega**, **Nils-Oliver Linden**, **Ke Liu**, **Sam Mardazad**, **Fabian-Heidrich Meisner**, **Marie Piraud**, **Lev Vidmar**, **Alex Wolf**, and all other (former) residents of the fourth floor for the great time spent together.

... **E. Altman**, **E. Arrigoni**, **M. Eckstein**, **F. Grusdt**, **E. Gull**, **Y.-C. He**, **M. Knap**, **A. M. Läuchli**, **G. Möller**, **K. Sun**, and **N. Yao** for inspiring discussions that helped to create this work. I would also like to thank **A. M. Läuchli** for sharing unpublished ED data on the HHMm.

...last but not least **my family**, whose unlimited support and love have always given me the strength and confidence to carry this work through. Thank you for teaching me respect for intellectual work, and giving me the opportunity to be here today.